Hydrodynamics of highly-loaded axial flow tidal rotors

Federico Zilic de Arcos

St Catherine's College

University of Oxford

A thesis submitted for the degree of

Doctor of Philosophy

Trinity Term 2021

Acknowledgements

The research project presented in this thesis followed, as I imagine most long-term research projects do, an almost chaotic progression. The research decisions I made often took me through paths different than I had expected and taught me things I was not even aware I had to know. It has been a fantastic journey that allowed me to achieve what I believe are some exciting findings. I have tried to share these in this document, hoping that the reader might find them, if not useful, at least interesting.

This doctoral research would have not been possible without my two excellent supervisors: Dr. soon-to-be-professor Christopher Vogel, and Prof. Richard Willden. I cannot thank them enough for their patience, support, encouragement, and apparently endless supply of red pens.

I would like to extend my gratitude to the old and new members of the Wind and Tidal Research Group at the University of Oxford. In no order in particular, many thanks to Aidan Wimshurst, Bowen Cao, Mohamad Bin Osman, James McNaughton, Steven Ettema, Taka Nishino, Jack Kelly, Xiaoshen 'Shaun' Chen, Sam Harvey, Marcus Juniper, Maria Marinari, Markella Zormpa, Daniel Dehtyriov, Daniel Rowe, Amanda Smyth, and Andrew Kirby. This research group has been a continuous supply of technical insight, support, feedback, collaboration, and much more. Being part of this group of extremely talented people has been critical for the development of my work.

I also want to acknowledge those who encouraged me to pursue doctoral studies from the undergraduate years, supporting me on every step way beyond their academic responsibilities: Profs. Tatiana Santander, Marcos Salas, Gonzalo Tampier and Richard Luco. Further acknowledgment to Profs. Milton Lemarie, Rogelio Moreno, and Ricardo Burdisso, who fostered my interest in research and studying abroad.

Finally, my gratitude extends to those who make life worth it. Thanks to my parents, Susana and Héctor, who will probably reckon that their love and encouragement took me way too far from them; to my family, spread on both sides of the Andes; and to my friends, old and new, spread all over the world. Last, but certainly not least, thanks to my beloved Giedrė, whose love supported me through light and darkness.

As somebody says in the soundtrack of my DPhil: Gracias totales.

Abstract

This thesis presents a study on the hydrodynamics of a highly loaded tidal rotor designed for blockage using numerical models. First, the thesis presents a thorough evaluation of flow analysis methods for CFD simulations. This is a methodological review that enables a coherent and consistent study of axial-flow rotors with blade-resolved CFD simulations under different operational conditions including blade deformations, blockage, and transient flow effects.

Following the methodological assessment, a hydrodynamic analysis of a parametrically deformed axial-flow tidal rotor blade is discussed. The study shows the importance of blade deformations in rotor loads and performance. The hydrodynamics are decoupled by their twist and flapwise deformation components, with only the twist deformation effects successfully explained through two-dimensional blade-element theory. The hydrodynamic changes due to flapwise deformations, with a significant impact on loads and performance, are explained by changes in radial flow through the rotor and across the wake not considered in blade-element theory. These changes in flow induce an inboard load augmentation and an increase in near-tip load shedding, both affecting sectional lift and drag coefficients. The hydrodynamics of both deformation components are shown to be approximately independent of each other, which further enables an exploratory analysis of passive control strategies. Blade deflections as parts of passive control strategies are then shown as a potential alternative to active pitch control systems for tidal turbines.

The high-fidelity simulations were also used to evaluate the constituent parts of blade-element momentum (BEM) models. The simulation data was used to correct the empirical momentum function used at high-load regimes, significantly improving the predictive capabilities of a BEM model, whereas tip-loss correction models were identified as the most significant shortcoming in BEM modelling, greatly affecting the accuracy of the load and performance predictions.

The final part of the thesis evaluates the hydrodynamics of a catamaran-style floating tidal platform, designed to assess transient load effects on rotor blades. Using a seakeeping time-domain hydrodynamic model, coupled with a dynamic BEM model, which is verified through comparison with experiments and high-fidelity simulations, the floating tidal turbine was analysed under the combined effects of waves and currents. The result of this analysis highlights a non-linear interaction

between waves, platform motions and loads, having a limited impact on average power and thrust but with a dramatic change in load fluctuations. The analysis highlights the challenges of operating floating tidal rotors near the free surface.

Prologue

Format and presentation

The contents in the thesis are organised and presented in an integrated format. This format includes a combination of papers and regular chapters. The papers included in this thesis are modular and self-contained documents in the context of a bigger story. This implies that the required information on a specific topic is, most of the time, close at hand. However, the drawback is that some pieces of information are repeated in different chapters. I've attempted to reduce this as much as possible, but I hope the reader forgives me for the repetitions I could not escape from.

Another challenge of the integrated format is shared authorship. Three papers, with me as first author, and at different stages of publication, are included in this thesis. The inclusion of this papers counts with the approval of my co-authors, who also happen to be my doctoral supervisors. A statement of my contributions to each paper can be found below.

Scope and objectives

The main focus of my doctoral research was the study of the hydrodynamics of deforming tidal rotor blades. This involves understanding the hydrodynamic mechanisms that affect loads and performance on rotor blades as they deform, alongside with exploring the potential of passive blade deformations for practical applications. The study was made using, mostly, blade-resolved CFD (Computational Fluid Dynamics) simulations.

The main objectives of the thesis are summarised as:

1. Study the mechanisms driving hydrodynamic changes on deformed tidal rotor blades.

2. Explore the potential of deforming blades for practical tidal rotor applications.

3. Study the dominant dynamic flow effects on tidal rotors and their implications.

In addition, some secondary objectives were defined:

1. Explore and/or develop analysis methodologies for the study of blade-resolved CFD computations, to assist the study of blade deformation hydrodynamics.

2. Assist the development and/or improvement of engineering models for tidal rotors based on observations made from high-fidelity simulations.

3. Gain a further understanding of aspects that differentiate tidal stream energy from wind energy.

Thesis organisation and contributions

The thesis is divided in five main parts, each of these containing a varying number of chapters. The parts separate the document by different topics, and the chapters separate different work packages. Papers are introduced under the hierarchical level of chapters.

- **Part I: Introduction and literature review**

  Presentation of the background and motivations for the thesis, followed by a review of the state of the art.

- **Part II: Methods**

  1. *Rotor characteristics:*

     Chapter where details about the tidal rotor used throughout the thesis are provided.

  2. *Computational Fluid Dynamics:*

     Chapter dedicated to describe the simulation methods I used to generate research data.

  3. *Flow-field analysis techniques - Extracting angles of attack from blade-resolved rotor CFD simulations:*

     This chapter corresponds to a paper where I studied different methods to sample the flow field on blade-resolved CFD computations, as needed to extract the spanwise distribution of angles of attack or of any other flow-field. This paper sets the methodological base for the post-processing of high-fidelity simulations used throughout the thesis.

     My contributions to this paper include: conceptualising the study; preparing and running the CFD simulations of a tidal rotor; coding the different analysis methods; using the methods for analysing the tidal rotor simulations and an existing CFD dataset of a wind rotor; presenting the results and discussion; and writing the manuscript.

- **Part III: Hydrodynamics of rotor blade deformations**

1. *A parametric study on the hydrodynamics of tidal turbine blade deformations:*

   This chapter corresponds to a paper that analyses the hydrodynamics of the main blade deformation components.

   My contributions include: conceptualising the study; preparing and running the CFD simulations; post-processing and analysing the data; presenting the results and discussion; and writing the manuscript.

2. *A CFD study on the hydrodynamic independence of the twist and flapwise deformations on tidal rotor blades:*

   Chapter that corresponds to a paper that studies the hydrodynamic interactions between the two main deformation components. The paper is separated in two parts: in the first part, the independence of blade deformation components is assessed. In the second part, the findings of the first part are exploited to explore the potential of blade deformations as part of passive control strategies.

   My contributions to this paper are: conceptualising the study; preparing and running the CFD simulations; post-processing and analysing the data; presenting the results and discussion; and writing the manuscript.

- **Part IV: Observations on the engineering modelling of tidal rotors**

1. *Blade Element Momentum Theory:*

   This is a chapter where I present and discuss observations made from the blade-resolved CFD simulations in terms of the blade element momentum (BEM) model, suggesting improvements and potential areas for further improvement.

2. *Engineering modelling of transient flow effects:*

   Discussion of a dynamic BEM model, validated in literature against experiments of a tidal rotors under the influence of surface waves. The model was modified to account for rigid body motions, and verified against results from experiments and high-fidelity CFD simulations.

- **Part V: Hydrodynamics of a floating tidal turbine**

1. *Floating tidal rotors*

   This chapter presents the analysis of a floating tidal rotor based on a seakeeping time-domain model coupled with the dynamic-BEM model. Using this numerical model, I analysed floating and fixed rotors under the combined influence of currents and waves, comparing cases and highlighting interesting areas for future research.

List of publications

Journal publications

- F. Zilic de Arcos, C. R. Vogel, R. H. J. Willden. "A parametric study on the hydrodynamics of tidal turbine blade deformations". In: *Journal of Fluids and Structures*. Submitted.

- F. Zilic de Arcos, C. R. Vogel, R. H. J. Willden. "Extracting angles of attack from blade-resolved rotor CFD simulations". In: *Wind Energy* 23(9) (2020), pp. 1868-1885.

- F. Zilic de Arcos, G. Tampier, C. R. Vogel. "Numerical analysis of blockage correction methods for tidal turbines". In: *Journal of Ocean Engineering and Marine Energy* 6 (2020), pp. 183–197.

Conference publications

- F. Zilic de Arcos, C. R. Vogel, R. H. J. Willden. "Hydrodynamic analysis of turbine control through blade-deformation". In: *Developments in Renewable Energies Offshore: Proceedings of the 4th International Conference on Renewable Energies Offshore (RENEW 2020)* (2020).

- J. McNaughton, B. Cao, S. Ettema, F. Zilic de Arcos, C. R. Vogel, R. H. J. Willden. "Hydrodynamic analysis of turbine control through blade-deformation". In: *Developments in Renewable Energies Offshore: Proceedings of the 4th International Conference on Renewable Energies Offshore (RENEW 2020)* (2020).

- F. Zilic de Arcos, C. R. Vogel, R. H. J. Willden. "Hydrodynamic modelling of flexible tidal turbine blades". In: *Proceedings of the Thirteenth European Wave and Tidal Energy Conference (EWTEC 2019)* (2019).

- F. Zilic de Arcos, C. R. Vogel, R. H. J. Willden. "'Hydroelastic modelling of composite tidal turbine blades"'. In: *Developments in Renewable Energies Offshore: Proceedings of the 3rd International Conference on Renewable Energies Offshore (RENEW 2018)* (2018).

- G. Tampier, F. Zilic de Arcos. "Blade-resolved CFD analysis and validation of blockage correction methods for tidal turbines". In: *Developments in Renewable Energies Offshore: Proceedings of the 3rd International Conference on Renewable Energies Offshore (RENEW 2018)* (2018).

Contents

Nomenclature

Common Variables

α	Angle of attack
β	Twist angle
λ	Tip speed ratio
ω	Rotational speed of a rotor
ϕ	Inflow angle
ρ	Fluid density
σ	Rotor solidity
θ	Tangential coordinate
A	Rotor swept area
a	Axial induction factor
a'	Tangential induction factor
c	Local chord
C_θ	Tangential force coefficient
C_D	Drag coefficient
C_L	Lift coefficient
C_P	Power coefficient

C_T Thrust coefficient

C_x Axial force coefficient

D Drag force

g Gravitational acceleration

L Lift force

P Power

p Static pressure

p_∞ Undisturbed static pressure

R Rotor radius

r Local radius and radial coordinate

T Thrust

t Time

u Flow velocity expressed in Cartesian or cylindrical coordinates

V_∞ Undisturbed flow velocity

V_θ Tangential velocity component

V_r Radial velocity component

V_x Axial velocity component

W Local inflow speed.

x Axial coordinate

Z Number of blades

Part II - Methods

δ_{ij}	Kronecker delta
ℓ	Turbulence length scale
ϵ_{ijk}	Permutation symbol
μ	Dynamic viscosity
μ_t	Turbulent viscosity
ν	Kinematic viscosity
Ω	Rotational speed of a reference frame
ω	Specific dissipation rate
τ	Stress tensor
$\vec{\gamma}$	Bound circulation
$\vec{e_r}$	Unit vector in the radial direction
$\vec{U_\gamma}$	Circulation-induced velocity at a measuring point
$\vec{U}_{MP}$	Velocity sampled at a measuring point
ζ/c	Distance of a measuring point to the blade measuring over a constant radius
B	Blockage
C_μ	A constant of the $k-\omega$ SST turbulence model
I	Turbulence intensity
k	Turbulent kinetic energy
R_n	Reynolds number
$R_S(x)$	Radius of a streamtube expressed as a function of the axial coordinate
U_τ	Velocity at the edge of the boundary layer

u_τ Friction velocity

u_{avg} Mean velocity used for the calculation of turbulence intensity

y/c Cartesian distance from the blade to a measuring point

y^+ Non-dimensional wall distance

Part III - Hydrodynamics of rotor blade deformations

χ Change in axial momentum in the context of the radial loss analysis

$\delta\beta$ Twist deformation measured at the tip of the blade

$\delta x/R$ Non-dimensional flapwise deformation measured at the tip of the blade

γ Local bending angle of a blade with flapwise deformations

$\hat{n}_j$ Tangential-component of the surface-normal vector

$\mathcal{G}$ Global frame of reference

$\mathcal{L}$ Local frame of reference

Ψ Radial loss

$\vec{F}$ Force vector

$\vec{n}$ Surface-normal vector

h Distance from the rotor plane

p_0 Static pressure measured at a distance from the rotor

S Shear stress

Part IV - Observations on the engineering model of tidal rotors

κ, κ' Non-dimensional axial and tangential parameters

λ_r Local speed ratio at a specific radius

ω^* Non-dimensional pendular frequency

ω_e Wave encounter frequency

ω_W Wave frequency

ω_{osc} Dimensional pendular frequency

ω_{rot} Rotation frequency of a rotor under prescribed pendular motions

Φ, Θ, Ψ Roll, pitch and yaw angles.

Ψ Radial loss

Θ_i Azimuthal angle of blade i

$\vec{\eta}$ Wave elevation

$\vec{F}_a$ Added-mass force

$\vec{F}_{FK}$ Froude-Krylov force

$\vec{F}_{inertial}$ Inertial force

$\vec{V}_{motion}$ Motion-induced velocity relative to a blade section

$\vec{V}_{rel}$ Velocity relative to a blade section

$\vec{V}_{rot}$ Rotation velocity of a blade section

$\vec{V}_W$ Wave-induced velocity on a blade section

$\vec{W}$ Vector of axial and tangential induced velocities on a blade section

ζ_a Wave amplitude

A_0 Amplitude of a pendular motion

A_i Cross-sectional area of an aerofoil

C_L^{inv} Linear fit of a foil lift coefficient at pre-stall angles of attack

C_L^{st} Steady-state lift coefficient

f_s Separation function as a portion of foil chord

k_W Wave number

L_W Wave length

R_Φ, R_Θ, R_Ψ Roll, pitch and yaw rotation matrices

R_{Ω_i} Rotation matrix for blade i

T_L Tip loss correction factor

T_W Wave period

W_{qs} Steady-state induced velocity

Part V - Hydrodynamics of a floating tidal turbine device

$\bar{A}$ Added-mass matrix

τ Integration time variable

$\vec{F}_{ext}$ Vector of external forces applied to a rigid body

B_{tot} Total damping matrix

M_{RB} Rigid body mass matrix

T_e Encounter wave period

$X, \dot{X}, \ddot{X}$ Position, velocity and acceleration of a floating platform

Part I

Introduction and literature review

We often talk of saving the planet, but the truth is that we must do these things to save ourselves.

Sir David Attenborough

1 Background

Over the last decades, our world has seen a major increase in population and human activity. By 1950, the world was inhabited by an estimate of 2.5 billion humans. Since then, the world's population has risen to approximately 7.8 billion people [5], who now live longer and better than their ancestors did. The different phases of the industrial and scientific revolutions have increased almost every measure of human well-being through these years, with a consequent increase in our environmental footprint [13].

The rise in human activity in recent generations was powered, mostly, by burning coal, oil and gas. These fossil fuels are energy (and carbon) accumulated through millions of years of geological history by ancient photosynthesis. This legacy from past geological ages is not a renewable resource, and its combustion releases different compounds to the atmosphere. Combustion by-products, including carbon dioxide, contribute to the greenhouse effect that is driving climate change at a global scale [10].

The Paris agreement, an international treaty to tackle climate change, was signed in 2016 by 196 states. This is a long-term global strategy where countries agreed to reduce their greenhouse gas emissions to limit the rise in the average global temperature to values well below 2 degrees Celsius compared with pre-industrial levels. This level of reduction requires a significant financial and technological

commitment from the world's economies, that now need to quickly evolve towards carbon neutrality [12].

The level of commitment to this agreement varies between countries. The most developed economies are expected to contribute the most. The UK, for example, presented a plan to reduce its emissions by 68% by 2030 compared with 1990 levels, and to reach carbon neutrality by 2050.[11]. The European Union proposed to cut greenhouse emissions by 55% by 2030 [6] and reaching carbon neutrality by 2050 [7]. Developing countries are expected to make smaller but still significant contributions. Chile, for example, aims to reduce its emissions by 30% in 2030 compared with 2007 levels [2], and China aims to reach peak emissions before 2030 and reach net-zero by 2060 [1].

Despite some concerns that the commitment shown by the signatories of the Paris Agreement might not be enough [3], the Paris Agreement is an important declaration of principles and an instrument to drive action. This is of uttermost importance since significant scientific and technological challenges are still to be solved before reaching carbon neutrality.

From a macro perspective, there are two main technical challenges associated with decarbonisation. Firstly, we need to produce cost-efficient energy from renewable sources. This objective is well under way given the combined contributions of mature renewable energy technologies (hydropower, bioenergy and geothermal) alongside the fast development of utility-scale wind and solar energy industries, two sources which are already cost-competitive without subsidies [8]. The second challenge, however, is to have a stable and robust energy supply regardless of, for example, weather conditions.

The intermittent nature of wind and solar energy demands the implementation of balance systems in electricity networks. Networks must be capable of delivering a stable power supply when some resources are unstable or unavailable. A further penetration of renewables in general, thus, requires residual systems (i.e. non-intermittent energy sources and buffers such as batteries) to adapt to fast changing conditions, as well as improvements in network planning and stabilisation [4, 9].

Energy predictability, then, is a desirable feature for future installations, and is likely to play a significant role in the decarbonisation agenda.

References

[1] CGTN. *Full text: Xi Jinping's speech at Climate Ambition Summit 2020.* https://news.cgtn.com/news/2020-12-12/Full-text-Xi-Jinping-s-speech-at-Climate-Ambition-Summit-2020-WaztGQcuBO/index.html. Accessed:2021-09-19. 2021.

[2] Chilean Government. *Chile's nationally determined contribution, update 2020.* https://www4.unfccc.int/sites/ndcstaging/PublishedDocuments/Chile%20First/Chile%27s_NDC_2020_english.pdf. Accessed:2021-06-17.

[3] Climate Action Tracker. *Warming projections global update.* Cologne, Germany: New Climate Institute. Sept. 2020.

[4] P. Das et al. "Implications of short-term renewable energy resource intermittency in long-term power system planning". In: *Energy Strategy Reviews* 22 (2018), pp. 1–15.

[5] Department of Economic and Social Affairs, Population Division, United Nations. *World population prospects 2019: highlights (ST/ESA/SER. A/423).* 2019.

[6] European Union. *2030 climate energy framework.* https://ec.europa.eu/clima/policies/strategies/2030_en. Accessed:2021-06-17.

[7] European Union. *2050 long-term strategy.* "https://ec.europa.eu/clima/policies/strategies/2050_en". Online; Accessed:2021-06-17.

[8] IRENA. *Renewable power generation costs in 2019.* Abu Dhabi: International Renewable Energy Agency, 2020.

[9] X. Li, M. Paster, and J. Stubbins. "The dynamics of electricity grid operation with increasing renewables and the path toward maximum renewable deployment". In: *Renewable and Sustainable Energy Reviews* 47 (2015), pp. 1007–1015.

[10] V. Marchal et al. "OECD environmental outlook to 2050". In: *Organization for Economic Co-operation and Development* 8 (2011), pp. 397–413.

[11] UK Government. *Press release: UK sets ambitious new climate target ahead of UN Summit.* https://www.gov.uk/government/news/uk-sets-ambitious-new-climate-target-ahead-of-un-summit. Accessed:2021-06-17.

[12] UNFCCC Secretariat. "Report of the Conference of the Parties on its twenty-first session, held in Paris from 30 November to 13 December 2015". In: *United Nations Framework Convention on Climate Change, COP Report No. 21.* 2015.

[13] United Nations Development Programme. *Human Development Report 2020.* 2020th ed. United Nations, 2020.

2 Fundamentals of tidal stream energy

2.1 The tidal resource

The tides are a predictable and renewable energy resource. They occur due to the gravitational attractions of the Moon and the Sun on Earth, affecting the masses of water on Earth by deforming their surface in periodic motions that we call tides. The magnitude of these deformations depend on the relative position of the Moon and the Sun, with respect to the Earth, and the interaction between the masses of water in motion and local bathymetric conditions. Most oceanic tides in the world have relatively small tidal amplitudes, however sites such as the Bay of Fundy (Canada) or Avonmouth (England), for example, have tidal ranges in excess of 12 metres [16].

There are two main approaches to exploit the energy contained in the tides: tidal barrages, and tidal stream energy. The first approach exploits the oscillatory motion of the tides with artificial barriers, separating a basin from the sea similar to dams on rivers, to create one or more energy reservoirs. Energy is then extracted from the water when the level of the sea and the basin are different, constraining the inflow and the outflow with energy converters. The second approach, tidal stream energy, exploits the periodic and energy-dense currents in tidal channels with devices that convert mostly kinetic energy. These devices display similarities

with wind turbines, an established industry which benefits the tidal energy sector with a direct transfer of knowledge.

Tidal barrages, despite their predictability and encouraging results displayed by some large-scale projects in terms of energy production [52], have a significant environmental impact. They impose major disruptions to estuaries and coastal environments, changing the hydrology, salinity and other variables that affect the delicate balance of the ecosystems [74]. On the contrary, tidal stream devices, despite early concerns about the impact of rotors on marine life [20], can be designed to allow the passage of fish, water and sediment [74], with an overall environmental impact which is considered to be limited [81, 87]. The implementation of tidal stream energy converters is also compatible with a shared scheme of the maritime space, as farms could be designed to occupy only a fraction of the channel width and water column [68]. Tidal stream energy is also likely to have positive implications for the maritime sector and associated supply chains with a subsequent impact in coastal communities, making this energy source an appealing alternative from different perspectives.

The tidal stream resource is significant across the globe. In Europe, for example, there is a potential to generate approximately 102 TWh per year, with a technically feasible resource estimated in 50.2 TWh per year only in the UK [39]. This figure is similar to the 50.3 TWh produced with nuclear energy in the UK in 2020 [84]. Other examples are the United States, with a technical potential of 222-334 TWh/year [70]; and Chile, with a potential of ca. 11 TWh/year [19] that represents approximately 14% of the electricity generated by the country in 2020.

The technology to generate electricity from tidal streams appears to have converged towards axial-flow rotors, similar in concept to those used to extract energy from the wind. Several pre-commercial projects based on this technology have been developed, implemented and connected to utility networks: Orbital Marine's O2 [71], Simec Atlantis AR1500 [6], Hammerfest Strøm HS1000 [3], among others. These projects have been successful in proving the technological feasibility of tidal stream energy. Nevertheless, technological improvements are still required to enable cost reductions for this energy source to become competitive at large scale.

Operating in marine environments, as opposed to wind rotors, still involves significant challenges. Some of the differences between wind and tidal stream include the larger density of the fluid, with seawater approximately 800 times larger than air; the significant levels of environmental turbulence, shear, and surface waves, variables that affect loading and performance; the blockage effects experienced by the rotors, both global and local, that increase energy yields but also loads; the risk of cavitation with potentially harmful effects; the effects of the marine environment and living organisms on energy converters, including bio-fouling and corrosion; the significant influence of platform motions that affects floating devices; and the challenges for the installation, operation and maintenance required for long-term deployments, which are severely constrained by the availability of supply chains and suitable weather conditions [1].

2.2 Steady-state performance and load characterisation of axial-flow tidal rotors

Axial-flow rotors operate by removing energy from the flow. To do so, they impose a resistance in the form of a thrust force, T, to extract an amount of power P from the flow. The steady-state performance and loading of axial-flow rotor are typically characterised by the non-dimensional power and thrust coefficients, C_P and C_T:

$$C_P = \frac{P}{\frac{1}{2}\rho V_\infty^3 A} \tag{2.1}$$

$$C_T = \frac{T}{\frac{1}{2}\rho V_\infty^2 A} \tag{2.2}$$

where ρ is the fluid density, V_∞ is the undisturbed flow velocity, and A the swept-area of the rotor.

The power and thrust coefficients are characteristics of each rotor design, and the most basic characterisation of the performance and loading is made by the C_P and C_T curves, presented as functions of the tip-speed ratio λ:

$$\lambda = \frac{\omega R}{V_\infty} \tag{2.3}$$

where ω is the rotational speed and R the rotor radius.

Despite the effects of the Reynolds number R_n (especially when R_n is below the Reynolds-independent region [57]) and blockage, the power and thrust curves allow the steady-state power and loads on a rotor to be estimated at different flow speeds.

The performance characteristics of a tidal rotor can also be measured against an idealised criterion for optimal operation. Lanchester [48] and Betz [10] determined, independently from each other, that the maximum power that can be extracted by a rotor operating in an unconstrained flow (i.e. a flow where the boundaries are sufficiently far as to not affect the rotor loads nor its performance) is determined by a maximum power coefficient of $C_{PMax} = 16/27 \approx 0.593$ [1]. This maximum power coefficient is known as the Lanchester-Betz limit and is an expression of a theoretical limit for rotors in unconstrained flows. This limit, however, can be affected in the case of tidal turbines.

2.3 Blockage

Blockage is normally described as the interaction phenomena between a body immersed in a flow-field, and the boundaries that constrain the flow. Often observed in experimental facilities such as wind tunnels, flumes and towing tanks (see e.g. Glauert [32], Bahaj et al. [7]), blockage has significant implications for tidal energy, where a rotor or a fence of rotors could block a significant part of a channel. Under such conditions, a tidal rotor would operate differently from one operating in an unconstrained flow.

In the case of axial-flow rotors, blockage effects are often observed as an increase in power and thrust, compared with the same rotor in an unconstrained flow at the same flow speed. The change in performance occurs as a consequence of changes in flow speed across the rotor, an acceleration of the bypass flow due

[1] A complete derivation of the Lanchester-Betz limit can be found in Burton et al. [15].

to the confinement, differences in flow development, wake mixing and expansion, and due to longitudinal pressure variations due to the rotor operation, boundary layers and fluid losses in general [32].

Blockage also affects the theoretical limit for power extraction. Garrett and Cummins [30] demonstrated that the Lanchester-Betz limit could be exceeded in a blocked flow, leading to a maximum power coefficient of $C_{PMax} = 16/27(1 - B)^{-2}$, where B is the global blockage determined by the ratio between the rotor swept area and the channel cross-sectional area. This implies that the performance of tidal stream rotors could be, at least theoretically, larger than their wind counterparts.

The idea of blockage can be further extended to a collection of rotors, forming a fence or a farm, that completely or partially spans a channel. Nishino and Willden [68] explored, using a two-scales model based on actuator-disc theory, the efficiency of an array of tidal turbines partially blocking a channel, introducing the concepts of global and local blockage as parameters for optimisation. The first one is defined as the ratio of the total swept area of the rotors that form a fence, to the total channel cross-sectional area. The second is defined as the ratio between the swept area of one rotor to the local passage area, determined by the space between consecutive rotors in a fence. Those two parameters were found to have an impact in the global efficiency of tidal farms, and they determined a maximum power coefficient of $C_{PMax} = 0.798$ for an array in an infinitely wide channel, a potential limit which is 35% larger than Lanchester-Betz's.

Exploiting this larger energy extraction potential in constrained flows requires bespoke rotors. Schluntz and Willden [79] developed a design methodology to optimise rotors for different blockage conditions. Using three-dimensional CFD (Computational Fluid Dynamics) RANS (Reynolds-Averaged NavierStokes) simulations that considers the rotor as a disc where, based on the forces predicted by a blade-element model, a pressure discontinuity and a swirl velocity are prescribed onto the flow, they optimised rotor designs for four different blockage conditions. Their research showed that rotors with larger chords are generally more effective operating at high-blockage conditions. Wimshurst and Willden [88] further explored these

designs by performing blade-resolved RANS CFD simulations of two rotors from the previous study at different blockages and tip-speed ratios. Their results confirmed that blockage increases loads and performance for the two analysed designs, and showed that higher-solidity blades (designed for higher blockages) outperform those with a lower-solidity (optimised for low blockage) at higher blockage ratios. These high-fidelity simulations also demonstrated the feasibility of achieving C_P values above the Lanchester-Betz limit for a real tidal rotor.

Most of the design tools that the tidal energy sector inherited from the wind energy industry were developed for unconstrained flows. Similarly, different experimental facilities for model testing may recreate different blockage ratios, which could also differ from deployment sites for real-scale rotors. To account for this type of problem, methods have been developed to calculate the performance of rotors under varying blockage conditions from known C_P and C_T at a specific B.Zilic de Arcos et al. [89] assessed 7 different blockage correction methods, including one proposed by the authors, using blade-resolved RANS CFD simulations. They simulated 5 different blockage cases, from 1% to 40%, with the rotor operating at 4 different tip-speed ratios, from 4.0 to 7.0. The study showed that the correction proposed by Mikkelsen and Sørensen [60] produced the best predictions, although closely followed by the correction proposed by Bahaj et al. [7]. A prediction method proposed by the authors was shown to produce accurate results, but the inclusion of an empirical parameter required further validation.

Note that the correction methods studied by Zilic de Arcos et al. [89] were developed for isotropic blockages. This specific form of blockage considers a rotor positioned at the centre of a cylindrical domain, and differences are likely to occur in channels with different shapes and aspect ratios, as shown by Nishino and Willden [69] using actuator-disc RANS models. To the best of the author's knowledge, correction methods have not been developed for non-isotropic blockage conditions.

The positioning of the rotor also plays a role in the interactions with channel boundaries. A special case of boundary interaction is that between a rotor and the free surface in an open-channel flow, which some authors describe as a form

of blockage that can influence rotor performance [46]. Houlsby et al. [40] and Whelan et al. [86] explored the free surface past a tidal rotor by formulating novel actuator-disc models. They demonstrated that a head reduction occurs past the rotor, changing the cross-sectional area and bypass flow characteristics, affecting rotor loading and performance. These simple models open the discussion for more detailed analyses of the consequences of free surface interactions. Kolekar et al. [46], for example, ran an experimental campaign using a constant chord and constant pitch rotor. Their research showed that an asymmetric bypass flow develops as the rotor distance to both the free surface and the bottom change. They also determined that power is affected by the tip clearance to the free surface, and the optimum mean power was not found at the smallest nor the largest tip clearance, suggesting a potential for optimisation.

The development of asymmetric flows have implications in terms of blade loading. Even for a simplified steady-state case of a rotor operating in non-isotropic blockage conditions, the rotor blades will sample different flow speeds at different azimuthal positions. The azimuth-varying flow speeds seen by a blade, then, will induce time-varying loads.

2.4 Transient loads on rotor blades

The highly-energetic sites where rotors are likely to be deployed display site-specific time-varying flow conditions. These transient flow effects act on the rotors and are likely to induce transient loads and long-term fatigue effects that could induce premature blade failure [45]. The main transient flow phenomena that affect rotors are shear flow, environmental turbulence, and surface waves, as shown in fig. 2.1. However, even steady non-isotropic interactions between the rotor and its surroundings can induce time-varying loads.

2.4.0.1 Shear flows

Shear in the flow is a depth-dependent variation in flow speed that occurs as a consequence of friction between the flow and the seabed. Field measurements show

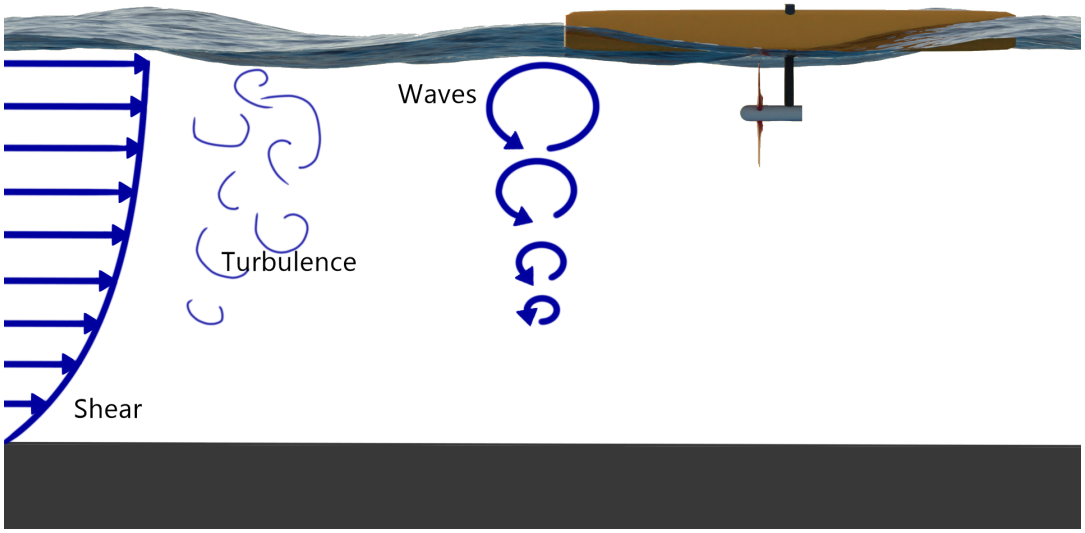

Figure 2.1: Diagram of the environmental conditions affecting a floating tidal rotor.

high levels of shear in tidal channels, with flow speed variations that could be larger than 50% near the bottom (see e.g. Gunn and Stock-Williams [37], Mason-Jones et al. [56]). Most of these variations tend to occur in close proximity to the bottom, but their influence can be extended over a significant part of the channel depth, with characteristics that are strongly dependent on local bathymetry.

Similarly to anisotropic blockages, for the simplest case of a steady state shear flow, rotor blades sample depth-varying flow velocities, inducing fluctuations in the local angles of attack, and affecting loads. The magnitude of these fluctuations, however, were shown by Scarlett and Viola [78] to be relatively small for a tidal rotor compared with waves and turbulence.

2.4.0.2 Turbulence

Turbulence is an apparently chaotic three-dimensional phenomenon that appears as irregularities in the flow. These take the form of changes in flow speed and pressure that occur due to vortices of different scales and intensities. Turbulence affects the flow mechanics and, thus, the loads and performance of tidal rotors.

Turbulence is typically quantified by the turbulence intensity, the standard deviation of velocity fluctuations normalised by the mean flow speed; and length

scales, which can be understood as the size of the eddies that contain most of the turbulent kinetic energy. Tidal channels of energetic interest often display high turbulence levels: typical intensities can be in the range of 6-15% [36, 61, 62, 80], and length scales in the order of 10-14 m for a typical rotor hub height [62, 88]. These characteristics, however, tend to be site-specific, anisotropic, and depend on the time and the location of the measurements [11].

The effects of turbulence on blade loading and performance can be significant. Fernandez-Rodriguez et al. [27] studied the turbulent effects on thrust on a model scale turbine. Using an extreme-event analysis, they determined that the 0.01% exceedance forces could reach values 1.59 times the average thrust. Mycek et al. [65] performed towing tank experiments of a model turbine and reported significant effects of turbulent intensity on wake recovery and performance. Specifically, they report mild reductions in mean power and thrust coefficients after increasing the turbulence intensity from 3% to 15%, with a considerable increase in the standard deviation on the thrust and power over time. Similarly, Milne et al. [62] report that blade root bending moments can exceed the steady values by 25% where delayed separation and dynamic stall occurs. Blackmore et al. [11] studied experimentally the effects of turbulence on a scaled tidal rotor. They also reported a negative influence of turbulent intensity in rotor mean power and thrust, along with an increase in load variability. The variations were reported to be in the order of 10% and 15% of the mean power and thrust coefficients, respectively, for a turbulent intensity of 14.3%. The individual blade fluctuation intensity of root moments, however, were observed to reach maximum variations in the order of 18 and 55% on the flapwise and edgewise directions, respectively, while operating at a turbulence intensity of 14.3%.

2.4.0.3 Waves

Waves are a form of energy propagation across the ocean. They originate from perturbations on the free surface typically due to an energy exchange with the atmosphere, although different perturbations may also generate them. Waves affect offshore structures not only by perturbing the free surface level, but also due to

time and depth-dependent velocity and pressure oscillations. For the practical study of waves, these are typically categorised in regular and irregular; the first case being a sea state determined by a single wave harmonic, and the second by multiple harmonics which can be characterised by a spectrum.

Waves are, potentially, the largest contribution to the unsteady loading on tidal rotors. Barltrop et al. [8] presented one of the first experimental studies on the current-wave interaction and its effects on axial-flow rotors. Using towing tank experiments, they determined that the presence of regular waves does not affect significantly the mean thrust, but they showed them to have a significant effect on load oscillations. They also showed that a simple quasi-static model based on blade-element momentum (BEM) theory and first-order wave theory can accurately describe the impact of waves on rotor loads and performance for relatively small waves. A similar observation was made by Faudot and Dahlhaug [25], while adding to the discussion that the added-mass effects, not considered by the previous study, are small for a fixed and rigid rotor. Gaurier et al. [31] and Luznik et al. [51] gave further confirmation of the importance of transient loads caused by waves, which Galloway et al. [29] quantified by a maximum of 175% of the median flapwise root bending moment on a blade, and 100% of the median edgewise root moment, again without reporting significant changes to the mean power and thrust. Jesus Henriques et al. [42] and Guo et al. [38] also confirmed those observations, reporting no significant changes to the mean power and thrust of a rotor in waves, although observing significant oscillatory loads.

Martinez et al. [55] tested a 1.2 metre diameter rotor in the FloWave experimental facility under the effect of oblique currents and waves. Their results showed a mild increase in power coefficient for a yaw angle of 10 degrees (maximum in the order of 10%) and reported the standard deviations of thrust and power to double on the cases with waves. Draycott et al. [21] analysed the impact of regular waves on a 1.2m diameter turbine, also at FloWave. They observed large variations in power and thrust that increase with wave amplitude and decrease with frequency. They report the peak values for thrust and power to exceed the current-only cases by 7% to

65% and 13% to 160%, respectively. Using the same rotor and experimental facility, Draycott et al. [22] studied the impact of irregular waves based on realistic open-ocean spectra over a full tidal cycle, showing similar trends to those observed with regular waves. They also report an impact on the current-wave interaction which is observed as changes to wave heights, reporting wave heights nearly four times larger under opposing currents. No effects were observed under these conditions to the mean thrust and power under the presence of waves. Draycott et al. [23] add to the discussion the azimuthal variation of the blade root bending moments under irregular waves, showing higher loads around the top dead centre and confirming the concentration of the wave effects closer to the free surface. This follows the discussion presented by Guo et al. [38], who observed a reduction on transient wave loads when increasing the rotor submergence depth.

2.4.0.4 Floating platforms

Both academia (Brown et al. [13], Ransley et al. [77], Turnock et al. [83]) and industry (Orbital's O2 [71], Sustainable Marine Energy's Plat-I [41], Magallanes Renovables' Atir [54]) have shown an interest in the design, development and implementation of floating tidal turbine devices due to the higher flow speeds at the top layers of the water column and advantages in installation, operation and maintenance [14]. Nevertheless, floating tidal rotors add an extra layer of complexity to rotor analysis associated with the rigid-body motions of the whole system in response to environmental loads.

The rigid-body motions of a floating tidal device are a consequence of the dynamic behaviour and interaction of all its components, both between themselves and with the environment. The rotor(s), float(s) and moorings, are dynamically excited by currents, waves, tides and wind.

Platform motions can be represented by six degrees of freedom, three translational (surge, sway and heave) and three rotational (roll, pitch and yaw), as shown in fig. 2.2. Only three degrees of freedom on a floating tidal platform are self-restoring due to hydrostatics and their response is a function of platform design

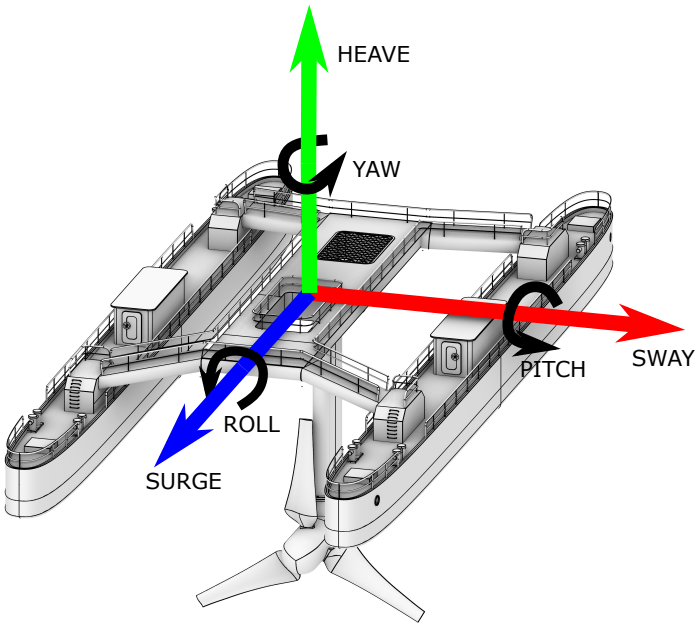

Figure 2.2: Representation of the motions of a floating tidal platform by six degrees of freedom.

(heave, roll and yaw), while the dynamics of the remaining three is governed by moorings and/or by other station-keeping solutions [28].

Platform motions induce time and position-dependent variations in the relative flow seen by the rotor blades. Osman et al. [73] and Osman and Willden [72] studied the effects of prescribing surge and pendular (an angular oscillation around an axis located far from the rotor, mimicking the pitch of a floating platform) motions on a tidal rotor, respectively, under a steady inflow. They demonstrated, using blade-resolved CFD RANS simulations , that the transient load variations due to rigid-body motions are likely to be of the same order of magnitude as those induced by surface waves (sec. 2.4.0.3). Their simulations also demonstrate a modest impact on average thrust and power for modest oscillations. Nevertheless, they showed that, where oscillations are large enough to create flow separation on the blades, mean thrust and power can be affected.

The coupled problem of a tidal rotor attached to a floating platform has not been thoroughly studied yet. One of the few studies on the subject, to the best of the author's knowledge, was performed by Brown et al. [14]. They analysed a

catamaran-style floating tidal device in a flume, where the rotor was modelled using a porous disc and catenary moorings for station-keeping. They found a significant impact of platform motions on rotor loads, especially for pitch (consistent with the observations of Osman and Willden [72]); a limited effect of waves and motions on average thrust; and recognised challenges in power delivery and fatigue for such devices due to the large amplitude of load oscillations.

2.5 Loads and blade deformations

As a consequence of the loads described in previous sections, tidal rotor blades deform. The deformations can be significant, depending on the structural and material configuration. Rotor blades designed with flexible composite materials are likely to exhibit large deformations: Nicholls-Lee [67], for example, calculated a tip deflection of 1.48 m for a 10 m radius tidal rotor; Grogan et al. [35] predicted a deflection of 1.75 m for a 12 m length tidal rotor blade; and Rafiee et al. [76] a maximum deformation of 1.46 m for a 23.50 m radius wind rotor. These magnitudes of blade deformation, as will be discussed later in this thesis, can induce changes in rotor thrust and performance. Such effects can be exploited from design to achieve specific control objectives, for which bespoke control strategies as well as a thorough understanding of the deformation hydrodynamics is required.

Blade deformations can be decomposed in three main components: flapwise or out-of-plane deformation; edgewise or in-plane deformation; and twist deformation. The flapwise deformation originates from the thrust forces acting on the blades; the edgewise deformation by the tangential forces that make the rotor spin; and the twist deformation which is driven by the torsional moments acting on the blade and structural deformation couplings and material anisotropy, affecting the spanwise angle of attack distribution. A schematic of the blade deformations is provided in part III.

Blade deformations are hydrodynamically similar to blade coning. Madsen and Rasmussen [53] studied different flapwise coning configurations (including geometric configurations that resemble blade deflection) with a constant-load axisymmetric

actuator-disc CFD model. Their research showed that coning affects axial and radial flow velocities across the rotor, although they concluded that the power coefficient is independent from the coning shape and angle. Mikkelsen et al. [59] analysed the flow field around a coned rotor, using a blade element momentum method and an actuator-disc CFD approach. Their results confirm the conclusions of Madsen and Rasmussen [53], extending it to an actual rotor with a non-constant load distribution: despite observing local power variations at different spanwise locations, the projected-area C_P appeared to be constant regardless of the cone angle. Crawford [18] studied the same coned rotor as Mikkelsen et al. using a novel BEM model. His results, however, showed thrust reductions across the entire span of the blade along with significant drops in C_P compared with Mikkelsen et al. [59] results.

The early analyses on coned rotors did not account for the interaction between the fluid mechanics and the structural reactions. Many authors, however, have also proposed methods of different fidelity to analyse the complex fluid-structure interaction problem on axial-flow rotors, improving the understanding on the impact of blade deformations in rotor aero- or hydrodynamics. Typical models for fluid-structure interaction are implemented by coupling a solver for the fluid dynamics (e.g. BEM, CFD) and a solver for the structural mechanics (e.g. a finite elements solver with beam elements), with both of them sharing information and iterating until some kind of convergence is achieved.

Engineering models for aeroelastic axial-flow rotor modelling, typically based on blade-element momentum and simple structural models, are normally preferred for commercial rotor design and to perform large-scale computations. OpenFAST [43] and HAWC2 [49] are probably the most established models of this kind. Their relatively low computational cost allow performing a large number of calculations as required in, e.g., rotor optimisation, or in the computation of long time-series for offshore analyses (see e.g. Jonkman and Buhl [44], McWilliam et al. [58]). Their reliance on basic modelling assumptions and/or empirical corrections, however, can make them inadequate for analyses outside their intended scope of application.

Apart from the established models, many authors have described different models of relatively low computational cost. Murray et al. [63], for example, developed a design tool coupling BEM with a shell-based finite elements solver, using 2D lift and drag coefficients from XFoil [24] and applying point loads at 10 spanwise locations. Murray et al. [64] presented a comparison between their design tool and towing-tank experiments, showing a relatively good agreement in terms of the integrated power and thrust, and presenting a flexible blade design capable of reducing peak loads. Zilic de Arcos et al. [90] coupled a BEM solver with a shell-based finite elements solver. The load cases were created by generating three-dimensional pressure fields from 2D pressure distributions pre-calculated with CFD, and interpolated at the BEM-computed local angle of attack. The authors verified load-cases generated with this model with blade-resolved CFD RANS computations, and then used the model to calculate the steady performance of a flexible carbon fibre tidal rotor blade. The model showed a non-negligible influence of blade deformations in rotor loads and performance, despite the high stiffness of the structural arrangement. Rafiee et al. [76] also coupled a finite elements software with BEM, applying the thrust and tangential forces as distributed loads at the aerodynamic centre of each aerofoil section. The authors first analysed the steady performance of a 660kW wind rotor, showing a performance reduction on the deformed blade. The steady analysis was followed by a dynamic study that determined that the structure was stable at rated flow speed but with fluttering risk near cut-out speed.

Using a different approach, Nicholls-Lee [67] and Nicholls-Lee et al. [66] developed a design methodology based on a potential-flow model coupled with a shell-based finite-elements structural solver. Their model worked by iterating between a three-dimensional panel code, which generates load cases based on operational conditions, and then applying the hydrodynamic pressures on the structural model. The structural solver then resolves the static deformation for that load case, and returns the deformations back to the hydrodynamic solver, iterating until a steady-state convergence is achieved. This model was employed as a design

tool to optimise the structural configuration of a tidal rotor blade, exploiting bend-twist material couplings.

High-fidelity models, integrating blade-resolved CFD computations with structural solvers, have also been proposed. Such models are able to implicitly capture the hydrodynamic changes that occur as a consequence of blade deformations, but their computational cost still limits their applicability for practical applications. Bazilevs et al. [9] presented the first fully-coupled unsteady blade-resolved CFD solver with a shell-based structural model, testing it with the NREL 5MW wind turbine, and showing a relatively good agreement in terms of torque. More recently, Lothodé et al. [50] used blade-resolved CFD simulations coupled with dynamic beam elements to model the tidal rotor designed by Bahaj et al. [7]. Their model was used to simulate the rotor with three different stiffness configurations, showing a significant decrease in power coefficient for the most flexible blade, and a very limited impact of stiffness in integrated thrust. Their model was used to study the interaction between the rotor and the supporting tower, finding transient effects that could contribute to fatigue failure. Grinderslev et al. [33] analysed a 2.3 MW wind rotor with an in-house FSI code. Their code coupled the RANS CFD solver EllipSyS3D with the aeroelastic model HAWC2, blending the BEM-based and CFD hydrodynamic loads over a multi-stage solution process to enhance convergence, ultimately solving the structural problem with beam elements with the loads from the CFD solver. The model was employed to analyse three cases: a simple homogeneous flow, a case with shear flow, and a case with sheared and yawed flow. Their paper reports small variations between the cases with rigid and flexible blades, presumably due to the pre-coning of the rotor and low flapwise and twist deformations, alongside a good agreement with experiments (5% to 7% of error for the integrated loads). Finally, Grinderslev et al. [34] extended their previous model to include variants of the detached eddy simulation (DES) and large eddy simulation (LES) turbulence models. The turbulence models were used to simulate complex atmospheric conditions, yet again small variations were observed between the rigid and flexible blades.

Blade deformations could also play an important role in the development of a next generation of reduced-LCOE axial-flow rotors. The practical research of Ashwill [5], for example, demonstrated the potential in terms of steady-state load control. In their work, they discussed two projects executed by the Sandia Laboratories for wind rotor passive load control. These include two rotor concepts for passive blade deformations that were tested with large-scale experiments. The rotors had different mechanisms for blade deformation: one exploited bending-twist structural couplings along the span using anisotropic composite materials [91], and the other exploited a geometric sweep in the edgewise direction to induce a torsional moment on the blade [4]. Both concepts aimed to change the spanwise angle of attack distribution, and were proven to reduce loads effectively. Nonetheless, no comparison with active-pitch systems or a complete description of the aerodynamics were provided.

The potential and limits of blade deformations on rotor control are not yet clear. Kooijman [47], Branner et al. [12] and Fedorov and Berggreen [26], for example, show an interesting potential of the flapwise-twist deformation couplings from a material perspective, while Albanesi et al. [2] used an inverse finite-elements method applied to wind rotor blades to find a material configuration capable of providing a pre-defined blade deformation. On the hydrodynamic side, Cognet et al. [17] demonstrated experimentally that flexible blades could be controlled and tuned to increase the performance of rotor blades. They showed an improvement of up to 35% on power production for a constant-chord constant-twist rotor blade using flexible materials, but they don't discuss the extent of the deformations and their effects in the flow and performance.

Transient load mitigation on axial-flow rotors is an area of active research. Tully and Viola [82] studied the fundamental problem of a flexible aerofoil in waves using a flume, showing reductions of up to 30% in transient loads. Porter et al. [75] discussed the use of flexible blades on a model-scale turbine to reduce transient loads. They tested a tidal rotor model with flexible blades in a towing tank with blades designed to exploit bend-twist coupling on the material. Their tests reduced the wave-induced variations on power and thrust by up to 10% and 14%, respectively. Viola et al.

[85] demonstrated, using a BEM-based numerical model and CFD simulations, that a passive pitch 1MW rotor (where the pitch is assumed to be obtained by the deformation of a spring at the root of the blade) could reduce thrust and torque fluctuations by 80% and 25%, respectively, under a sheared flow profile. Viola et al. [85] also argue that a full cancellation of unsteady loads should be attainable by controlling the flexibility of an independent spring on each blade section.

References

[1] T. A. A. Adcock et al. “The fluid mechanics of tidal stream energy conversion”. In: *Annual Review of Fluid Mechanics* 53 (2021), pp. 287–310.

[2] A. Albanesi et al. “Application of the inverse finite element method to design wind turbine blades”. In: *Composite Structures* 161 (2017), pp. 160–172.

[3] Andritz Hydro Hammerfest. *Renewable energy from tidal currents*. `https://www.andritz.com/resource/blob/61614/cf15d27bc23fd59db125229506ec87c7/hy-hammerfest--1--data.pdf`. Accessed:2021-06-23.

[4] T. Ashwill et al. “Development of the sweep-twist adaptive rotor (STAR) blade”. In: *48th AIAA Aerospace Sciences Meeting Including the New Horizons Forum and Aerospace Exposition*. 2010, p. 1582.

[5] T. Ashwill. “Passive load control for large wind turbines”. In: *51st AIAA/ASME/ASCE/AHS/ASC Structures, Structural Dynamics, and Materials Conference 18th AIAA/ASME/AHS Adaptive Structures Conference 12th*. 2010, p. 2577.

[6] Atlantis Resources. *AR1500 tidal turbine*. `https://simecatlantis.com/wp-content/uploads/2016/08/AR1500-Brochure-Final-1.pdf`. Accessed:2021-06-23.

[7] A. S. Bahaj et al. “Power and thrust measurements of marine current turbines under various hydrodynamic flow conditions in a cavitation tunnel and a towing tank”. In: *Renewable Energy* 32.3 (2007), pp. 407–426.

[8] N. Barltrop et al. “Investigation into wave-current interactions in marine current turbines”. In: *Proceedings of the Institution of Mechanical Engineers, Part A: Journal of Power and Energy* 221.2 (2007), pp. 233–242.

[9] Y. Bazilevs et al. “3D simulation of wind turbine rotors at full scale. Part II: Fluid-structure interaction modeling with composite blades”. In: *International Journal for Numerical Methods in Fluids* (2011), 65:236–254.

[10] A. Betz. “Das Maximum der theoretisch möglichen Ausnützung des Windes durch Windmotoren”. In: *Zeitschrift für das gesamte Turbinenwesen* 26 (1920).

[11] T. Blackmore, L. E. Myers, and A. S. Bahaj. “Effects of turbulence on tidal turbines: Implications to performance, blade loads, and condition monitoring”. In: *International Journal of Marine Energy* 14 (2016), pp. 1–26.

[12] K. Branner et al. “Anisotropic beam model for analysis and design of passive controlled wind turbine blades”. In: *DTU Wind Energy report E-0001 (EN)* (2012).

[13] S. A. Brown et al. “Development of a fully nonlinear, coupled numerical model for assessment of floating tidal stream concepts”. In: *Ocean Engineering* 218 (2020), p. 108253.

[14] S. A. Brown et al. “On the impact of motion-thrust coupling in floating tidal energy applications”. In: *Applied Energy* 282 (2021), p. 116246.

[15] T. Burton et al. *Wind energy handbook*. Wiley, 2011.

[16] CMPT. *Floating structures: A Guide for Design and Analysis*. Ed. by N. D. P. Barltrop. Vol. 1. The Centre for Marine and Petroleum Technology, 1998.

[17] V. Cognet et al. “Bioinspired turbine blades offer new perspectives for wind energy”. In: *Proceedings of the Royal Society A: Mathematical, Physical and Engineering Sciences* 473.2198 (2017), p. 20160726.

[18] C. Crawford. “Re-examining the precepts of the blade element momentum theory for coning rotors”. In: *Wind Energy: An International Journal for Progress and Applications in Wind Power Conversion Technology* 9.5 (2006), pp. 457–478.

[19] J. Cruz, M. D. Thomson, and E. Stavroulia. *Preliminary Site Selection - Chile Marine Energy Resources*. Tech. rep. Garrad Hassan, 2009.

[20] M. J. Dadswell and R. A. Rulifson. “Macrotidal estuaries: a region of collision between migratory marine animals and tidal power development”. In: *Biological Journal of the Linnean Society* 51.1-2 (1994), pp. 93–113.

[21] S. Draycott et al. “An experimental investigation into non-linear wave loading on horizontal axis tidal turbines”. In: *Journal of Fluids and Structures* 84 (2019), pp. 199–217.

[22] S. Draycott et al. “Experimental assessment of tidal turbine loading from irregular waves over a tidal cycle”. In: *Journal of Ocean Engineering and Marine Energy* 5.2 (2019), pp. 173–187.

[23] S. Draycott et al. “Rotational sampling of waves by tidal turbine blades”. In: *Renewable Energy* 162 (2020), pp. 2197–2209.

[24] M. Drela. “XFOIL: An analysis and design system for low Reynolds number airfoils”. In: *Low Reynolds number aerodynamics*. Springer, 1989, pp. 1–12.

[25] C. Faudot and O. G. Dahlhaug. “Prediction of wave loads on tidal turbine blades”. In: *Energy Procedia* 20 (2012), pp. 116–133.

[26] V. Fedorov and C. Berggreen. “Bend-twist coupling potential of wind turbine blades”. In: *Journal of Physics: Conference Series*. Vol. 524. 1. IOP Publishing. 2014.

[27] E. Fernandez-Rodriguez, T. J. Stallard, and P. K. Stansby. “Experimental study of extreme thrust on a tidal stream rotor due to turbulent flow and with opposing waves”. In: *Journal of Fluids and Structures* 51 (2014), pp. 354–361.

[28] T. I. Fossen. *Handbook of marine craft hydrodynamics and motion control*. John Wiley & Sons, 2011.

[29] P. W. Galloway, L. E. Myers, and A. S. Bahaj. “Quantifying wave and yaw effects on a scale tidal stream turbine”. In: *Renewable Energy* 63 (2014), pp. 297–307.

[30] C. Garrett and P. Cummins. “The efficiency of a turbine in a tidal channel”. In: *Journal of Fluid Mechanics* 588 (2007), pp. 243–251.

[31] B. Gaurier et al. “Flume tank characterization of marine current turbine blade behaviour under current and wave loading”. In: *Renewable Energy* 59 (2013), pp. 1–12.

[32] H. Glauert. “Wind Tunnel Interference on Wings, Bodies and Airscrews”. In: *Aeronautical Research Committee* 1566 (1933), pp. 1–52.

[33] C. Grinderslev, S. González Horcas, and N. N. Sørensen. “Fluid–structure interaction simulations of a wind turbine rotor in complex flows, validated through field experiments”. In: *Wind Energy* (2021), pp. 1–17.

[34] C. Grinderslev et al. “Wind turbines in atmospheric flow: fluid–structure interaction simulations with hybrid turbulence modeling”. In: *Wind Energy Science* 6.3 (2021), pp. 627–643.

[35] D. M. Grogan et al. “Design of composite tidal turbine blades”. In: *Renewable Energy* 57 (2013), pp. 151–162.

[36] M. Guerra et al. “Tidal energy resource characterization in Chacao Channel, Chile”. In: *International Journal of Marine Energy* 20 (2017), pp. 1–16.

[37] K. Gunn and C. Stock-Williams. “On validating numerical hydrodynamic models of complex tidal flow”. In: *International Journal of Marine Energy* 3 (2013), pp. 82–97.

[38] X. Guo et al. “The surface wave effects on the performance and the loading of a tidal turbine”. In: *Ocean Engineering* 156 (2018), pp. 120–134.

[39] T. J. Hammons. “Tidal power in the UK and worldwide to reduce greenhouse gas emissions”. In: *International Journal of Engineering Business Management* 3.2 (2011), pp. 16–28.

[40] G. T. Houlsby, S. Draper, and M. L. G. Oldfield. *Application of linear momentum actuator disc theory to open channel flow*. Tech. rep. No. OUEL 2296/08. University of Oxford, 2008.

[41] P. Jeffcoate and J. McDowell. “Performance of PLAT-I, a Floating Tidal Energy Platform for Inshore Applications”. In: *Proceedings of the 12th European Wave and Tidal Energy Conference*. 2017.

[42] T. A. de Jesus Henriques et al. “The effects of wave–current interaction on the performance of a model horizontal axis tidal turbine”. In: *International Journal of Marine Energy* 8 (2014), pp. 17–35.

[43] J. Jonkman. “The new modularization framework for the FAST wind turbine CAE tool”. In: *51st AIAA Aerospace Sciences Meeting including the New Horizons Forum and Aerospace Exposition*. 2013, p. 202.

[44] J. M. Jonkman and M. L. J. Buhl. *Loads analysis of a floating offshore wind turbine using fully coupled simulation*. Tech. rep. National Renewable Energy Lab.(NREL), Golden, CO (United States), 2007.

[45] C. R. Kennedy, S. B. Leen, and C. M. Brádaigh. “A preliminary design methodology for fatigue life prediction of polymer composites for tidal turbine blades”. In: *Proceedings of the Institution of Mechanical Engineers, Part L: Journal of Materials: Design and Applications* 226.3 (2012), pp. 203–218.

[46] N. Kolekar, A. Vinod, and A. Banerjee. “On blockage effects for a tidal turbine in free surface proximity”. In: *Energies* 12.17 (2019), p. 3325.

[47] H. J. T. Kooijman. *Bending-torsion coupling of a wind turbine rotor blade*. Netherlands Energy Research Foundation ECN Petten, Netherlands, 1996.

[48] F. W. Lanchester. “A contribution to the theory of propulsion and the screw propeller”. In: *Journal of the American Society for Naval Engineers* 27.2 (1915), pp. 509–510.

[49] T. J. Larsen and A. M. Hansen. “How 2 HAWC2, the user’s manual”. In: (2007).

[50] C. Lothodé et al. “Investigation of blade-mast fluid-structure interaction of a tidal turbine”. working paper or preprint. Oct. 2020.

[51] L. Luznik et al. “The effect of surface waves on the performance characteristics of a model tidal turbine”. In: *Renewable Energy* 58 (2013), pp. 108–114.

[52] V. M. Lyatkher. *Tidal Power: Harnessing Energy from Water Currents*. John Wiley & Sons, 2014.

[53] H. A. Madsen and F. Rasmussen. “The influence on energy conversion and induction from large blade deflections”. In: *EWEC-CONFERENCE*. 1999, pp. 138–141.

[54] Magallanes Renovables. *Technology*. `https://www.magallanesrenovables.com/technology/`. Accessed:2021-09-19.

[55] R. Martinez, G. S. Payne, and T. Bruce. “The effects of oblique waves and currents on the loadings and performance of tidal turbines”. In: *Ocean Engineering* 164 (2018), pp. 55–64.

[56] A. Mason-Jones et al. “Influence of a velocity profile & support structure on tidal stream turbine performance”. In: *Renewable Energy* 52 (2013), pp. 23–30.

[57] J. McNaughton et al. “Experimental testing of the performance and interference effects of a cross-stream array of tidal turbines”. In: *Developments in Renewable Energies Offshore*. CRC Press, 2020, pp. 563–570.

[58] M. K. McWilliam et al. “Optimal aero-elastic design of a rotor with bend-twist coupling”. In: *Journal of Physics: Conference Series*. Vol. 1037. 4. IOP Publishing. 2018, p. 042009.

[59] R. Mikkelsen, J. N. Sørensen, and W. Z. Shen. “Modelling and analysis of the flow field around a coned rotor”. In: *Wind Energy* 4.3 (2001), pp. 121–135.

[60] R. Mikkelsen and J. N. Sørensen. “Modelling of Wind Turbine Blockage”. In: *EWEC*. Paris, 2002.

[61] I. A. Milne et al. “Characteristics of the turbulence in the flow at a tidal stream power site”. In: *Philosophical Transactions of the Royal Society A: Mathematical, Physical and Engineering Sciences* 371.1985 (2013).

[62] I. Milne et al. “The characterisation of the hydrodynamic loads on tidal turbines due to turbulence”. In: *Renewable and Sustainable Energy Reviews* 56 (2016), pp. 851–864.

[63] R. E. Murray et al. “Passively adaptive tidal turbine blades: Design tool development and initial verification”. In: *International Journal of Marine Energy* 14 (2016), pp. 101–124.

[64] R. E. Murray et al. “Towing tank testing of passively adaptive composite tidal turbine blades and comparison to design tool”. In: *Renewable Energy* 116 (2018), pp. 202–214.

[65] P. Mycek et al. “Experimental study of the turbulence intensity effects on marine current turbines behaviour. Part I: One single turbine”. In: *Renewable Energy* 66 (2014), pp. 729–746.

[66] R. F. Nicholls-Lee, S. R. Turnock, and S. W. Boyd. "Application of bend-twist coupled blades for horizontal axis tidal turbines". In: *Renewable Energy* 50 (2013), pp. 541–550.

[67] R. Nicholls-Lee. "Adaptive Composite Blades for Horizontal Axis Tidal Turbines". PhD thesis. University of Southampton, 2011.

[68] T. Nishino and R. H. J. Willden. "The efficiency of an array of tidal turbines partially blocking a wide channel". In: *Journal of Fluid Mechanics* 708 (2012), pp. 596–606.

[69] T. Nishino and R. H. Willden. "Effects of 3-D channel blockage and turbulent wake mixing on the limit of power extraction by tidal turbines". In: *International Journal of Heat and Fluid Flow* 37 (2012), pp. 123–135.

[70] Office of Energy Efficiency and Renewable Energy, US Government. *Marine Energy Resource Assessment and Characterization.* `https://www.energy.gov/eere/water/marine-energy-resource-assessment-and-characterization/#tidalstreams`. Accessed:2021-06-23.

[71] Orbital Marine Power. *Orbital O2 2MW.* `https://orbitalmarine.com/O2`. Accessed:2021-06-23. 2021.

[72] M. H. B. Osman and R. H. J. Willden. "Unsteady loading of a floating tidal turbine oscillating in a pendulum motion". In: *Developments in Renewable Energies Offshore*. CRC Press, 2020, pp. 563–570.

[73] M. H. B. Osman, R. H. J. Willden, and C. R. Vogel. "The effects of surge motion on floating horizontal axis tidal turbines". In: *Proceedings of the Thirteenth European Wave and Tidal Energy Conference*. EWTEC. 2019.

[74] R. Pelc and R. M. Fujita. "Renewable energy from the ocean". In: *Marine Policy* 26.6 (2002), pp. 471–479.

[75] K. E. Porter et al. "Flume testing of passively adaptive composite tidal turbine blades under combined wave and current loading". In: *Journal of Fluids and Structures* 93 (2020), p. 102825.

[76] R. Rafiee, M. Tahani, and M. Moradi. "Simulation of aeroelastic behavior in a composite wind turbine blade". In: *Journal of Wind Engineering and Industrial Aerodynamics* 151 (2016), pp. 60–69.

[77] E. J. Ransley et al. "Coupled RANS-VOF modelling of floating tidal stream concepts". In: *Proceedings of the 2nd International Conference on Offshore Renewable Energy (CORE)*. Glasgow, Scotland, 2016.

[78] G. T. Scarlett and I. M. Viola. "Unsteady hydrodynamics of tidal turbine blades". In: *Renewable Energy* 146 (2020), pp. 843–855.

[79] J. Schluntz and R. H. J. Willden. "The effect of blockage on tidal turbine rotor design and performance". In: *Renewable Energy* 81 (2015), pp. 432–441.

[80] J. Thomson et al. "Measurements of turbulence at two tidal energy sites in puget sound, WA". In: *IEEE Journal of Oceanic Engineering* 37.3 (2012), pp. 363–374.

[81] D. Tollit et al. "Detection of marine mammals and effects monitoring at the NSPI (OpenHydro) turbine site in the Minas Passage during 2010". In: *Report to Fundy Ocean Research Centre for Energy* (2011).

[82] S. Tully and I. M. Viola. "Reducing the wave induced loading of tidal turbine blades through the use of a flexible blade". In: *16th International Symposium on Transport Phenomena and Dynamics of Rotating Machinery (ISROMAC 2016).* 2016.

[83] S. R. Turnock et al. "Development of a floating tidal energy system suitable for use in shallow water". In: *Proceedings of the Seventh European Wave and Tidal Energy Conference.* 2007.

[84] UK Government. *Energy trends UK, October to December 2020 and 2020.* Tech. rep. Department for Business, Energy & Industrial Strategy, 2021.

[85] I. M. Viola et al. "Morphing blades Theory and proof of principles". In: *Proceedings of the Fourteenth European Wave and Tidal Energy Conference.* EWTEC. 2021.

[86] J. I. Whelan, J. M. R. Graham, and J. Peiro. "A free-surface and blockage correction for tidal turbines". In: *Journal of Fluid Mechanics* 624 (2009), pp. 281–291.

[87] M. Willis et al. "Tidal turbine deployment in the Bristol Channel: A case study". In: *Proceedings of the Institution of Civil Engineers-Energy* 163.3 (2010), pp. 93–105.

[88] A. Wimshurst and R. H. J. Willden. "Computational analysis of blockage designed tidal turbine rotors". In: *Progress in Renewable Energies Offshore - Proceedings of 2nd International Conference on Renewable Energies Offshore, RENEW 2016* Emec (2016), pp. 587–597.

[89] F. Zilic de Arcos, G. Tampier, and C. R. Vogel. "Numerical analysis of blockage correction methods for tidal turbines". In: *Journal of Ocean Engineering and Marine Energy* 6.2 (2020), pp. 183–197.

[90] F. Zilic de Arcos, C. Vogel, and R. Willden. "Hydroelastic modelling of composite tidal turbine blades". In: *Advances in Renewable Energies Offshore: Proceedings of the 3rd International Conference on Renewable Energies Offshore (RENEW 2018), October 8-10, 2018, Lisbon, Portugal.* 2018, p. 877.

[91] M. D. Zuteck. *Adaptive blade concept assessment: curved planform induced twist investigation.* Sandia National Laboratories Clear Lake Shore, Texas, USA, 2002.

Part II

Methods

3
Rotor characteristics

The main rotor used in this thesis is a 3-bladed 10 metre radius axial-flow tidal rotor designed originally by Schluntz and Willden [11] using a RANS-BE design algorithm. The rotor was designed using the Risø-A1-24 aerofoil profile across the entire span centred around the quarter-chord line. The design aimed to maintain the optimum angle of attack of 7° along the blade when operating at a tip-speed ratio $\lambda = 5.0$. The rotor was designed to maximise power extraction operating at a blockage ratio of 19.6%.

Considering the large blade solidity near the root of the original design, Wimshurst and Willden [13] introduced modifications to the inboard of $r/R = 0.25$, with a sharp transition and a linear interpolation from the aerofoil to a cylindrical cross section at the nacelle, linearly reducing chord and twist, and ultimately resulting in a more practical blade design. The modified rotor characteristics, both twist and solidity, can be seen in fig. 3.1. Zilic de Arcos et al. [16] introduced further modifications to the root region to ensure surface continuity between the nacelle and $0.25R$, allowing a reduction of the stress concentrations observed in previous work (Zilic de Arcos et al. [17]). The modified root area can be seen in 3.2, and the full design of the main rotor used in this thesis can be seen in fig. 3.3.

This rotor is referenced in this thesis as Sch15B.

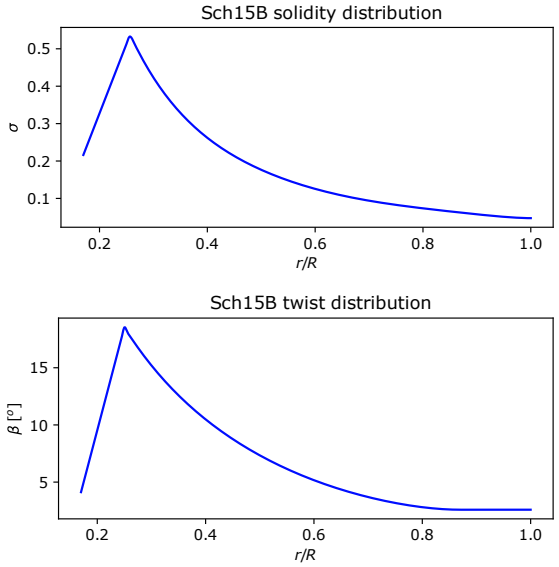

Figure 3.1: Spanwise solidity (top) and twist (bottom) distributions of the Sch15B rotor.

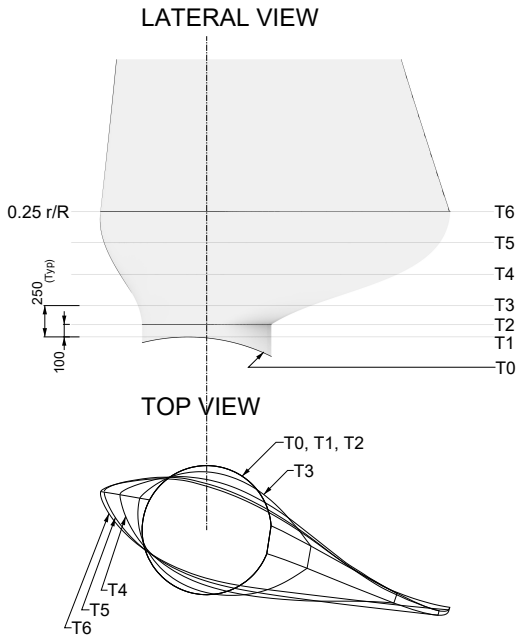

Figure 3.2: Modified root region of the Sch15B rotor. Cross sectional cuts T0 to T6 presented for reference. Units in mm.

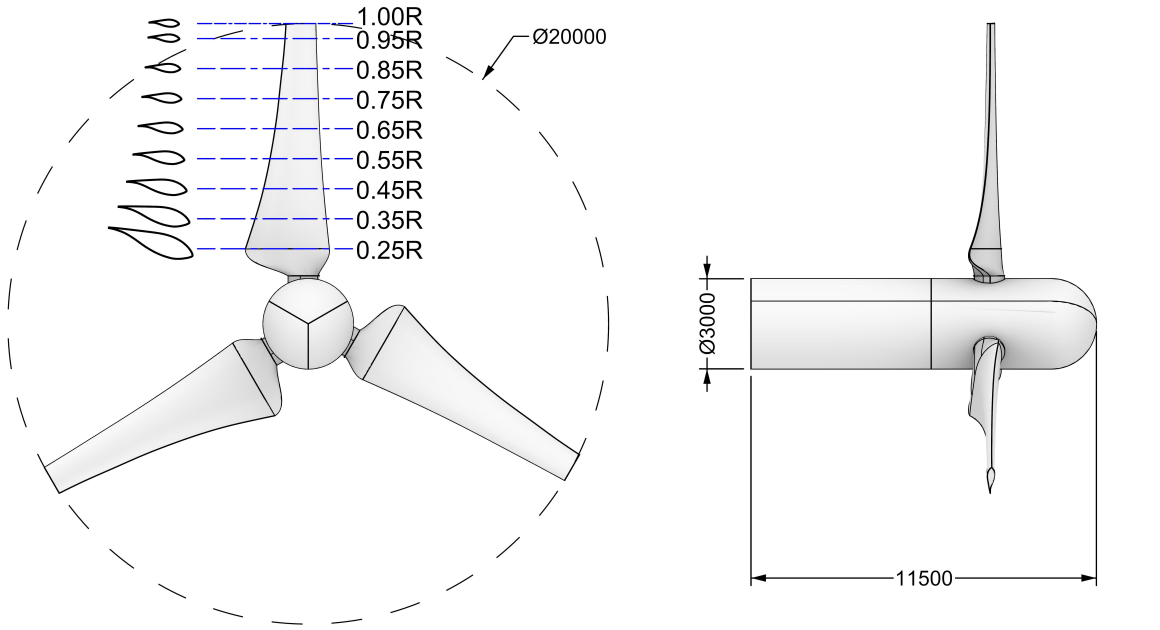

Figure 3.3: General layout of the Sch15B rotor. Units in mm.

4 Computational Fluid Dynamics

4.1 Introduction

The Sch15B rotor was simulated in this thesis inside a cylindrical domain using an incompressible steady-state RANS (Reynolds-Averaged Navier-Stokes) CFD model. The modelling strategy exploits the azimuthal symmetry of the problem by modelling a single blade and one third of the cylindrical domain, using periodic boundary conditions. The steady-state modelling of the rotor's rotation was achieved with the multiple reference frame (MRF) model [6], and a $k-\omega$ SST (shear stress transport) turbulence model is used for the closure of the momentum equation. The discretised problem was solved using the commercial solver Fluent 19.0 with a pressure-based coupled solver. Velocity residuals were reduced by at least six orders of magnitude, and five orders of magnitude for the turbulence scalars.

4.1.1 Governing equations

The modelling approach, based on Luo and Gosman [6] MRF model, enables the steady-state simulation of the rotor blades by solving the mass and momentum conservation equations in terms of a local, rotational or stationary, frame of reference. The velocities in two neighbouring reference frames, $frame-1$ and $frame-2$, are related to each other by the following equation, written in index notation:

$$u_i^{frame-1} = u_i^{frame-2} + \epsilon_{ijk}(\Omega_j^{frame-2} - \Omega_j^{frame-1})x_k \tag{4.1}$$

where u and x are the velocity and coordinate vectors, respectively, Ω the rotational velocity of a rotating frame, and ϵ_{ijk} the permutation symbol.

The continuity equation is defined as:

$$\frac{\partial \rho u_i}{\partial x_i} = 0 \tag{4.2}$$

where ρ is the fluid density.

The momentum conservation equation is modified to account for reference frame rotations:

$$\frac{\partial \rho u_j u_i}{\partial x_j} + 2\rho\epsilon_{ijk}\Omega_j u_k - \rho\Omega_j(\Omega_j x_i - \Omega_i x_j) = -\frac{\partial p}{\partial x_i} + \frac{\partial \tau_{ij}}{\partial x_j} \tag{4.3}$$

with p the static pressure, and τ the stress tensor.

The second and third terms on the left hand side of eq. 4.3 correspond to the Coriolis and centrifugal accelerations, respectively. For the particular case where $|\Omega| = 0$, equation 4.3 is reduced to its non-rotational form.

Equations 4.2 and 4.3 are solved for each subdomain using the rotational speed that corresponds to the local reference frame. The subdomains are implicitly coupled with each other, and information is transferred between them by transforming velocities and velocity gradients at the interfaces, from the external to the local frame of reference, using eq. 4.1. No transformations are required for scalar quantities.

The momentum equation was solved using a RANS approach. Under this model, flow velocities are divided into a time-averaged and a fluctuating component. The averaging of the momentum equation introduces an extra term defined as the Reynolds stress to equation 4.3 which accounts for velocity fluctuations that are not explicitly solved in RANS models. The Reynolds stress tensor is, instead, modelled in terms of the mean flow velocity and a proportionality constant defined as eddy viscosity. The turbulence model is introduced in eq. 4.3 through the stress tensor:

$$\tau_{ij} = (\mu + \mu_t)\left[\left(\frac{\partial u_i}{\partial x_j} + \frac{\partial u_j}{\partial x_i}\right) - \frac{2}{3}\frac{\partial u_k}{\partial x_k}\delta_{ij}\right] \tag{4.4}$$

where δ_{ij} is the Kronecker delta, μ the molecular viscosity, and μ_t the turbulent viscosity.

In this work, the momentum equation was closed with the $k-\omega$ SST (Shear Stress Transport) turbulence model, with the updated constants presented by Menter et al. [9]. This model adds two scalar transport equations for the turbulent kinetic energy, k, and its specific dissipation rate, ω. This turbulence model uses a blending function to switch between the $k-\omega$ model in close proximity to walls, and the $k-\epsilon$ model in the freestream. The two turbulence scalars, k and ω, define the eddy viscosity μ_t, enabling the closure of the momentum equation:

$$\mu_t = \frac{\rho k}{\omega}\frac{1}{\max[\frac{1}{\alpha^*}, \frac{S^* F_2}{\alpha_1 \omega}]} \tag{4.5}$$

where α^* is a damping coefficient, S^* the strain rate magnitude, F_2 a blending function, and α_1 a model constant, as fully explained by Menter [8].

The $k-\omega$ SST model was used in this work as it has been shown to agree well with experiments and higher-order turbulence closure models (including Reynolds Stress Models and Large Eddy Simulations) for turbine applications in terms of mean loads, pressures and mean wake profiles. For further details, the reader is referred to Shives and Crawford [12], Abolghasemi et al. [1], McNaughton et al. [7], and Afgan et al. [2].

The wall boundaries were treated with a blending-function wall-modelling approach. This 'enhanced wall modelling', as it is referred to in Fluent, resolves the boundary layer when the wall-adjacent cell centroid falls within the laminar sublayer ($y^+ < 5$, with y^+ the non-dimensional wall distance defined as $y^+ = yu_\tau/\nu$, where y is the distance from the wall, u_τ the friction velocity and ν the kinematic viscosity), applies a logarithmic law of the wall where the wall-adjacent centroid falls in the wall-modelling region ($y^+ > 30$), and a blended solution between the two functions if the wall-adjacent centroid is in the buffer region ($5 \leq y^+ \leq 30$) [4]. The use of the $k-\omega$ SST model with wall functions was validated for tidal turbine applications by McNaughton et al. [7], and Afgan et al. [2].

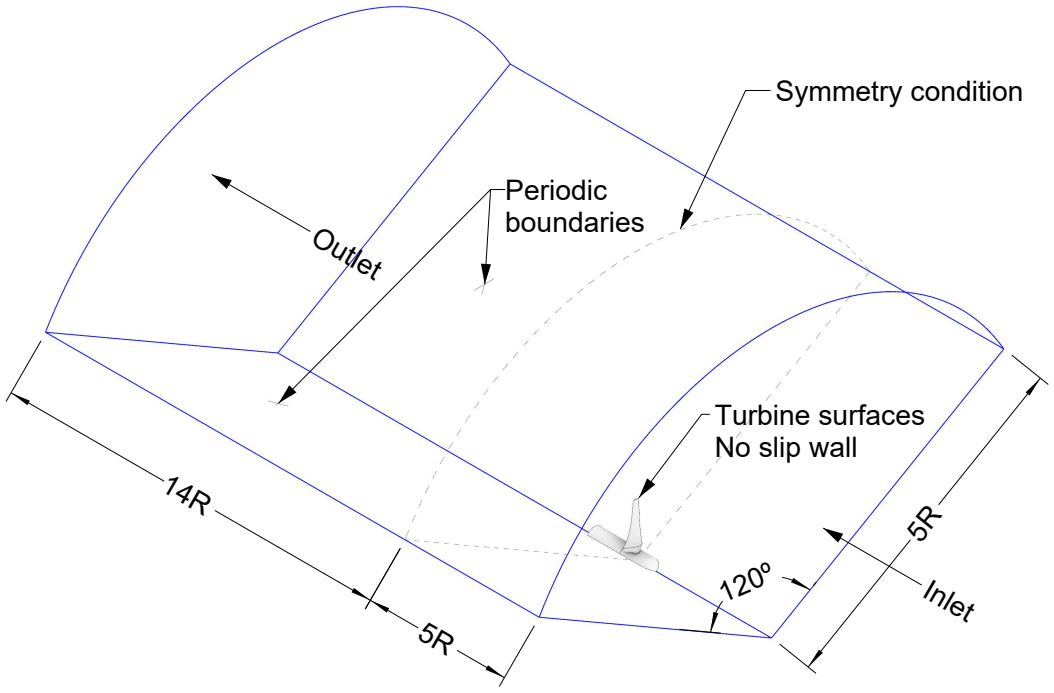

Figure 4.1: Simulation domain for the Sch15B rotor simulations.

4.1.2 Control volume and boundary conditions

The rotor was simulated inside a cylindrical domain exploiting the azimuthal symmetry of the problem, modelling one blade and a 120° wedge, as shown in fig. 4.1, using non-conformal periodic boundary conditions. This approach drastically reduces the computational cost of the simulations while maintaining accuracy in the results [14].

The outer domain was modelled with a radius equivalent to 5 times the rotor radius R to reduce blockage effects (blockage ratio of 4%). The length was defined as $5R$ upstream from the rotor plane, and $14R$ downstream, allowing sufficient distance for the flow to fully develop without a significant influence from the boundaries on rotor loads and performance [13]. The domain was divided into two subdomains: a stationary or external subdomain, and a rotary subdomain with a radius of $1.2R$

where the rotor is contained. The rotary domain is where the rotational speed is prescribed to the local frame of reference to model the turbine rotation.

The inlet upstream was defined by a uniform flow speed of 4.5 m/s, with turbulence characteristics based on the work of Wimshurst and Willden [13] and data presented by Gant and Stallard [5]: a turbulence intensity of 10% and a length scale of 14 m equivalent to 70% of the rotor diameter. The turbulence characteristics are introduced into the CFD model through the turbulence scalars k and ω [4]:

$$k = \frac{3}{2}(u_{avg}I)^2 \tag{4.6}$$

where u_{avg} is the mean flow velocity, I the turbulence intensity, and:

$$\omega = \frac{k^{1/2}}{C_\mu^{1/4}\ell} \tag{4.7}$$

where C_μ is a constant specified in the $k-\omega$ SST model [9], and ℓ the length scale.

The external domain boundary was defined by a symmetry condition; the rotor blade and nacelle surfaces were defined as no-slip smooth walls; the outlet far downstream by an undisturbed pressure; periodic boundary conditions on the wedge sides; and finally non-conformal interfaces between the stationary and rotary subdomains. The boundaries can be seen in the diagram in fig. 4.1.

4.1.3 Mesh study

Structured meshes made with ICEM 19.0 were used to model the rotor. The cross sections for the stationary and rotary subdomains follow a Y-mesh topology, extruded along the axial direction and refined in proximity to the rotor, as shown in fig. 4.2. The blade was meshed using an O-grid topology around the blade and transitioned smoothly to the rest of the subdomain, as shown in figs. 4.3 and 4.4.

Mesh sensitivity studies were conducted to determine a final mesh configuration within the grid-independent region on the rotary and outer subdomains.

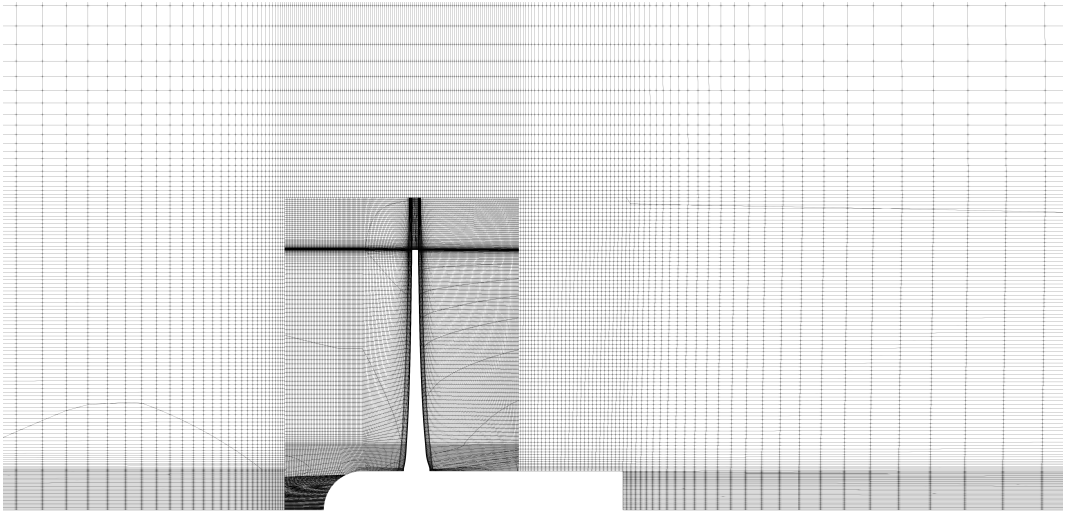

Figure 4.2: Longitudinal mesh slice highlighting regions of increased mesh resolution.

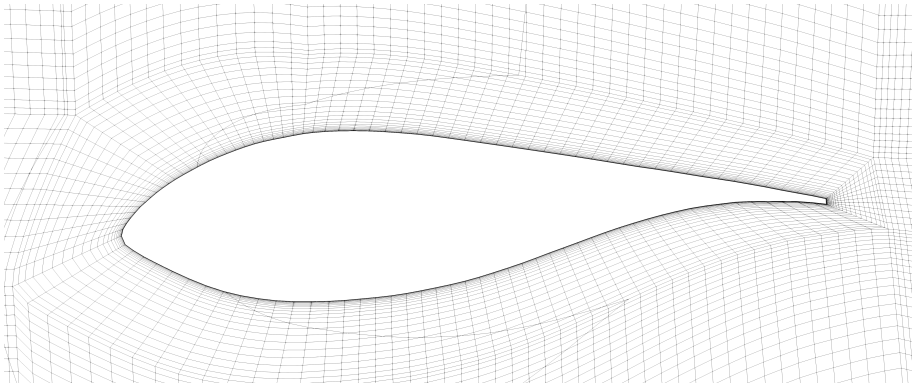

Figure 4.3: O-grid mesh around a typical blade cross section.

4.1.3.1 Rotary subdomain

A systematic analysis of the mesh sensitivity was performed based on the Grid Convergence Index (GCI) introduced by Roache [10]. To quantify the discretisation error, this method extrapolates the values of a quantity of interest (e.g. power or thrust coefficient) where the number of elements $n_c = \infty$ using Richardson extrapolation. To do so, the initial mesh is refined by a uniform factor k_i. This factor indicates the number of subdivisions performed on each cell in each dimension, leading to an increment of k_i^3 in the number of cells for a three-dimensional mesh.

In this study, an initial mesh topology was prepared with 128 cells over the

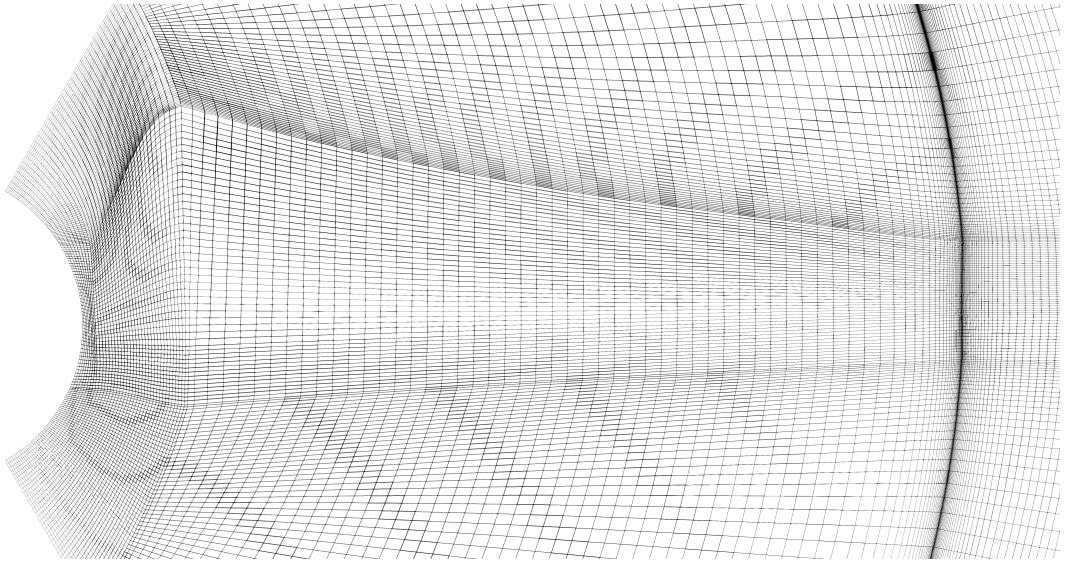

Figure 4.4: Transverse cut of the mesh in close proximity to the blade.

chord, 110 in the spanwise direction, and 25 elements in the O-grid around the blade, with a growth rate of 1.05 and a first layer thickness of $\Delta Y = 0.250\,\text{mm}$[1], leading to 5.41 million elements for the rotary domain. This initial grid is referenced by the subindex $i = 2$, and by the refinement factor $k_2 = 2.0$, as two other meshes were obtained by coarsening and refining this mesh. The other two meshes are referenced by $i = 3$ for the coarse case ($k_3 = 1$), and $i = 1$ ($k_1 = 4$) for the fine mesh, leading to 0.70 and 43.28 million cells, respectively. Each mesh was used to simulate the rotor operating at the highest thrust conditions ($\lambda = 7.0$) as this would impose the highest shear in the flow and, thus, the highest demand on the model numerics. From each solution, the non-dimensional power and thrust coefficients were calculated and extracted as variables of interest for the mesh sensitivity study.

Following the original method, the fine-grid and coarse-grid Richardson error estimators, E_1 and E_2, can be calculated as:

$$E_1 = \frac{f_2 - f_1}{1 - (k_1/k_2)^{\mathscr{O}}} \tag{4.8}$$

[1]The first layer thickness was studied in more detail, for a different set of simulations based on the same rotor, in Zilic de Arcos et al. [16].

Table 4.1: Mesh sensitivity analysis for the turbine domain, where n_c is the number of elements and k_i the refinement factor.

		Thrust			Power		
# of elements n_c	Refinement factor k	C_T [-]	E_R [%]	GCI [%]	C_P [-]	E_R [%]	GCI [%]
0.70M	1.00	1.024	-	-	0.297	-	-
5.41M	2.00	1.064	3.72	1.54	0.345	13.95	0.99
43.28M	4.00	1.059	-0.50	0.54	0.344	-0.32	0.35
∞	∞	1.062	0.00	0.00	0.344	0.00	0.00

$$E_2 = \frac{(f_2 - f_1)(k_1/k_2)^{\mathscr{O}}}{1 - (k_1/k_2)^{\mathscr{O}}} \tag{4.9}$$

where f is the variable of interest and $\mathscr{O}$ the order of accuracy of the algorithm.

In the case of a constant refinement factor, the order of accuracy can be calculated using the solution from three different meshes:

$$\mathscr{O} = ln\left(\frac{f_3 - f_2}{f_2 - f_1}\right) \tag{4.10}$$

where the subscript $i = 1$ corresponds to the fine mesh.

Finally, the Grid Convergence Index (GCI) is defined as:

$$GCI_1^{fine} = F_S|E_1| \tag{4.11}$$

$$GCI_2^{coarse} = F_S|E_2| \tag{4.12}$$

where F_S is a safety factor.

For the rotary domain, the coarse solution falls outside the asymptotic convergence region [3]. Thus, the GCI was calculated only for the base and fine meshes using and estimated order $\mathscr{O} = 1.5$ based on the observations made in Zilic de Arcos et al. [15], and a safety factor of 2. The GCI results are shown in table 4.1, together with data used for calculation, and the relative error (E_R) between two consecutive meshes.

The variations in power and thrust across the span, between the different meshes, are small. A further inspection demonstrates that these variations are

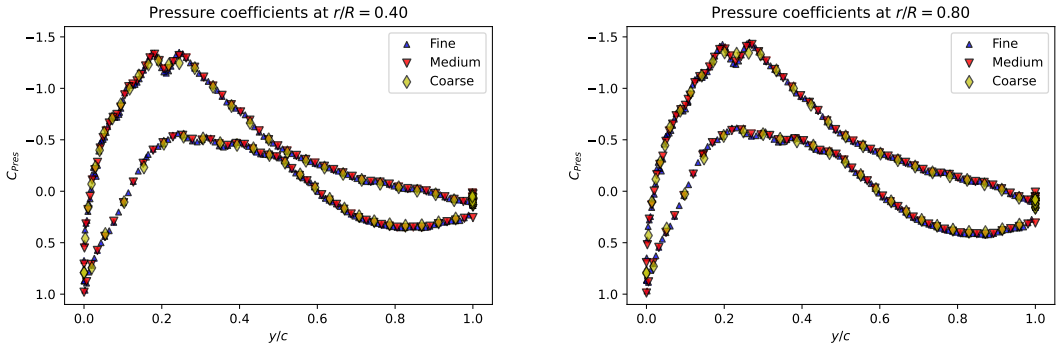

Figure 4.5: Chordwise distribution of pressure coefficients for the three meshes used in the mesh sensitivity study at two radial locations.

not the consequence of mutually cancelling errors across the span or the chord, but minor variations in the blade loads distributed across the blade. This can be observed in figure 4.5 where the pressure coefficients for the three meshes, at two radial locations ($r/R = 0.40$ and $r/R = 0.80$), and normalised by the undisturbed local velocity, are presented.

Following the previous observations, the medium mesh is deemed appropriate for this study considering the small discretisation uncertainty, estimated in a conservative maximum of 1.54% by the GCI, and its reasonable computational cost.

4.1.3.2 Outer domain sensitivity

The sensitivity of the power and thrust coefficients to the number of elements in the outer domain was determined following the previously described methodology. In this case, however, small variations were observed between the three grids, with the coarse mesh within the asymptotic convergence region, as described by Celik and Karatekin [3]. Thus, the order of accuracy $\mathscr{O}$ was estimated using eq. 4.10 and a less conservative safety factor of $F_S = 1.25$ was used [10].

The grid sensitivity results are shown in table 4.2. Following this analysis, the medium mesh was considered appropriate as it has a discretisation uncertainty of 0.11% without adding a significant computational cost to the simulations.

Table 4.2: Mesh sensitivity analysis for the stationary outer domain.

		Thrust			Power		
# of elements n_c	Refinement factor k	C_T [-]	E_R [%]	GCI [%]	C_P [-]	E_R [%]	GCI [%]
0.42M	1.00	1.065	-	0.14	0.346	-	0.41
3.32M	2.00	1.064	-0.11	0.01	0.345	-0.24	0.11
26.58M	4.00	1.064	-0.01	0.00	0.344	-0.06	0.03
∞	∞	1.064	0.00	0.00	0.345	0.00	0.00

4.2 Summary of available CFD datasets

The research projects in this thesis have been enabled by the development of different blade-resolved CFD datasets. In addition, some sets of simulations have been provided by the Wind and Tidal Research Group at the University of Oxford for analysis.

4.2.1 Sch15B base simulations

Blade-resolved CFD simulations of the Sch15B rotor inside a cylindrical domain with a 4% blockage and tip-speed ratios $\lambda \in \{4.0, 5.0, 6.0, 7.0\}$ were performed. These simulations consider an undisturbed flow speed of 4.5 m/s, a turbulence intensity of 10% and a length scale of 14 m.

These results were studied in most chapters. These include the evaluation of CFD flow sampling techniques (chapter 5), the study on blade deflections (part III), and the analysis, verification and modification of engineering models (chapter 8).

4.2.2 Parametric deformation study

The Sch15B rotor under parametric twist and flapwise deformations was modelled using blade-resolved CFD simulations. The rotor was modelled in a cylindrical domain following the same model, meshing approach and general configuration as for the Sch15B base simulations (sec. 4.2.1).

The parametric deformation cases include 6 different twist-only deformations, 6 different flapwise-only deformations, and 5 cases with coupled twist and flapwise

deformations. Each of these cases was simulated at the same 4 tip-speed ratios as the base simulations.

This dataset was used in part III to study the hydrodynamics and the potential use of blade deformations, as well as for the evaluation of an engineering model in chapter 8.

4.2.3 Blockage study

The Sch15B rotor was modelled under different blockage configurations. These simulations are based on the same configuration as the Sch15B base case (sec. 4.2.1), but with a modified outer domain radius to simulate different isotropic blockages $B \in \{0.01, 0.05, 0.10, 0.20, 0.40\}$, with B defined as the ratio between the rotor swept area and cross-sectional area of the channel. The rotor was simulated at the same tip-speed ratios as the base case.

This dataset was prepared and used to assess different blockage correction methods (results published by Zilic de Arcos et al. [15]) and to determine the implications of blockage for engineering models in chapter 8.

4.2.4 MEXICO rotor

This is a set of blade-resolved CFD simulations prepared and validated by [14] under negligible blockage effects. The rotor was simulated at a range of tip-speed ratios and inflow velocities, from which three cases ($\lambda \in \{4.16, 6.67, 10.00\}$) were used. These simulation results were provided by the Wind and Tidal Energy Research Group at the University of Oxford and were re-analysed for the testing and verification of CFD flow-sampling techniques (chapter 5) and in the evaluation of engineering models in chapter 8.

References

[1] M. A. Abolghasemi et al. “Simulating Tidal Turbines with Multi-Scale Mesh Optimisation Techniques”. In: *Journal of Fluids and Structures* 66 (2016), pp. 69–90.

[2] I. Afgan et al. “Turbulent flow and loading on a tidal stream turbine by LES and RANS”. In: *International Journal of Heat and Fluid Flow* 43 (2013), pp. 96–108.

[3] I. Celik and O. Karatekin. “Numerical Experiments on Application of Richardson Extrapolation With Nonuniform Grids”. In: *Journal of Fluids Engineering* 119.3 (Sept. 1997), pp. 584–590.

[4] A. Fluent. “ANSYS Fluent theory guide 19.0”. In: *ANSYS, Canonsburg, PA* (2018).

[5] S. Gant and T. Stallard. “Modelling a tidal turbine in unsteady flow”. In: *Proceedings of the Eighteenth (2008) International Offshore and Polar Engineering Conference*. 2007. 2008, pp. 473–479.

[6] J. Y. Luo and A. D. Gosman. “Prediction of impeller-induced flow in mixing vessels using multiple frames of reference”. In: INSTITUTE OF CHEMICAL ENGINEERS SYMPOSIUM SERIES. 1994.

[7] J. McNaughton et al. “CFD prediction of turbulent flow on an experimental tidal stream turbine using RANS modelling”. In: *1st Asian Wave and Tidal Energy Conference*. 2012.

[8] F. R. Menter. “Two-equation eddy-viscosity turbulence models for engineering applications”. In: *AIAA journal* 32.8 (1994), pp. 1598–1605.

[9] F. R. Menter, M. Kuntz, and R. Langtry. “Ten Years of Industrial Experience with the SST Turbulence Model”. In: *Turbulence Heat and Mass Transfer 4* 4 (2003), pp. 625–632.

[10] P. J. Roache. “Perspective: A Method for Uniform Reporting of Grid Refinement Studies”. In: *Journal of Fluids Engineering* 116.3 (Sept. 1994), pp. 405–413.

[11] J. Schluntz and R. H. J. Willden. “The effect of blockage on tidal turbine rotor design and performance”. In: *Renewable Energy* 81 (2015), pp. 432–441.

[12] M. Shives and C. Crawford. “Adapted Two-Equation Turbulence Closures for Actuator Disk RANS Simulations of Wind & Tidal Turbine Wakes”. In: *Renewable Energy* 92 (July 2016), pp. 273–292.

[13] A. Wimshurst and R. H. J. Willden. “Computational analysis of blockage designed tidal turbine rotors”. In: *Progress in Renewable Energies Offshore - Proceedings of 2nd International Conference on Renewable Energies Offshore, RENEW 2016* Emec (2016), pp. 587–597.

[14] A. Wimshurst and R. H. J. Willden. “Extracting lift and drag polars from blade-resolved computational fluid dynamics for use in actuator line modelling of horizontal axis turbines”. In: *Wind Energy* 20.5 (May 2017), pp. 815–833. arXiv: `arXiv:1006.4405v1`.

[15] F. Zilic de Arcos, G. Tampier, and C. R. Vogel. “Numerical analysis of blockage correction methods for tidal turbines”. In: *Journal of Ocean Engineering and Marine Energy* 6.2 (2020), pp. 183–197.

[16] F. Zilic de Arcos, C. R. Vogel, and R. Willden. "Hydrodynamic modelling of flexible tidal turbine blades". In: *Proceedings of the Thirteenth European Wave and Tidal Energy Conference*. ISSN: 2309-1983. EWTEC. 2019.

[17] F. Zilic de Arcos, C. Vogel, and R. Willden. "Hydroelastic modelling of composite tidal turbine blades". In: *Advances in Renewable Energies Offshore: Proceedings of the 3rd International Conference on Renewable Energies Offshore (RENEW 2018), October 8-10, 2018, Lisbon, Portugal*. 2018, p. 877.

Paper published in the Wind Energy Journal:

Extracting angles of attack from blade-resolved rotor CFD simulations. Wind Energy 23(9), 1868-1885. (2020)

Federico Zilic de Arcos, Christopher R. Vogel,
Richard H. J. Willden

5

Flow-field analysis techniques: Extracting angles of attack from blade-resolved rotor CFD simulations

5.1 Abstract

The distribution of the angles of attack over the span of a rotor blade, together with blade element theory, provides a useful framework to understand forces, power performance and other fluid dynamic phenomena of axial-flow rotors. However, the angle of attack is not straightforward to define for a three-dimensional rotor, where the flow is perturbed by the blade circulation, shed vorticity and wake development.

This paper evaluates six methods to extract the angles of attack from blade-resolved CFD simulations of axial-flow turbines. Simulations of two different rotors are presented: a low solidity rotor designed for wind, and a higher solidity rotor designed for tidal stream energy conversion. Of the analysed methods, five were obtained from the literature and are tested in terms of their internal parameters. The remaining method is named the Streamtube Analysis Method (SAM) and is presented as an improvement on analysis methods that azimuthally average the flow data on the rotor plane, referred to as Azimuthal Averaging Techniques (AAT). The SAM method accounts for the expansion of the streamtubes in flow-field

velocity sampling, and exhibits improved convergence on the internal parameters compared to AAT.

The six methods are benchmarked in terms of the angles of attack, axial induction factors and the local lift and drag coefficients, identifying that most perform well and agree with each other despite the different underlying assumptions or modelling approaches. However, given the limitations and inherent dependency on internal parameters, the Line Averaging and Streamtube Analysis Method are suggested for general flow analysis application.

5.2 Introduction

The forces on axial-flow turbines are typically characterised through the steady two-dimensional framework described by blade-element momentum theory[3]. This model describes the turbine as a disc positioned perpendicular to the flow with no thickness. Its blades are represented as collections of independent aerofoil sections over a finite number of concentric annuli, with the flow through each annulus being homogeneous, and the forces on each section considered as functions of the local flow conditions. This two-dimensional framework is a useful model to describe and analyse the performance of axial-flow rotors and has been widely used for turbine design and analysis (see e.g. Burton et al. [3], Ning [18]) despite its limitations in representing three-dimensional flow-effects near the tip and the root of the blades (e.g. Glauert [5], Shen et al. [23]) and in misaligned flow conditions. Thus, it is desirable to analyse blade-resolved turbine simulations, experiments and even full-scale rotor flows in similar terms to those described by the blade-element momentum theory.

The inverse problem is also relevant. Extracting the spanwise distribution of the lift and drag polars in order to use them with lower order models (see e.g. Wimshurst and Willden [26]) requires resolving the local force vector, extracted by integrating pressure and shear force on the blade surfaces, in terms of a frame of reference defined by the local flow and, thus, by the local angle of attack.

The problem, however, is non-trivial. The flow around a turbine varies across the azimuthal and axial coordinates, with strong gradients near the blades. Furthermore,

the local flow over a specific annular section is the result of the inflow characteristics, the operation of the turbine, and the development of the wake, making it difficult to define an undisturbed upstream velocity such as that used for defining lift and drag characteristics in wind tunnel experiments. Finally, the concept of a zero-thickness disc cannot be directly applied to a three-dimensional rotor, so the velocities cannot be extracted at that specific plane.

Given these challenges, several flow-analysis methods have been proposed in the literature. One of the first approaches developed is to use an inverse Blade-Element Momentum method that entails finding the tangential and axial induction factors to describe the local flow velocity based on the measured thrust and torque distributions and using pre-determined two-dimensional lift and drag coefficients along with empirical correction factors (see e.g. Lindenburg [14]).

Hansen et al. [8] proposed the Azimuthal Averaging Technique (AAT) which consists of extracting the azimuthally-averaged velocities at different fixed radial coordinates upstream and downstream of the turbine and averaging these to obtain the azimuthally-averaged axial and tangential velocities from which the local flow angle can be determined. This method was tested by Johansen and Sørensen [11] by using the blade-resolved CFD simulations of three different rotors (NREL Phase VI, Tellus 95kW and LM19.1 500kW) maintaining a fixed rotational speed and a set of inflow velocities ranging from 7 to 20 m/s. Results of their flow analysis were presented in the form of radially varying lift and drag coefficients [7] without discussing the flow-analysis method details.

Shen et al. [22] introduced an iterative method to analyse the Tellus 95kW turbine that considered the flow velocity near the blade to be a combination of the local incident velocity and the perturbations caused by the bound circulation on the blades. The influence from the blades was modelled through lifting-line theory, placing vortices along the blade span with a circulation distribution determined using Kutta-Jowkowski's theorem. The authors compared the method with the AAT and showed good agreement in the midspan in terms of the extracted polar coefficients, but also significant sensitivity to the distance between the monitor

point and the blade[22]. This method was then used to evaluate experimental data of the MEXICO rotor by Yang et al. [27].

Shen et al. [21] proposed another method based on blade-surface vortex sheets where a distributed circulation was determined directly from a pressure distribution. This method was also tested using the Tellus 95kW rotor and proved to be more independent of the position of the monitor points than the lifting-line method through comparison of the results in terms of local lift and drag coefficients.

Bak et al. [1] proposed fitting two-dimensional pressure distributions extracted from wind-tunnel experiments to the pressure distributions extracted at different radial positions along a turbine blade. In their paper the authors used the pressures extracted at four radial positions from the experiments of a DANAERO NM80 2MW turbine, fitting the pressure surface data to determine the angle of attack.

The pressure-fitting method was regarded as not being reliable enough by Guntur and Sørensen [6] as it depends on the flow not being separated, in a paper that reviewed four methods using CFD simulations of the MEXICO rotor at three different tip-speed ratios. Their review also tested the inverse BEM, AAT and a variation of the AAT method that extracts the velocity at the blade rather than the azimuthal-average. The paper showed a relatively good agreement between the four described methods in terms of the lift and drag coefficients, but poor agreement when compared to results presented by other authors.

Jost et al. [12] performed a thorough review of four different analysis methods using CFD simulations of the DTU 10MW and the AVATAR turbines. In their paper, the AAT, the two vortex methods described by Shen et al. [22] and Shen et al. [21], and a new method called "Line Average" are analysed under steady-state and transient conditions, showing results in the form of lift and drag coefficients, blade-span distributions of angles of attack and discussing the differences between the methods under steady- and transient-flow conditions.

The Line Average method takes a closed path around each blade cross-section and extracts the velocity around this path, assuming that the influence of the circulation will be negated by averaging the flow velocity components. The method

showed a good agreement with AAT on the midspan and a faster response to transient changes [12].

Another method is described by Herráez et al. [9], where the authors propose that extracting the velocities directly from the bisectrix between two blades will provide an approximation to the undisturbed flow velocity. They demonstrate the validity of the assumption with lifting-line theory, and the method is tested using experiments and simulations of the MEXICO rotor, and compared to results published in the literature.

Rahimi et al. [19] published another review similar to that published by Jost et al. [12] using the same two rotors but only simulating them under steady-state conditions. As in the other review papers, the authors found a good agreement over the midspan of the blades but discrepancies at the tip and the root. They also identify limitations in the methods associated with wake expansion after the flow passes through the turbine.

Even though most methods have a relatively good agreement at high tip-speed ratios over the midspan, angle of attack discrepancies of about 1 or 2 degrees can be observed in some papers. Whether this difference is acceptable or not will largely depend on the operational regime of the turbine. Tip and root sections escape also the scope for which the concept of angle of attack can be applied as these regions are significantly influenced by three-dimensional effects. Furthermore, most methods exhibit some kind of convergence limitation. For example, the AAT results are influenced by the distance between the upstream and downstream cuts and the rotor plane. The bound circulation line method described in Shen et al. [22] requires the monitor point to be placed at least two chords from the blade, which can be complicated in high-solidity rotors, and a similar problem is observed with the Line Average method.

Some methods, such as the inverse BEM and pressure fitting rely on two-dimensional data, which is not ideal as the lift and drag characteristics can change with radial position [26]. The circulation-based methods, on the other hand, have inviscid-flow assumptions, and despite demonstrating good performance, a method

used to analyse high-quality 3D turbulent CFD simulations should, arguably, be free of lower-order model assumptions.

In this paper, a method based on the concept of expanding streamtubes is discussed. This is based on the work from Hunter [10], and is analysed in this paper and proposed as an improvement on the classical AAT. This method works by considering the expansion of the flow while passing through the turbine and interpolating the azimuthally-averaged velocities not at a constant radial position as in AAT, but over the corresponding expanding streamtubes. The advantage of this method is an improved convergence, the lack of 2-D assumptions and that no smoothing of the data is required after the calculation.

For this benchmark study, two axial-flow turbines were employed: The MEXICO rotor, a widely studied wind turbine, and a higher-solidity tidal turbine originally designed for blocked-flow conditions by Schluntz and Willden [20]. Blade-resolved CFD simulation data of these two rotors over a range of tip-speed ratios was used to evaluate the different methods in terms of their convergence relative to model parameters, and then the methods are compared with each other in terms of the angles of attack, the axial induction factors and the inferred lift and drag coefficients.

5.3 Methodology

5.3.1 Turbine descriptions

Table 5.1: Main design and operational parameters of the Sch15B and MEXICO rotors, displaying type of turbine, number of blades Z, diameters Ø, rotational speed ω, original design tip-speed ratio λ_D and velocity V_D, simulated tip-speed ratios λ, flow velocities V_∞ and chord-based Reynolds number $Rn_{0.75}$ evaluated at $r/R = 0.75$.

Turbine	**Type**	**Z**	**Rotor Ø [m]**	**Hub Ø [m]**	ω **[rpm]**	λ_D	V_D **[m/s]**	λ	V_∞ **[m/s]**	$Rn_{0.75}$
Sch15B	Tidal	3	20.00	3.00	Variable	5.5†	2.0	4.0, 5.5 & 7.0	4.5	∼16 - 31 $\times 10^6$
MEXICO	Wind	3	4.50	0.54	424.50	6.7	15.0	10.00, 6.67 & 4.17	10, 15 & 24	∼0.5 $\times 10^6$

† Design tip-speed ratio with a blockage of $B = 0.196$

Two axial-flow turbines were employed in this work to test the different methods of determining radially varying angles of attack: a tidal rotor optimised for a blocked-flow condition with high solidity and high thrust [20] [25] designated as Sch15B, and the test rotor used during the Model Experiments in Controlled

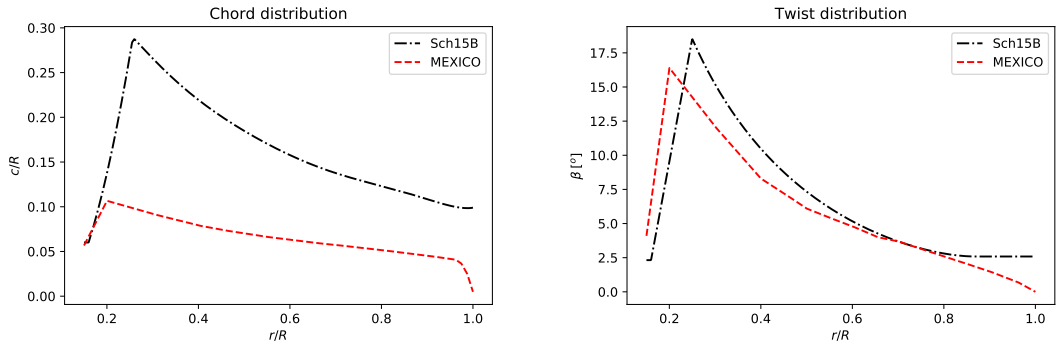

Figure 5.1: Approximate chord and twist distributions presented as functions of the non-dimensional radial position, r/R, for the Sch15B and MEXICO rotors.

Conditions (MEXICO), a wind turbine for which considerable experimental and numerical data have been published [24] [2].

The tidal rotor is a three-bladed turbine designed by Schluntz and Willden [20] and further modified by Wimshurst and Willden [25] and Zilic de Arcos et al. [29] . This rotor has a diameter of 20 m and was optimized to operate under a blocked-flow condition with a blockage, defined as the ratio of turbine swept area to channel cross-sectional area, of $B = 19.6\%$. This rotor uses the Risø A1-24 aerofoil aligned along the blade's quarter-chord.

The MEXICO turbine is a three-bladed wind rotor with a diameter of 4.5 m designed for an FP5 project partly funded by the European Commission. Its blades were comprised of three different aerofoils (DU-91-W2-250, Risø A1-21 and NACA64-418) with transition regions between them. The simulations used in this work consider a fixed pitch angle of -2.3 degrees [25].

The two turbines were analysed at three tip-speed ratios, λ, covering a wide range of cases: 4.0, 5.5 and 7.0 with a variable rotational speed and a fixed inflow of 4.5 m/s for the Sch15B turbine; and 4.17, 6.67 and 10.00 with a fixed rotational speed of 424.5 rpm and variable inflow speed for the MEXICO rotor.

Details of the rotors are summarised in table 5.1, and the chord and twist characteristics are plotted in fig. 7.2. The reader should note how the tidal turbine features a larger chord over the blade-span as a consequence of its blockage-oriented design. A render comparison of the two rotors is also provided in fig. 5.1.

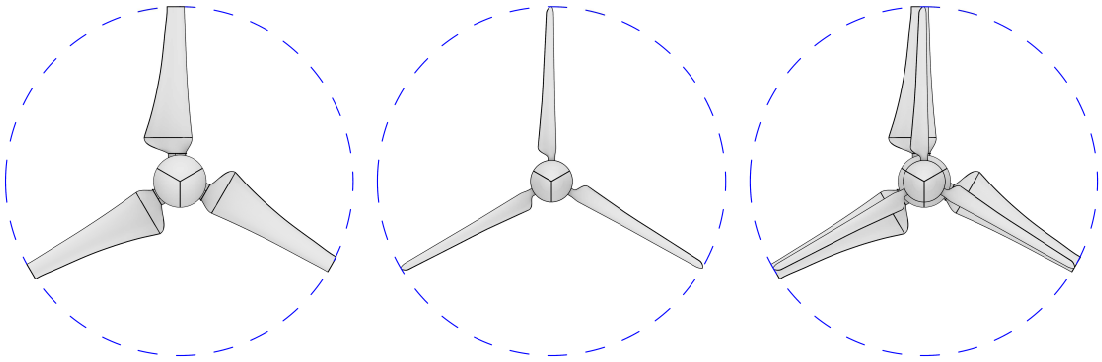

Figure 5.2: Comparison of the Sch15B (left), MEXICO rotor (middle), and an overlay of both rotors (right). Geometries are non-dimensionalised by the corresponding rotor radius.

5.3.2 Numerical models

The datasets employed for this study come from steady-state Reynolds-Averaged Navier-Stokes (RANS) CFD simulations. The blade rotation was modelled in both cases using the Multiple Reference Frame approach (MRF) [15] , modelling one-third of the domain with periodic boundary conditions, and the $k-\omega$ SST turbulence model [16] with updated constants[17] was used to close the RANS equations.

The data sets were generated for different research projects, and hence there are differences in the CFD strategies employed. The Sch15B rotor was simulated with the commercial code Fluent 19.0 with second-order upwind discretisation scheme and a coupled-pressure algorithm, whereas the MEXICO rotor was simulated with OpenFOAM 2.3.1 and the SIMPLE algorithm for pressure-velocity coupling. In both cases, the residuals were reduced by at least 5 orders for the velocity components and typically 5 orders for the turbulence scalars.

Structured meshes were employed in both cases. Non-dimensional wall distances of $30 < y^+ < 300$ for the Sch15B and $y^+ < 5$ for the MEXICO rotors were defined, employing an enhanced wall-modelling approach for the first case [4] and a wall resolved boundary layer on the second. More details of the simulations can be found in Zilic de Arcos et al. [28] and Wimshurst and Willden [26] for the Sch15B and MEXICO rotors, respectively.

5.3.3 Flow-field analysis methods

5.3.3.1 Azimuthal Averaging Technique (AAT)

This method operates by obtaining the azimuthally-averaged flow-speeds at different radial coordinates and axial distances from the rotor plane. Differences in the implementations stem from where the analysis sections are drawn and interpolated between to obtain the velocity at the turbine plane while avoiding the steep velocity gradients that arise on the rotor plane.

The interpolation can be done in different ways. The most straightforward way is to define an arbitrary fixed distance upstream and downstream and average the velocities. Another approach is to describe the velocities as functions of the axial coordinate, and using data at multiple points to perform a higher-order interpolation.

Once the axial and tangential velocity components relative to the blade have been extracted, the inflow angle ϕ can be calculated as

$$\phi = \tan^{-1}(V_x/V_\theta) \tag{5.1}$$

$$W = \sqrt{V_x^2 + V_\theta^2} \tag{5.2}$$

with V_x and V_θ the axial and tangential velocity components, respectively, as obtained from the analysis method utilised.

Despite some authors assigning V_θ to be equal to ωr [6, 11], with ω the rotational speed and r the local radius, the present work considers the tangential induction factor a' such that :

$$V_\theta = \omega r(1 + a') \tag{5.3}$$

The influence of the tangential induction factor, a', is not significant in the mid- and outboard regions of the blades. However, near the root and where the rotational speed is lower, a' can generate some non-negligible variations in the angle of attack.

Once the inflow angle, ϕ, has been determined, the angle of attack is calculated by subtracting the twist angle β:

$$\alpha = \phi - \beta \tag{5.4}$$

In this work, the velocities were extracted by calculating the mean of the azimuthally-averaged velocities at planes located upstream and downstream of the turbine plane, at distances x/c expressed as functions of the local chord c and the axial coordinate x.

Applying the AAT analysis process to the CFD simulations, a sensitivity analysis was performed with the results plotted in fig. 5.3 in terms of the angle of attack for the Sch15B and MEXICO rotors at the analysed operational cases. The MEXICO turbine was analysed with monitor distances from $x/c = 0.25$ to $x/c = 4.0$, whereas the tidal turbine was limited to a maximum $x/c = 2.0$ as, due to its large chord at the root sections, using any value larger than this meant extracting data at a distance that was regarded as being too far from the turbine plane.

From the convergence plots, a spread of about 0.5 degrees is observed but no convergence with x/c is observed. It is noteworthy that, for the high-TSR cases where the angles of attack are small, the relative error of this spread is in the order of 25-30%.

5.3.3.2 Vortex Sheet method

This method is part of a family of techniques that assume the flow velocity to be the sum of the undisturbed velocity and a velocity induced by the turbine's circulation. Hence, if the turbine circulation-induced velocity U_Γ can be estimated, the undisturbed velocity can be calculated by subtracting the induced component from the velocity at a measuring point located on the turbine's plane.

Shen et al. [22] introduced a method to calculate the induced velocity U_Γ by modelling the turbine using lifting-line theory [22]. This method requires the force distribution over the blade span, the lift component which provides a circulation distribution, and the velocity at different measuring points. The induced velocity

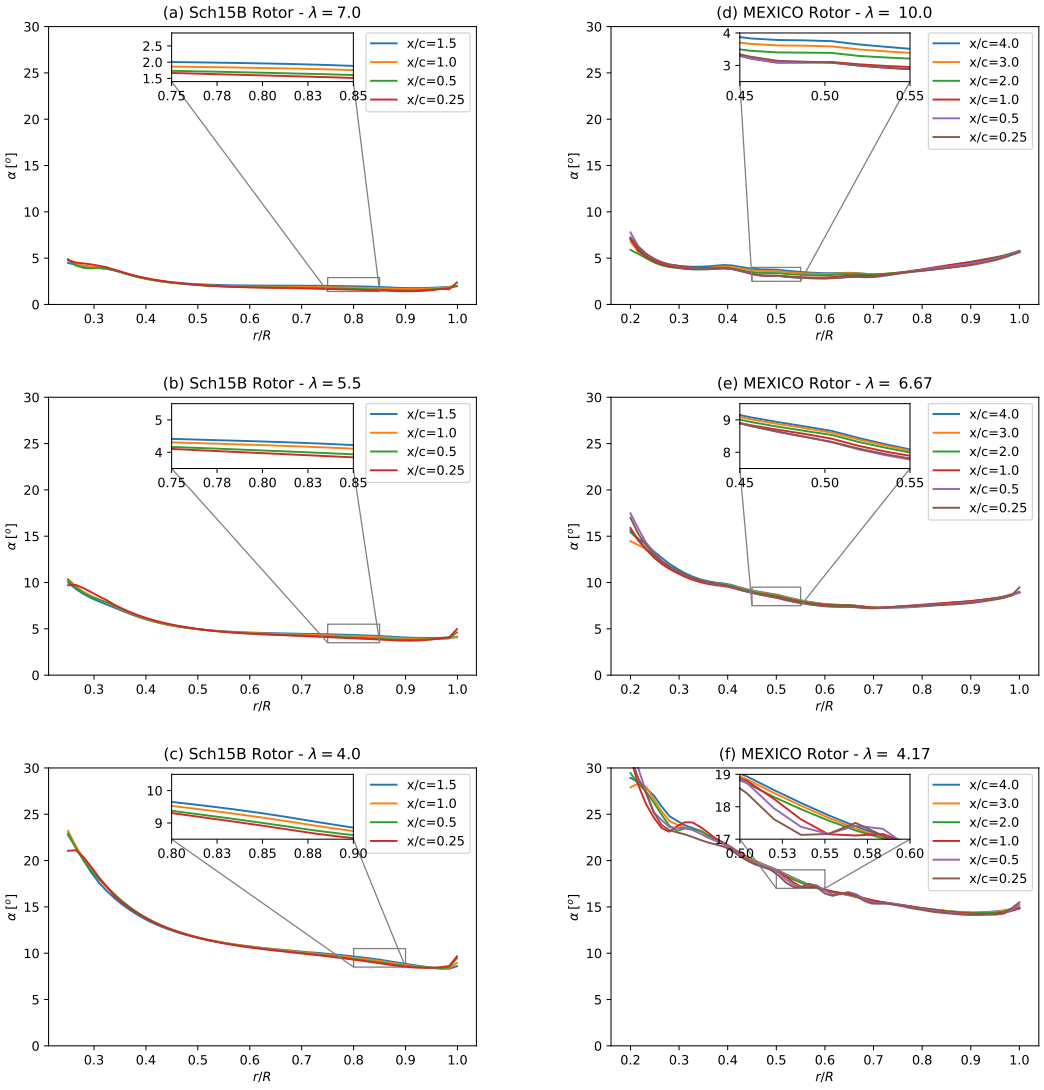

Figure 5.3: Angles of attack obtained with the AAT method with different monitor positions, x/c, for three different tip-speed ratios: (a) $\lambda = 7.0$, (b) $\lambda = 5.5$ and (c) $\lambda = 4.0$, for Sch15B, and (d) $\lambda = 10.0$, (e) $\lambda = 6.67$, (f) $\lambda = 4.17$ for MEXICO.

is calculated from the Biot-Savart law and is then subtracted from the measured velocity to calculate the inflow angle ϕ, iterating until convergence is achieved. The method, despite showing promising results, exhibits a dependency on the chord-wise location of the measuring points. Shen et al. [22] recommended placing the measuring points at a distance of at least 2 chords, which might not be practical in some cases.

Shen et al. [21] presented another method based on potential flow theory, introduced as an improvement to the lifting-line method. This method, instead of

modelling each blade as a vortex line, employs vortex sheets to model the blade surfaces, thus considering the chordwise distribution of the circulation and reducing solution dependency on the chord-wise distance [21]. This method is of an increased complexity in comparison to the one presented by [22] as it requires the pressure distribution over the blade sections and, according to the authors, identification of the stagnation and separation points. However, as they describe it to have a better performance, this method will be analysed in this study as the most complete potential flow analysis method.

Method description The method requires the velocities at different measuring points located on the turbine plane, as well as the pressure distribution over the corresponding sections. Assuming the pressure to be constant through the boundary layer, the velocity at its edge U_τ is calculated using Bernoulli's equation:

$$p + \frac{1}{2}\rho|U_\tau|^2 = p_\infty + \frac{1}{2}\rho U_\infty^2 \tag{5.5}$$

with p and p_∞ the pressure at a point on the blade surface and the undisturbed pressure, respectively, $U_\infty = (V_\infty^2 + \omega^2 r^2)^{1/2}$ the relative flow speed at a certain radial position r and V_∞ the undisturbed flow velocity. Then, the edge velocity is calculated as:

$$U_\tau = U_\infty \sqrt{1 - \frac{2(p - p_\infty)}{\rho U_\infty^2}} \tag{5.6}$$

which is used to calculate the local bound circulation density at different points around the cross section as a velocity jump over the boundary layer:

$$\vec{\gamma}(\vec{y}) = \delta U|_{wall}\, \vec{e_r} = \pm(U_\tau - 0)\vec{e_r} \tag{5.7}$$

where $\delta U|_{wall}$ is the velocity change through the boundary layer, $\overrightarrow{y}$ the coordinates of a point on the blade section, and $\overrightarrow{e_r}$ is a unitary radial vector aligned with the blade spanwise axis.

Shen et al. [21] indicate that the sign of the bound circulation density should be defined according to the location of the stagnation and separation points: positive

between the stagnation and the separation points, negative between the stagnation point and the trailing edge along the pressure surface and, finally, negative between the separation point and the trailing edge. Nonetheless, we consider that this suction surface post separation sign change is inconsistent with the development of this model, which will be discussed below.

With the circulation defined, the induced velocity is computed using the Biot-Savart law, integrating numerically in both the chordwise and spanwise directions for each blade:

$$\overrightarrow{U_\Gamma}(\vec{x}) = \frac{1}{4\pi}\sum_{i=1}^{Z}\iint_S \frac{\vec{\gamma}(\vec{y})\times(\vec{x}-\vec{y})}{|\vec{x}-\vec{y}|^3}d\tau dr \tag{5.8}$$

with Z the number of blades, S the blade surface, $\overrightarrow{x}$ the coordinates of the flow analysis point where the velocity is measured, $d\tau$ the chordwise and dr the radial directions.

Then, the undisturbed velocity used to calculate the angle of attack is obtained by subtracting the induced velocity from the velocity at the measuring point $\overrightarrow{U}_{MP}(\overrightarrow{x})$:

$$\overrightarrow{U}(\vec{x}) = \overrightarrow{U_{MP}}(\vec{x}) - \overrightarrow{U_\Gamma}(\vec{x}) \tag{5.9}$$

Finally, the inflow angle and the angle of attack can be calculated according to eqs. 5.1 and 5.4, respectively.

Shen et al. [21] state that the separation point should be identified and, from that point to the trailing edge, the local bound circulation density should become negative. Most turbines are not designed to operate with a detached flow because of the transient phenomena associated with this regime and the reduced predictive capacity of CFD, potential-flow and BEM techniques. If separation occurs on a turbine under normal operation, it would typically occur over a very limited portion of the blade. Nonetheless, for the MEXICO turbine operating at $\lambda = 4.17$, the separated region occupies most of the suction surface, as can be seen in fig. 5.4.

The assumption of the circulation changing sign after separation occurs results from the observation that the surface flow direction reverses after the separation

(a) $\lambda = 10.0$

(b) $\lambda = 6.67$

(c) $\lambda = 4.17$

Figure 5.4: Streamlines over the suction surface of the MEXICO rotor plotted using the line integral convolution technique, with the black line highlighting the approximate location where separation occurs. The three analysed tip-speed ratios are displayed.

point and beneath the separated shear layer. However, as the edge velocity, defined previously, only applies outside the shear layer, which is above the separation bubble, we consider that this assumption is not valid. Considering the change in tangential velocity from the wall to above the separated shear layer, the net circulation should still remain positive despite the circulation being negative immediately adjacent to the wall. Hence, there should be no change in the sign of the circulation density.

Furthermore, it is worth noting that the sign change makes no significant difference in the results for other cases except for the MEXICO rotor at the lower TSR analysed and, to a lesser extent, to the $\lambda = 6.67$ case. Figure 5.5 shows a comparison of the angle of attack without correction and the two approaches with regards to the circulation. Additionally, the results obtained with the streamtube analysis method (SAM), presented in section 5.3.4, are provided for comparison.

From the figure it can be seen how correcting for the post separation circulation improves the agreement with the alternative method which samples directly from the flow field and makes no assumption about separation.

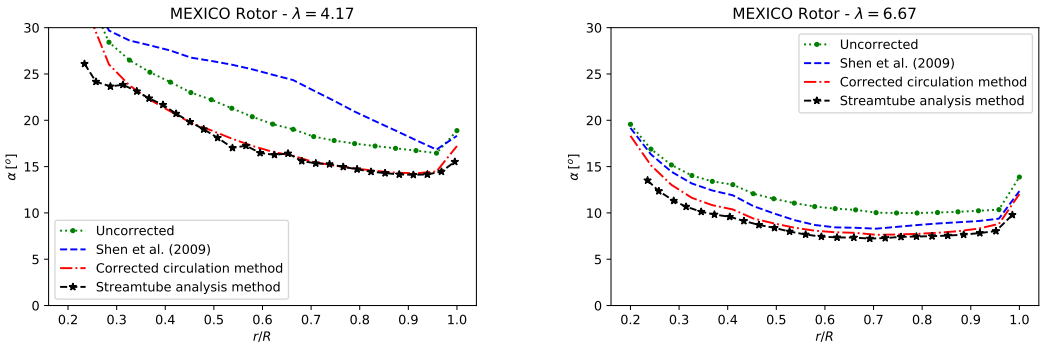

Figure 5.5: Computed angle of attack for the MEXICO turbine at tip-speed ratios of 4.17 and 6.67. Lines shown are for angles of attack derived from the flowfield without considering velocity induction (uncorrected), with velocity induction correction derived from Shen et al. [21] model, with the post separation correction to the circulation method, and using an alternative streamtube analysis method (see section 5.3.4).

As previously stated, the circulation method requires the velocity at a monitoring point. Shen et al. [21] suggest that the Vortex Sheet method should not be sensitive to the location of this point, while the bound circulation line method presented in Shen et al. [22] requires at least two chords of separation to the sampling point.

In the present work, we tested the sensitivity of the Vortex Sheet method to the location of the monitor points by placing them immediately in front of the analysed section and over the rotor plane to upstream chord-wise distances y/c of 0.5, 1.0, 1.5 and 2.0, as shown in fig. 5.6. While good convergence between the different cases is seen for the case of the MEXICO rotor for $y/c >= 1.0$, errors occur when $y/c = 0.5$ due to the local distortion of the flow-field and associated large velocity gradients close to the blade. The inclusion of a core radius model may further improve this singularity based method [13]. A significant divergence in the root section is also observed for the Sch15B rotor when distances are presented in terms of y/c. This divergence is a consequence of the high solidity of the rotor, where at an upstream distance of 2 chords (measured aligned with the local chord) the radial coordinate of the measuring point has substantially changed.

As an improvement, the monitor points can be placed at a constant radius and the chord-wise distance projected over the constant-radius arc ζ. This limits the distance at which the monitor points can be placed near the root for a high-solidity turbine, as the points quickly fall into the next blade. Hence, the analysis was performed placing the monitoring points at ζ/c values of 0.5, 0.75, 0.95 and, as a special case, over the bisectrix between two consecutive blades (thus, at varying ζ/c with r/R). The results in fig. 5.6 show good agreement at the root section for the Sch15B turbine, eliminating the problem seen using a linear chordwise extrapolation to the monitoring points, with some spread in results for $\zeta/c = 0.5$ associated with the local flow perturbation caused by the blade, which is particularly apparent for the low λ case. For the MEXICO rotor, similar divergence of results are seen for low sampling distances, and also for analysis using the bisectrix as this is now a large number of chords from the blade for this lower solidity rotor.

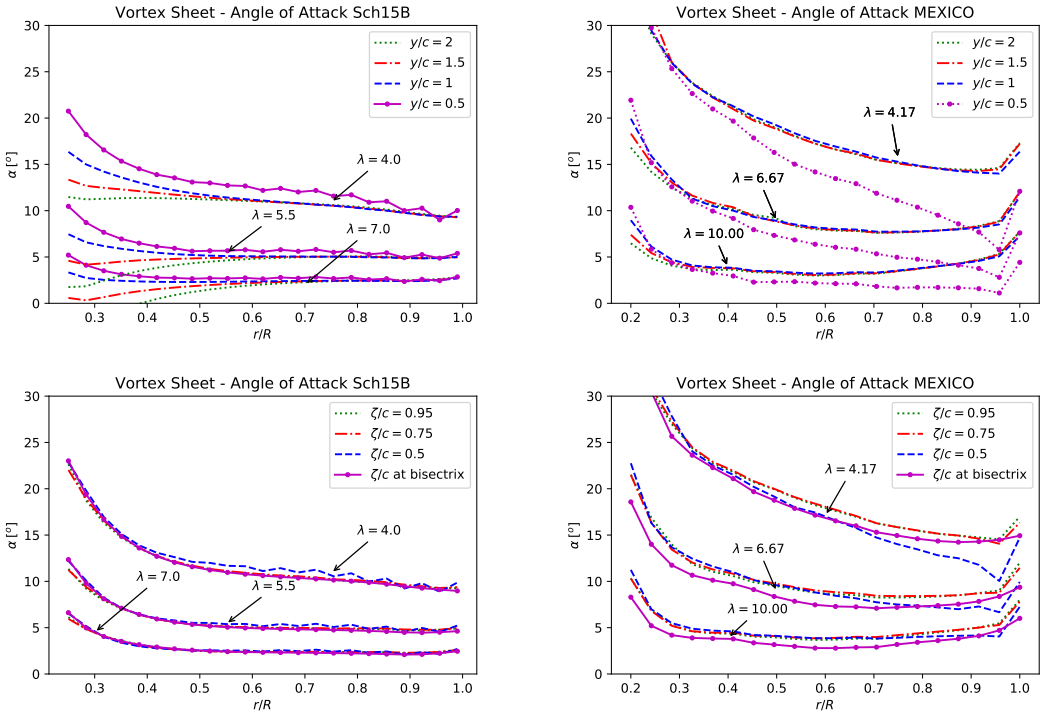

Figure 5.6: Convergence study of the Vortex Sheet method. Results are presented for the linear, y/c, and the arc segment, ζ/c, distances to the monitor point.

5.3.3.3 Pressure fitting

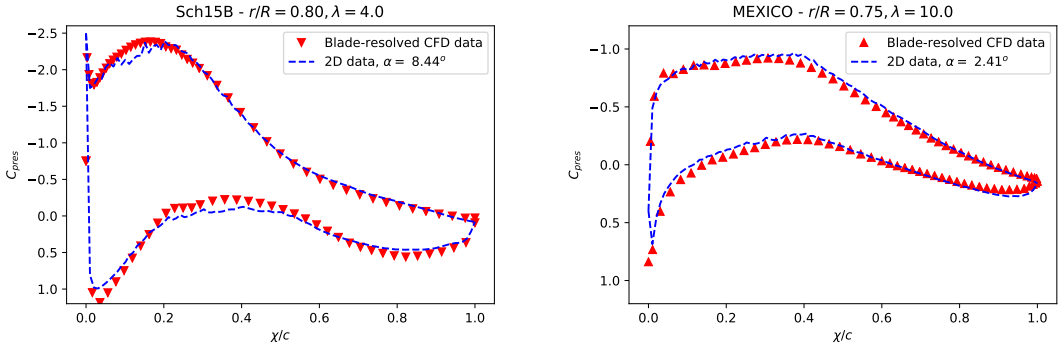

Figure 5.7: Examples of the pressure-fitting technique applied to two arbitrary cases for the Sch15B (left) and MEXICO (right) rotors.

This method was originally described by Bak et al. (2011) and entails fitting two-dimensional pressure coefficient distributions to the surface pressure fields extracted from three-dimensional simulations. The method was developed as an approach to process experimental data but can also be used to analyse blade-resolved CFD simulation data. Despite being disregarded by Guntur and Sørensen [6], this method is included in the analysis.

The original authors state that, to implement the method, the pressure should be fitted only to the pressure side of the blades, where separation is unlikely to occur. Then, the least squares method can be applied to minimise the value of a residual S by varying the angle of attack α and the inflow velocity W:

$$S = \sum_{i=1}^{n} \left(P_i - \frac{1}{2} \rho W^2 C_{pres}(\chi_i/c, \alpha) \right)^2 \tag{5.10}$$

with χ/c the non-dimensional chord-wise coordinate, n the number of points along the chord where pressure data is available at a given radius r, P_i the pressure as measured at the $i-th$ point, ρ the flow density, W the inflow velocity and C_{pres} the pressure coefficient as a function of the position of the point χ_i/c and the angle of attack α.

In this analysis, it is worth noting that the Sch15B turbine consists of a single Risø A1-24 aerofoil, whereas the MEXICO rotor comprises three different aerofoils

with corresponding transition regions. The analysis presented herein covers the entire Sch15B turbine, but was limited to the NACA 64-418 aerofoil which is used from 74.4% of the span up to the tip on the MEXICO rotor.

The two-dimensional pressure coefficient distributions C_{pres} were extracted from 2D simulations following the CFD configuration described in section 5.3.2, using high quality structured meshes made with ICEM 19.0. Three different meshes were tested for each aerofoil, showing negligible variations and leading to a final cell count of about 3.9×10^5 for the NACA and 2.0×10^5 for the Risø aerofoils. The simulations were conducted for angles of attack from -20 up to 60 degrees in steps of 1 degree, and intermediate pressure distributions were obtained by linear interpolation.

The results of the pressure fitting process can be seen, for two typical blade sections, in fig. 5.7. Good agreement is observed between the two-dimensional CFD data and the pressure field extracted from the blade-resolved rotor CFD. This method, despite showing promise across the blade mid-span where the flow is well attached and largely two-dimensional, has significant problems where the flow separates, and, due to the assumption that the flow is two-dimensional, where three-dimensional effects distort the blade pressure fields from those of two-dimensional aerofoil sections (Wimshurst and Willden [26]).

5.3.3.4 Bisectrix

This method, introduced by Herráez et al. [9], works on the assumption that a location on the turbine plane exists where the effects caused by the blades circulation are balanced resulting in net zero velocity induction, allowing the flow velocities to be directly extracted from the flow field.

For a uniform axial-flow condition, Herraez et al. prove using the Biot-Savart theorem and a description of the blades based on lifting-line theory, that the velocities sampled at the bisectrix between two consecutive blades are free from any blade-induction effects (see fig. 5.8 for bisectrix location definition).

The main virtue of this approach is its inherent simplicity: it just requires sampling the axial and tangential velocities from the flow (V_x and V_θ) and employing

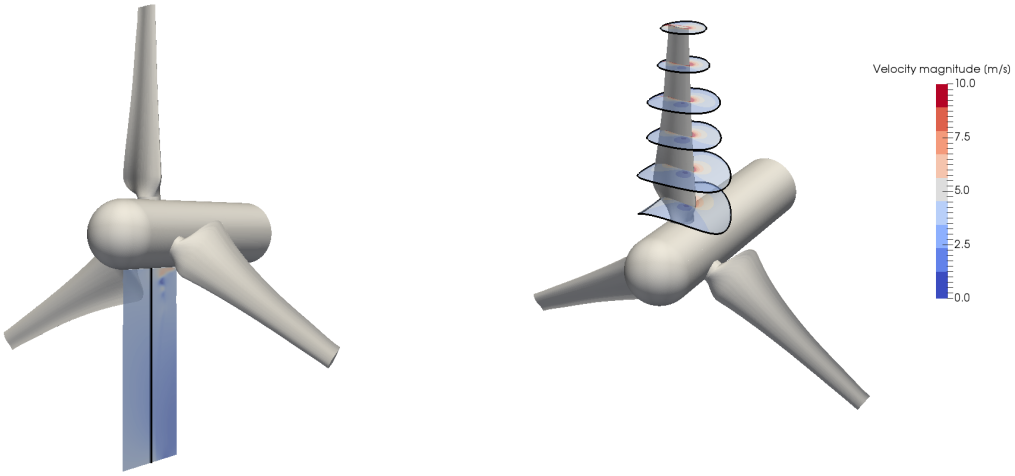

Figure 5.8: Schematics of the velocity extraction regions in the Bisectrix (left) and Line Average methods (right).

these to directly calculate the angles of attack (eqs. 5.1 and 5.4) without any further manipulation. However, a limitation is that any non-homogeneity in the flow, such as environmental turbulence or boundary-layer shear effects are neglected which would negatively impact the extracted results.

5.3.3.5 Line Average

Jost et al. [12] introduced this method, which works with a similar circulation based framework as others previously discussed. It assumes that each blade section produces a circulation effect that can be removed from the flow-field to obtain the inflow angles. Despite using a similar underlying assumption to other methods discussed, this method does not directly model the blade as a set of bound vortices to obtain the induced velocity, but averages the velocity components V_x and V_θ over a symmetric closed pathline centred on the blade quarter chord for different radial positions, as shown schematically in fig. 5.8. As the average is taken around the blade, not only does the circulation influence vanish, but the method should also be capable of capturing local and even transient effects.

The major drawback of the method is associated with trailing vorticity, which if captured around the pathline averages, can negatively influence the accuracy of the

results. For this reason, the method was tested with circular pathlines projected over constant radii, and a convergence study was performed extracting the angles of attack for the two rotors under different conditions, using different radii pathlines expressed as a function of the local chord c. The results can be seen in fig. 5.9, showing that the method is almost invariant to variations in the pathline radius used to enclose the blade sections in the mid-span sections, with some small divergence of the results observed at the tip and root of the blades.

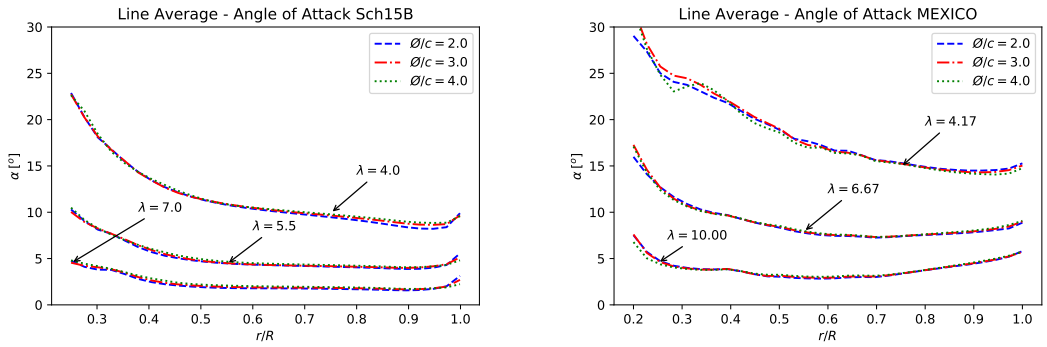

Figure 5.9: Angles of attack obtained from the velocities averaged around closed circular pathlines enclosing the local blade as a function of pathline diameter, $Ø/c$, for the Sch15B and MEXICO rotors at the three tip-speed ratios.

5.3.4 Streamtube Analysis Method

The concept of using the Streamtube Analysis Method (SAM) to extract the angles of attack and the flow velocity components at the turbine plane was originally developed by Hunter [10] in an attempt to improve the convergence of the traditional Azimuthal Averaging Techniques by additionally considering the expansion of the streamtube in the velocity-extraction process. In common with the Line Average and Bisectrix methods, this approach has the advantage of taking the data directly from the flow and not requiring any form of post-processing or smoothing. However, the definition of a streamtube in a viscous flow is not as straightforward as in momentum theory. When a viscous flow passes through a turbine, it develops strong local gradients, vortices of different scales, and a wake that will mix and exchange energy with the surrounding fluid.

In the viscous-flow scenario, the behaviour of the flow past a turbine can be analysed using sets of independent streamlines seeded over the azimuth at a constant radius. In appendix 5 we provide more details on the streamlines behaviour, tracking their radial position and showing a low spread from the average radial position. The streamlines analysis, expensive in computational terms, shows that the streamtubes can be approximated to have a circular cross-section of radius $R_S(x)$ tangent to the azimuthally-averaged flow speed. This approach is introduced in the next section as a simplified and more practical method, as well as less expensive in computational resources, to build the tube surface using the azimuthal-averages of the axial and radial flow speeds, in a similar way to the AAT but integrating these velocities in the axial direction to obtain the expanding streamtube surface. A comparison of both the streamlines and streamtubes approach is also provided in appendix 5, showing an excellent agreement except near the tip where strong gradients and three-dimensional flow effects dominate.

5.3.4.1 Azimuthally-averaged streamtubes

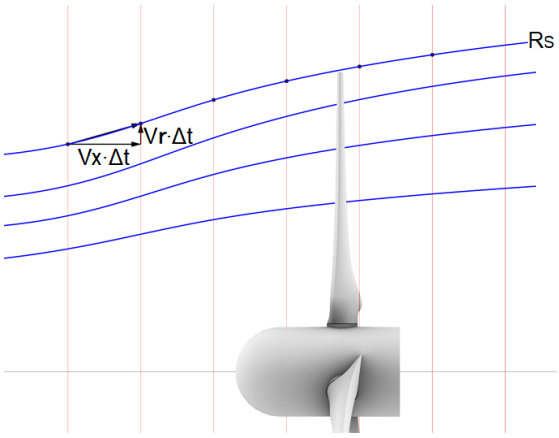

Figure 5.10: First order numerical integration scheme to obtain the azimuthal-averaged streamtubes.

Assuming the streamtubes to maintain a circular cross-section, as detailed in appendix 5, we can numerically integrate the azimuthally-averaged radial and axial velocities to construct a set of streamtube surfaces. For the case of steady-state simulations, we can define the streamlines as a function of the axial coordinate

Algorithm 1 Reconstruction of the azimuthally-averaged streamtubes

```
Define x values // Set of axial coordinates
Define r_0 values // Initial radii at x_0
i = 0
j = 1
for i do //Loop across radii
    r = r_{i,0}
    for j do //Loop across axial positions
        Extract V_x(r_{i,j}, x_i)
        Extract V_r(r_{i,j}, x_i)
        Calculate r_{i,j+1} = f(V_x, V_r) //(See e.g. fig 5.10)
        j=j+1
    end for
    Define the streamtube R_S(x) as the collection of r_i points
    Extract velocities to calculate α
    i=i+1
end for
```

x. Defining V_x and V_R to be the azimuthally-averaged axial and radial velocity components, respectively and as introduced in section 5.3.3.1, and noting the streamtube of radius R_S will be tangent to the local flow we may write:

$$\frac{dR_S}{dx} = \frac{V_R(x,r)}{V_x(x,r)} \tag{5.11}$$

$$\Rightarrow R_S(x) = \int \frac{V_r}{V_x} dx \tag{5.12}$$

which can be solved numerically as a function of x for any given value of r, as shown schematically in fig. 5.10 for a first-order numerical integration method.

Once the streamtubes have been reconstructed, the averaged velocity components over the streamtube $R_S(x)$ (i.e. at varying radial positions) can be used to calculate the angle of attack as described in section 5.3.3.1. This requires interpolating upstream and downstream along the identified streamtube to extract the velocities either side of the turbine plane. The same first-order interpolation scheme as used in 5.3.3.1 is employed to interpolate along the streamtube. The full approach is summarised in algorithm 1.

The streamtubes reconstruction approach is tested by integrating the velocities using 1st and 4th order Runge-Kutta methods, each with axial steps of $\Delta x/R = 1/30$ and $\Delta x/R = 1/60$, for $x/R \in [-0.5, +0.5]$. The results from this analysis are shown in fig. 5.11 in the form of a set of streamtubes for the Sch15B rotor at two operational conditions, showing little variation between the four different cases except in zones near the tip, where the strong gradients are better captured by the higher order integration scheme. In fig. 5.12 the results for the different integration schemes and $\Delta x/R$ values are presented for the MEXICO and Sch15B rotors in terms of the angle of attack distribution α, also showing a good agreement between the cases except near the tip.

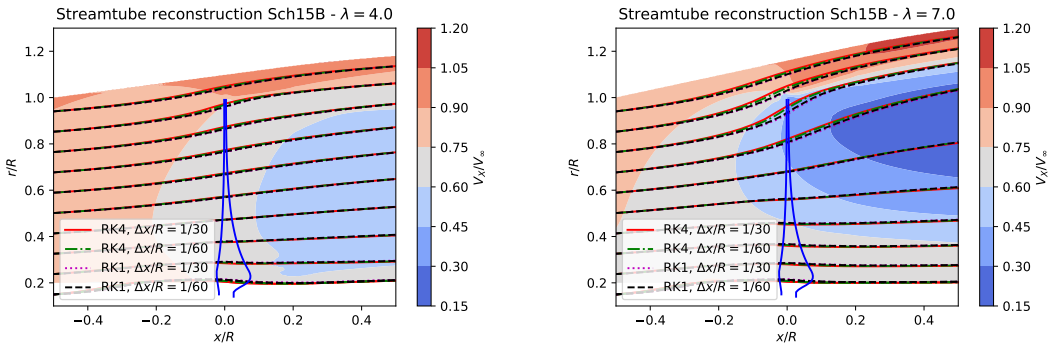

Figure 5.11: Streamtube reconstruction for the Sch15B rotor using 1st and 4th order Runge-Kutta methods (labelled as RK1 and RK4, respectively) and axial-resolutions $\Delta x/R$ for tip-speed ratios of 4.0 and 7.0.

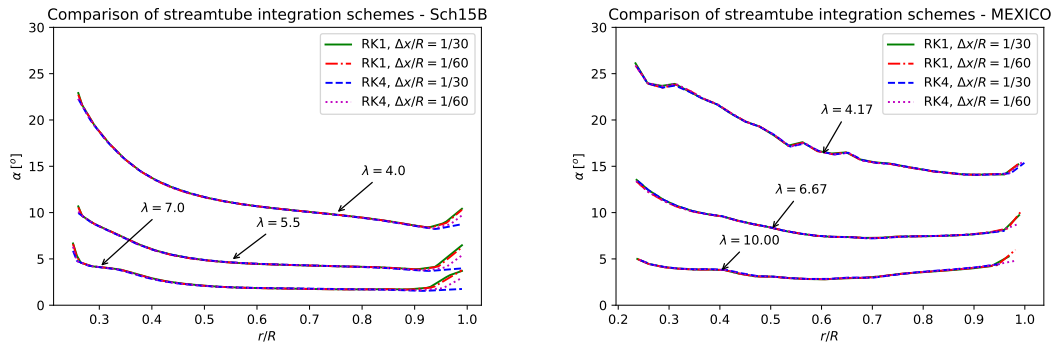

Figure 5.12: Comparison of the angles of attack calculated with the streamtube analysis method using 1st and 4th order Runge-Kutta integration schemes and different step-sizes $\Delta x/R$.

Finally, the streamtube method sensitivity to x/c is analysed on the same basis as the AAT method in section 5.3.3.1, i.e. at the same values that were used, and the results are plotted in fig. 5.13. From these plots, it can be observed that the spread of α is reduced in the inboard sections and root proximities when compared to the AAT, whereas some variations with x/c can still be observed towards the tip. The reduction in spread of α, and therefore insensitivity to x/c, is particularly apparent for the lower solidity MEXICO rotor for higher tip speed ratios where the flow remains attached.

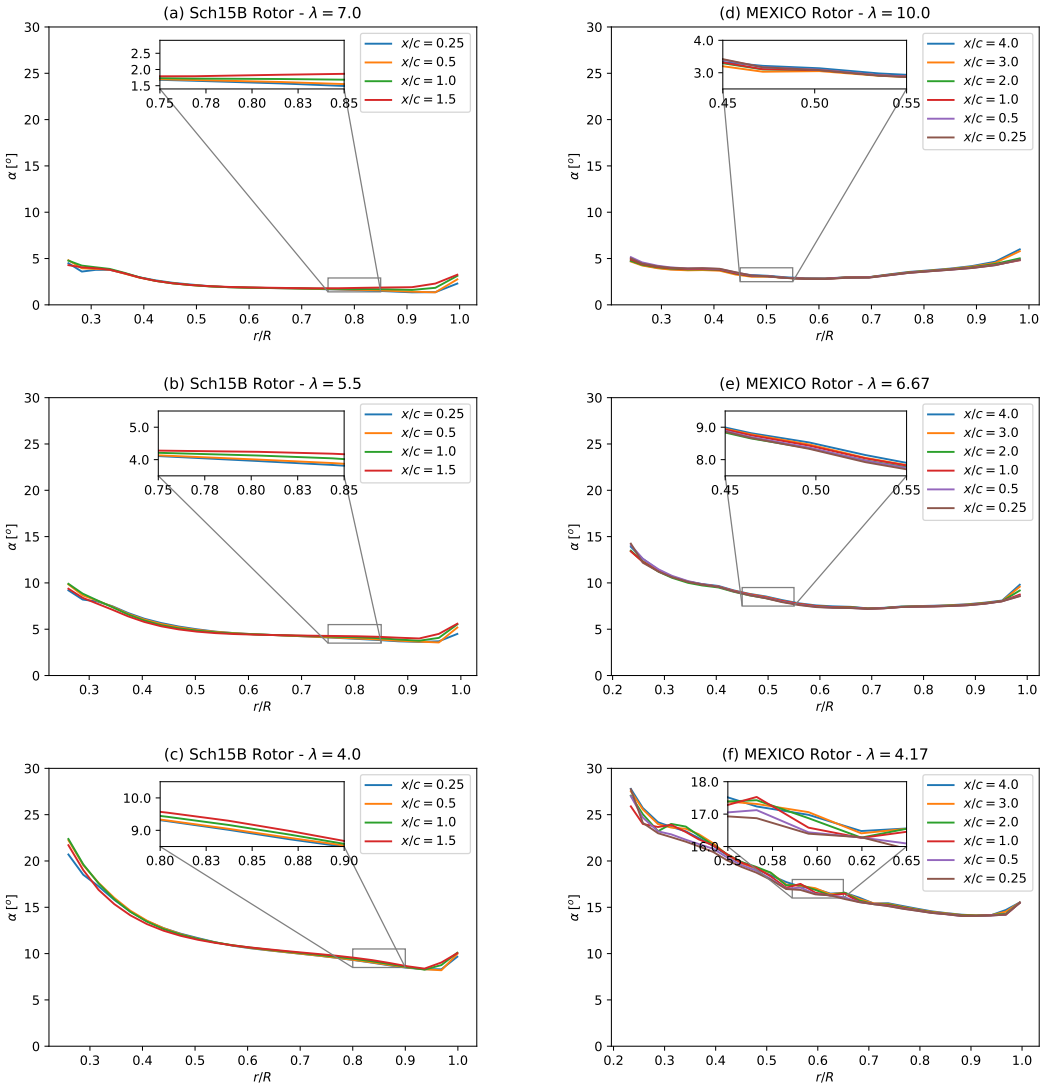

Figure 5.13: Angles of attack obtained with the SAM method with different data probing values, x/c, for three different tip-speed ratios: (a) $\lambda = 7.0$, (b) $\lambda = 5.5$ and (c) $\lambda = 4.0$, for Sch15B, and (d) $\lambda = 10.0$, (e) $\lambda = 6.67$, (f) $\lambda = 4.17$ for MEXICO.

Table 5.2: Parameters used by different methods for the benchmarking exercise.

		AAT	SAM	Vortex Sheet	Line Average	Pressure	Bisectrix
Sch15B	Parameter	x/c	x/c	ζ/c	$\emptyset/c$	Side	-
	Value	1.00	1.00	0.95	2.00	Pressure side	-
MEXICO	Parameter	x/c	x/c	y/c	$\emptyset/c$	Side	-
	Value	1.00	1.00	1.5	2.00	Pressure side	-

5.4 Benchmark and discussion

The concept of α is non-trivial to define for a rotating blade in three dimensions, and hence it is not possible to conclusively validate the methods with reference to any metric. Instead, this analysis evaluates how the different methods converge with each other in terms of three different variables: the spanwise distribution of the angle of attack α, the spanwise distribution of the axial induction factor a and the local lift and drag coefficients at two radial positions (from the computed relationship between angle of attack and normal and tangential force coefficients), one in the mid-span region and one close to the tip, providing different levels of detail and error-masking. Each method is presented for a representative case of internal model variables. Typically, the presented case should be for a converged value (where convergence can be achieved), and the details are presented in table 5.2.

Notice in table 5.2 that two different variables for the MEXICO and Sch15B rotors were used to assess the Vortex Sheet method. This is because we considered the selected variables and their respective values that achieve the best performance of the method for each rotor, as presented in section 5.3.3.2.

5.4.1 Angles of Attack

The angles of attack are the first set of results to be analysed as they are the key focus of the current work. In fig. 5.14 the reader will note that most methods converge with each other quite well even though they are based on very different assumptions and theories, with the pressure method being the outlier.

The pressure method had already been reported by Guntur and Sørensen [6] as not being reliable; and the present analysis agrees with their conclusion. The

pressure method displays good agreement in the mid-span region for the TSRs of 7.0 and 5.5 for the Sch15B rotor, where the flow behaves mostly as two-dimensional, with no separation and at relatively low angles of attack. However, outside of this well behaved region the results diverge from other methods considerably. A similar trend is observed for the MEXICO rotor, even though the data is more limited; recall that only the NACA profile occupying the outer region of the blade is analysed here.

The vortex sheet method diverts slightly from the rest of the methods in some of the cases, without observing a specific pattern, but even running on a completely different theoretical basis, it still displays a good agreement with the rest of the analysed methods. The Bisectrix method also shows some minor differences, especially for the Sch15B case at higher angles of attack and between the mid-span and blade root. This is due to the higher local blade solidity of the inboard region, which is more pronounced for this turbine. This high local solidity is sufficient to perturb the flow as far as the local bisectrix, rendering the assumption of undisturbed flow, once lifting line effects mutually cancel along the bisectrix, invalid.

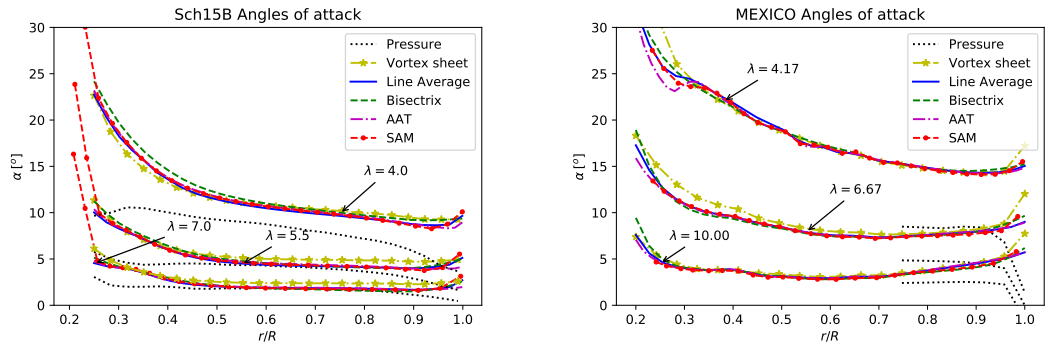

Figure 5.14: Angles of attack computed using various analysis methods for two rotors, Sch15B and MEXICO, at various tip-speed ratios.

5.4.2 Axial induction factors

Blade angles of attack are generally small and subject to small angle differences between analysis methods, partially due to the dominance of the rotational velocity component in determining the inflow angle. It is therefore instructive to examine

the different analysis methods to calculate the axial induction factors, defined according to equation 7.6, and plotted in fig. 5.15.

$$a = 1 - V_x/V_\infty \tag{5.13}$$

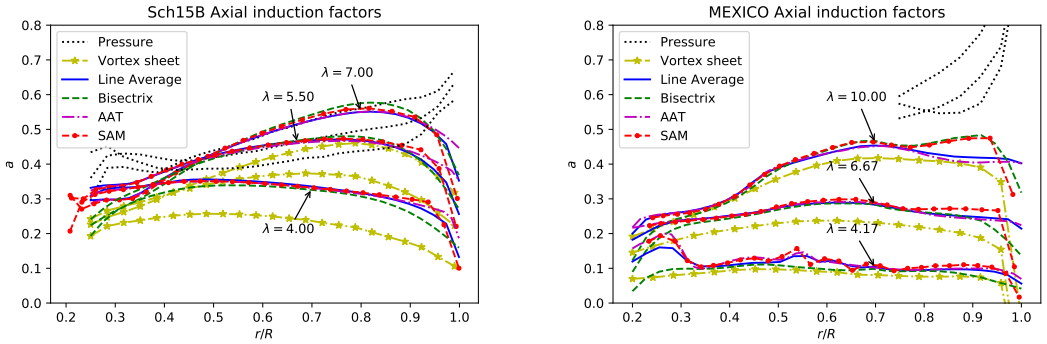

Figure 5.15: Axial induction factors computed using various analysis methods for two rotors, Sch15B and MEXICO, at various tip-speed ratios.

The induction factors uncover more significant differences in the calculations. They show a significant divergence of the Vortex Sheet method from the other methods, which was masked in the angle of attack analysis. This is likely due to the inviscid nature of the Vortex Sheet method considering the circulation around the blades without capturing viscous drag effects. The drag contributes significantly to overall thrust and thus flow deceleration. The lack of drag considerations in the vortex sheet model leads to an overestimation of through-rotor flow speed, and thus an underestimation of the induction factor. The error is relatively higher for the Sch15B rotor than the MEXICO rotor, due to the relatively higher thrust loading of the former.

The figure also shows how the Bisectrix method diverges near the root, departing from the other solutions as the bisectrix gets closer to the blades and their influence becomes stronger, as discussed previously. Note also how the AAT, SAM and Line Average methods maintain relatively good agreement with each other, with the exception of the tip regions, where three-dimensional flow effects dominate, and at higher tip-speed ratios where thrust tends to be higher, increasing the wake

expansion and the three-dimensional effects at the outboard blade sections. Those three methods also appear to capture some of the separation-induced effects on the MEXICO rotor at $\lambda = 4.17$ around the midspan, which manifest as wiggles or rapid spanwise changes in induction factor.

5.4.3 Force coefficients

The lift and drag coefficients at different radii can be used as a metric to evaluate different methods (See e.g. Johansen and Sørensen [11], Shen et al. [22], Guntur and Sørensen [6]). First, the distributions of thrust and tangential force per unit length, F_X and F_T respectively, are extracted from the CFD simulations by integrating the pressure and shear forces over a finite number of blade slices normal to the blade axis [26, 28]. These forces are then resolved into components parallel and normal to the local flow to yield blade sectional lift and drag coefficients:

$$C_L = \frac{L'}{1/2\rho W^2 c} \tag{5.14}$$

$$C_D = \frac{D'}{1/2\rho W^2 c} \tag{5.15}$$

where L' and D' are the sectional lift and drag forces, respectively.

In this analysis, we consider two radial positions; one at the mid-span region ($r/R = 0.65$), where a small spread is seen between the angles of attack provided by the analysed methods, and one at the near tip region ($r/R = 0.97$) where the spread is larger. Each simulation is analysed to yield single lift and drag coefficients at the corresponding radial position using the local angle of attack. Simulations at multiple tip-speed ratios are used to generate dependency with angle of attack. The results of this analysis can be seen in figs. 5.16 and 5.17 for the Sch15B and MEXICO rotors, respectively.

Disregarding the pressure-fitting method for the moment, we note that the spread between the computed coefficients is low even for the $r/R = 0.97$ cases on the two rotors. As with the previous analysis, it can be seen that some divergence is present for the Vortex Sheet method shows the same general trend as the other methods.

From this analysis technique it is difficult to draw further conclusions, as force coefficient analysis masks the error sources. Recalling eqs. 5.14 and 5.15, it is noted that the flow analysis methods differ in the calculation of W, which is dominated by the $V_\theta \approx \omega r$ component, and by the trigonometric relationship between the rotor-based frame of reference (thrust and torque) and the flow-based frame of reference (lift and drag).

The trigonometric relationship between the two different frames of reference depends on the inflow angle ϕ and not directly on α. Despite the absolute error for α and ϕ are equivalent (the difference between α and ϕ being the local blade twist angle β), ϕ is generally larger than α especially at high twist (inboard) regions of the blade, and thus the relative error passed to the force calculations will be lower.

Comparison of the local lift and drag coefficients inferred from each model demonstrates that in certain applications the variations in coefficients determined by the different flow analysis methods may be negligible.

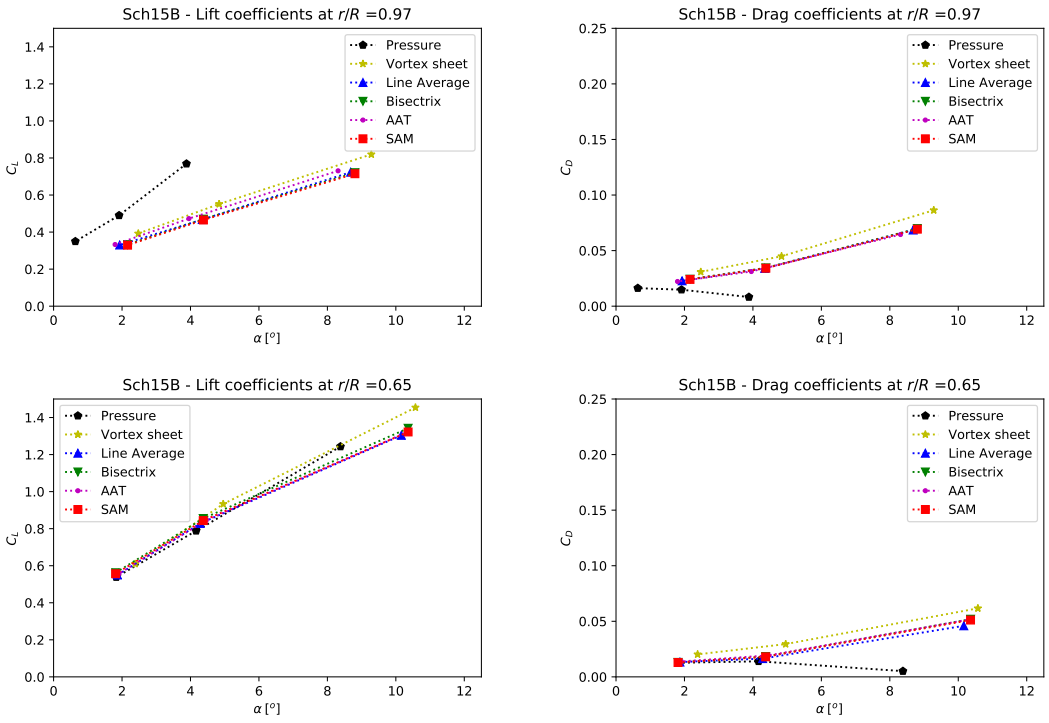

Figure 5.16: Sectional lift and drag coefficients for the Sch15B rotor.

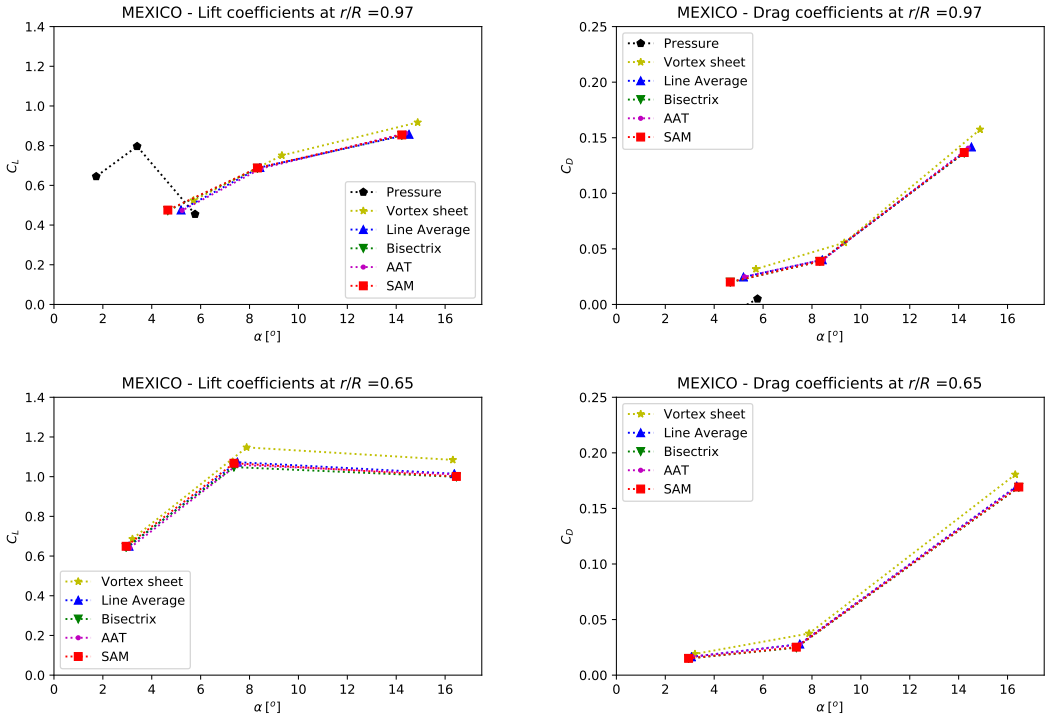

Figure 5.17: Sectional lift and drag coefficients for the MEXICO rotor.

5.5 Conclusions

This work has analysed six different methods based on different underlying assumptions to extract the angle of attack from three-dimensional blade resolved CFD simulations. These methods are based variously on circulation theory, streamtube interpolation, and least-squares fitting of two-dimensional surface pressures. Five of the six methods analysed showed good agreement with each other in calculating the spanwise distribution of angle of attack, particularly over the midspan of the two rotors analysed in this work. The pressure method was the only exception, which has also been reported to provide inaccurate results in other studies [6].

Although the remaining methods generally performed well, a number of limitations arising from their underlying assumptions and the physics of rotor blades were identified. The strong radial-flow velocity components and trailing vortices which arise near blade tips render two-dimensional concepts such as angle of attack less appropriate and hence these regions should not be treated in the same way as

the rest of the blade. However, as the angle of attack calculation is dominated by the tangential speed, the spread between different models in the tip region tends to be small. The differences between methods were highlighted by comparing the axial induction factor.

The Vortex Sheet method is developed from potential flow hypotheses and thus models the turbine under inviscid assumptions. It was found that, after correcting the post-separation assumption in the original method [21], better alignment of the predicted axial induction factor was achieved between this and the other flow-analysis methods for the MEXICO rotor than it was achieved for the Sch15B rotor. The lower solidity and thrust characteristics of the former rotor results in a smaller flow perturbation that in turn requires smaller flow correction.

The Line Average and Bisectrix methods showed good agreement in all of the analysed flow metrics. Of the two methods, we consider that the first is preferable as the latter could be significantly affected by ambient flow conditions such as environmental turbulence and shear. Both methods are influenced by the shed vortices and other blade generated flow phenomena, especially near the root. This can be especially significant for high solidity rotors.

The Streamtube Analysis Method (SAM) provided improved performance over the Azimuthal Averaging Techniques (AAT) in terms of the internal parameter x/c, reducing uncertainty in the computed flow-field values. Furthermore, the analysis of the streamtubes can also provide a valuable tool in exploring the flow phenomena around a rotor more generally, such as understanding near-rotor wake development.

Although it is not possible to conclusively validate the accuracy of the methods with respect to an independent model of angle of attack variation, we consider that the SAM and the Line Average methods are the most appropriate for general applications. They both have low sensitivity to their internal parameters (x/c and $\emptyset/c$ respectively), demonstrate good agreement with the other methods evaluated, work by directly sampling the flow field, and are relatively straightforward to implement.

Acknowledgments

This work was supported in part by CONICYT PFCHA/BECAS CHILE DOCTORADO EN EL EXTRANJERO 2016 /72170292. RHJW would like to acknowledge EPSRC who support his fellowship through grant number EP/R007322/1. The authors would also like to acknowledge the use of the University of Oxford Advanced Research Computing (ARC) facility in carrying out this work. http://dx.doi.org/10.5281/zenodo.22558 .

References

[1] C. Bak, N. Troldborg, and H. Madsen. "DAN-AERO MW : Measured airfoil characteristics for a MW rotor in atmospheric conditions". In: *Scientific Proceedings: European Wind Energy Association* (2011), pp. 171–175.

[2] A. Bechmann, N. N. Sørensen, and F. Zahle. "CFD simulations of the MEXICO rotor". In: *Wind Energy* 14.5 (2011), pp. 677–689.

[3] T. Burton et al. *Wind energy handbook*. Wiley, 2011.

[4] A. Fluent. "ANSYS Fluent theory guide 19.0". In: *ANSYS, Canonsburg, PA* (2018).

[5] H. Glauert. *Airplane propellers*. Springer, 1935.

[6] S. Guntur and N. N. Sørensen. "An evaluation of several methods of determining the local angle of attack on wind turbine blades". In: *Journal of Physics: Conference Series* 555.1 (2014).

[7] M. O. L. Hansen and J. Johansen. "Tip studies using CFD and comparison with tip loss models". In: *Wind Energy* 7.4 (2004), pp. 343–356.

[8] M. O. L. Hansen, N. N. Sørensen, and J. A. Michelsen. "Extraction of lift, drag and angle of attack from computed 3-D viscous flow around a rotating blade". English. In: European Wind Energy Conference, EWEC '97. 1997.

[9] I. Herráez, E. Daniele, and J. G. Schepers. "Extraction of the wake induction and angle of attack on rotating wind turbine blades from PIV and CFD results". In: *Wind Energy Science* 3.1 (2018), pp. 1–9.

[10] W. Hunter. "Actuator disk methods for tidal turbine arrays". PhD thesis. Department of Engineering Science: University of Oxford, 2015.

[11] J. Johansen and N. N. Sørensen. "Aerofoil characteristics from 3D CFD rotor computations". In: *Wind Energy* 7.4 (2004), pp. 283–294.

[12] E. Jost et al. "Extracting the angle of attack on rotor blades from CFD simulations". In: *Wind Energy* 21.10 (2018), pp. 807–822.

[13] J. Katz and A. Plotkin. *Low-speed aerodynamics*. Vol. 13. Cambridge university press, 2001.

[14] C. Lindenburg. "Investigation into rotor blade aerodynamics". In: *Energy research Centre of the Netherlands (ECN) Wind Energy publication, ECN-C–03-025* (2003).

[15] J. Y. Luo and A. D. Gosman. "Prediction of impeller-induced flow in mixing vessels using multiple frames of reference". In: INSTITUTE OF CHEMICAL ENGINEERS SYMPOSIUM SERIES. 1994.

[16] F. R. Menter. "Two-equation eddy-viscosity turbulence models for engineering applications". In: *AIAA journal* 32.8 (1994), pp. 1598–1605.

[17] F. R. Menter, M. Kuntz, and R. Langtry. "Ten Years of Industrial Experience with the SST Turbulence Model". In: *Turbulence Heat and Mass Transfer 4* 4 (2003), pp. 625–632.

[18] S. A. Ning. "A simple solution method for the blade element momentum equations with guaranteed convergence". In: *Wind Energy* 17.9 (2014), pp. 1327–1345.

[19] H. Rahimi et al. “Evaluation of different methods for determining the angle of attack on wind turbine blades with CFD results under axial inflow conditions”. In: *Renewable Energy* 125 (2018), pp. 866–876. arXiv: 1709.04298.

[20] J. Schluntz and R. H. J. Willden. “The effect of blockage on tidal turbine rotor design and performance”. In: *Renewable Energy* 81 (2015), pp. 432–441.

[21] W. Z. Shen, M. O. L. Hansen, and J. N. Sørensen. “Determination of the angle of attack on rotor blades”. In: *Wind Energy* 12.1 (2009), pp. 91–98.

[22] W. Z. Shen, M. O. L. Hansen, and J. N. Sørensen. “Determination of angle of attack (AOA) for rotating blades”. In: *Wind Energy: Proceedings of the Euromech Colloquium* (2006).

[23] W. Z. Shen et al. “Tip loss corrections for wind turbine computations”. In: *Wind Energy: An International Journal for Progress and Applications in Wind Power Conversion Technology* 8.4 (2005), pp. 457–475.

[24] H. Snel, J. G. Schepers, and B. Montgomerie. “The MEXICO project (Model Experiments in Controlled Conditions): The database and first results of data processing and interpretation”. In: *Journal of Physics: Conference Series* 75.1 (2007), p. 012014.

[25] A. Wimshurst and R. H. J. Willden. “Computational analysis of blockage designed tidal turbine rotors”. In: *Progress in Renewable Energies Offshore - Proceedings of 2nd International Conference on Renewable Energies Offshore, RENEW 2016* Emec (2016), pp. 587–597.

[26] A. Wimshurst and R. H. J. Willden. “Extracting lift and drag polars from blade-resolved computational fluid dynamics for use in actuator line modelling of horizontal axis turbines”. In: *Wind Energy* 20.5 (May 2017), pp. 815–833. arXiv: arXiv:1006.4405v1.

[27] H. Yang et al. “Extraction of airfoil data using PIV and pressure measurements”. In: *Renewable Energy* (2011).

[28] F. Zilic de Arcos, C. R. Vogel, and R. Willden. “Hydrodynamic modelling of flexible tidal turbine blades”. In: *Proceedings of the Thirteenth European Wave and Tidal Energy Conference*. ISSN: 2309-1983. EWTEC. 2019.

[29] F. Zilic de Arcos, C. Vogel, and R. Willden. “Hydroelastic modelling of composite tidal turbine blades”. In: *Advances in Renewable Energies Offshore: Proceedings of the 3rd International Conference on Renewable Energies Offshore (RENEW 2018), October 8-10, 2018, Lisbon, Portugal*. 2018, p. 877.

Appendix A - Streamtubes as collections of streamlines

Sets of 500 streamlines at different radii are used to capture the distribution of streamlines that arises in a viscous wake. The seeding plane is located at 0.5R downstream of the turbine plane, and 50 radial locations are considered.

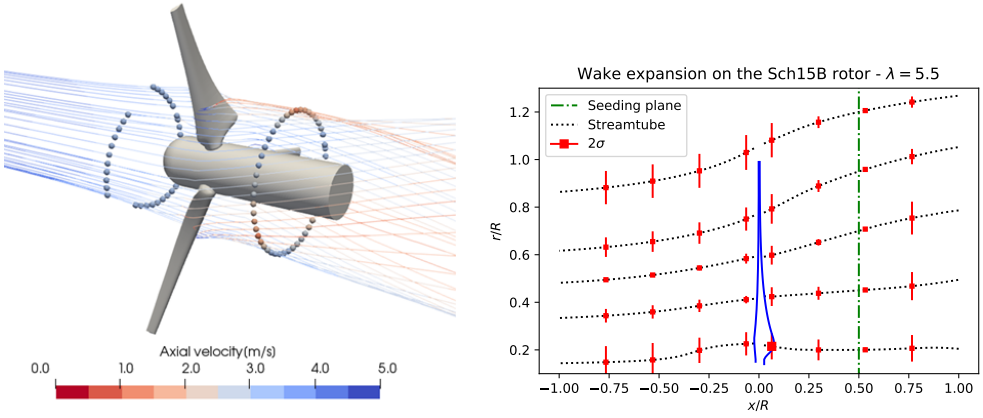

Figure 5.18: Streamtubes built from the collections of streamlines for the Sch15B rotor at $\lambda = 5.5$. Streamtubes shown in right image are azimuthally-averaged, and error bars are two standard deviations of the radial position of the streamtube.

The streamlines are constructed in both upstream and downstream directions by integrating through the flow-field using a Runge-Kutta 4-5 adaptive integration scheme. This approach allows the streamtube to be tracked even if wake mixing or flow separation occurs, and to determine the variability of the radial coordinate of the streamlines at different axial locations, enabling assessment of the radial spread. Each streamline is observed to spiral into or away from the flow centreline due to radial velocity components. Hence, an initial circular streamtube distorts from the circular geometry as it evolves up or downstream (see the three-dimensional flow image in fig. 5.18). Fig. 5.18 also shows the azimuthally-averaged streamtubes and error bars computed as twice the standard deviation of the radial position of the streamlines. The error bars remain small showing a small spread in radii, from which we conclude that the streamtube can be approximated by its azimuthally-averaged position.

Following this analysis, a comparison of the angle of attack calculated with the azimuthally-averaged streamtubes (integrated with fourth order Runge-Kutta) and the streamlines-tracking approach for all the tip-speed ratios and at interpolating the velocities at two chord-wise distances ($x/c = 1.0$ and $x/c = 2.0$) is shown in fig. 5.19. The two methods show an excellent agreement except for the tip-region,

proving the streamtubes approach as a viable estimation to include the expansion of the streamtubes in the azimuthally-averaged field determination.

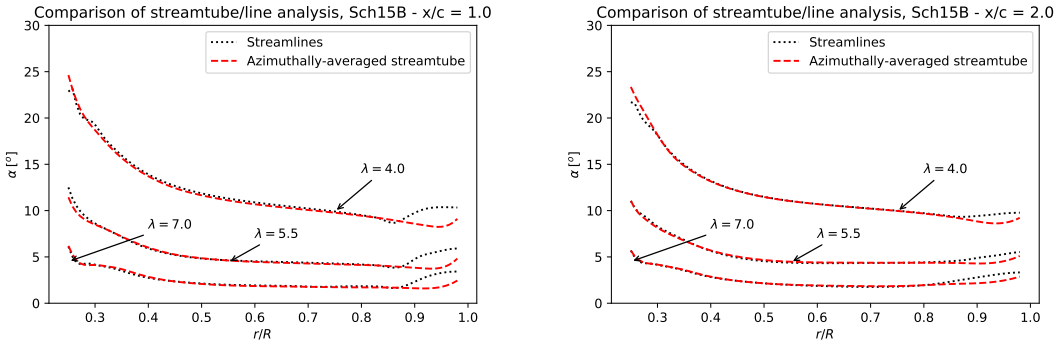

Figure 5.19: Comparison between the angles of attack extracted with the sets of streamlines and the azimuthally-averaged streamtubes. The velocities were extracted at $x/c = 1.0$ (left) and $x/c = 2.0$ (right) from the turbine plane on both cases.

Part III

Hydrodynamics of rotor blade deformations

Paper submitted to the Journal of Fluids and Structures:

A parametric study on the hydrodynamics of tidal turbine blade deformations. In: Journal of Fluids and Structures. Submitted.

Federico Zilic de Arcos, Christopher R. Vogel, Richard H. J. Willden

6

A study on the hydrodynamics of tidal turbine blade deformations

6.1 Abstract

The blades of axial-flow rotors, which are typically made of flexible composite materials, can experience significant deformations through their operation. However, the impact of these deformations on rotor hydrodynamics is not well understood.

Blade deformations can be separated into three main components: flapwise, a thrust-driven deformation in the direction of the flow; edgewise, relatively small deformations in the plane of rotor motion and driven by rotor torque; and twist deformations that affect each blade's angle of attack distribution and are generated by the torsional moment acting about the blade's spanwise axis as well as by structural interactions.

This work evaluates the hydrodynamic effects of the decoupled flapwise and twist deformations on a tidal turbine blade, using blade-resolved Computational Fluid Dynamics (CFD) simulations with the objective of identifying and quantifying the associated flow phenomena. The deformation cases were generated by scaling the static deformation shapes from a structural model of the turbine blade. The analysed dataset consists of 68 blade-resolved Reynolds-Averaged Navier-Stokes CFD steady-state simulations.

It was found that twist deformation effects are significant, and can be adequately described using blade element theory. Flapwise deformations, on the other hand, produce different phenomena affecting the rotor loading and performance in ways that cannot be explained on a blade sectional basis through blade element theory.

It is found that the hydrodynamic impact of flapwise deformations can be explained through two different mechanisms: a pressure drop on the suction side of the blade that generates inboard load augmentation, and an increase in near-tip radial flow effects that moves the onset of tip-loss effects, and shedding of thrust and power, further inboard. The studied cases show a significant impact of flapwise deformation on integrated power (up to a 20% drop), while the impact on integrated thrust remains limited, with variations between -4% to +2% in thrust coefficient observed depending on blade bending.

6.2 Introduction

The design and optimisation of turbine blades is a well studied area for which some established methodologies allow the designer to obtain optimised aero- or hydrodynamic geometries. These methods are typically based on Blade-Element Momentum Theory (BEMT) in which the flow through the turbine is discretised using a set of concentric annuli, and the forces on each blade section described as a result of the incident relative flow-velocity and the two-dimensional polar characteristics of the foil section (Glauert [10], Burton et al. [5]). However, during operation, the blade geometry can deform due to the forces acting on the blade. These deformations can change the aero- or hydrodynamics of the blade, further affecting the forces acting on it and thus its deformation, driving fluid-structure interaction (FSI) phenomena.

Blade fluid dynamics are optimised for a range of different objectives. These include for open-flow operation, in the case of wind turbines (e.g. Chehouri et al. [6]), farm optimisation or even local optimisations based on blockage and array configurations (e.g. Schluntz and Willden [29]). These analyses typically assume the blade structure to be rigid, thus neglecting potential FSI effects and blade

deformations which can be of significant magnitude. For example, Nicholls-Lee [25] predicted a maximum tip deflection of 1.48 m for a 10 m radius tidal rotor; Grogan et al. [11] predicted a maximum deflection of 1.75 m for a 12 m length tidal turbine blade; and Rafiee et al. [26] a maximum deflection of 1.46 m for a 23.50 m radius wind rotor.

Efforts have been made to model the FSI phenomena on axial-flow rotors by solving the structural and fluid mechanics problems in parallel with varying degrees of complexity and coupling. The simplest approach and common engineering practice is to use one-way coupling methods, applicable where the deformations are deemed small and the resultant change in hydrodynamic loads due to these deformations negligible. The loads from an aero-/hydrodynamic solver are applied directly to a structural model to determine deformations or structural stress distributions (e.g. Bir [3], Grogan et al. [11]) without iteration of the fluid loading. However, when the deformations are significant, two-ways coupled methods are better suited. In these methods, the deformed blade data from the structural solution is used within the fluid-dynamics solver to generate new loads, iterating until convergence is achieved (e.g. Bazilevs et al. [2], Nicholls-Lee et al. [24], Rafiee et al. [26]).

Amongst the different methods proposed to analyse the FSI phenomena on axial-flow rotors [32], lower-order models (e.g. models based on BEMT coupled with 1D structural beam elements) are generally desirable for practical applications. Such models typically have a sufficiently low computational cost that enables a large number of cases to be simulated, as required for the design and optimisation of commercial rotors. Engineering models for axial-flow turbine FSI have been developed and used in both academic and commercial environments (see, e.g., Vorpahl et al. [30], Guntur et al. [12], Larsen and Hansen [15]).

Previous research performed by the authors of this study highlighted some limitations of the assumptions of blade element theory that are fundamental for the aforementioned engineering models [38]. Literature also suggests that a consensus regarding the fluid dynamics of rotor blade deformations has not yet been achieved. In the related area of wind energy, for example, investigations have been conducted

for the similar fluid mechanics problem of coned rotors. Madsen and Rasmussen [18] studied the hydrodynamic effects of out-of-plane coning and bending using an axisymmetric actuator-disc CFD approach, and showed how blade bending alters the axial and radial flow velocities through the disc. They demonstrated that the integrated power coefficient for the rotor is independent of the out-of-plane deflection for uniform rotor thrust loading. Mikkelsen et al. [22], also using actuator-disc CFD simulations, observed power reductions with coning, although also reported that the non-dimensional power coefficient based on the projected rotor area is largely unaffected. Mikkelsen et al. [22] argue that the changes in radial flow cannot be captured by BEMT without violating the annular independence assumption of the theory. However, Crawford [7] maintained the streamtube independence requirement to formulate a modified BEMT model for coned rotors, reporting power and thrust reductions across most of the span of a wind rotor. In contrast, the results presented by Zilic de Arcos et al. [38], obtained through blade-resolved CFD simulations, showed increased loading around the inboard of a rotor blade bent in the flapwise direction, even in parts of the blade with small deformations. Ultimately, this lack of consensus presents difficulties for assessing the accuracy and scope of application of the available FSI engineering models for axial-flow rotors.

Passive rotor control through blade deformations seeks to exploit the FSI phenomena on axial rotors to achieve control objectives such as load and power shedding above rated flow speed (e.g. Wada et al. [31], Murray et al. [23], Kaufmann et al. [14]). These strategies often rely on large deformations that are expected to occur in a controlled manner, and their design and optimisation is likely to rely on engineering models. This area, however, is particularly affected by the aforementioned limitations on the understanding of deformed blade hydrodynamics. Such an understanding is not only a prerequisite for the accurate modelling of deformed rotor blades, but also for determining the feasible limits of passive control technologies.

This study seeks to identify and quantify the significance of the hydrodynamic effects of tidal rotor blade deformations, presenting the findings in terms that are

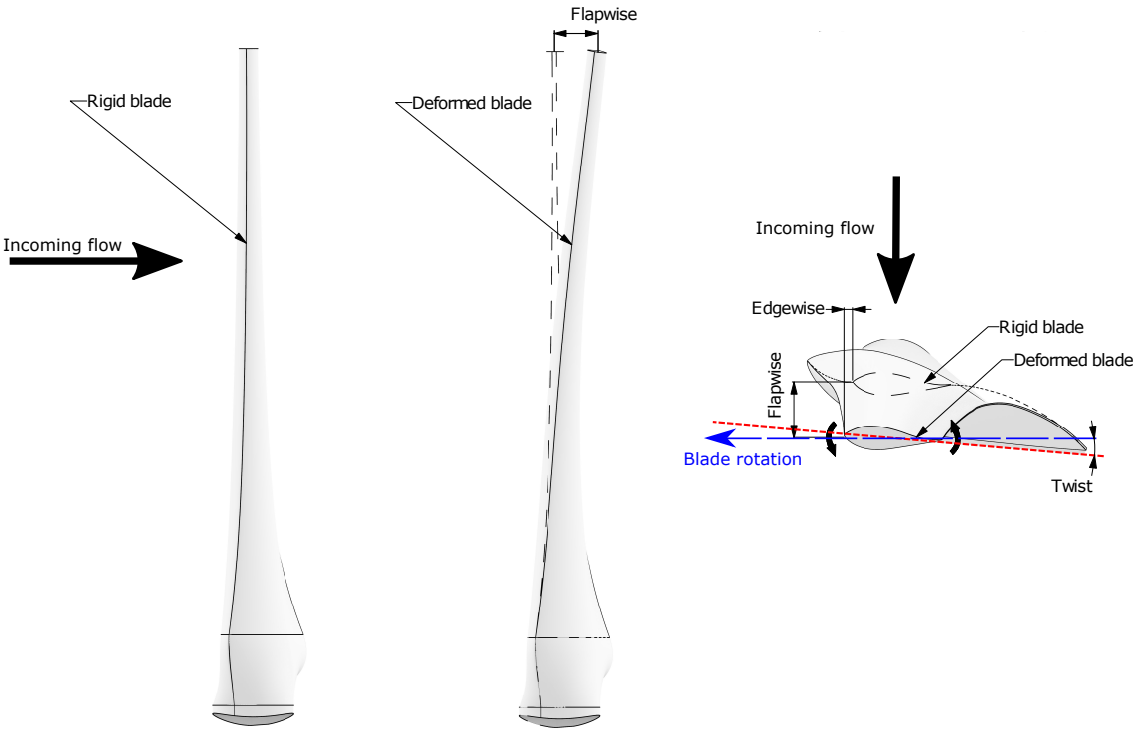

Figure 6.1: Deformation degrees of freedom for a turbine blade as seen from side and blade tip-to-root views. The two views show a render of the deformed blade alongside an outline of the undeformed blade.

relevant for the development and improvement of engineering models. We decoupled the deformations into three main components: flapwise deformation, driven by thrust forces and typically the largest deformation component in magnitude; edgewise deformation, driven by blade torque and typically small in comparison; and twist deformations that modify the spanwise twist angle distribution along the blade and are driven by the moment caused by structural coupling effects and the misalignment of the structural centre and the centre of pressure. These principal deformation components are depicted for a turbine blade in fig. 6.1.

An extensive suite of blade-resolved Computational Fluid Dynamics (CFD) simulations were performed to investigate the impact of twist and flapwise deflections. The effect of deflection magnitude has been assessed parametrically based on the scaled static response from structural analysis of a composite tidal turbine blade [38]. The blade geometry, designed by Schluntz and Willden [29], modified by Wimshurst and Willden [34] and Zilic de Arcos et al. [38], was evaluated for 6 cases

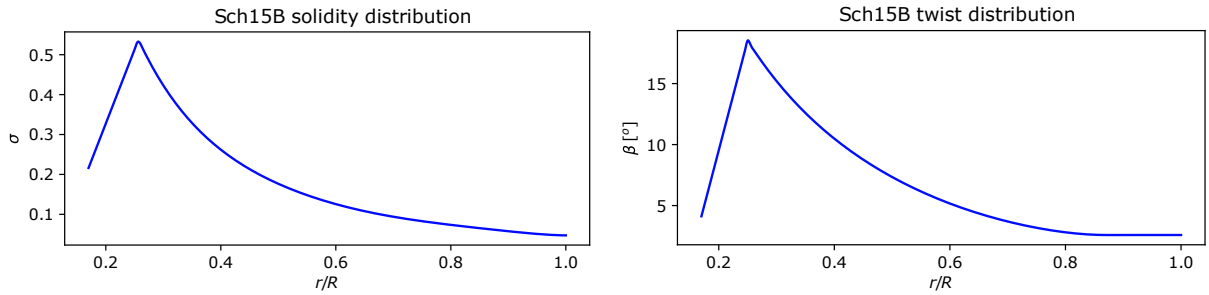

Figure 6.2: Characteristics of the Sch15B rotor: Spanwise distributions of the blade solidity σ, and twist angle β.

of twist-only deformation, 5 cases of flapwise-only deformation and 5 flapwise-twist coupled deformation cases. Each of these cases, in addition to a case with no deformation, was meshed and simulated at four different tip-speed-ratios λ each.

The resulting dataset was used in this work to identify the hydrodynamic effects associated with the decoupled deformations twist-only and flapwise-only, providing insights into the phenomena affecting forces and flow development, alongside with an understanding that can be later used to improve the accuracy and predictive capabilities of engineering models.

6.3 Rotor characteristics

The rotor used in this study is a tidal turbine design developed by Schluntz and Willden [29] for a blockage ratio (ratio of turbine swept area to surrounding flow passage cross-sectional area) of 0.197, and modified by Wimshurst and Willden [34] and by Zilic de Arcos et al. [38] in the root region. It is a three-bladed 20 m diameter rotor based on a single Risø A1-24 aerofoil from 25% of the rotor radius to the blade tip and a transition surface from the aerofoil cross-section to a cylindrical root between 25% and 15% of the rotor radius, where the blade is attached to the nacelle. The aerofoil's quarter-chord is aligned with the blade's pitch axis. The distribution of twist angle β and solidity $\sigma = cZ/(2\pi r)$ where c is the local chord, Z the number of blades, and r the local radius, are shown in fig. 6.2.

The root region was modified from the original design as described in Zilic de Arcos et al. [38] to provide a smoother geometrical transition from the aerofoil

section to the circular coupling point at the nacelle, avoiding stress concentrations due to the abrupt cross-section change seen in earlier geometries.

6.4 Parametric space

The parameter space includes, in addition to the undeformed blade geometry, five flapwise-only deformation cases, six twist-only deformation cases, and five coupled twist-flapwise deformation cases.

The twist deformation was applied as a linear function over the span of the blade, starting from no deformation at $0.25R$, with R the blade radius, to a value $\delta\beta$ at the tip, with the tip twist being used to label and identify the different cases. The use of a linear twist deformation distribution is a simplification of a complex fluid-structural phenomenon that involves the moment distribution over the blade, the position of the structural centre and the bending-twist coupling mechanisms [16]. This simplification is supported as an approximation to the solution extracted from an engineering FSI model [39]. The analysed cases are $\delta\beta \in [-5.0, -2.5, 0.0, 2.5, 5.0, 10.0, 15.0]$ [°]

The flapwise deformation was generated by scaling the flapwise component of the static deflection of the quarter-chord line as extracted from the shell-element structural model in Zilic de Arcos et al. [39] at a tip-speed-ratio of $\lambda = 5.5$ and a flow speed of $V_\infty = 4.5$m/s. This specific case was chosen to form the flapwise deformation mode, as it exhibited negligible twist deformations. The flapwise deformation cases are labelled and identified by the flapwise deformation value at the tip, $\delta x/R$, with the cases analysed being $\delta x/R \in [0.000, 0.075, 0.100, 0.125, 0.150, 0.175]$.

Additionally, five coupled twist-flapwise deformation cases were simulated to evaluate the deformation-component independence hypothesis introduced in Zilic de Arcos et al. [38]; cases being $\{\delta x/R = 0.075, \delta\beta = -2.5°\}$, $\{\delta x/R = 0.075, \delta\beta = 2.5°\}$, $\{\delta x/R = 0.100, \delta\beta = 2.5°\}$, $\{\delta x/R = 0.100, \delta\beta = 5.0°\}$ and $\{\delta x/R = 0.150, \delta\beta = 15.0°\}$.

The blade surfaces were constructed using the Algorithmic-Aided Design package Rhinoceros 6.0 with Grasshopper 1.0. The different blade geometries were built by

Table 6.1: Testing matrix of simulated cases for $\delta\beta$ and $\delta x/R$. Each point in the matrix was simulated at tip-speed-ratios $\lambda \in [4.0, 5.0, 6.0, 7.0]$.

$\delta x/R$	$\delta\beta$ [°]						
	−5.0	−2.5	0.0	2.5	5.0	10.0	15.0
0.000	✓	✓	✓	✓	✓	✓	✓
0.075		✓	✓	✓			
0.100			✓	✓	✓		
0.125			✓				
0.150			✓				✓
0.175			✓				

interpolating NURBS surfaces over 100 transverse sections, controlling the individual twist angle of each section, and specifying the required deformation values.

Each of the aforementioned cases were simulated at four tip-speed-ratios $\lambda = \omega R/V_\infty$, with ω the rotational speed and V_∞ the undisturbed flow velocity. The simulated tip-speed-ratios were $\lambda \in [4.0, 5.0, 6.0, 7.0]$, simulated by varying the rotational speed, and completing a stencil of 68 blade-resolved CFD simulations used to build the dataset. The spanwise twist distribution of the twist-deformation cases, as well as the deformed quarter-chord line for the flapwise deformation cases described above can be seen in fig. 6.3. A summary of the simulation case matrix is provided in table 6.1.

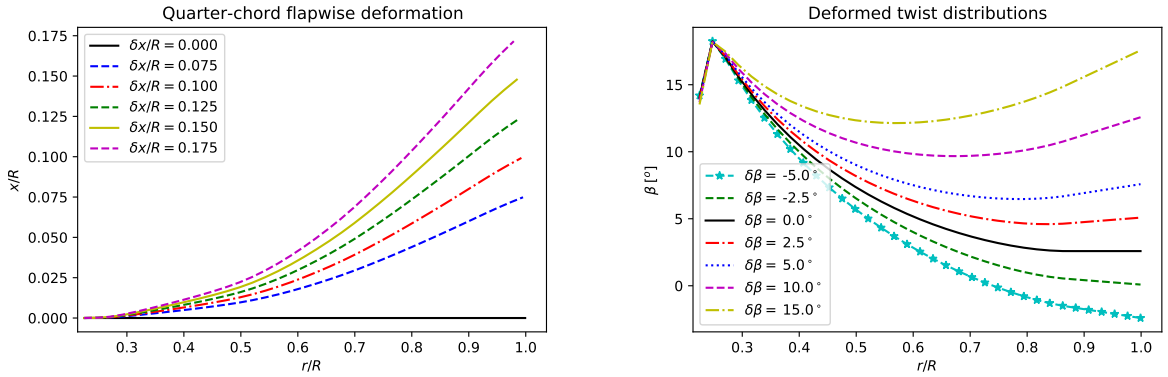

Figure 6.3: Axial-position of the quarter-chord line for the different flapwise deformation cases $\delta x/R$ (left), and twist distributions for the twist deformation cases $\delta\beta$ (right).

6.5 CFD model

6.5.1 Model details

The cases were modelled with a Reynolds-Averaged Navier Stokes (RANS) CFD approach under incompressible steady-state assumptions using the commercial solver Fluent 19.0. The closure of the RANS equations was made through the $k-\omega$ SST turbulence model [20] with the updated constants of Menter et al. [21] and a blending-function wall-modelling approach [8]. This model selection is supported by the work of McNaughton et al. [19] and Afgan et al. [1] where they show this turbulence closure model to agree well with experiments and higher-order turbulence closure models. A cell-centred finite volume discretisation scheme was used with a second-order upwind spatial discretisation and a coupled-pressure algorithm, which provides robustness and efficiency in single phase flows under steady-state conditions [8].

To model the turbine rotation under steady-state conditions we used the Multiple Reference Frame model described by Luo and Gosman [17] with a rotatory region for the turbine and stationary region for the remainder of the domain, each region having a different rotational speed ω defined by its local frame of reference. Across the interface, reference frame transformations are performed to enable the transport of fluxes from one sub-domain to another, as described in the original reference.

The entire domain was modelled using a cylindrical volume, exploiting the rotational symmetry of the problem and modelling only one blade in a 120° wedge with periodic boundary conditions along the azimuthal boundaries ($x-r$ planes). The remaining boundary conditions were defined as: velocity inlet with a uniform speed of 4.5 m/s with a turbulence intensity of 10% and a length scale of 0.7 times the rotor diameter, following Wimshurst and Willden [34] and based on data presented by Gant and Stallard [9]; the rotor blade surfaces as non-slip smooth walls; the outlet by a constant-pressure equal to that of the undisturbed flow, and the outer-cylindrical domain surface defined with a symmetry condition. Finally, the internal sub-domain interfaces are non-conformal.

The outer domain was modelled with a radius of 5 times the rotor radius to minimise blockage effects (blockage ratio 4%), with a length upstream equal to 5 times the rotor radius and 14 radii downstream. These dimensions provide sufficient space for flow development without undue influence of the boundaries on rotor performance or flow behaviour, as described by Wimshurst and Willden [34].

This modelling approach was selected as it provides accurate blade-resolved results and reduces the computational time by exploiting symmetry and steady-state conditions. A full validation of the methodology is presented in Wimshurst and Willden [36], where comparisons of blade resolved wind turbine CFD results and the MEXICO experiments (Schepers et al. [28], Boorsma and Schepers [4]) are provided in terms of spanwise force distributions and sectional pressure coefficients.

The simulations were performed on the ARCUS HPC facilities at the University of Oxford. For each simulation the solver iterated 20,000 times running on 96 cores and reducing the scaled residuals by at least 6 orders of magnitude for the continuity and velocity components, and at least 5 orders for the turbulence scalars.

6.5.2 Mesh study

Structured meshes were prepared for this study based on previous numerical studies, building a different mesh for each of the deformation cases described in section 6.4. The general mesh topology, presented by Zilic de Arcos et al. [38], consists of a Y-grid general layout and an O-grid mesh around the blade surfaces, following the geometries defined by the parametrically-generated NURBS surfaces.

The meshes of the different cases maintained a very similar near-blade region, providing good resolution of the near-wall flow features, and adapting buffer regions upstream and downstream of the rotor plane to absorb the deformations, with the number of elements n_c remaining constant. The non-dimensional wall distance y^+ was kept within the wall-modelling region (i.e. $30 \leq y^+ \leq 300$). The near-wall O-grid region has a first-layer thickness close to the blade surfaces of $\Delta y = 2.5 \times 10^{-4}\,\mathrm{m}$ (giving $8.5 \times 10^{-5} \leq \Delta y/c \leq 2.5 \times 10^{-4}$ along the blade), a wall normal growth-rate of 1.05 over 25 layers that smoothly transitions to the rest of the domain.

The original rotor subdomain [38] was modified to accommodate the blade deformations, and so a new mesh convergence study was performed. Three different turbine meshes were simulated at the highest thrust condition, $\lambda = 7.0$, as this presents the most sheared, and therefore most numerically demanding, flow condition. A subsequent refinement factor k_i of 2.0 was applied in each linear element dimension.

To assess the numerical uncertainty of the simulations, the grid-convergence index (GCI) described by Roache [27] and a relative error measure between meshes were used. The relative error E_R is defined as:

$$E_{R,i} = (\xi_i - \xi_{i-1})/\xi_i \tag{6.1}$$

with ξ is the analysed variable and the subscripts i and $i-1$ correspond to the current and coarser meshes, respectively. The analysed variables for this mesh study are the integrated power and thrust coefficients:

$$C_P = \frac{P}{1/2\rho A V_\infty^3} \tag{6.2}$$

$$C_T = \frac{T}{1/2\rho A V_\infty^2} \tag{6.3}$$

with P the integrated power, T the integrated rotor thrust and A the turbine's cross-sectional frontal area.

The coarse mesh was found to be outside the asymptotic convergence range, and so the GCI was only calculated for the medium and fine meshes, using an estimated effective order for the numerical method of $\mathscr{O} = 1.50$ based on previous observations [37] and a safety factor of 2 [27] (see table 6.2). Using GCI, the numerical uncertainty of the medium mesh shows a maximum relative error of 0.5% with respect to the fine mesh, and its uncertainty is estimated to be a conservative 1.54%. Thus, we consider the medium mesh appropriate to conduct the parametric study.

Table 6.2: Mesh sensitivity analysis for the turbine domain, where n_c is the number of elements and k_i the refinement factor, E_R the relative error between two meshes, and GCI the grid convergence index.

		Thrust			Power		
# of elements n_c	Refinement factor k_i	C_T [-]	E_R [%]	GCI_i [%]	C_P [-]	E_R [%]	GCI_i [%]
0.70M	1.00	1.024	-	-	0.297	-	-
5.41M	2.00	1.064	3.72	1.54	0.345	13.95	0.99
43.28M	4.00	1.059	-0.50	0.54	0.344	-0.32	0.35
∞	∞	1.062	0.00	0.00	0.344	0.00	0.00

6.5.3 Flow field post-processing

The results of the CFD simulations are presented in terms of the spanwise distributions of forces in the axial, tangential and radial directions, F_x, F_θ and F_r, respectively, and with the flow-field analysis performed using the Streamtube Analysis Method (SAM) developed by Hunter [13] and reviewed by Zilic de Arcos et al. [40]. SAM works by sampling the flow-field over a series of concentric streamtubes centred around the rotor axis, with each crossing the rotor at a different radial location, to develop the spanwise variation in flow-field parameters, such as axial or tangential flow speed at the rotor. Each streamtube may expand or contract in the stream direction, as required by mass conservation, and the flow at each streamwise position is azimuthally averaged for analysis.

The spanwise force distributions $\vec{F} = [F_x, F_\theta, F_r]$ are obtained by integrating the pressures and shear forces over C, the blade cross-section at radius r, according to the following equation, in which p is the pressure, $\vec{n}$ is the unitary surface-normal vector, and $\vec{S}$ the wall shear stress vector.

$$\vec{F}(r) = \oint (p\vec{n} + \vec{S}) dC \tag{6.4}$$

The SAM method is used to extract the angles of attack $\alpha(r)$ from the simulations through reconstructed azimuthally-averaged streamtubes where:

$$\alpha = \phi - \beta \tag{6.5}$$

and $\phi(r)$ is the angle of the local flow relative to the rotor plane, and $\beta(r)$ is the blade's geometric twist at radius r, as shown in fig. 6.4. Here, $\phi(r)$ is

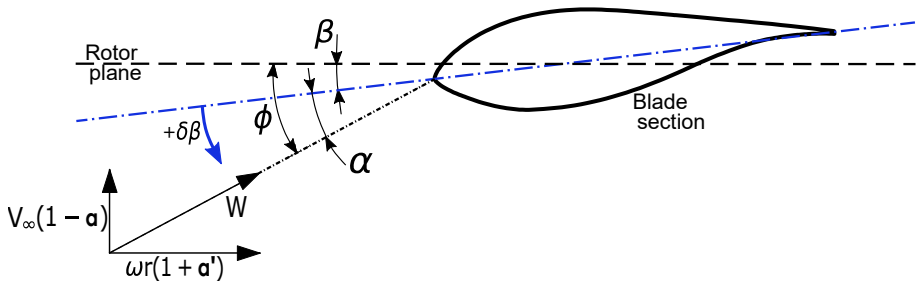

Figure 6.4: Flow diagram over an arbitrary blade section, indicating the positive direction for twist deformations $\delta\beta$ (blue arrow).

calculated including the influence of the blade on the flow, and sampled directly from the CFD results:

$$\phi = \tan^{-1}\left(\frac{V_x}{V_\theta}\right) \tag{6.6}$$

with V_x and V_θ the axial and tangential velocities, respectively.

The flow velocities are extracted from the azimuthally-averaged streamtubes at a non-dimensional distance upstream and downstream of the rotor plane, $\Delta x/c$, from where Δx is measured in the local axial coordinate direction and c is the local chord. Unless otherwise stated in the corresponding results, a value of $\Delta x/c = 1.0$ was used, as this has previously been found to achieve parameter-independent results, as reported in Zilic de Arcos et al. [40].

The blade's local lift and drag coefficients, C_L and C_D, are calculated by projecting the axial and tangential forces F_x and F_θ in a frame of reference aligned with the flow incident on the blade W. The incident flow speed is itself determined through:

$$W(r) = \sqrt{V_x^2 + V_\theta^2} \tag{6.7}$$

6.6 Results and discussion

6.6.1 Twist deformation analysis

Fig. 6.5 shows the variations in thrust and tangential force caused by the twist deformation for the different $\delta\beta$ deformation cases, with the turbine operating at

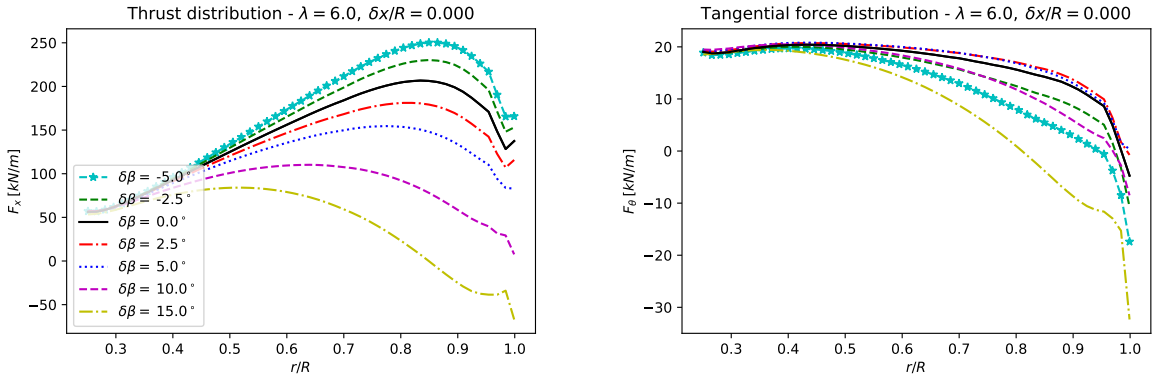

Figure 6.5: Spanwise thrust (left) and tangential force (right) distributions for the rotor blade with twist only deformation at a tip-speed ratio $\lambda = 6.0$.

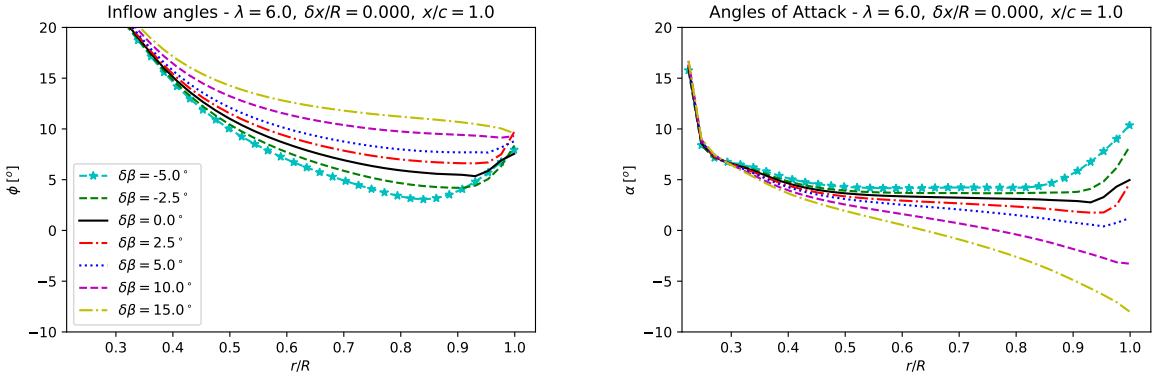

Figure 6.6: Spanwise distributions of the flow angle ϕ (left) and angle of attack α (right) for the rotor blade with twist only deformation at a tip-speed ratio $\lambda = 6.0$.

a tip-speed ratio $\lambda = 6.0$, while fig. 6.6 shows the changes in the flow angles ϕ and angles of attack α for those same cases.

From the results, we observe that increases in $\delta\beta$, i.e., deformation towards feather, reduce the angle of attack, with an attendant reduction in thrust force, while a negative $\delta\beta$, i.e., deforming towards stall, produces the opposite effect. The thrust changes due to $\delta\beta$ can be explained following the projection of the local thrust and tangential force coefficients (C_X and C_θ respectively), in terms of the sectional lift and drag coefficients (C_L and C_D):

$$C_X = C_L(\alpha)\cos\phi + C_D(\alpha)\sin\phi \tag{6.8}$$

$$C_\theta = C_L(\alpha)\sin\phi - C_D(\alpha)\cos\phi \tag{6.9}$$

For small ϕ, as occurs across the mid and outboard sections of the blade, $\cos\phi \approx 1$ and $\sin\phi \approx \phi$. In addition, $C_L \gg C_D$ at small angles of attack for a typical aerofoil and equation 6.8 is thus dominated by the first term. It follows for the attached-flow regime that the thrust coefficient can be approximated as $C_X \approx C_L(\alpha)$ for the mid and outboard sections of the blade span, which accounts for the changes in thrust displayed in fig. 6.5.

The changes in tangential force are more complex, since eq. 6.9 is not necessarily dominated by either of the lift or drag terms. We observe in fig. 6.5 that the tangential force drops in most cases, which is attributed to the local aerofoil operating away from its design conditions. However, a slight increase in the tangential force component, associated with the rotor operating at a blockage lower than its design condition, is observed along the entire blade span for twist angle cases of 2.5° and 5.0°. This increase in tangential force is due to the non-linearity of eq. 6.9 and to the change in $\delta\beta$ not being transformed in an equivalent change to the angle of attack seen in fig. 6.6. Instead, both α and the inflow angle ϕ are affected. Specifically for the $\delta\beta = 2.5°$ and $\delta\beta = 5.0°$ cases, a smaller angle of attack leads to a reduction in C_L and C_D, but also to an increase in ϕ. The consequence is that, for the $\delta\beta = 2.5°$ and $\delta\beta = 5.0°$ cases, the changes in the trigonometric functions in eq. 6.9 offset the changes in the lift and drag coefficients, leading to higher torque but smaller thrust forces.

In fig. 6.7 we analyse the changes in aerofoil characteristics extracted from the rotor simulations. Each simulated tip-speed ratio is analysed at a set of radial locations, and at each radial location the actual angle-of-attack, relative inflow speed, and resultant sectional lift and drag coefficients are determined. By looping over the tip-speed ratios simulated we are then able to reconstruct lift and drag coefficient curves as a function of angle-of-attack for each radial location.

In contrast to the flapwise deformation cases to be discussed in the following section (Sec. 6.6.2), we observe relatively small changes in the aerofoil's lift and drag coefficients arising from blade twist deformations, especially in comparison to the larger differences observed at different radial positions, as shown in fig. 6.7.

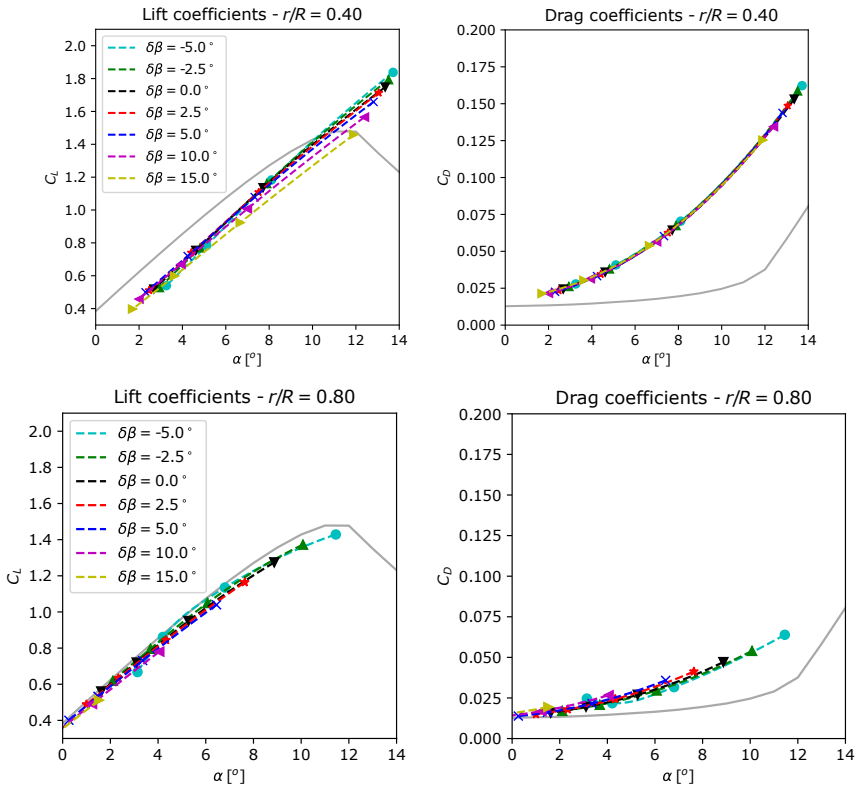

Figure 6.7: Sectional lift and drag coefficients at two radial locations for different twist deformation cases. Sectional data are extracted from blade resolved simulations, in which each simulated tip-speed ratio λ provides data for a single angle of attack α at each spanwise location. The grey line corresponds to the two-dimensional lift and drag coefficients.

We observe that most deformation cases converge with each other over a narrow spread for both lift and drag, although a maximum spread of approximately 9% in lift for the largest deformation cases ($\delta\beta = 10.0°$ and $\delta\beta = 15.0°$), highest angle of attack and closer to the root is observed. We attribute the larger spread to three-dimensional flow effects close to the transitional sections around the root ($0.15 \leq r/R \leq 0.25$), pre-stall effects, and to the analysis methodology itself, and not necessarily to strong variations caused by deformation.

Changing the radial coordinate affects the polar coefficients more significantly than twist deformation. For the cases analysed in fig. 6.7, the drag coefficient shows relative differences of approximately 100% at the highest angle of attack, although with a similar change in lift in absolute terms. On the lift coefficients, a stall delay is also observed closer to the root at the highest angles of attack. The changes in

the two-dimensional polars over the blade span, while significant, are a phenomenon that has been widely discussed in literature (see e.g., Wimshurst and Willden [36]) and will not be further discussed as it falls outside the scope of this work.

Finally, we conclude from these observation that the changes in force distributions caused by twist deformations can be explained through variations in the local velocity triangle (i.e., changes in induction factors, inflow angles and angles of attack) as well as angle of attack related changes to the blade two-dimensional lift and drag coefficients, $C_L(\alpha)$ and $C_D(\alpha)$.

6.6.2 Flapwise deformation analysis

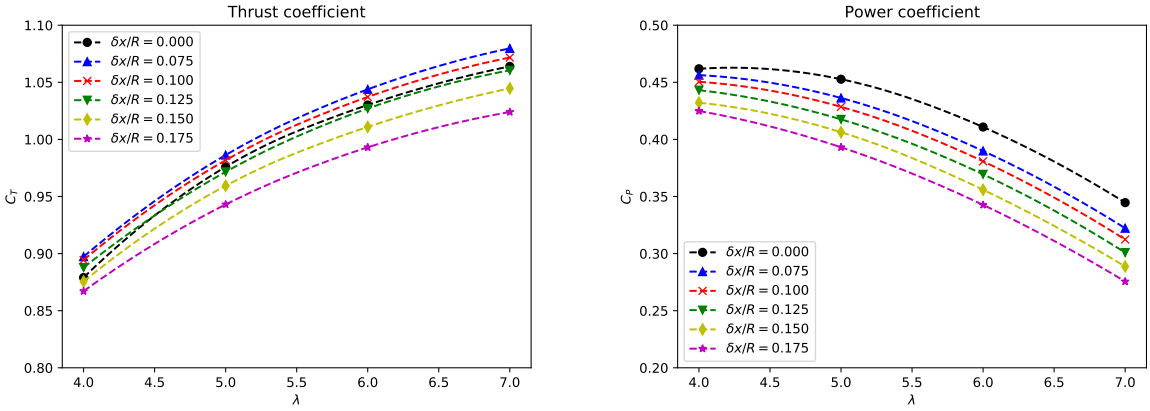

Figure 6.8: Integrated thrust (left) and power (right) coefficients for different flapwise deformations. The coefficients are normalised by the undeformed rotor swept area.

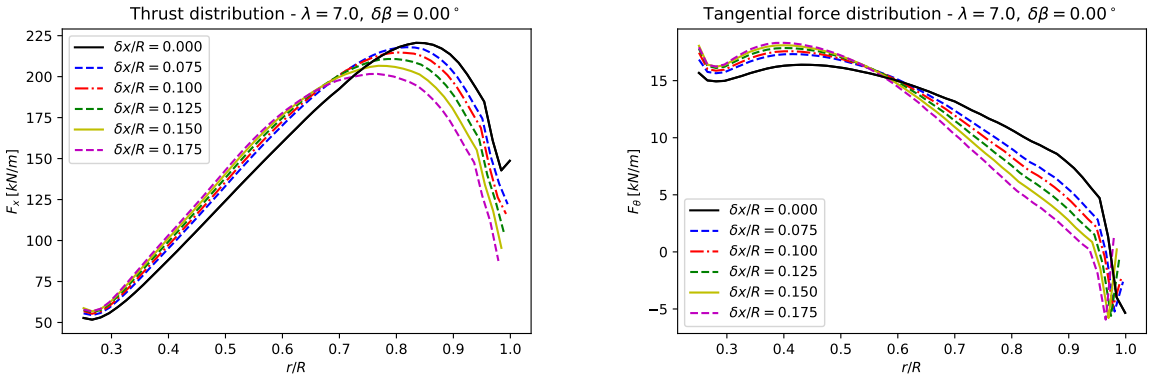

Figure 6.9: Spanwise thrust (left) and tangential force (right) distributions for the rotor blade under flapwise deformation only at a tip-speed ratio $\lambda = 7.0$.

The flapwise deformation hydrodynamic effects are more complex to analyse than the effects of twist deformation as the annular independence assumed in blade-element momentum theory is violated by the development of spanwise flows along the blade, and hence the changes in forces cannot be simply explained by changes in angles of attack.

Fig. 6.8 shows the thrust and power coefficients for the whole rotor, normalised by the momentum and kinetic energy flux through the undeformed rotor swept area respectively. The coefficients show the impact of flapwise deformation on power and thrust. Increasing flapwise deformations produce an increasing reduction in C_P, with a maximum power loss of approximately 20% for the largest deformation case. On the contrary, flapwise deformations show a smaller impact on thrust coefficient, with an increase in C_T for modest flapwise deformations (ca. +2%), and a reduction in C_T for larger deformations (maximum of approximately -4% for the largest deformation).

From the force distributions in fig. 6.9, presented for the different flapwise-deformation cases, we observe how the deformed cases exhibit increased loading in the inboard region of the blade where the flapwise deformations are small, and increased load shedding near the tip, which resembles a tip-loss effect but with increased magnitude and radial variation. These changes in spanwise force distribution are associated with two different effects acting on the blade which are discussed in the following sections: a decrease in static pressure on the suction side of the blade that results from radial flow expansion (sec. 6.6.2.1), and an increased radial loss that moves the onset of tip-loss effects inboard towards the blade root (sec. 6.6.2.2). Although these changes result from three-dimensional flow effects, it is also instructive to interpret the flow-field changes in terms of changes to two-dimensional sectional blade characteristics which we present in sec. 6.6.2.3.

6.6.2.1 Inboard load augmentation

An undeformed blade projects a very small radial-area as viewed along the radial axis from the blade tip. As the flapwise deformation increases so too does this

radial-area projection, and due to the pressures acting on the blade surfaces, the blade starts to act as a significant source of radial momentum to the flow.

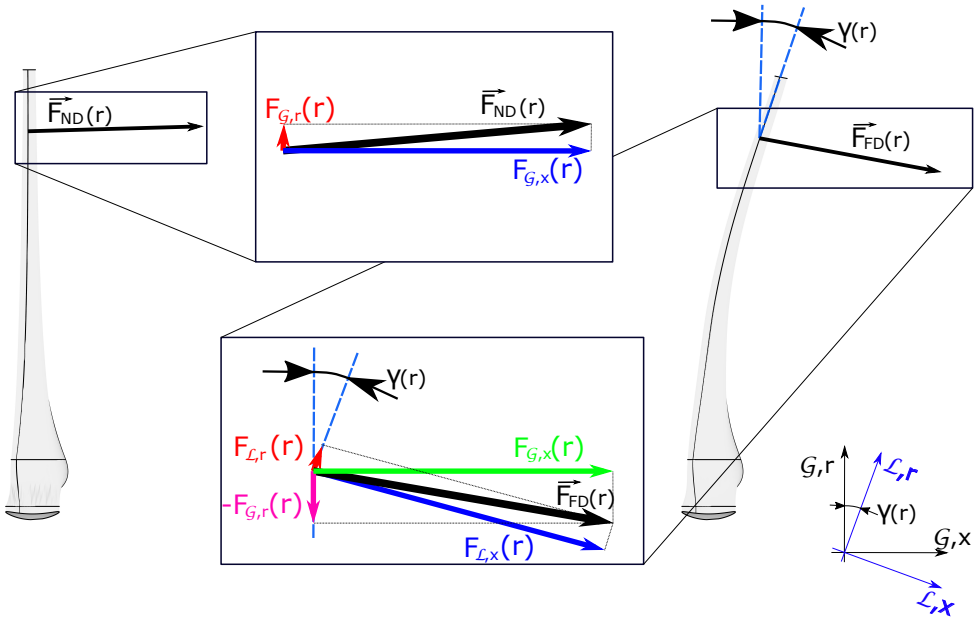

Figure 6.10: Diagram comparing the axial and radial forces acting on a blade with no deformation (left, subscript ND) and on a deformed blade (right, subscript FD). The forces on the undeformed case ($\vec{F_{ND}} = [F_{\mathcal{G},x}, F_{\mathcal{G},r}]$, where x and r stand for axial and radial components, respectively, and G for the global frame of reference) are equal in both the local and global frames of reference. On the deformed blade, the resulting force vector $\vec{F_{FD}}$ is decomposed in both the global and local frame of reference (components with the $\mathcal{G}$ and $\mathcal{L}$ sub-indices, respectively), with γ the deflection angle. Diagram not to scale.

For the undeformed case, we observe a small radial fluid force that acts on the blade in the same (outwards) direction as the centrifugal forces, i.e. $F_{\mathcal{G},r} > 0$, see fig. 6.10 for definitions. As the tip deformation δx increases the local radial force, $F_{\mathcal{L},r}$, as well as the local thrust force, $F_{\mathcal{L},x}$, are rotated by an angle, $\gamma(r)$, corresponding to the tangent of the deformed quarter-chord line, as shown in fig. 6.10. This leads to a significant force component in the global radial direction, $F_{\mathcal{G},r}$, that acts on the blades towards the nacelle, as shown in fig. 6.11.

If changes to the flow streamlines are negligible as the blade bends, the radial and thrust forces on the flapwise-deformation case can be estimated by projecting the undeformed case axial and radial forces onto the rotated quarter-chord line

of the flapwise-deformed case, as described before:

$$F_{\mathcal{G},x} \approx F_{\mathcal{L},r} \cdot \sin\gamma + F_{\mathcal{L},x} \cdot \cos\gamma \tag{6.10}$$

$$F_{\mathcal{G},r} \approx F_{\mathcal{L},r} \cdot \cos\gamma - F_{\mathcal{L},x} \cdot \sin\gamma \tag{6.11}$$

with $F_{\mathcal{G},x}$ and $F_{\mathcal{G},r}$ the estimated thrust and radial forces referenced to the global frame of reference for a flapwise-deformed case, $F_{\mathcal{L},x}$ and $F_{\mathcal{L},r}$ the thrust and radial forces from the undeformed case projected onto the local frame of reference (note that the local and global frames of reference are the same for the undeformed blade).

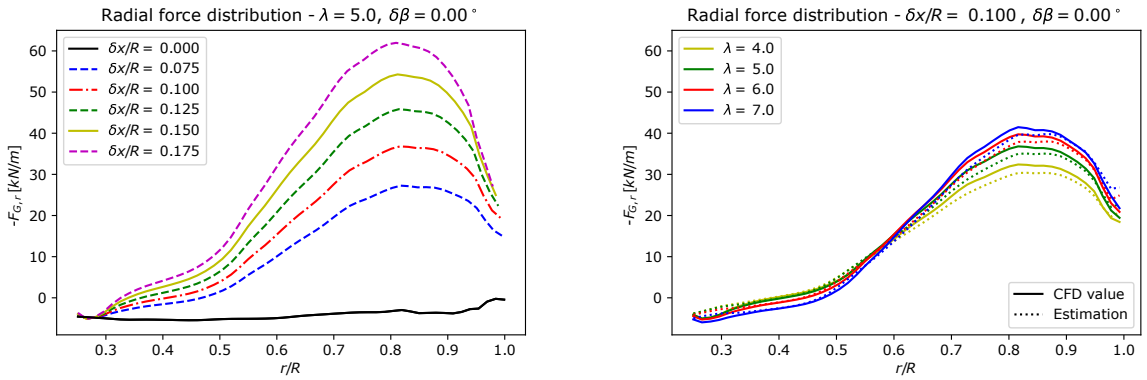

Figure 6.11: Spanwise radial force distribution for various tip deflections $\delta x/R$ (left) and comparison between the spanwise force distribution extracted from the deformed blade CFD results and an approximation based on the vectorial projection of the undeformed force vector onto the local frame of reference of a deformed blade, for different tip-speed ratios (right). Both plots correspond to cases under flapwise deformation only.

The radial forces predicted for the flapwise deformed blade using eq. 6.11, which re-orientates the forces of the undeformed blade according to its shape, are compared with the radial forces from the deformed blade CFD simulations in fig. 6.11. These plots show good agreement across large parts of the blade between the approximation, which neglects any feedback effects on the flow, and the deformed blade CFD extracted results, reaching a maximum integrated-load error of approximately 3% primarily due to discrepancies observed between $r/R = 0.6$ and $r/R = 0.9$. This demonstrates that the primary mechanism for generation of the radial component of the force acting on the blade is due to the reorientation of the thrust loading acting on the blade rather than from any changed radial flow physics.

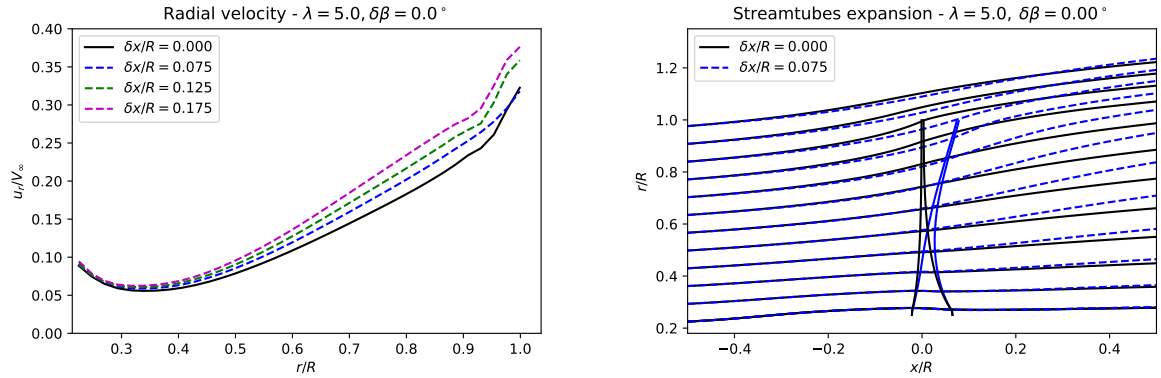

Figure 6.12: Spanwise distribution of radial velocity u_r/V_∞ for different values of flapwise deformation (left) and comparison of annular streamtubes passing the blade for two flapwise deformation cases (right). Data in both plots correspond to a tip-speed ratio $\lambda = 5.0$.

The radial force experienced by the blade impacts the flow as it passes through the rotor. As the radial force on the blade is generally inboard, $F_{\mathcal{G},r} < 0$, the reaction experienced by the flow is in the outboard direction and results in an increase in radial momentum flux. Thus the flow expands radially as it passes through the rotor and an increase in radial velocity is observed at the rotor plane as the blade deformation increases, as shown in fig. 6.12. The increased radial momentum results in increased wake expansion which we visualize in fig. 6.12 through the streamtube expansion past the rotor for two cases, with an expanded wake being observed for all λ considered.

The force changes observed in the axial and tangential directions, cannot however be fully explained by the vectorial reorientation and decomposition applied to estimate the radial force. Following eq. 6.10, significant axial loading changes would not be expected in the inboard regions of the blade for small flapwise deformations.

The load augmentation in the inboard regions is a consequence of wake expansion. Observing fig. 6.12, which shows streamtubes for the $\delta x/R = 0.075$ and undeformed cases, the close comparability of the streamtube widths in the inboard region of the undeformed and deformed blades, both upstream of and through the rotor, along with equivalent conditions upstream, imply a similar mass flux through the inboard streamtubes of both rotors.

Downstream of the rotor the inboard streamtubes expand at different rates, resulting in greater wake expansion and a smaller wake velocity for the deformed blade. The static pressure on the downstream side of a rotor with flapwise deformation, then, is reduced as the streamtubes are forced to expand radially by the bent blades, affecting thrust and tangential force distribution.

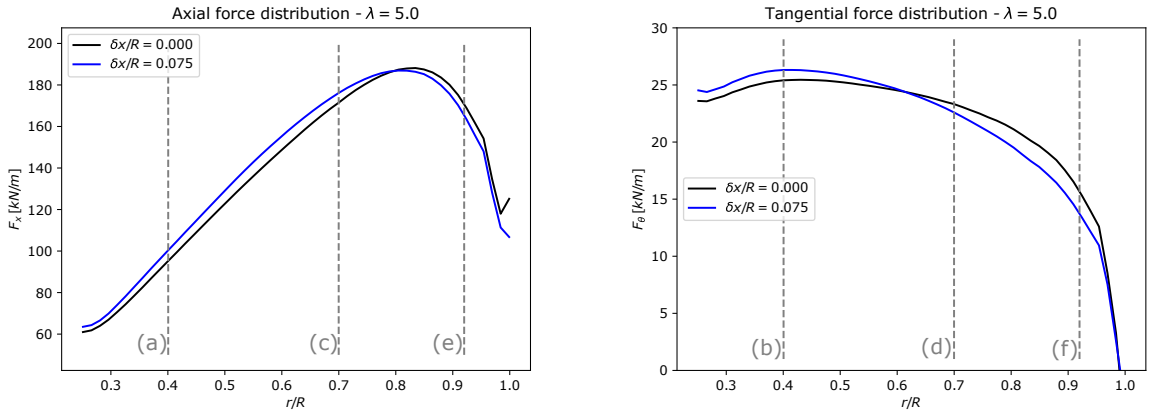

Figure 6.13: Spanwise thrust (left) and tangential force (right) distribution comparison for the rotor with two different flapwise deformations ($\delta x/r = 0.000$ and $\delta x/r = 0.075$) at $\lambda = 5.0$. The vertical lines indicate the analysed radial locations and the letters are references to the corresponding sub-figures in fig. 6.14.

The pressure drop effects can be observed in the CFD results. In fig. 6.13 we present a comparison of the thrust and tangential force distributions for two typical cases, with and without flapwise-deformation at $\lambda = 5.0$. In each of these plots we include three vertical lines marking different locations on the blade span: the first lines (a and b) in a region where both thrust and tangential force increase with deformation, the second pair (c and d) show an area of the blade where thrust increases whilst the tangential force decreases, and the third pair (e and f) show the region where both thrust and tangential forces decrease. Whilst these plots show the case for $\lambda = 5.0$ the same observations can be made for different tip deformation $\delta x/R$ cases at all the analysed tip-speed ratios.

At the first analysed location, $r/R = 0.40$, we observe an increase in both thrust and tangential force. Figs. 6.14 (a) and (b) show the cumulative chordwise distribution of the thrust and tangential force on this section. These plots show

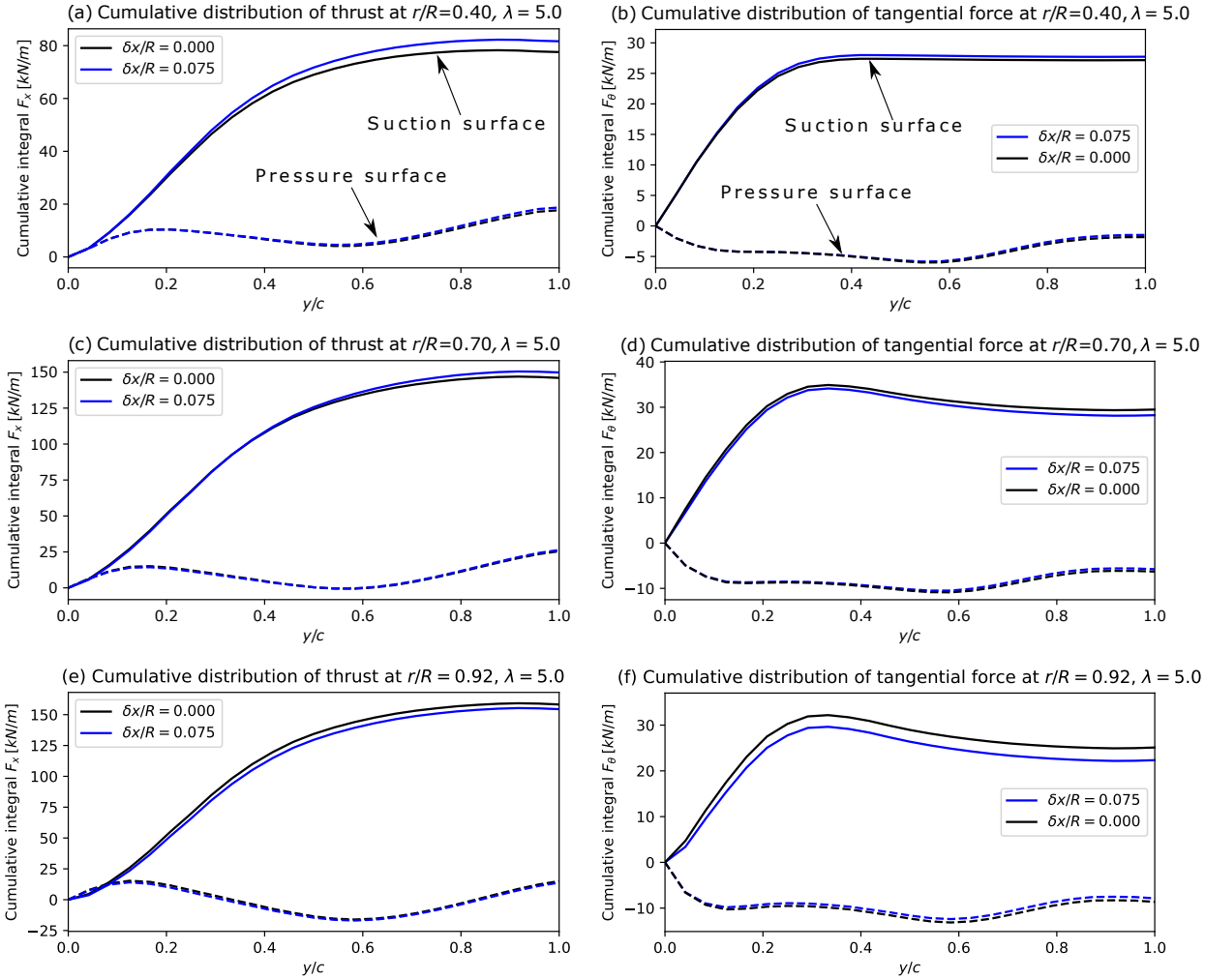

Figure 6.14: Cumulative force distributions at $r/R = 0.40$, $r/R = 0.70$ and $r/R = 0.92$ for the undeformed and deformed $\delta x/R = 0.075$ cases at $\lambda = 5.0$. The continuous lines correspond to the suction surface and the dashed lines to the pressure surface of the blade, and y/c is the local chordwise coordinate.

how the flapwise deformation pressure variations are localised on the suction (downstream) side of the blade. The plots also show how the thrust differences between deformed and undeformed blades are generated over most of the blade chord (increasing monotonically until approximately 80% of the chord), whereas the tangential force differences are generated over a smaller portion of the hydrofoil, between approximately 25% and 35% of chord, as a consequence of the suction increase but also due to the local foil geometry.

At $r/R = 0.70$, an increase in thrust and reduction in tangential force due to flapwise deformation is observed. Figs. 6.14 (c) and (d) show that the differences

are still concentrated on the suction side of the blade, and that these variations occur over a smaller portion of the chord for the thrust and concentrated towards the trailing edge. The tangential force shows a slight reduction for the deformed case that starts close to the leading edge.

Near the tip at $r/R = 0.92$, where three-dimensional flow effects and tip-loss phenomena are significant, figs. 6.14 (e) and (f) show that both thrust and tangential force are reduced with flapwise deformation.

The cumulative force plots (figs. 6.14) are consistent with the static pressure reduction described for cases with flapwise deformation. The force changes are concentrated on the suction side of the blade, and are most evident around the inboard section of the blade, as observed for the $r/R = 0.40$ and $r/R = 0.70$ sections. As sections get closer to the tip, however, there is an increasing preponderance of the near-tip load shedding effect augmented by increased radial flow, as seen for the $r/R = 0.92$ section. This phenomenon is discussed in sec. 6.6.2.2.

The pressure change around the suction side of the blade affects thrust and tangential force distributions differently. On the suction side of the blade any change in pressure, such as that created by flapwise deformation, will lead to a change in thrust. This is a result of geometry as most of the suction surface area is projected in the streamwise direction. However, the area projection of the suction surface in the tangential direction changes significantly with aerofoil shape and local twist angle. Consequently, depending on the chordwise distribution of the suction increase around the foil section and the local distribution of the tangentially projected area, the change in tangential force that occurs with blade deformation can be quite varied at different spanwise locations.

Fig. 6.15 (left) displays the change in the pressure coefficients on the suction side for the rigid and flapwise deformed blades at the analysed radial locations, with the pressure coefficients normalised by the local dynamic pressure $1/2\rho W^2$. A negative ΔC_{Pres} indicates an increase in suction for the deformed case relative to the undeformed case. Fig. 6.15 (right) shows the tangential-component of the blade's suction-side normal vector, $\hat{n}_j$; positive $\hat{n}_j$ is in the direction of positive

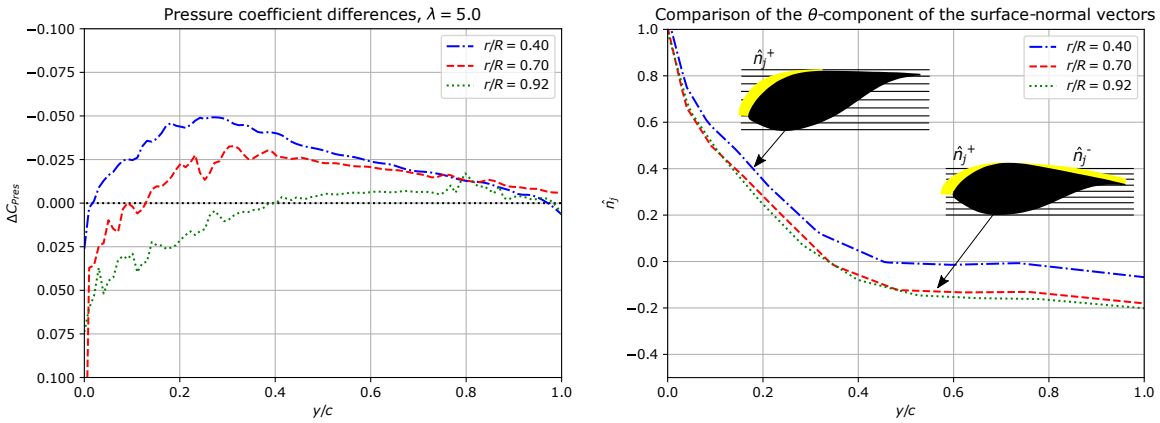

Figure 6.15: Difference between the suction surface pressure coefficients of the $\delta x/R = 0.000$ and $\delta x/R = 0.075$ cases at different radial locations (left) and tangential-component of the blade's suction-side normal vector ($\hat{n_j}$) at the same radial locations (right). The right plot includes diagrams that highlight the magnitude of the tangential component of the surface-normal vector $\hat{n_j}$ over the foil sections at the two pointed radial locations, with the horizontal lines marking the tangential direction and the yellow zones showing the magnitude of $\hat{n_j}$.

torque generation, whilst negative $\hat{n}_j$ is in the torque resisting direction. These plots show how the changes to the tangential force result from the interaction between the pressure differences induced by the flapwise deformation, and the suction surface-normal vectors, which are a function of the hydrofoil shape and the blade twist (neither of which are affected by $\delta x/R$).

Fig. 6.15 shows that $\hat{n}_j$ is mostly positive near the root, and hence the observed increase in suction results in an increase in the local tangential force. However, as we move towards the outboard section of the blade, $r/R = 0.70$, the change in twist distribution results in $\hat{n}_j$ being positive towards the leading edge and negative towards the trailing edge of the hydrofoil. At this location a small but consistent increase in suction is observed across most of the blade chord. Hence there is a tangential force balance with increased torque contribution towards the leading edge and reduced torque contribution towards the trailing edge, with the overall balance being a very small decrease in local torque contribution once forces are integrated around the blade chord.

6.6.2.2 Radial loss augmentation

Returning to the force distributions in fig. 6.9 we observe that, with increasing $\delta x/R$, the magnitude of the outboard load shedding is increased, and its onset is displaced inboard, affecting both thrust and tangential force distributions. The observed effects are similar to those normally associated with tip losses.

The changes in force and pressure near the tip are related to three-dimensional flow variations. This complex flow phenomena can be analysed by examining the governing Navier-Stokes equations, focusing on the axial pressure gradient. We note that the underlying simulations assume steady state flow, and thus we neglect temporal derivatives in the momentum equations. Eq. 6.12 presents the axial-flow component of the Navier-Stokes equation in cylindrical coordinates, where u is a velocity component; p the static pressure; the indices x, θ and r the axial, tangential and radial coordinates respectively; and μ the fluid viscosity:

$$\rho\left(u_r\frac{\partial u_x}{\partial r}+\frac{u_\theta}{r}\frac{\partial u_x}{\partial \theta}+u_x\frac{\partial u_x}{\partial x}\right)=-\frac{\partial p}{\partial x}+\mu\left[\frac{1}{r}\frac{\partial}{\partial r}\left(r\frac{\partial u_x}{\partial r}\right)+\frac{1}{r^2}\frac{\partial^2 u_x}{\partial \theta^2}+\frac{\partial^2 u_x}{\partial x^2}\right] \tag{6.12}$$

We assume the viscous effects to be negligible outside the blade boundary layer where the following analysis will be applied, and thus we neglect the viscous term in eq. 6.12. We seek an azimuthally-averaged analysis in the context of the Streamtube Analysis Method, and hence u_x, u_r and u_θ become the azimuthal-average of the velocity components. Thus, the circumferential gradients of azimuthally-averaged quantities are assumed zero, i.e., $\partial u_x/\partial\theta = 0$. These assumptions result in:

$$\frac{\partial p}{\partial x}\approx-\rho\left(u_r\frac{\partial u_x}{\partial r}+u_x\frac{\partial u_x}{\partial x}\right) \tag{6.13}$$

for which the velocities and their gradients can be readily extracted from the simulations. The pressure gradient $\partial p/\partial x$ can then be integrated in the axial direction to obtain an approximation of the pressure p^* (relative to a constant p_0) as a function of the axial-coordinate x for each radial coordinate:

$$p^* = \int \frac{\partial p}{\partial x} dx + p_0 = -\rho \int \left(u_r \frac{\partial u_x}{\partial r} + u_x \frac{\partial u_x}{\partial x} \right) dx + p_0 \tag{6.14}$$

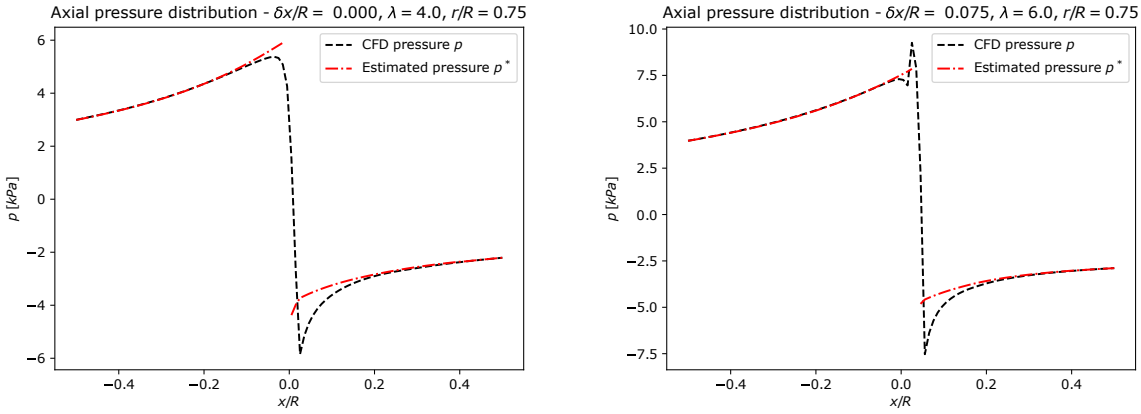

Figure 6.16: Comparison of the pressure extracted from CFD simulation, p, and the approximation p^* for two illustrative cases; left, rigid blade at a tip-speed ratio $\lambda = 4.0$; right, deformed blade ($\delta x/R = 0.075$) at $\lambda = 6.0$, at $r/R = 0.75$.

The integral of eq. 6.14 can be evaluated in two branches, upstream and downstream of the rotor, to avoid the large gradients that occur near to the rotor plane, and where the neglected terms in eq. 6.13 are likely to be significant. Fig. 6.16 shows a comparison of the pressure p extracted from CFD simulations and the estimated pressure p^* for two different flapwise deformation cases, showing good agreement at distances greater than $\pm 0.1R$ away from the blade.

By evaluating the pressure, p^*, at both sides of the turbine at different radial locations, the thrust distribution per unit span can be estimated, as in classical momentum theory, from the difference in static pressure between the upstream and downstream sides of the rotor plane, p^{*+} and p^{*-}:

$$F_x(r) \approx F_x^*(r) = (p^{*+} - p^{*-}) 2\pi r \tag{6.15}$$

Eq. 6.15 can be decomposed into the contributions from the change in axial momentum:

$$\chi = -2\pi r \rho \left(\int_{-h}^{0^+} u_x \frac{\partial u_x}{\partial x} dx - \int_{+h}^{0^-} u_x \frac{\partial u_x}{\partial x} dx \right), \tag{6.16}$$

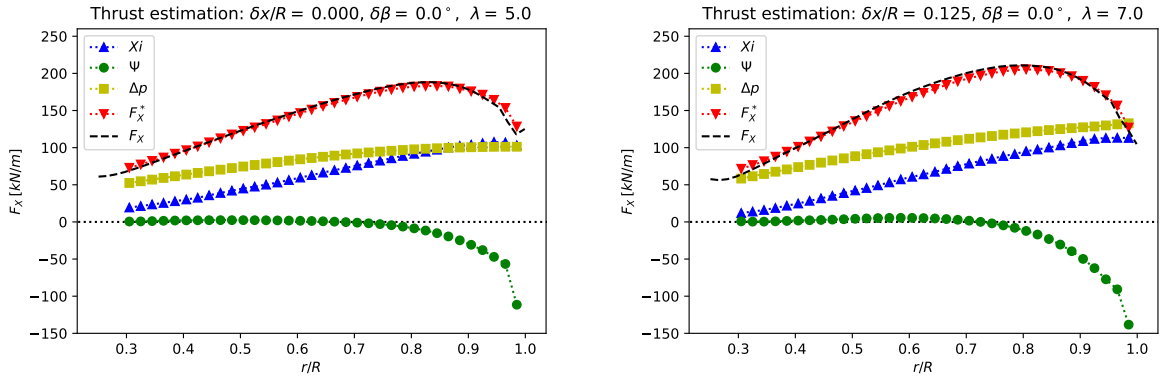

Figure 6.17: Verification of the thrust estimation on a rotor blade based on eqs. 6.16-6.18 comparing it to the force calculated by integrating pressure and shear stresses on the blade surface for undeformed $\delta x/R = 0.000$ and deformed $\delta x/R = 0.125$ cases at $\lambda = 5.0$ and $\lambda = 7.0$, respectively. The plots display the thrust approximation F_x^* as well as the constituents χ, the change in axial momentum, ψ, the radial loss, and Δp, the difference in static pressure from upstream to downstream of the rotor at a distance $h = R/2$ from the rotor.

the radial loss which we define as:

$$\psi = -2\pi r\rho\left(\int_{-h}^{0^+} u_r \frac{\partial u_x}{\partial r} dx - \int_{+h}^{0^-} u_r \frac{\partial u_x}{\partial r} dx\right), \tag{6.17}$$

and a contribution from the difference in static pressure Δp from a distance h upstream and downstream of the rotor plane. Hence we determine an estimate to the spanwise variation in axial thrust through:

$$F_x^* = \chi + \psi + 2\pi r \Delta p \tag{6.18}$$

Fig. 6.17 shows a comparison between the thrust estimation F_x^* and the thrust calculated by integrating pressure and shear stress over the blade surfaces F_x for example undeformed and deformed cases. Alongside the force estimations, the contributions from χ, ψ and Δp are provided. These figures show how F_x^* provides a good description of the thrust force on the blade for cases with and without flapwise deformation. The approximation enables the quantification and further inspection of the main terms driving the forces on the blade.

The difference between the static pressures up- and downstream, Δp, is plotted in fig. 6.17. Over the axial distance used to integrate the axial pressure estimation ($x/R = \pm h/R = \pm 0.5$), a static pressure difference was observed which was

evaluated directly from the CFD simulations. If the gradient was integrated at sufficient distance from the rotor in unblocked conditions, the static pressure is expected to be the same far upstream and far downstream of the rotor, and so $\Delta p \rightarrow 0$ as $h \rightarrow \infty$.

Fig. 6.17 also shows that the terms χ and ψ act in different directions. χ represents changes in axial momentum, and contributes to thrust generation, whilst ψ represents the loss or leakage of axial momentum due to three-dimensional radial flow effects, and captures the causes ofnear-tip load-shedding effects.

The radial loss ψ has a similar shape to the models used to correct for tip losses in BEMT (e.g. Glauert [10], Wimshurst and Willden [33]). In particular, in the absence of flapwise deformation, the radial loss has a negligible effect on the inboard region and decreases in an exponential-like manner close to the tip, similar to conventional tip-loss models. However, ψ encapsulates both the tip losses as well as the load reduction effects associated with radial flow.

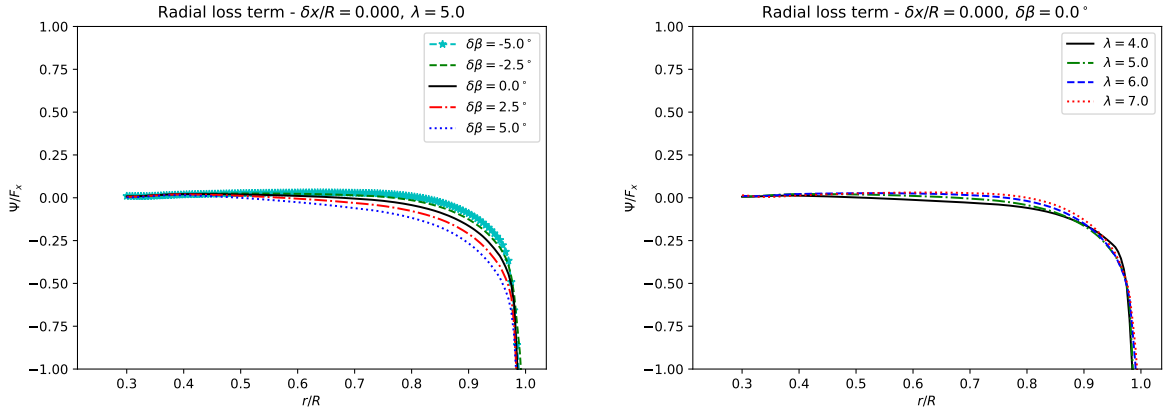

Figure 6.18: Changes in the non-dimensional radial loss term for different twist deformations $\delta\beta$ cases at $\lambda = 5.0$ (left) and the undeformed rotor at different tip-speed ratios (right).

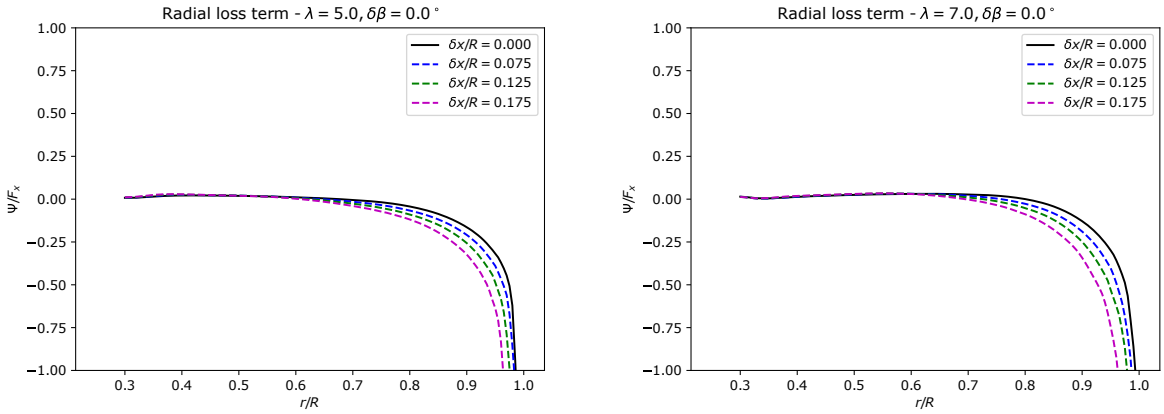

Figure 6.19: Changes in the non-dimensional radial loss term for different flapwise deformation $\delta x/R$ cases at $\lambda = 5.0$ (left) and $\lambda = 7.0$ (right).

In figs. 6.18 and 6.19 we examine the variation of the radial loss term, presented as a fraction of the local thrust force. We note that ψ/F_x may go below -1 near the blade tip to balance the radially increasing contributions of χ/F_x and Δp, which collectively result in a reduction in magnitude of F_x but maintain an overall positive value. We examine the form of the radial loses for different cases of blade twist deformation $\delta\beta$ and flapwise deformation $\delta x/R$, and with tip-speed ratio λ for an undeformed blade.

The plots show that negative blade twist deformation reduces the radial loss whilst positive blade twist increases the loss. A small dependency on λ for the undeformed blade is also observed. For the cases with no flapwise deformation, despite changes in radial loss magnitude across the inboard of the blade, the radial losses collapse near the tip at approximately $r/R = 0.98$ for all the λ and $\delta\beta$ cases.

Fig. 6.19 shows that the radial loss term increases with flapwise deformation, with the onset of the radial loss moving inboard along the blade as tip deformation increases. This confirms that the reductions in near-tip loads in cases with flapwise deformation are a consequence of the spanwise flow effects induced by this deformation component.

Larger radial losses with flapwise deformation result in the reduction in pressure difference between suction and pressure surfaces of the blade near the tip, as observed in the cumulative force distributions (fig. 6.14). Here we note that any

increase in suction surface pressure caused by downstream wake expansion is offset, near the tip, by the increase in radial loss as the tip is approached, and hence the overall thrust and tangential forces decrease in the near tip region.

6.6.2.3 Influence of the flapwise deformation on two-dimensional polar coefficients

The inboard load augmentation and the increased radial losses affect how the hydrodynamic forces develop on the blade. Although these are three-dimensional flow phenomena it is instructive to interpret the flow-field changes in terms of changes to two-dimensional sectional blade characteristics, as these are most normally used in the design and analysis of rotors. Fig. 6.20 shows the blade sectional lift and drag coefficients, as well as the foil efficiency C_L/C_D, computed from analysis of the different simulated flapwise deformation cases at four radial stations and presented as functions of the local angle of attack α, which is itself not know a priori and is an output of the flow-field analysis.

As the blade deforms we observe that the sectional lift coefficients increase for inboard sections of the blade and reduce towards the tip, across all the analysed angles of attack. This is a consequence of the inboard load augmentation and the radial loss. The shape and slope of the C_L curves as functions of α remain similar between the $\delta x/R$ cases at equivalent radial locations. However, the vertical offsets of these curves change as functions of radial position, r/R, and deformation, $\delta x/R$.

A monotonic increase of C_L with increasing flapwise deformation is observed on inboard blade sections until around $r/R = 0.70$, where the trend starts to change. There, we observe an increase in C_L up to $\delta x = 0.075$, remaining at the same level for higher values of $\delta x/R$. Finally, near the tip, we observe that the lift coefficient is reduced with increasing flapwise deformation. The differences between the undeformed and deformed cases, for $C_L(\alpha)$, generally show a stronger dependency on r/R and $\delta x/R$ than on α itself.

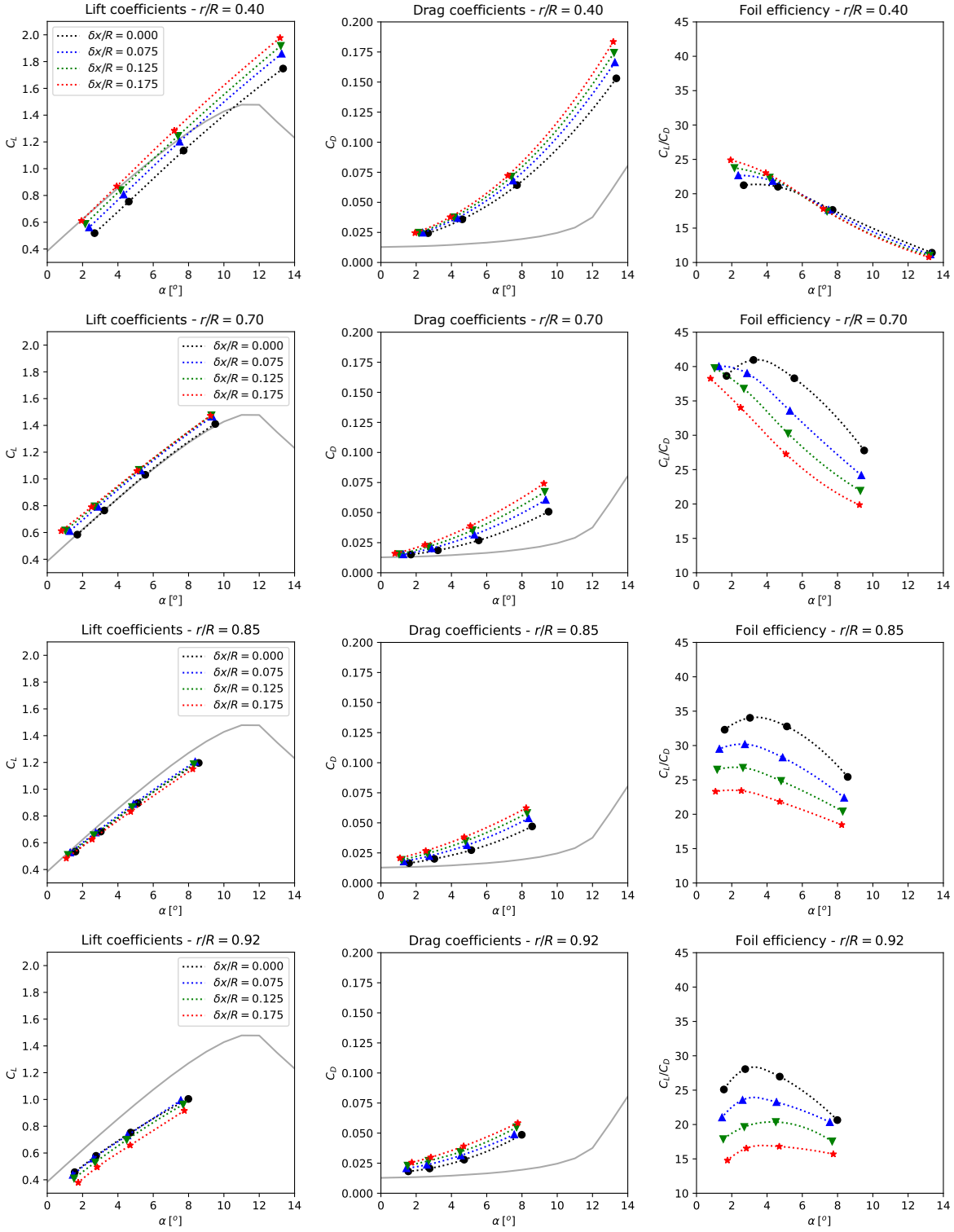

Figure 6.20: Lift, drag and aerofoil efficiency (lift-to-drag ratio) at different radial locations for various flapwise-deformation cases. Values calculated using the SAM with $x/c = 1.0$. Note that each simulated tip-speed ratio case provides foil data at a single α at the corresponding radial location. The grey line corresponds to the two-dimensional lift and drag coefficients.

For the drag coefficient, we observe that the difference between the undeformed and deformed cases shows a stronger dependency on the angle of attack, increasing towards larger values of α, as well as displaying a monotonic increase with $\delta x/R$ for the entire blade span.

Only a small gain in hydrofoil efficiency is observed for the deformed cases at low angles of attack on sections closer the root of the blade. However, most of the observed changes in lift and drag have a dramatic impact on foil efficiency in the outboard half of the blade across the entire α range, related to the rotor performance loss due to the flapwise deformation.

These changes in efficiency also show that the lift and drag coefficients change in different proportions as functions of the angle of attack (i.e. changes in tip-speed ratio), flapwise deformation and radial location. If correction factors are to be developed and included in engineering models based on two-dimensional aerofoil theory, separate correction factors should be generated either for the lift and drag coefficients, or for the tangential and thrust coefficients, as has been previously suggested by Wimshurst and Willden [35] for the development of tip-loss correction factors.

6.7 Conclusions

Our work presents a novel insight into the hydrodynamic mechanisms driving thrust and power changes in deforming rotor blades. We have highlighted the importance of twist and flapwise deformations and the role of spanwise flows on predicting the load distribution along deformed blades.

Twist deformations cause a substantial change to the blade loading and performance, even for small angles of deformation. These changes are straightforward to analyse using two-dimensional blade-element theory for modest twist angles, as it provides a framework which predicts the hydrodynamic effects of changing the twist angle distribution through lift and drag coefficients.

Flapwise deformations, which cannot be analysed through blade element theory, also affect rotor blade hydrodynamics. Substantial modifications to the spanwise

thrust and tangential force distributions occur due to flapwise deformations, with a significant impact observed for the integrated power and a more limited impact on the integrated thrust due to the presence of two opposing hydrodynamic mechanisms: inboard load augmentation and an increase in near-tip load shedding with flapwise deformation.

The inboard load augmentation is caused by a reduction in static pressure on the suction side of the blade. This is generated by the increased radial force acting on the blade due to changes in the surface-normal orientation as a consequence of blade deformation, which induces an outwards radial flow velocity, driving greater wake expansion. This change in wake expansion results in a static pressure drop on the downstream side of the rotor, increasing lift and drag forces, with a larger relative increase for the latter and consequent reduction in foil efficiency across much of the blade. The effect and its causes, to the best of our knowledge, have not previously been described in the literature.

The increase in near-tip load shedding is generated by the onset of three-dimensional flow effects moving inboard along the blade, reducing both thrust and torque due to faster static pressure equalisation between both sides of the blade near the tip. This phenomenon was characterised and quantified through the radial loss analysis, and is in qualitative agreement with results presented by Crawford [7] and Mikkelsen et al. [22] that show an increase in load shedding as the tip is approached for cases with downstream coning.

The inboard load augmentation and near-tip load shedding mechanisms observed with the flapwise deformation also affect the tangential force, but with more pronounced force reductions across a greater part of the span, thus significantly affecting the integrated power. These result are in disagreement with those presented by Madsen and Rasmussen [18] and Mikkelsen et al. [22] regarding the invariability of the power coefficient with rotor coning, and can be explained by methodological differences. The actuator disc model, as opposed to the blade-resolved simulations used in our study, is unable to capture the geometry- and location-dependent changes in tangential force that affect power performance.

The impact of flapwise deformations on reducing hydrofoil efficiency and rotor performance could enable power shedding through blade deformations if coupled with suitable control strategies. This topic, alongside with a study on the interactions between coupled flapwise and twist deformations, will be addressed in future work.

Acknowledgments

This work was supported in part by CONICYT PFCHA/BECAS CHILE DOCTORADO EN EL EXTRANJERO 2016 /72170292. RHJW would like to acknowledge EPSRC who support his fellowship through grant number EP/R007322/1. The authors would also like to acknowledge the use of the University of Oxford Advanced Research Computing (ARC) facility in carrying out this work. http://dx.doi.org/10.5281/zenodo.22558 .

References

[1] I. Afgan et al. “Turbulent flow and loading on a tidal stream turbine by LES and RANS”. In: *International Journal of Heat and Fluid Flow* 43 (2013), pp. 96–108.

[2] Y. Bazilevs et al. “3D simulation of wind turbine rotors at full scale. Part II: Fluid-structure interaction modeling with composite blades”. In: *International Journal for Numerical Methods in Fluids* (2011), 65:236–254.

[3] G. S. Bir. “Computerized Method for Preliminary Structural Design of Composite Wind Turbine Blades”. In: *Journal of Solar Energy Engineering* 123.4 (2001), p. 372.

[4] K. Boorsma and J. Schepers. *New MEXICO experiment: Preliminary overview with initial validation*. Tech. rep. Energy Research Centre of the Netherlands (ECN), 2014.

[5] T. Burton et al. *Wind energy handbook*. John Wiley & Sons, 2011.

[6] A. Chehouri et al. “Review of performance optimization techniques applied to wind turbines”. In: *Applied Energy* 142 (2015), pp. 361–388.

[7] C. Crawford. “Re-examining the precepts of the blade element momentum theory for coning rotors”. In: *Wind Energy: An International Journal for Progress and Applications in Wind Power Conversion Technology* 9.5 (2006), pp. 457–478.

[8] A. Fluent. “ANSYS Fluent theory guide 19.0”. In: *ANSYS, Canonsburg, PA* (2018).

[9] S. Gant and T. Stallard. “Modelling a tidal turbine in unsteady flow”. In: *Proceedings of the Eighteenth (2008) International Offshore and Polar Engineering Conference*. 2007. 2008, pp. 473–479.

[10] H. Glauert. *The elements of aerofoil and airscrew theory*. Cambridge University Press, 1947.

[11] D. M. Grogan et al. “Design of composite tidal turbine blades”. In: *Renewable Energy* 57 (2013), pp. 151–162.

[12] S. Guntur et al. “FAST v8 verification and validation for a MW-scale wind turbine with aeroelastically tailored blades”. In: *34th Wind Energy Symposium*. 2016, p. 1008.

[13] W. Hunter. “Actuator disk methods for tidal turbine arrays”. PhD thesis. Department of Engineering Science: University of Oxford, 2015.

[14] N. Kaufmann, T. H. Carolus, and R. Starzmann. “On the Effect of elastic Blade Deformation on the Performance of a horizontal Axis Tidal Current Turbine”. In: *Proceedings of the Thirteenth European Wave and Tidal Energy Conference*. ISSN: 2309-1983. EWTEC. 2019.

[15] T. J. Larsen and A. M. Hansen. “How 2 HAWC2, the user’s manual”. In: (2007).

[16] D. W. Lobitz and P. S. Veers. “Load mitigation with bending/twist-coupled blades on rotors using modern control strategies”. In: *Wind Energy: An International Journal for Progress and Applications in Wind Power Conversion Technology* 6.2 (2003), pp. 105–117.

[17] J. Y. Luo and A. D. Gosman. “Prediction of impeller-induced flow in mixing vessels using multiple frames of reference”. In: INSTITUTE OF CHEMICAL ENGINEERS SYMPOSIUM SERIES. 1994.

[18] H. A. Madsen and F. Rasmussen. "The influence on energy conversion and induction from large blade deflections". In: *EWEC-CONFERENCE*. 1999, pp. 138–141.

[19] J. McNaughton et al. "CFD prediction of turbulent flow on an experimental tidal stream turbine using RANS modelling". In: *1st Asian Wave and Tidal Energy Conference*. 2012.

[20] F. R. Menter. "Two-equation eddy-viscosity turbulence models for engineering applications". In: *AIAA journal* 32.8 (1994), pp. 1598–1605.

[21] F. R. Menter, M. Kuntz, and R. Langtry. "Ten Years of Industrial Experience with the SST Turbulence Model". In: *Turbulence Heat and Mass Transfer 4* 4 (2003), pp. 625–632.

[22] R. Mikkelsen, J. N. Sørensen, and W. Z. Shen. "Modelling and analysis of the flow field around a coned rotor". In: *Wind Energy* 4.3 (2001), pp. 121–135.

[23] R. E. Murray et al. "Towing tank testing of passively adaptive composite tidal turbine blades and comparison to design tool". In: *Renewable Energy* 116 (2018), pp. 202–214.

[24] R. F. Nicholls-Lee, S. R. Turnock, and S. W. Boyd. "Application of bend-twist coupled blades for horizontal axis tidal turbines". In: *Renewable Energy* 50 (2013), pp. 541–550.

[25] R. Nicholls-Lee. "Adaptive Composite Blades for Horizontal Axis Tidal Turbines". PhD thesis. University of Southampton, 2011.

[26] R. Rafiee, M. Tahani, and M. Moradi. "Simulation of aeroelastic behavior in a composite wind turbine blade". In: *Journal of Wind Engineering and Industrial Aerodynamics* 151 (2016), pp. 60–69.

[27] P. J. Roache. "Perspective: A Method for Uniform Reporting of Grid Refinement Studies". In: *Journal of Fluids Engineering* 116.3 (Sept. 1994), pp. 405–413.

[28] J. G. Schepers et al. *Final report of IEA Task 29, Mexnet (Phase 1): analysis of Mexico wind tunnel measurements*. Tech. rep. Energy Research Centre of the Netherlands (ECN), 2012.

[29] J. Schluntz and R. H. J. Willden. "The effect of blockage on tidal turbine rotor design and performance". In: *Renewable Energy* 81 (2015), pp. 432–441.

[30] F. Vorpahl et al. "Verification of aero-elastic offshore wind turbine design codes under IEA Wind Task XXIII". In: *Wind Energy* 17.4 (2014), pp. 519–547.

[31] H. Wada et al. "Deformation evaluation of elastic composite blade models for tidal power generation by fluid–structure interaction analysis". In: *18th international conference on composite materials*. 2011.

[32] L. Wang, X. Liu, and A. Kolios. "State of the art in the aeroelasticity of wind turbine blades: Aeroelastic modelling". In: *Renewable and Sustainable Energy Reviews* 64 (2016), pp. 195–210.

[33] A. Wimshurst and R. H. J. Willden. "Analysis of a tip correction factor for horizontal axis turbines". In: *Wind Energy* 20.9 (2017), pp. 1515–1528.

[34] A. Wimshurst and R. H. J. Willden. “Computational analysis of blockage designed tidal turbine rotors”. In: *Progress in Renewable Energies Offshore - Proceedings of 2nd International Conference on Renewable Energies Offshore, RENEW 2016* Emec (2016), pp. 587–597.

[35] A. Wimshurst and R. H. J. Willden. “Computational observations of the tip loss mechanism experienced by horizontal axis rotors”. In: *Wind Energy* 21.7 (2018), pp. 544–557.

[36] A. Wimshurst and R. H. J. Willden. “Extracting lift and drag polars from blade-resolved computational fluid dynamics for use in actuator line modelling of horizontal axis turbines”. In: *Wind Energy* 20.5 (May 2017), pp. 815–833. arXiv: `arXiv:1006.4405v1`.

[37] F. Zilic de Arcos, G. Tampier, and C. R. Vogel. “Numerical analysis of blockage correction methods for tidal turbines”. In: *Journal of Ocean Engineering and Marine Energy* 6.2 (2020), pp. 183–197.

[38] F. Zilic de Arcos, C. R. Vogel, and R. Willden. “Hydrodynamic modelling of flexible tidal turbine blades”. In: *Proceedings of the Thirteenth European Wave and Tidal Energy Conference*. ISSN: 2309-1983. EWTEC. 2019.

[39] F. Zilic de Arcos, C. Vogel, and R. Willden. “Hydroelastic modelling of composite tidal turbine blades”. In: *Advances in Renewable Energies Offshore: Proceedings of the 3rd International Conference on Renewable Energies Offshore (RENEW 2018), October 8-10, 2018, Lisbon, Portugal*. 2018, p. 877.

[40] F. Zilic de Arcos, C. Vogel, and R. Willden. “Extracting angles of attack from blade-resolved rotor CFD simulations”. In: *Wind Energy* 23.9 (2020), pp. 1868–1885.

Hydrodynamic independence and passive control application of twist and flapwise deformations of tidal turbine blades. To be submitted.

Federico Zilic de Arcos, Christopher R. Vogel,
Richard H. J. Willden

7

Hydrodynamic independence and passive control application of twist and flapwise deformations of tidal turbine blades

7.1 Abstract

The deformations experienced by axial-flow rotor blades can induce significant hydrodynamic effects. These changes in hydrodynamics are dominated by the flapwise and twist deformation components, both affecting blade loading and performance. This work explores the hydrodynamic interactions of coupled flapwise and twist deformations, and their potential for passive control strategies using blade-resolved CFD simulations .

The rotor blades were simulated under parametrically prescribed flapwise-only, twist-only and coupled flapwise-twist deformations. The results show that the hydrodynamic effects are adequately described by blade-element theory for twist deformations regardless of the presence of flapwise deformations, whereas flapwise deformations induce changes in the local lift and drag coefficients that are independent of twist. For moderate blade deflections, the hydrodynamic changes generated by the two deformation components can be approximated to be independent from each other.

The independence between the two deformation components is used to explore passive deformation strategies for a tidal rotor. By extrapolating an existing dataset containing CFD simulations of twist-only and flapwise-only deformation cases at different tip-speed ratios, control paths are designed within a tip-speed ratio, flapwise and twist deformation parameter space. These control paths show passive control strategies as a potential alternative to active pitch control on tidal turbines, showing similar performance and maximum loading over a full tidal cycle.

7.2 Introduction

Tidal streams are an abundant and renewable energy resource which is highly predictable, an advantage over other, more intermittent, renewables such as photovoltaic and wind. However, converting tidal stream energy into electricity at utility scale has not yet been achieved due to the technological and operational complexities of the marine environment.

Significant progress has been observed in recent years for tidal stream energy, with megawatt-scale devices at pre-commercial stages deployed and connected to electricity grids (e.g. Orbital Marine's O2 [27], Simec Atlantis AR1500 [2], Hammerfest Strøm HS1000 [1]). However, efforts are still required to reduce the Levelised Cost of Energy (LCOE) for this energy resource to be competitive at a utility scale, for which significant technological improvements are still required [33].

Axial-flow tidal turbines, the most widespread technology for tidal stream energy conversion, exhibit similarities with large-scale wind turbines, with direct knowledge transfers in terms of designing, manufacturing and operating rotors. However, the design of cost-effective rotors also requires considering the differentiating aspects from wind: the increased flow density and relatively lower flow speeds observed in tidal channels, blockage effects (Schluntz and Willden [32], Zilic de Arcos et al. [39]), cavitation (Wimshurst et al. [35]), high environmental turbulence (Milne et al. [23]), sheared flows (Wimshurst and Willden [38]), surface waves (Ordonez-Sanchez et al. [28], Draycott et al. [8]), biofouling and corrosion (Polagye and Thomson [30]), among others. Achieving competitive costs also requires cost reductions in

operation and maintenance (O&M), currently estimated to be larger than CAPEX, alongside improvements in reliability to reduce the cost of capital [34].

The differentiating elements of tidal stream energy suggest that some of the concepts transferred from the wind sector should be reassessed. This includes developing a further understanding of the relevant physics and the development of improved modelling tools which are required to devise optimised solutions.

7.2.1 Turbine control as a driver for LCOE reduction

Tidal and wind rotors are typically designed to extract a rated power P_R, defined from design and obtained at a rated flow speed V_R, with P_R normally close to the maximum capacity of the power take-off (PTO) system. Between the cut-in speed V_{CI} (the minimum flow speed required for the turbine to start) and V_R, the turbine normally operates to maximise energy yield. When the flow speed exceeds V_R, however, the absorbed power is limited to P_R in order to protect the PTO. This is achieved by operating at below the maximum power capture efficiency.

Strategies to fulfill the aforementioned objective vary. Small and mid-sized wind rotors often employ pure speed control to limit power above rated, adjusting the turbine's rotational speed (i.e. the tip-speed ratio λ) as the flow speed varies. However, this typically implies lower efficiencies compared with large-scale rotors, and operating either at high rotational speeds, risking the onset of cavitation (Wimshurst et al. [35]) and the production of environmentally-harmful noise pollution (Hastie et al. [12]), or at low rotational speeds where flow separation is likely to induce fatigue loads.

Modern large-scale rotors, both wind and tidal, typically base their control strategies on changing the turbine rotational speed and the blades' pitch angles (Burton et al. [6]). Below V_R, the rotor operates at its optimum point both in terms of tip-speed ratio and pitch angle, maximising power extraction. Above V_R the turbine sheds power by collectively pitching the blades, changing the angles of attack along the blade span and thus reducing blade forces, until P_R is achieved. This strategy has been proven to be effective at capping power and providing high

energy yields, while also limiting the maximum thrust on the turbine, which occurs at V_R rather than at the maximum flow speed [6].

A benefit of a clearly defined maximum load at rated flow speed and an effectively capped power above, attained through appropriate control strategies, is that it enables the design of less conservative structures, mechanisms, PTOs, foundations and other subsystems. The operational design and optimisation of the rotors is then driven by normal flow conditions and not by extreme yet statistically unlikely events. Despite their increased complexity, maintenance requirements and potentially lower reliability, utility-scale wind rotors with active pitch control still achieve an overall reduction of LCOE.

Tidal rotors, however, with pressing demands to increase reliability and reduce O&M costs, might not benefit from active pitch control strategies to the same extent as wind rotors. Pitch systems have been identified by Le Diagon et al. [16] as one of the most critical components affecting the availability (and, thus, revenue) of tidal stream energy converters. Thus, devices of reduced mechanical complexity, with lower failure rates and maintenance requirements, might be a more suitable alternative.

7.2.2 Passive turbine control

Passive turbine control is a concept that relies on rotor blade deformations to achieve control objectives. The concept stems from the observation that the blade deformations, driven by hydrodynamic loads through complex fluid-structure interactions, can significantly influence rotor loads and/or performance.

Rotor blade deformations are typically separated into three main components: flapwise, edgewise and twist, illustrated in fig. 7.1. The three deformation components are caused by, respectively: the thrust force; the tangential force that drives the rotation of the blades; and the torsional moment created by the offset between the hydrodynamic centre of pressure and the structural centre, as well as from bending-twist structural couplings [9].

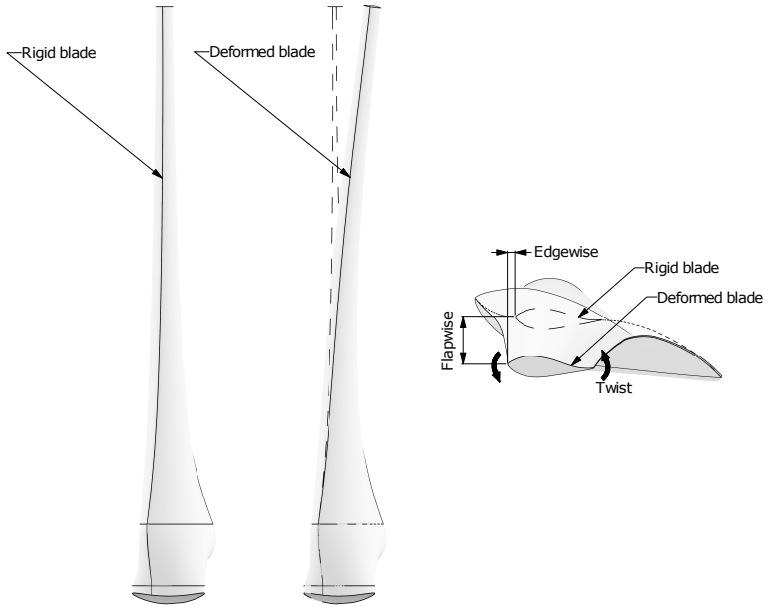

Figure 7.1: Diagram of the different blade deformation mechanisms as seen from side (left) and top (right) views.

Blade deflections can be significant for the flapwise and twist components, especially when blades are designed using flexible composite materials. Flapwise deformations, for example, can reach values up to 10% - 15% of the turbine radius while operating at maximum flow speeds (see e.g. Nicholls-Lee [25], Grogan et al. [11] and Rafiee et al. [31]), whilst twist deformations have been reported to reach values of approximately 2.5° to 5.0° at the tip when anisotropic composite materials are used (see e.g. Ostachowicz et al. [29] Murray et al. [24], De Goeij et al. [7], Lobitz and Veers [17]). Edgewise deformations, in contrast, are of lesser importance because they are caused by tangential forces, typically an order of magnitude smaller than the axial forces and oriented in a direction where blade stiffness tends to be higher ([19, 41]).

The exploitation of the structural reactions of the blade to the flow conditions, relying on the hydrodynamics to deform the blades, and on the structural design to provide a desired response, requires a detailed knowledge of the loading and structural response. The problem is complex, however, since the deformation of the blades affect hydrodynamic loads, which in turn affect blade deflections.

Fluid-structure interactions (FSI) for wind and tidal rotors have been investigated using methods of varying complexity. Such models are typically developed by integrating structural and fluid dynamics solvers. For fluid dynamics modelling, blade-element momentum (BEM) type models (see e.g. Murray et al. [24] and Zilic de Arcos et al. [41]), potential flow solvers (Nicholls-Lee [25]) and blade-resolved unsteady CFD computations (Bazilevs et al. [3], Grinderslev et al. [10]) have been used. On the structural side, FSI models typically use finite element solvers with either beam [13, 15] or shell elements [25, 41].

Tightly-coupled high-fidelity FSI models, capable of implicitly capturing the hydrodynamics of blade deformations as well as the structural dynamics, tend to have a prohibitively high computational cost for engineering design and optimisation. Conversely, engineering models, typically based on one-dimensional beam structural models coupled with BEM-based aero- or hydrodynamic solvers (e.g. OpenFAST [13], HAWC2 [15]), are preferred in engineering practice due to their relatively low computational cost. Such models necessarily involve simplifying assumptions that may not capture all of the important FSI physics of the problem being modelled.

In previous research, we demonstrated that the flapwise and twist deformation components produce significant changes in blade hydrodynamics [40]. The twist deflections change the spanwise distribution of angle of attack, changing the forces along the blade. Even modest twist deformations can create a significant impact on blade thrust and power, effects that can largely be described using blade-element theory. On the contrary, flapwise deformations generate two different and opposing effects on the blade. Firstly, the bent blade creates a radial force on the flow which increases the radial velocity and wake expansion, thereby generating a static pressure drop on the suction surface and increasing loads on the inboard sections of the blade. Secondly, due to the increase in spanwise flow along the blade, the onset of near-tip losses move inboard, increasing the load shedding on sections closer to the tip. These two opposing effects of three-dimensional nature affect the sectional lift and drag polar curves along the span of the blade, giving rise to significant errors in BEM computations based on two-dimensional blade-element theory [40].

This paper aims to expand this previous work with an analysis of the hydrodynamic interactions between the flapwise and twist deformation components on a tidal rotor. The discussion is divided in two sections. Sec. 7.4 discusses the fundamental fluid dynamics, independence and implications of coupling the two deformation components, noting possibilities for the development and improvement of BEM-based engineering models. Sec. 7.5, presents a practical application of these findings, where flapwise and twist deformations are used to determine possible passive control strategies for a 20m diameter tidal rotor.

7.3 Methods

7.3.1 Rotor characteristics

A 20m diameter tidal rotor designed for a blocked-flow condition was employed in this analysis. The blades were designed by Schluntz and Willden [32] for an optimum tip-speed ratio $\lambda = 5.5$, with $\lambda = \omega R/V_\infty$, ω the rotational speed, R the rotor radius and V_∞ the undisturbed flow speed, operating under an isotropic blockage (defined as the ratio between the turbine swept area and the channel cross sectional area) of $B = 0.196$.

The blade geometry consists of a single Risø A1-24 aerofoil section centred around the quarter-chord line from 25% of the span to the tip. The spanwise distribution of blade solidity ($\sigma(r) = Zc(r)/2\pi r$), with Z the number of blades, $c(r)$ the local chord and r the local radius) and twist angles β are presented in fig. 7.2. Further details about the rotor geometry and design methodology can be found in Schluntz and Willden [32].

7.3.2 Blade deformations parameter space

The original rotor was parametrically deformed to obtain an array of deformation cases accounting for flapwise-only, twist-only and flapwise-twist coupled deformation cases, in addition to the original undeformed rotor. The geometries were generated using a CAD model with the algorithmic-aided design software Rhinoceros 6.0 with Grasshopper 1.01.

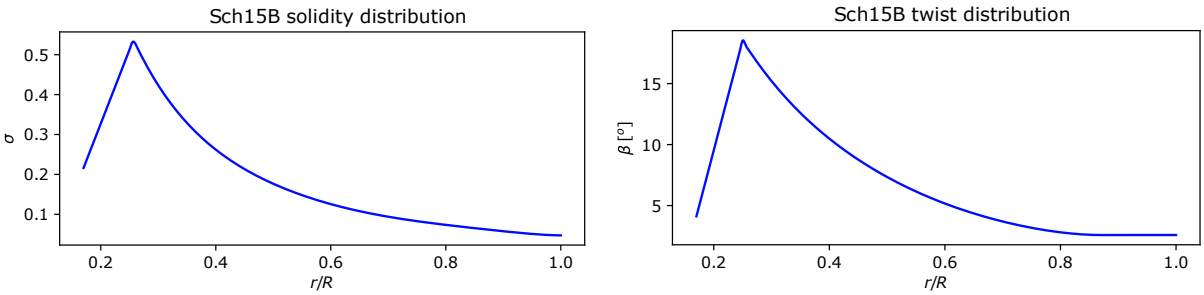

Figure 7.2: Characteristics of the Sch15B rotor: spanwise distributions of the blade solidity σ (left), and twist angle β (right).

The deformed shapes were obtained by scaling the static response of a shell-based structural model under realistic loading conditions, as described by Zilic de Arcos et al. [41]. For the flapwise deformation, the shape of the deformed quarter-chord line was scaled to achieve the desired deformation at the tip. For the twist deflections, considering the high dependency and non-linear behaviour caused by the loading and the case-specific structural configurations, a linear approximation from $r/R = 0.25$ towards the tip was employed.

The blade surfaces were generated for six twist-only cases ($\delta\beta$ between $-5.0°$ and $+15.0°$, with positive values deforming towards feather), 5 flapwise-only cases ($\delta x/R$ between 0.075 and 0.175), and 5 cases with coupled deformations, in addition to the original rotor geometry referred to as the undeformed case. Each of the cases is labelled based on the twist and flapwise deformation at the tip, and the deformations are presented in fig. 7.3. Each deformation case was simulated at four tip-speed ratios ($\lambda \in \{4.0, 5.0, 6.0, 7.0\}$).

Each case is referenced in terms of the combination of $\delta x/R$, $\delta\beta$ and λ. A summary of simulated cases is presented in table 7.1.

7.3.3 CFD modelling

The simulation strategy presented in this work follows the work presented in Zilic de Arcos et al. [40]. The simulations were performed using a RANS (Reynolds-Averaged Navier Stokes) CFD (Computational Fluids Dynamics) model with a $k-\omega$ SST turbulence model [21, 22] under steady-state assumptions and using the Luo and

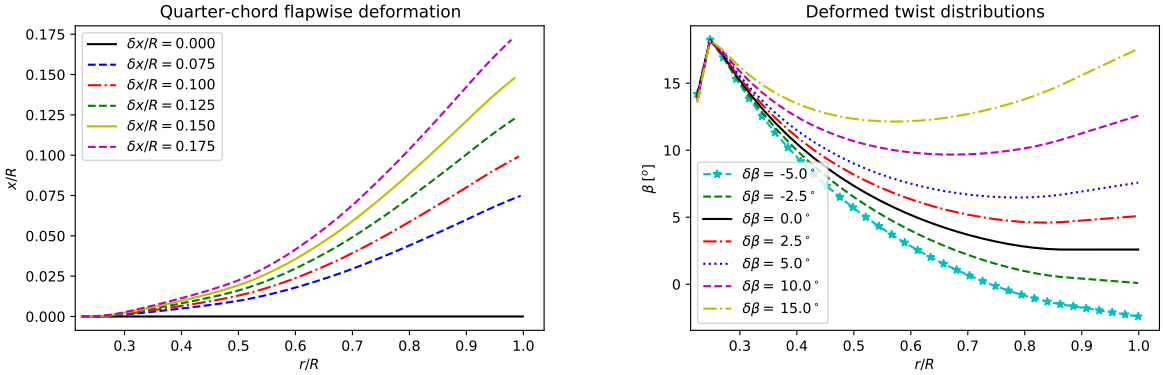

Figure 7.3: Spanwise distribution of the axial-position of the quarter-chord line for different flapwise deformation cases (left) and spanwise twist distribution for different twist deformation cases (right).

Table 7.1: Testing matrix of simulated cases for twist ($\delta\beta$) and flapwise ($\delta x/R$) deformations. Each point in this matrix was simulated the tip-speed ratios $\lambda \in [4.0, 5.0, 6.0, 7.0]$. The point highlighted in red corresponds to the undeformed case.

$\delta x/R$	$\delta\beta$ [°]						
	−5.0	−2.5	0.0	2.5	5.0	10.0	15.0
0.000	✓	✓	✓	✓	✓	✓	✓
0.075		✓	✓	✓			
0.100			✓	✓	✓		
0.125			✓				
0.150			✓				✓
0.175			✓				

Gosman [20] MRF (Multiple Reference Frame) model. The model discretisation consists of a cell-centred finite volume scheme with second-order spatial discretisation and a coupled velocity-pressure algorithm for the solution of the equations. The computations were made with the commercial software ANSYS Fluent 19.0.

A 120° segment of a cylindrical domain with a diameter equivalent to 5 times the rotor diameter was used, permitting low blockage effects (blockage of 4%), and with boundary conditions defined as: velocity inlet (4.5 m/s, turbulence intensity of 10% and length scale 0.7 times the rotor diameter), pressure outlet, symmetry condition for the outer domain walls, periodic conditions that limit the effective solution of the equations to a 120 degrees wedge, and non-conformal interfaces between the two subdomains, as described in Zilic de Arcos et al. [40].

Structured meshes were built for every case using ICEM 19.0, maintaining the O-grid topology around the blade surfaces between cases and adapting buffer regions both up- and downstream of the rotor to allow blade deformations.

A full mesh sensitivity study is presented by Zilic de Arcos et al. [40], and a validation of the simulation strategy can be found in the work presented by Wimshurst and Willden [37].

7.3.4 Simulation post-processing

The spanwise force distributions were calculated integrating pressure (p) and shear stresses (S) over the aerofoil sections at different radial locations. The resulting forces are then presented as components in the global frame of reference:

$$\vec{F}(r) = \oint (p\hat{n} + \vec{S})dC \tag{7.1}$$

with the integral solved over a blade slice C at r, where p is the static pressure, $\hat{n}$ the blade surface normal vector, S the shear stress, and ρ the fluid density.

The power and thrust coefficients were calculated, respectively, as:

$$C_P = \frac{P}{1/2\rho A V_\infty^3} = \frac{\omega \int F_\theta(r) r dr}{1/2\rho A V_\infty^3} \tag{7.2}$$

$$C_T = \frac{T}{1/2\rho A V_\infty^2} = \frac{\int F_x(r) dr}{1/2\rho A V_\infty^2} \tag{7.3}$$

where P and T are the integrated power and thrust, F_x and F_θ are components of $\vec{F}(r)$ in the axial and tangential directions, A the turbine swept area and V_∞ the undisturbed flow velocity.

Flow quantities, including induction factors and angles of attack, were sampled from the simulated flow using the Streamtube Averaging Method (SAM). This is a methodology that allows the determination of flow variables at the rotor plane based on an interpolation over a streamtube using the flow data up- and downstream from a rotor section, avoiding the strong gradients that arise near the rotor blade

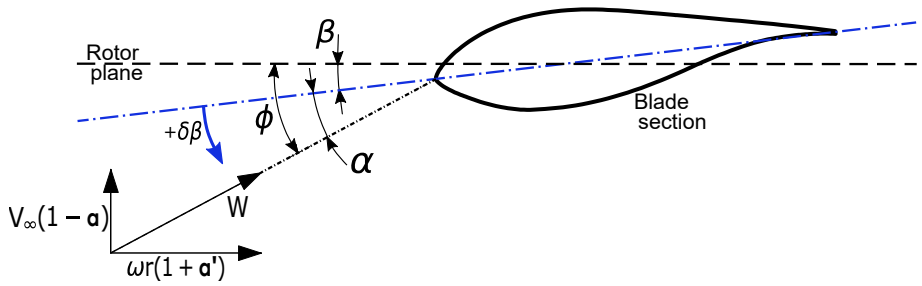

Figure 7.4: Flow diagram over an arbitrary section of the blade, as described by BEM theory.

itself. The method accounts for the expansion of the wake to sample the flow, as described by Zilic de Arcos et al. [42].

The data used for the interpolation was extracted at an axial distance of $x/c = \pm 1.0$ from the blade. The local deformation was accounted for, both to determine the location of the intersection between the streamtube and the rotor, as well as to establish the axial coordinates for interpolation.

The inflow angle ϕ and the local angle of attack α, for a blade section r/R, were calculated at each radial location using the axial and tangential velocities sampled from the simulated flow, V_x and V_θ. The inflow angle ϕ and the angle of attack α were determined as:

$$\phi(r) = tan^{-1}\left(\frac{V_x(r)}{V_\theta(r)}\right), \tag{7.4}$$

and

$$\alpha(r) = \phi(r) - \beta(r) \tag{7.5}$$

as displayed in fig. 7.4.

The interference of the rotor in the streamwise flow is represented by the axial induction factor a, defined as:

$$a(r) = 1 - \frac{V_x(r)}{V_\infty} \tag{7.6}$$

Finally, the flow velocities, angles of attack and inflow angles were used, in conjunction with the spanwise distribution of thrust and tangential forces, to determine the local lift and drag coefficients.

7.4 Hydrodynamic independence of twist and flapwise deformations

Blade element theory is a robust framework which, by assuming that the forces on a three-dimensional blade can be explained as a collection of two-dimensional foils, allows predicting the performance and load changes on a blade undergoing twist changes, either in the form of twist deformation or blade pitching. Many engineering tools, as discussed in sec. 7.2.2, rely on this assumption to predict blade loads and performance.

Our previous research, however, demonstrated that the effects of flapwise deformation on thrust and torque can be significant, with causes that cannot be tracked down to changes in angles of attack, relative inflow velocity or vector re-orientations [40]. This suggests that models based on two-dimensional blade element theory cannot capture the hydrodynamic effects of flapwise deformations, nor can these effects be exploited by design methods based on blade element theory.

In the following sections we study the hydrodynamics flapwise and twist deformations by looking at the effects of twist-only, flapwise-only and coupled flapwise and twist deformations on blade hydrodynamics. The focus of the analysis is to explore the independence and couplings between flapwise and twist deformation hydrodynamics, and the implications of such couplings for BEM-based models.

7.4.1 Force analysis

Figure 7.5 shows the spanwise thrust and tangential force distributions on a rotor blade for two sets of twist-only, flapwise-only, no deformation and coupled flapwise and twist deformation cases.

The twist-only and flapwise-only cases on both sets show the trends described in previous research [40]: the twist-only cases show changes on the spanwise force distribution due to local changes in angle of attack, seen as a monotonic increase ($\delta\beta = -2.5°$) or decrease ($\delta\beta = +5.0°$) in thrust, alongside reductions in tangential force along the span. The flapwise-only cases show a load augmentation at the inboard sections and an increase in load shedding near the tip.

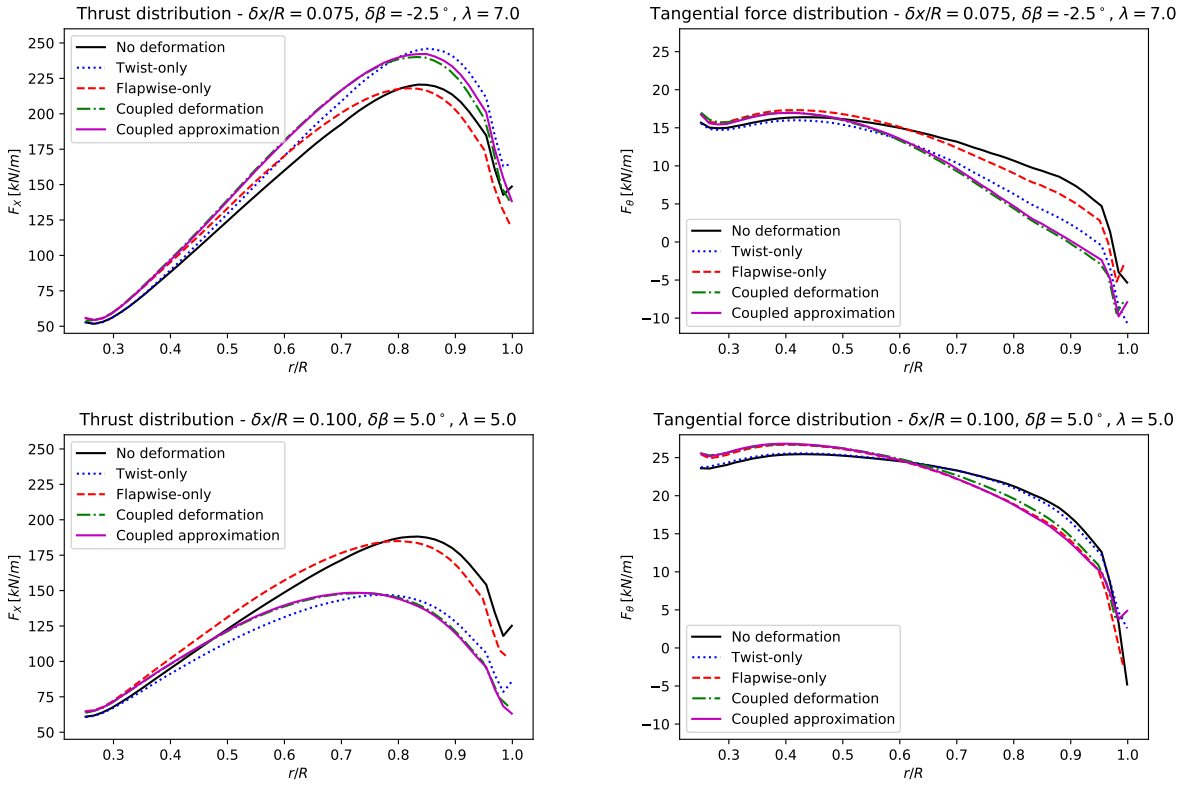

Figure 7.5: Test of the hydrodynamic independence hypothesis in terms of thrust and tangential force for two different sets of blade deformations, at two different tip-speed ratios.

The thrust and tangential forces on the coupled deformation cases appear to be dominated, in most cases, by the twist deformation effects. However, comparing the twist-only and coupled deformation cases reveals the inboard load augmentation and near-tip load shedding, effects that are characteristic of the flapwise deformation.

These observations are confirmed by isolating the effects of the flapwise and twist deformations, which are calculated as the difference in local thrust and tangential force between undeformed and deformed cases. Assuming the deformation effects to be independent from each other leads to the spanwise force distributions of a blade with coupled flapwise and twist deformations to be estimated as:

$$F^*_{CD} = F_{ND} + (F_{TO} - F_{ND}) + (F_{FO} - F_{ND}) \tag{7.7}$$

where F^*_{CD} is an approximation of the spanwise force distribution of a case with coupled deformations, for either thrust or tangential force. The sub-indices CD,

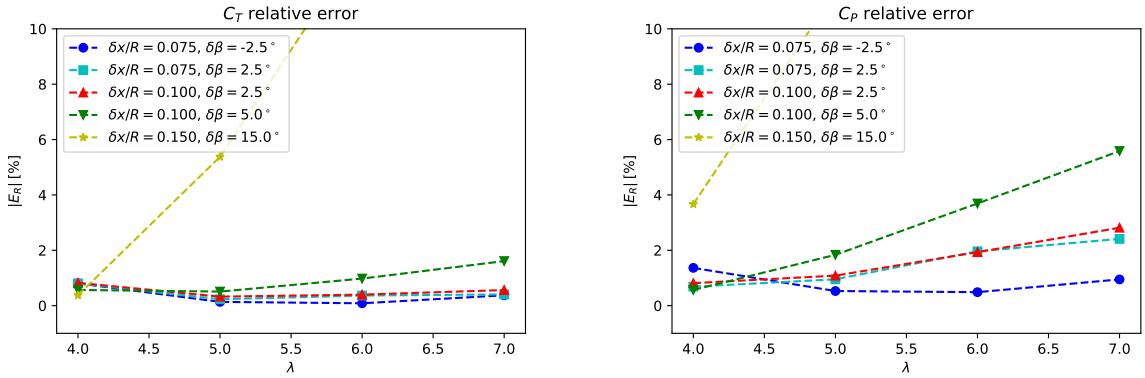

Figure 7.6: Relative error of the integrated power and thrust coefficients between the coupled deformation CFD results and an approximation based on the twist-only and flapwise-only results.

ND, TO and FO stand for coupled deformation, no deformation, twist-only and flapwise-only, respectively.

The results of eq. 7.7 are shown in fig. 7.5 under the label of 'Coupled approximation'. The plots show a good agreement between the simulated case with coupled deformations and the approximation F^*_{CD} for both tangential force and thrust.

A further analysis of the accuracy of eq. 7.7 can be seen in fig. 7.6. These plots show the relative error, calculated in terms of C_P and C_T, for the different cases simulated with coupled deformations at varying tip-speed ratios. The relative error plots confirm that assuming the force changes produced by the flapwise-only and twist-only deformations to be independent from each other produces a good agreement with the CFD simulations for moderate blade deflections. The results show a maximum relative error of 5.5% on C_P and below 2.0% on C_T for all cases except where $\{\delta x/R = 0.150, \delta\beta = 15°\}$. This case, the largest deformation simulated, shows a relative error in excess of 10%, suggesting significant interactions and higher-order effects. Nevertheless, for moderate blade deflections, the relatively low error observed suggests that the hydrodynamic effects of flapwise and twist deformation can be regarded as independent of each other.

In the following sections, we analyse the impact of this hypothesis in terms that are relevant for the development and improvement of engineering models, especially those based on BEM theory.

7.4.2 Axial induction factors

The relationship between the local thrust coefficient and the axial induction factor a is an important component of BEM models. This is typically represented by the axial momentum equation below a critical value a_c, and by an empirical function above. The empirical model is used to account for turbulent wake effects in high-load regimes where the validity of the analytical model breaks down [6].

Fig. 7.7 presents the relationship between axial induction factors and local thrust coefficients. The data points extracted from the CFD simulations, for different deformation cases, are displayed at two radial locations. Alongside the CFD data, the figure also shows the BEM analytical thrust model [6], the widespread empirical model for turbulent wake state of Buhl [5] (used by, e.g. Ning [26] and Jonkman et al. [14]), and the experimental data of Lock et al. [18] reproduced from Buhl [5].

The CFD data in fig. 7.7 spans a smaller range of a compared to Lock's experimental data, and shows that blade deformations do not appear to affect significantly the functional relationship between thrust and axial induction factors. However, the CFD data also highlights that radial location has a more significant impact on this function than blade deformations.

The relatively small spread in the CFD data with and without deformations, compared with Lock's data, suggests that the thrust function used for an undeformed blade should be sufficient to model a rotor with blade deformations within a BEM framework. The momentum model derived by Buhl [5], however, differs considerably from the CFD results especially around the inboard sections, which may be a potential source of error in BEM computations. The development of a correction to this model is beyond the scope of the this paper and will be addressed in future work.

7.4.3 Angles of attack

Fig. 7.8 shows the spanwise distribution of angles of attack for three sets of deformation cases at tip-speed ratios of 4.0 and 7.0. The first two sets include cases with varying twist deformations and fixed $\delta x/R$, alongside the undeformed case. The third set presents a fixed twist deformation at different $\delta x/R$ cases.

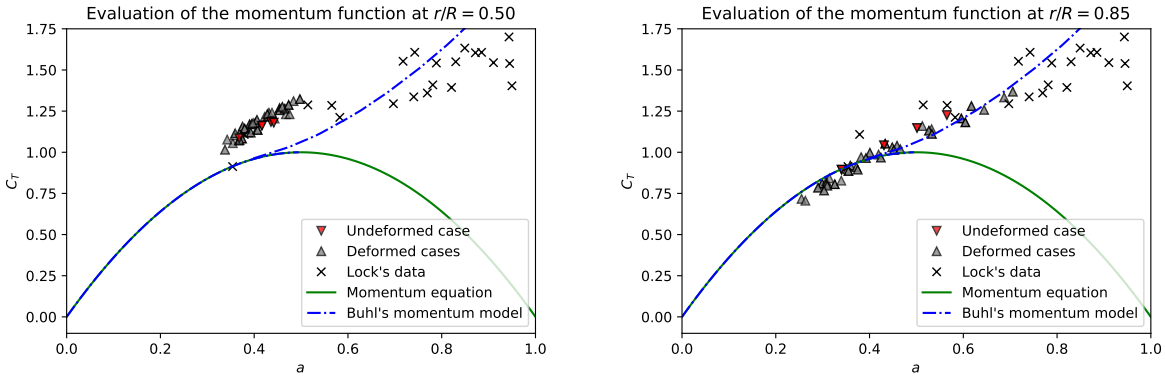

Figure 7.7: Relationship between the sectional thrust coefficients and the axial induction factors for different cases around the inboard ($r/R = 0.50R$, left) and approaching the tip of the blade ($r/R = 0.85$, right). Buhl's momentum model (dot-dash line) and the analytical axial momentum model (solid line) are plotted for reference.

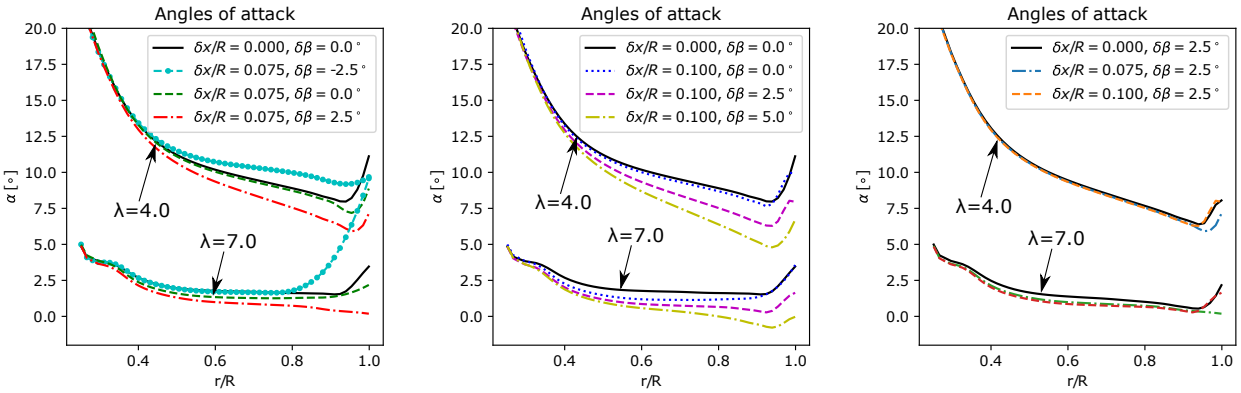

Figure 7.8: Spanwise distribution of angles of attack for three sets of deformation cases, each presented at two different tip-speed ratios. From left to right: varying $\delta\beta$ with $\delta x/R = 0.075$; varying $\delta\beta$ with $\delta x/R = 0.100$; and varying $\delta x/R$ with $\delta\beta = 2.5°$. The three sets are compared with the undeformed case (solid black line).

Twist deformations affect the angle of attack by altering the relative angle of the blade sections to the incoming flow. The change in α is different to that of the twist deflection due to the adjustment of the inflow angle. Positive (negative) twist deformations act to reduce (increase) angle of attack, typically reducing (increasing) thrust force and thus increasing (reducing) the axial flow speed and therefore the inflow angle ϕ.

The results demonstrate that flapwise deformations have a limited effect on the α distribution despite the force changes on both the inboard and near-tip sections of the blade. The inboard α variations are more evident for the high

tip-speed ratio cases, as shown in fig. 7.8 (right). Small reductions in the inboard angle of attack are observed as $\delta x/R$ increases due to the reduction in axial flow speed given the inboard load augmentation. As the blade tip is approached, the difference between the cases with and without flapwise deformation decrease, since ϕ and thus α are increasingly dominated by the rotational speed. Near the tip ($r/R \geq 0.90$) divergence between the cases is observed. This is an area of the blade where the concept of a two-dimensional angle of attack, in a flow dominated by three-dimensional flow effects, is no longer applicable [36].

7.4.4 Polar coefficients

Figs. 7.9 and 7.10 show lift and drag coefficients for the same sets of deformations described above. The coefficients were extracted from the blade-resolved CFD results and are presented for two spanwise locations: $r/R = 0.50$ and $r/R = 0.85$. Each data point corresponds to a specific λ, with C_L and C_D reconstructed considering the local flow and blade characteristics as described in section 7.3.4. Interpolating splines were added to the plots to reflect the general C_L and C_D dependency upon the angle of attack α.

Fig. 7.9 shows at $r/R = 0.50$ the inboard load augmentation caused by flapwise deformation for $\delta x/R = 0.075$ and $\delta x/R = 0.100$. This is observed as a significant step-increase in the lift coefficient, and an increase in drag dependent on α and $\delta x/R$. The influence of twist deformation in lift and drag is much smaller, especially at lower angles of attack, and is considered negligible.

Closer to the tip, the lift curves converge with each other for cases with and without flapwise deformation. This suggests that the inboard load augmentation previously mentioned, is neutralised by the onset of the tip-loss effects moving inboard. The cases with flapwise deformation still present an attendant increase in drag in the near-tip region. This effect, showing a small dependency on twist, can also be attributed to the tip-loss effects moving inboard, and the associated drag increase described by Wimshurst and Willden [36] due to tip-loss mechanisms influencing the outboard sections of the blade.

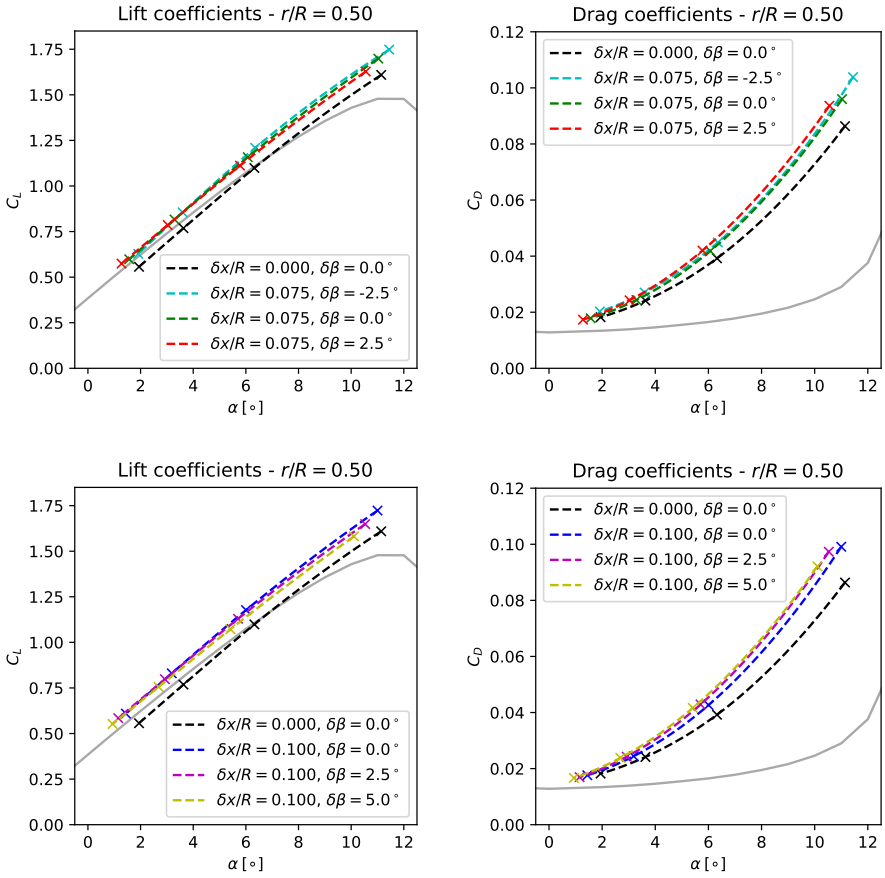

Figure 7.9: Polar lift (left) and drag (right) coefficients extracted from blade-resolved simulations at $r/R = 0.50$ for different deformation cases. Two-dimensional polars plotted for reference (grey solid line).

7.4.5 Hydrodynamic centre of pressure

The position of the hydrodynamic centre of pressure is relevant for the design and implementation of passive control strategies. These strategies rely on achieving desired deformations, using a bespoke or tailored structure, to fulfill specific control objectives. From an engineering perspective, if the blade loads and deformations are known, tailoring a structure involves solving an inverse structural problem where the structural and hydrodynamic centres are important variables. The centre of pressure is the location on the blade section around which the hydrodynamic forces are centred, and the structural centre depends on structural design and material selection. The offset between these two points along the blade creates a torque through the span which induces twist deformations.

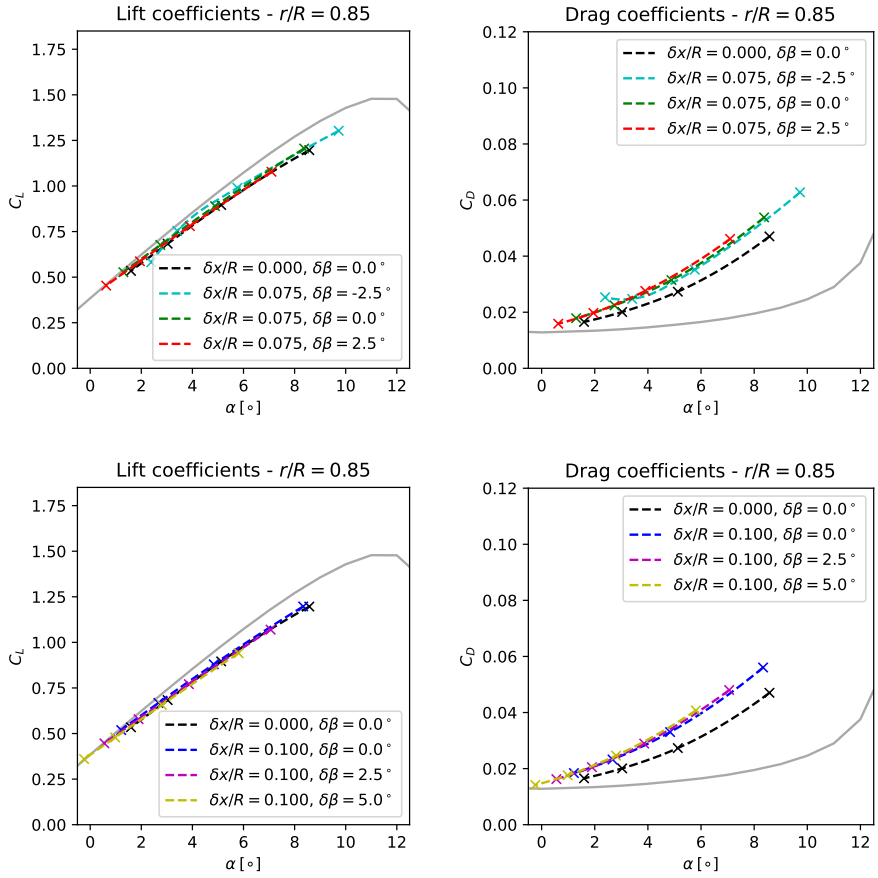

Figure 7.10: Polar lift (left) and drag (right) coefficients extracted from blade-resolved simulations close to the tip of the blade ($r/R = 0.85$) for different deformation cases. Two-dimensional polars plotted for reference (grey solid line).

As with the angles of attack, the position of the hydrodynamic centre appears to be dominated by twist rather than flapwise deformation. Fig. 7.11 shows that twist deflections acting to reduce the angle of attack (i.e. positive $\delta\beta$) shift the centre of pressure towards the trailing edge and vice-versa, with larger deformations driving the largest shift in the centre position. The results also show an influence of tip-speed ratio, as the centre shifts are larger for the cases operating at $\lambda = 7.0$ than for $\lambda = 4.0$.

Analysing the set of cases with fixed $\delta\beta$ and varying $\delta x/R$, we observe that flapwise deformations have a limited effect on the centre of pressure, with a maximum relative change of ca. 5% near the tip shifting towards the trailing edge, despite the significant changes in the polar coefficients discussed in sec. 7.4.4, and the implied changes to pressure distribution along the chord.

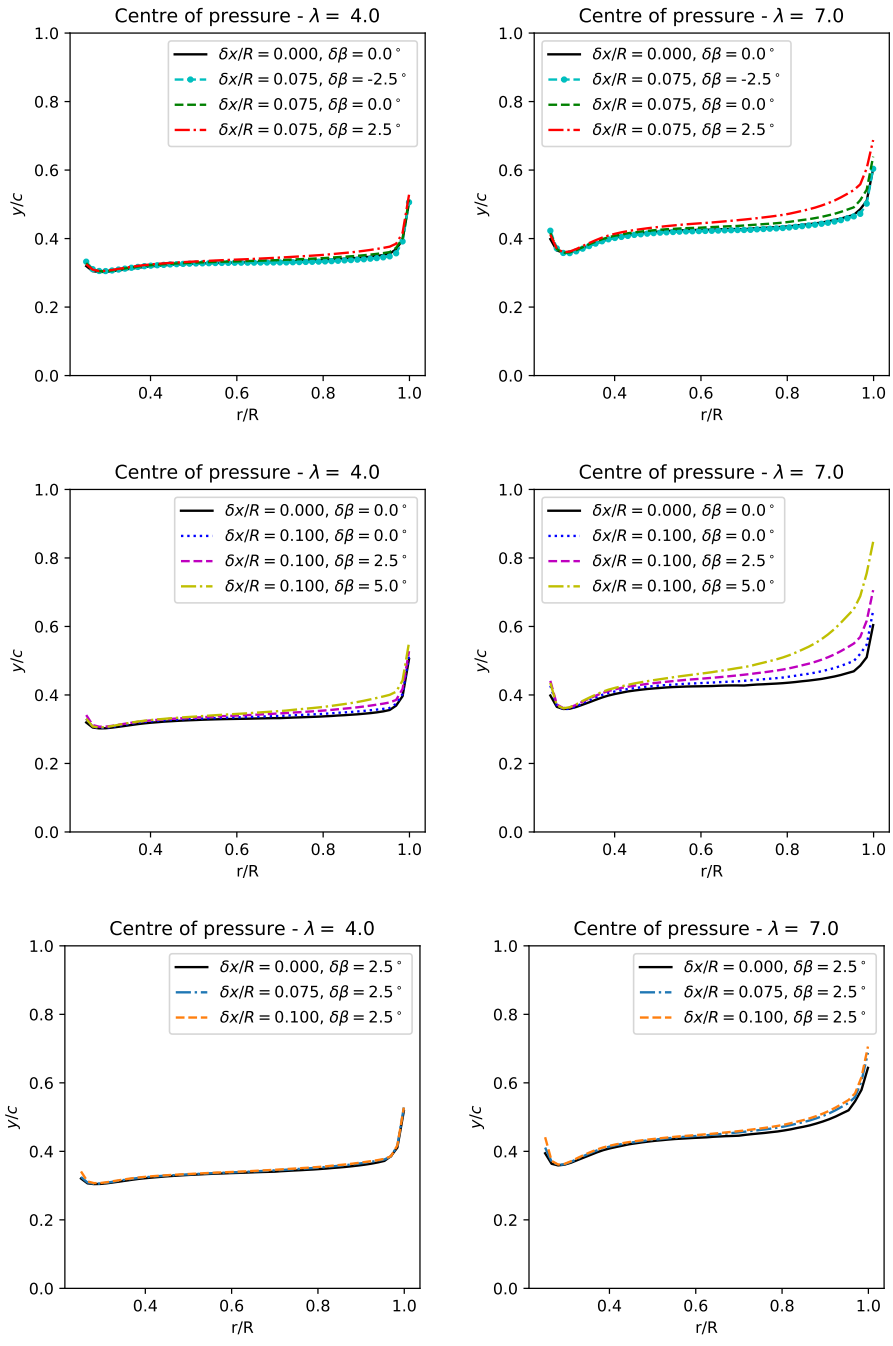

Figure 7.11: Spanwise distribution of the hydrodynamic centre of pressure for three sets of deformation cases at $\lambda = 4.0$ (left column) and $\lambda = 7.0$ (right column). The centre of pressure is plotted over a local tangential coordinate y, measured from the leading edge, and non-dimensionalised by the local chord. From left to right: varying $\delta\beta$ and $\delta x/R = 0.075$; varying $\delta\beta$ and $\delta x/R = 0.100$; and varying $\delta x/R$ with $\delta\beta = 2.5°$.

7.4.6 Summary

The analysed results show that, for moderate blade deflections, the hydrodynamic effects induced by the flapwise and twist deformation components can be approximated to be independent from each other.

In terms of the constituents of BEM theory, the relationship between thrust and axial induction factor shows no significant influence from blade deformations, while two-dimensional polar coefficients are affected only by flapwise deformations. These changes in lift and drag, which affect the functional relationship of C_L and C_D with α, show no significant coupling effects between flapwise and twist, nor a significant influence of twist deformations.

Angles of attack and centres of pressure showed negligible interactions between twist and flapwise deformation, with changes in this two variables dominated by twist deformations. Flapwise deformations showed a very limited influence in these variables.

The hydrodynamic independence of the two deformation components allows to estimate the forces on a rotor blade with coupled flapwise and twist deformations using twist-only and flapwise-only data, with a relatively low error for moderate deflections. The implications of this will be demonstrated in the following sections, where we explore passive control strategies for a tidal rotor.

7.5 Design of passive control strategies

Designing a passively deforming blade requires that an inverse structural problem be solved where the deformations and loads are known *a priori* to tailor a suitable structure. Our approach to this problem consists in finding a preliminary control path for the analysed rotor, defined by a set of $(C_P, C_T) = f(\delta x/R, \delta\beta, \lambda)$ points, where each point corresponds to a flow speed between the cut-in and cut-out speeds.

The parameter space $(C_P, C_T) = f(\delta x/R, \delta\beta, \lambda)$ was defined by combining the available CFD data (which includes the full range of twist-only and flapwise-only cases alongside a selection of cases with coupled twist and flapwise deformations,

Table 7.2: Comparison between the operational target parameters of three different control strategies

Strategy	C_{TR} $[-]$	T_{max} $[kN]$	$\delta x_{max}/R$ $[-]$	V_R $[m/s]$
Passive control 1	0.70	1,450.00	0.10	3.00
Passive control 2	0.80	1,600.00	0.15	3.00
Active pitch control	0.91	1,282.00	0.00	3.00

as described in sec. 7.3.2), with the results of eq. 7.7 used to estimate the force distributions of the coupled deformation cases that were not simulated. Integrating the forces lead to a fully-defined parameter space for C_P and C_T in terms of $\delta x/R$, $\delta\beta$ and λ, where control paths can be designed.

To find suitable control paths we specified target thrust curves for each strategy that monotonically increase with flow speed. These target thrust curves are considered to be the key input for two passive control strategies, since thrust is the main driver for blade deformations. The control paths are designed for a rotor expected to operate in currents between 0.5 to 4.5 m/s, and with a rated flow speed of 3.0 m/s. Note that this thrust-based approach contrasts the typical focus on power in the design of active-pitch control strategies.

The target thrust curves are defined by a fixed thrust coefficient C_{TR} below the rated flow speed and a linear function between V_R and a maximum thrust T_{max}, which is expected to occur at the cut-out speed V_{CO}. The thrust curves are thus fully determined by the cut-in, rated and cut-out flow speeds (V_{CI}, V_R and V_{CO}, respectively), the thrust coefficient at rated flow speed, and the maximum thrust.

Two thrust curves were designed for two different passive control strategies. These two curves allow exploring the trade-off between C_T and C_P, with higher thrust values typically enabling higher power coefficients but leading to higher maximum loads. The design variables defining the two curves are shown in table 7.2 in addition to the maximum allowable flapwise deformation $\delta x_{max}/R$. Alongside the thrust parameters for the passive strategies, reference values for an active pitch controlled turbine rated at 2 MW are provided.

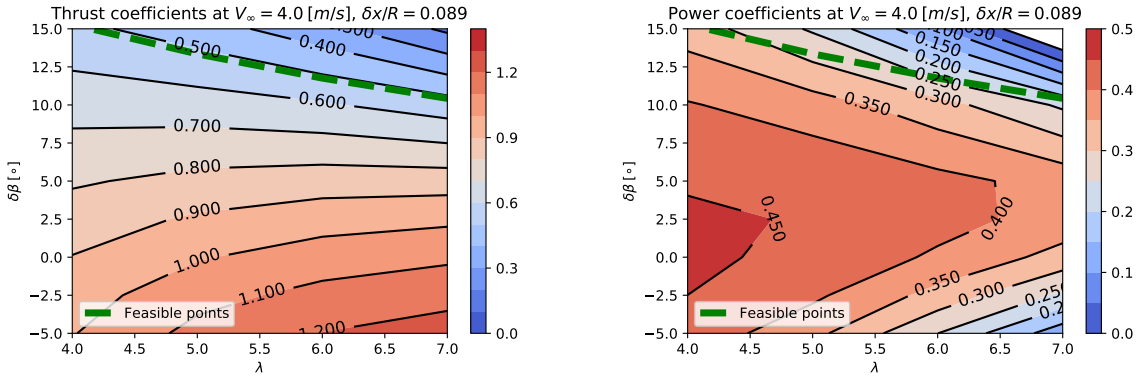

Figure 7.12: Contour plots of thrust (left) and power (right) coefficients for the Passive control 1 case at an inflow speed of $V_\infty = 4.0\,[m/s]$, with $V_\infty \geq V_R$, and under a flapwise tip deflection of $\delta x/R = 0.089$. Highlighted in green, the locus of feasible points where the desired thrust is achieved.

The flapwise deformation is assumed to be proportional to thrust ($\delta x \propto V_\infty^2$), with the maximum allowable thrust and flapwise deformation defined as design variables. This allows the three-dimensional parameter space $\{\delta x/R, \delta\beta, \lambda\}$ to be reduced to a two-dimensional space where C_T and C_P are functions of $\delta\beta$ and λ. By identifying the C_T required by the target thrust profile for a flow-speed V_i, the corresponding $\{\delta\beta, \lambda\}$ required to achieve this can be determined as a function of V_i. The set of $\{\delta\beta, \lambda\}$ where the target thrust is fulfilled is defined as the locus of feasible points.

Fig. 7.12 shows a typical example of the thrust and power planes obtained after reducing the parameter space for a flow speed above rated. This figure also highlights the locus of feasible points on both contours. Specifically, the locus of feasible points on the power contour shows how C_P varies for a constant value of C_T.

A C_P and corresponding $\{\delta\beta, \lambda\}$ pair is selected amongst the locus of feasible points that best matches the C_P objective at a given flow speed (power maximisation below P_R or power shedding to limit power capture in excess of P_R). Consequently, the required deformed blade geometry ($\delta\beta$ and estimated $\delta x/R$) and rotational speed λ that satisfy the required thrust, alongside with the best possible match to C_P within the operating constraints, are defined as functions of each flow speed V_i between cut-in and cut-out.

7.5.1 Control path results

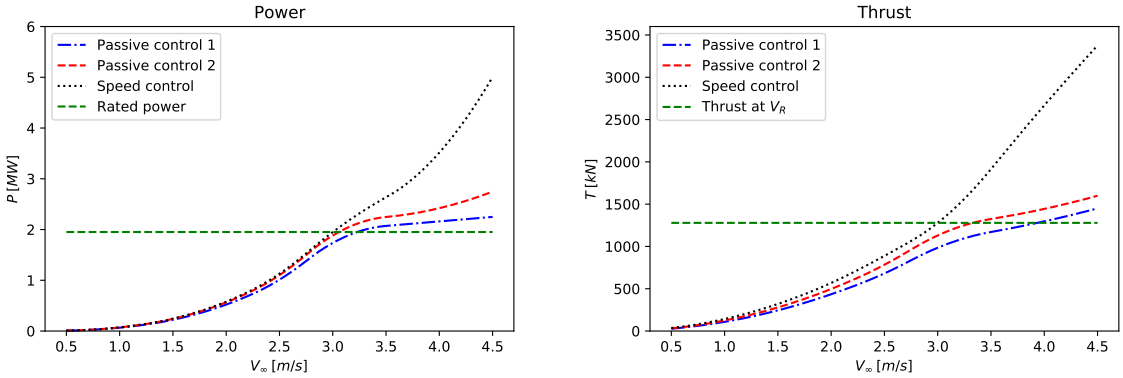

Figure 7.13: Power and thrust as functions of the undisturbed flow speed V_∞. The plots show the two passive control strategies, a rigid blade with speed control, and reference values that correspond to a rigid rotor with active pitch control.

Fig. 7.13 shows power and thrust as functions of the flow speed for the passive control 1 and passive control 2 strategies, designed with the methodology described above and defined by the parameters presented in table 7.2. Alongside the passive control strategies, two sets of results corresponding to the original blade design, assumed rigid, are provided for comparison: a speed-controlled rotor operating within the limits of the parameter space ($4.0 \leq \lambda \leq 7.0$); and reference values for rated power and thrust at rated flow speed, values assumed to be characteristic for an active-pitch controlled Sch15B rotor.

The results shown in fig. 7.13 highlight that passive control paths were found to fulfill the targeted thrust constraints across all flow speeds. The lower thrust values associated with the passive strategies, compared with the rigid speed-controlled rotor, result in a slightly lower power below rated flow speed. The advantage of the passive control is realised above the rated flow speed, where significant load shedding and power capping are achieved by both passive strategies when compared with the speed-only control.

The power at cut-out speed for the speed control case exceeds P_R by 150%. 55% and 45% of this power in shed by the passive control strategies 1 and 2, which exceed P_R at V_{CO} by only a 12% and 37%, respectively. Note that the difference in

maximum power between the two passive strategies is a consequence of the higher thrust of the passive strategy 2 defined from design.

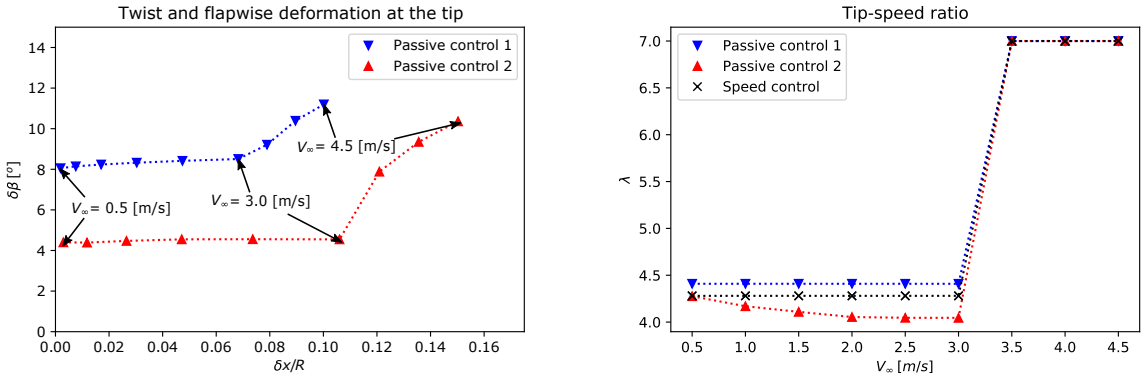

Figure 7.14: Blade twist deformation $\delta\beta$ as a function of blade tip deformation $\delta x/R$ for the two passive control cases (left) and tip-speed ratios as functions of the incoming flow speed required to provide passive turbine control. The required deformations are indicated at 0.5 $[m/s]$ increments between the cut-in $V_{ci} = 0.5\,[m/s]$ and cut-out $V_{co} = 4.5\,[m/s]$ flow speeds.

The blade deformation and control paths as functions of flow speed for the two passive control strategies, followed to achieve the power and thrust curves, are shown in fig. 7.14.

The flapwise and twist deformations plot in fig. 7.14 shows a significant twist deformation required at cut-in speed V_{CI} to enable the low C_{TR} required by the strategy design. In practice, this implies that the rotor needs to be pre-twisted, altering the original spanwise twist distribution optimised for performance. The pre-twist in this work is considered as a spanwise-varying modification of the original twist distribution, equivalent to the deformations described in sec. 7.3.2, that lead to rotor blades that are different from the original design when no forces are applied.

The pre-twist was found by extrapolating the deformation curves at $V_\infty = 0.00\,m/s$. The resulting pre-twists are $\delta\beta|_{V_\infty=0\,m/s} = 7.99°$ for the passive control strategy 1 and $\delta\beta|_{V_\infty=0\,m/s} = 4.41°$ for the passive control strategy 2. As with blade deformations, the angle refers to the pre-twist at the tip.

The deformations shown in fig. 7.14 demonstrate that the objectives achieved with the passive control strategies in terms of thrust shedding and power capping

can be realised with relatively modest changes in blade twist up to the cut-out velocity. This range is approximately 3.5 ° for the passive control strategy 1 and 6.0 ° for the passive control strategy 2. These maximum twist deformations are close to the ranges considered feasible by the literature reviewed in sec. 7.2.2 (approximately 2.5° to 5.0°) .

Fig. 7.14 also shows the tip-speed ratio as function of V_∞ for the two passive control strategies and the speed control case. The three cases show the same trend: below rated, the tip-speed ratio is maintained low and at its local optimum; while above V_R the control quickly saturates the output to the maximum possible λ to shed power. As λ reaches its maximum limit on the three cases, the power and load shedding is achieved through blade deformations. These deformations lead to the passive control strategies outperforming the speed control case in terms of power capping and load shedding.

7.5.2 Contribution of deformation components to passive control

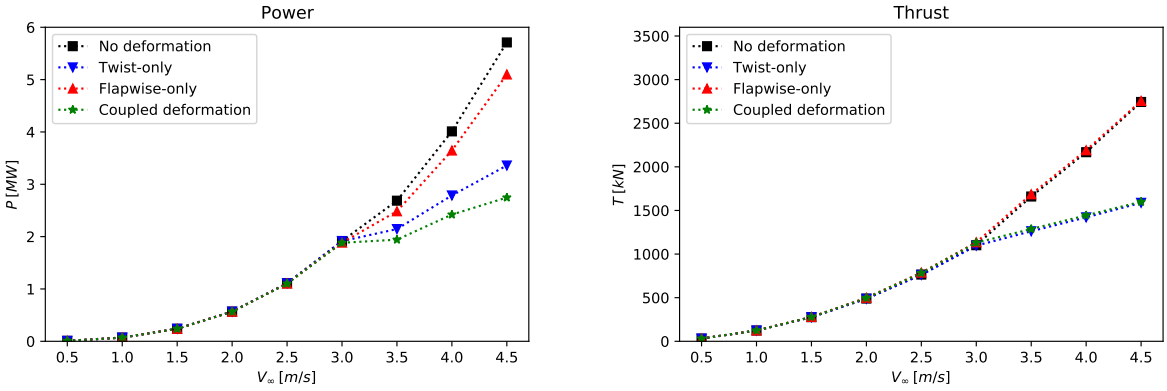

Figure 7.15: Generated power and thrust decoupled in blade deformation components. The results correspond to the passive control 2 strategy.

Fig. 7.15 shows the power and thrust as a function of flow speed for the different deformation components corresponding to the passive control 2 strategy, the case with the largest flapwise deformations. The points were calculated for the deformations and tip-speed ratios from the passive control path at the corresponding flow-speeds. The pre-twist angle was included for all deformation components.

The results show that power and thrust shedding is dominated by the twist deformation above rated flow speed. Although flapwise deformation has a negligible impact on thrust, it has a substantial impact on power capping above rated. Note that, at cut-out speed, the power for the twist-only case is approximately 22% larger than the case with coupled flapwise and twist deformations, highlighting the importance of considering both components in hydrodynamic analyses, especially when blade deflections are significant.

7.5.3 Net energy calculation

We estimate the average energy yield for the turbine control strategies over a full tidal cycle at two different sites with semi-diurnal tidal patterns. We selected the Pentland Skerries and the Race of Alderney as sites being considered for tidal development. The peak spring and neap tidal flow speeds are presented in table 7.3, with data from Black and Veatch [4]. The currents were estimated based on the principal lunar and solar semi-diurnal components M_2 and S_2, respectively, defining the flow speed as a time-dependant function:

$$V_\infty(t) = M_2 \cos(\omega_{M2} t) + S_2 \cos(\omega_{S2} t), \tag{7.8}$$

where ω_{M2} and ω_{S2} are the frequencies of the lunar and solar forces acting on the tides, corresponding to periods of 12.42 and 12 hours, respectively. M_2 and S_2 are the amplitudes of the tidal speeds, where the peak spring tide flow speed $V_{SP} = M_2 + S_2$ and the peak neap tide flow speed $V_{NP} = M_2 - S_2$.

The average power and maximum thrust through the tidal cycle were calculated under quasi-steady assumptions, and are presented in fig. 7.16. The passive control strategies are compared with the speed control strategy defined in sec. 7.5.1, and with an idealised active pitch control case based on the speed-controlled Sch15B rotor with rigid blades below rated, and on the thrust and power at V_R for flow speeds above.

The results presented in fig. 7.16 show that the speed-controlled strategy with rigid blades has a higher average power, 29% and 24 % higher than the active pitch strategy at Pentland Skerries and Race of Alderney, respectively. Nevertheless, the

Table 7.3: Spring and neap tidal currents at two sites considered for tidal stream turbine deployment.

Site	**Mean spring peak** (V_{SP}) $[m/s]$	**Mean neap peak** (V_{NP}) $[m/s]$
Pentland Skerries	6.18	2.64
Race of Alderney	4.38	2.41

increase in power occurs at the cost of maximum thrust that exceeds the active pitch strategy by 162% and 146%, respectively.

Passive control strategy 1 is the closest strategy in performance to a rotor with active pitch control. It shows an average power production 2% below the idealised active pitch control strategy at the Pentland Skerries, and 3% below at the Alderney Race. The passive control 2 strategy shows an average power that exceeds the active pitch case by a 9% and 8% at each site. The closeness of the power production results, despite the passive deformation strategies resulting in sub-optimal performance below rated flow speed, is achieved by compensating for this loss by exceeding the rated power by ca. 12% and 37% for passive control 1 and 2 strategies, respectively, at cut-out speed.

The substantial power capping above rated shown by the passive control strategies is linked to a moderate increase in maximum thrust, defined from design, compared to the active pitch strategy. The passive control 1 strategy shows a maximum thrust 11% (9%) higher than the active pitch case, while the passive control 2 shows an excess of 20% (18%) above the idealised active pitch strategy for a rotor located at the Pentland Skerries (Race of Alderney).

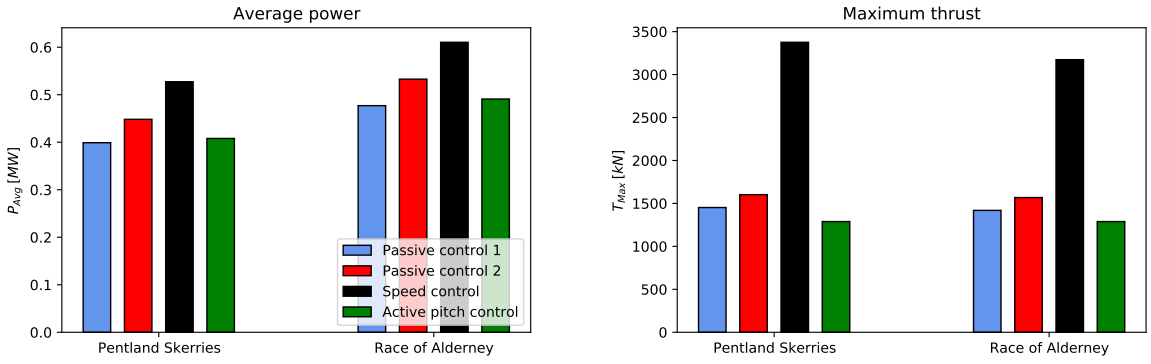

Figure 7.16: Results comparing the four different strategies at two different sites

7.6 Conclusions

The results presented in this work suggest that the hydrodynamics of flapwise and twist deformations on axial-flow rotor blades can be approximated to be independent of each other for moderate blade deflections.

The spanwise forces on a blade undergoing coupled flapwise and twist deflections are typically dominated by twist deformations. However, the inboard load augmentation and near-tip load shedding, characteristics of flapwise-only cases, were also found in cases with coupled deformations. The analysis of blade forces revealed that no significant couplings or interaction effects between the deformation components occur for moderate blade deflection. The results presented in this work suggest that the forces on a blade with coupled deformations can be estimated based on flapwise-only and twist-only force distributions.

In terms of the constituent of BEM models, we observed that the relationship between thrust coefficients and axial induction factors had no significant impact from either flapwise nor twist deformations. On the contrary, the two dimensional lift and drag coefficients displayed some influence from the deformation components. Twist deflections affect lift and drag simply through changes in angle of attack, while flapwise deformations change the functional relationship between the lift and drag coefficients with angle of attack. No significant interactions were observed, and twist deformations in presence of flapwise deformations did not induce deviations from the lift and drag functions corresponding to a specific flapwise deformation.

Despite the changes in polar coefficients caused by the flapwise deformations, which are a consequence of changes in the chordwise pressure distribution, flapwise deformations do not affect significantly the location of the hydrodynamic centre of pressure, which was shown to be dominated by twist and rotational speed (i.e. changes in angle of attack).

Based on the hydrodynamic independence hypothesis for the twist and flapwise deformation, the hydrodynamic performance of turbine blades with passively-controlled load alleviation was investigated to determine the range of flapwise and twist deformations required to satisfy turbine thrust and power objectives.

A parameter space of tip-speed ratio, flapwise and twist deformations was constructed based on the available flapwise-only and twist-only simulations, and explored by designing two control paths for passive blade deformation strategies. These strategies showed a substantial power capping above rated flow speed and maximum thrust reductions driven by blade deformations. These results suggest that passive control strategies are a potential alternative for tidal rotors as a replacement for, e.g., active pitch systems.

The passive strategies highlighted the importance of considering both the twist and flapwise deformation hydrodynamics. While turbine performance is dominated by twist deformations, the flapwise component showed a significant impact on power above rated flow speed, shedding an equivalent of up to 22% of power at cut-out for one of the strategies investigated.

Finally, the independence of the flapwise and twist hydrodynamics for moderate deformations offers potential for the development of improved design methods. Twist deformations, largely reflected in changes in angle of attack, are well-suited for representation in low-cost BEM models. Flapwise deformations could be included in computations either by using empirical corrections or by performing a reduced set of CFD simulations. This could enable a coupled hydrodynamic and structural design of rotors incorporating passive control strategies.

References

[1] Andritz Hydro Hammerfest. *Renewable energy from tidal currents*. `https://www.andritz.com/resource/blob/61614/cf15d27bc23fd59db125229506ec87c7/hy-hammerfest--1--data.pdf`. Accessed:2021-06-23.

[2] Atlantis Resources. *AR1500 tidal turbine*. `https://simecatlantis.com/wp-content/uploads/2016/08/AR1500-Brochure-Final-1.pdf`. Accessed:2021-06-23.

[3] Y. Bazilevs et al. "3D simulation of wind turbine rotors at full scale. Part II: Fluid-structure interaction modeling with composite blades". In: *International Journal for Numerical Methods in Fluids* (2011), 65:236–254.

[4] Black and Veatch. *UK Tidal Stream Energy Resource Assessment*. Tech. rep. Carbon Trust, 2005.

[5] M. L. Buhl. "A New Empirical Relationship between Thrust Coefficient and Induction Factor for the Turbulent Windmill State A New Empirical Relationship between Thrust Coefficient and Induction Factor for the Turbulent Windmill State". In: *Technical Report NREL/TP-500-36834* August (2005).

[6] T. Burton et al. *Wind energy handbook*. John Wiley & Sons, 2011.

[7] W. C. De Goeij, M. J. L. Van Tooren, and A. Beukers. "Implementation of bending-torsion coupling in the design of a wind-turbine rotor-blade". In: *Applied Energy* 63.3 (1999), pp. 191–207.

[8] S. Draycott et al. "An experimental investigation into non-linear wave loading on horizontal axis tidal turbines". In: *Journal of Fluids and Structures* 84 (2019), pp. 199–217.

[9] V. Fedorov and C. Berggreen. "Bend-twist coupling potential of wind turbine blades". In: *Journal of Physics: Conference Series*. Vol. 524. 1. IOP Publishing. 2014.

[10] C. Grinderslev et al. "Wind turbines in atmospheric flow: fluid–structure interaction simulations with hybrid turbulence modeling". In: *Wind Energy Science* 6.3 (2021), pp. 627–643.

[11] D. M. Grogan et al. "Design of composite tidal turbine blades". In: *Renewable Energy* 57 (2013), pp. 151–162.

[12] G. D. Hastie et al. "Harbour seals avoid tidal turbine noise: Implications for collision risk". In: *Journal of Applied Ecology* 55.2 (2018), pp. 684–693.

[13] J. Jonkman. "The new modularization framework for the FAST wind turbine CAE tool". In: *51st AIAA Aerospace Sciences Meeting including the New Horizons Forum and Aerospace Exposition*. 2013, p. 202.

[14] J. M. Jonkman et al. "AeroDyn v15 users guide and theory manual". In: *NREL Draft Report* (2015).

[15] T. J. Larsen and A. M. Hansen. "How 2 HAWC2, the user's manual". In: (2007).

[16] V. P. Le Diagon et al. “Increased reliability of tidal turbines thanks to a better knowledge of realistic tidal conditions, use of RAM analysis, advanced monitoring, maintenance strategies and intelligent design components”. In: *Proceedings of the Fourteenth European Wave and Tidal Energy Conference*. EWTEC. 2021.

[17] D. W. Lobitz and P. S. Veers. “Load mitigation with bending/twist-coupled blades on rotors using modern control strategies”. In: *Wind Energy: An International Journal for Progress and Applications in Wind Power Conversion Technology* 6.2 (2003), pp. 105–117.

[18] C. N. H. Lock, H. Bateman, and H. C. H. Townend. *An extension of the vortex theory of airscrews with applications to airscrews of small pitch, including experimental results*. HM Stationery Office, 1926.

[19] J. Locke, U. Valencia, and K. Ishikawa. “Design studies for twist-coupled wind turbine blades”. In: *ASME 2003 Wind Energy Symposium*. American Society of Mechanical Engineers. 2003, pp. 324–331.

[20] J. Y. Luo and A. D. Gosman. “Prediction of impeller-induced flow in mixing vessels using multiple frames of reference”. In: INSTITUTE OF CHEMICAL ENGINEERS SYMPOSIUM SERIES. 1994.

[21] F. R. Menter. “Two-equation eddy-viscosity turbulence models for engineering applications”. In: *AIAA journal* 32.8 (1994), pp. 1598–1605.

[22] F. R. Menter, M. Kuntz, and R. Langtry. “Ten Years of Industrial Experience with the SST Turbulence Model”. In: *Turbulence Heat and Mass Transfer 4* 4 (2003), pp. 625–632.

[23] I. A. Milne et al. “The characterisation of the hydrodynamic loads on tidal turbines due to turbulence”. In: *Renewable and Sustainable Energy Reviews* 56 (2016), pp. 851–864.

[24] R. E. Murray et al. “Passively adaptive tidal turbine blades: Design tool development and initial verification”. In: *International Journal of Marine Energy* 14 (2016), pp. 101–124.

[25] R. Nicholls-Lee. “Adaptive Composite Blades for Horizontal Axis Tidal Turbines”. PhD thesis. University of Southampton, 2011.

[26] S. A. Ning. “A simple solution method for the blade element momentum equations with guaranteed convergence”. In: *Wind Energy* 17.9 (2014), pp. 1327–1345.

[27] Orbital Marine Power. *Orbital O2 2MW*. `https://orbitalmarine.com/O2`. Accessed:2021-06-23. 2021.

[28] S. Ordonez-Sanchez et al. “Analysis of a horizontal-axis tidal turbine performance in the presence of regular and irregular waves using two control strategies”. In: *Energies* 12.3 (2019), p. 367.

[29] W. Ostachowicz et al. *MARE-WINT: new materials and reliability in offshore wind turbine technology*. Springer Nature, 2016.

[30] B. Polagye and J. Thomson. *Screening for biofouling and corrosion of tidal energy device materials: in-situ results for admiralty inlet, puget sound, Washington*. Tech. rep. 1. Northwest National Marine Renewable Energy Center, 2010.

[31] R. Rafiee, M. Tahani, and M. Moradi. "Simulation of aeroelastic behavior in a composite wind turbine blade". In: *Journal of Wind Engineering and Industrial Aerodynamics* 151 (2016), pp. 60–69.

[32] J. Schluntz and R. H. J. Willden. "The effect of blockage on tidal turbine rotor design and performance". In: *Renewable Energy* 81 (2015), pp. 432–441.

[33] G. Smart and M. Noonan. *Tidal Stream and Wave Energy Cost Reduction and Industrial Benefit: Summary Analysis*. Tech. rep. ORE Catapult, 2018.

[34] Vivid Economics et al. "Energy Innovation Needs Assessment: Tidal Stream". In: (2019).

[35] A. Wimshurst, C. Vogel, and R. Willden. "Cavitation limits on tidal turbine performance". In: *Ocean Engineering* 152.February (2018), pp. 223–233.

[36] A. Wimshurst and R. H. J. Willden. "Computational observations of the tip loss mechanism experienced by horizontal axis rotors". In: *Wind Energy* 21.7 (2018), pp. 544–557.

[37] A. Wimshurst and R. H. J. Willden. "Extracting lift and drag polars from blade-resolved computational fluid dynamics for use in actuator line modelling of horizontal axis turbines". In: *Wind Energy* 20.5 (May 2017), pp. 815–833. arXiv: `arXiv:1006.4405v1`.

[38] A. Wimshurst and R. H. J. Willden. "Tidal power extraction on a streamwise bed slope". In: *Ocean Engineering* 125 (2016), pp. 70–81.

[39] F. Zilic de Arcos, G. Tampier, and C. R. Vogel. "Numerical analysis of blockage correction methods for tidal turbines". In: *Journal of Ocean Engineering and Marine Energy* 6.2 (2020), pp. 183–197.

[40] F. Zilic de Arcos, C. R. Vogel, and R. Willden. "A parametric study on the hydrodynamics of tidal turbine blade deformation". In: *Journal of Fluids and Structures* (2021). In press.

[41] F. Zilic de Arcos, C. Vogel, and R. Willden. "Hydroelastic modelling of composite tidal turbine blades". In: *Advances in Renewable Energies Offshore: Proceedings of the 3rd International Conference on Renewable Energies Offshore (RENEW 2018), October 8-10, 2018, Lisbon, Portugal*. 2018, p. 877.

[42] F. Zilic de Arcos, C. Vogel, and R. Willden. "Extracting angles of attack from blade-resolved rotor CFD simulations". In: *Wind Energy* 23.9 (2020), pp. 1868–1885.

Part IV

Observations on the engineering modelling of tidal rotors

8 Blade Element Momentum Theory

8.1 Introduction

This chapter provides the theoretical and engineering modelling background that supports the last part of this thesis, wherein an analysis of transient loads on floating tidal rotors is presented. This chapter reviews blade element momentum theory in conjunction with the observations made from the blade-resolved CFD simulations from previous chapters, and serves as a transition towards improving the engineering modelling of a tidal rotor.

The interest in engineering models arises from the need to analyse large and complex cases such as rotors operating under transient environmental loads, fluid-structure interaction cases where blade deformations play an important role in rotor thrust and performance, or tidal rotors mounted on floating platforms. In all these cases, the computational cost of blade-resolved CFD is often prohibitively high, normally limiting the number of modelled cases to just a few of short duration.

In light of these computational limitations, engineering models, often based on simplifications of complex phenomena and empirical corrections, are still a fundamental element of engineering practice. This is especially relevant for the study of devices operating at sea where, due to the nature of the environment and

range of conditions experienced over device lifetime, a large number of cases with combined environmental and operational loads must be analysed.

Blade element momentum (BEM) models are probably the best example of engineering models for rotor blades, being widely used in both academia and industry to calculate loads and performance of axial-flow rotors. Most modern implementations are based on the classic work of Glauert [14], a model that stems initially from the slipstream momentum theory developed by Rankine [30] and the blade element model proposed by Froude [12]. Glauert presents the problem as a system of two-dimensional blade element and momentum equations, both of which are solved over a series of concentric annuli across a rotor. The flow is described by the axial and tangential momentum balance across an actuator disc, where the influence of the rotor is captured as an opposing force that changes the axial and tangential flow speeds (i.e. it induces velocities that are represented by axial and tangential induction factors), and the rotor blades which are modelled as a collection of two-dimensional aerofoils. The aerofoil forces and performance are then determined by the local relative flow speed and angle of attack, which depend on the induced velocities and blade characteristics [16].

The BEM method has been expanded to account for fluid-dynamic effects that were not considered in its basic formulation, increasing the model's fidelity and predictive capabilities. Possibly two of the most notable advances in this regard are the introduction of a correction for the finite number of blades [3, 28], and the correction of the momentum equation for high axial induction factors [16]. Other recent developments for axial-flow rotors include: enhancements in tip-loss modelling (e.g. Shen et al. [31], Wimshurst and Willden [35]); spanwise modifications to the two-dimensional polar coefficients to account for rotational effects [2]; blockage [33]; yawed flows [18]; and the inclusion of other transient flow effects [10]. BEM theory is widely employed in industry, is still an active area of research, and there is still significant scope for improvement.

The following sections present an analysis of a BEM model with comparison to blade-resolved simulations. This allows some of the shortcomings and causes for

accuracy losses in BEM when modelling highly-loaded tidal rotors to be identified, as well as highlighting potential improvements.

8.2 Model fundamentals

Ning [25] proposed an alternative formulation to Glauert's original derivation. Instead of manipulating the blade element and momentum equations to derive a system of two equations for the axial and tangential induction factors, Ning proposed a parametrisation of the equations based only on the inflow angle ϕ. The derivation starts from the definition of the thrust coefficient, defined not as a whole-rotor coefficient but for each annulus, both in terms of the blade element and momentum models:

$$C_T = \left(\frac{1-a}{\sin\phi}\right)^2 C_x\sigma \tag{8.1}$$

$$C_T = 4a(1-a)T_L \tag{8.2}$$

where a is the axial induction factor, C_x the normal force coefficient, σ the local blade solidity, and T_L a tip-loss correction [1]. Equating eqs. 8.1 and 8.2 and solving for a leads to:

$$a(\phi) = \frac{\kappa(\phi)}{(1+\kappa(\phi))} \tag{8.3}$$

with

$$\kappa(\phi) \equiv \frac{\sigma C_x(\phi)}{4T_L(\phi)\sin^2(\phi)} \tag{8.4}$$

Analogously, the tangential induction factor a' is defined by equating the torque predicted by the momentum and blade element theories:

$$a'(\phi) = \frac{\kappa'(\phi)}{(1-\kappa'(\phi))} \tag{8.5}$$

$$\kappa'(\phi) \equiv \frac{\sigma C_\theta(\phi)}{4T_L(\phi)\sin(\phi)\cos(\phi)} \tag{8.6}$$

[1] Note that σ and T_L are referenced as σ' and F, respectively, in the work of Ning [25].

where C_θ is the tangential force coefficient.

The axial and tangential inductions, functions of the inflow angle, are related by the following geometric relationship:

$$\tan(\phi) = \frac{1-a}{(1+a')\lambda_r} \tag{8.7}$$

where $\lambda_r = \omega r/V_\infty$ is the local tip-speed ratio, ω the rotational speed, r the local radius and V_∞ the undisturbed flow velocity. Finally, rearranging Eq. 8.7 as a residual function, it is possible to find a solution for ϕ that satisfies the residual equation:

$$f(\phi) = \frac{\sin(\phi)}{(1-a)} - \frac{\cos(\phi)}{(1+a')\lambda_r} = 0 \tag{8.8}$$

Ning's derivation of this BEM implementation includes Prandtl's tip-loss correction and Buhl [7] empirical momentum model for high axial inductions when $a > 0.40$ [25], two constituents of this model discussed in the following sections.

The advantage of this implementation of the BEM model lies on Ning's mathematical proof for the existence of an angle ϕ that fulfills eq. 8.8 and in the solution of a single residual equation rather than a system for the axial and tangential induction factors, as required in other derivations of the BEM model (e.g. Burton et al. [8]). Solving a single equation enables the use of fast and robust root-finding algorithms, guaranteeing the convergence to a solution for the entire span of the blade. Further details about the model derivation, implementation, and the mathematical proof for the existence of a solution ϕ to eq. 8.8 can be found in the original reference [25].

8.3 Empirical momentum model

A deficiency in the axial momentum model (eq. 8.2) was acknowledged by Glauert while comparing analytical model predictions with experiments. The analytical equation predicts a parabolic relationship between thrust coefficient and the axial induction factor, with a maximum $C_T = 1.0$ at $a = 1/2$. In practice, however, empirical evidence shows an increase in thrust well past the maximum defined by

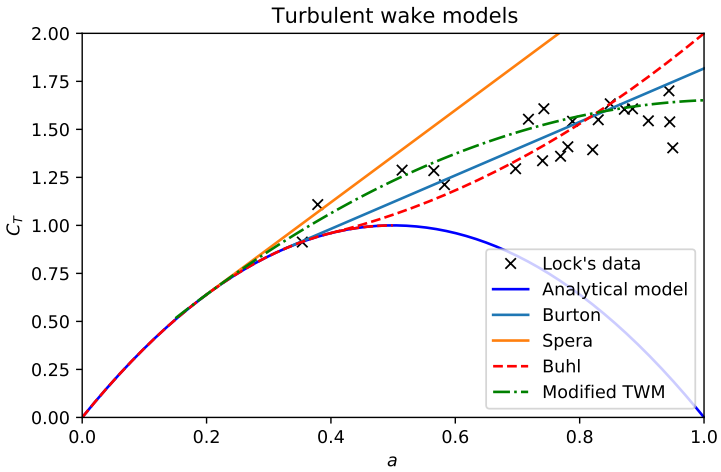

Figure 8.1: Comparison of different momentum models with turbulent wake correction with CFD and empirical data. Lock's empirical data is reproduced from [7].

momentum theory [15]. This increase in thrust occurs due to viscous effects on wake behaviour that drive a turbulent state characterised by the onset of large vortices and flow recirculation.

Glauert proposed a Turbulent Wake Model (TWM), an empirical correction to the momentum equation for high inductions based on the experimental data published by Lock et al. [23]. Following Glauert's work, other models have been proposed, including Buhl [7], Burton et al. [8] and Spera [32]. Buhl's TWM is identical to Glauert's except that it guarantees smoothness and continuity between the analytical and empirical $C_T(a)$ functions in the presence of a tip-loss correction. The Burton and Spera models are linear functions tangent to the analytical C_T at different axial induction factors ($a = 0.326$ and $a = 0.200$, respectively). These models can be seen in fig. 8.1 alongside with Lock's data reproduced from [7].

Buhl's empirical model was selected for this work since it was used by Ning [25] in the derivation of his BEM formulation, as well as more widely in AeroDyn v15 [20], part of the FAST/OpenFAST framework [19]. AeroDyn and OpenFAST are open source analysis suites for wind turbine modelling, and have been extensively validated and used in both industry and academia (e.g. Guntur et al. [17], Driscoll et al. [11]).

The general expression for Buhl's momentum model consists in a function with two branches, separated by a critical induction factor a_c. When the induction factor

is small, the momentum equation corresponds to the analytical model, whereas when the induction factor is above a_c, an empirical formulation is used:

$$C_T = \begin{cases} b_0 + b_1 a + b_2 a^2 & \text{if } a \geq a_c, \\ 4a(1-a)T_L & \text{if } a < a_c \end{cases} \tag{8.9}$$

with b_0, b_1 and b_2 empirical constants. The continuity and smoothness constraints are imposed by enforcing the value and first derivatives between the two models in eq. 8.9 at a_c, where the transition between functions occurs. These continuity and smoothness constraints then lead to:

$$b_2 = 4T_L(1-2a_0) - 2b_1 a_0 \tag{8.10}$$

$$b_3 = 4T_L a_0(1-a_0) - b_1 a_0^2 - b_2 a_0 \tag{8.11}$$

with b_1 a free variable that can be fitted to empirical data or determined otherwise. Buhl, instead of directly fitting the data, closed the system by further assuming that $C_T(1) = 2.0$, and determined a value of $a_c = 0.40$ for the transition between models.

Despite the widespread acceptance of this TWM as part of OpenFAST, this does not guarantee accurate predictions for highly-loaded tidal rotors. Wind turbines normally operate at relatively low induction factors (e.g. the DTU 10 MW rotor is designed to operate at an axial induction factor in the order of 0.30 [29], the AVATAR rotor at around 0.24 [29], and the MEXICO rotor at approximately 0.26 [40]), an operational regime at which the empirical function is unlikely to be triggered. Tidal turbines, on the contrary, are more likely to operate at high thrust regimes, and thus are prone to larger errors when modelled using BEM methods.

8.3.1 Corrections to the empirical momentum model

Lock's data, used by Glauert and Buhl as the basis for the derivation of their empirical momentum models, show a significant scatter, attributed to the unsteadiness of this operational regime [9]. Alongside the complex fluid-mechanics of the turbulent wake regime, however, the challenge and uncertainty of extracting flow data from

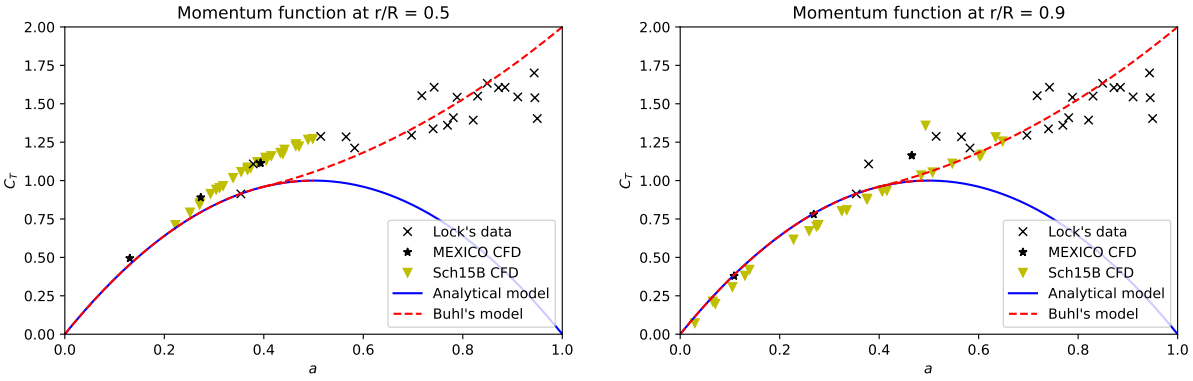

Figure 8.2: Comparison between the momentum functions with Lock's experiments (black crosses, reproduced from Buhl [7]) and available CFD data at two radial locations. The CFD data includes the Sch15B results under different twist deformations and at four tip-speed ratios (yellow triangles), and the MEXICO data at three tip-speed ratios (black stars). The analytical and empirical models are provided with no tip-loss correction to highlight the impact of tip proximity on the empirical results.

experiments must also be acknowledged. These challenges are not only due to the problem of sampling the flow around spinning blades in terms that are compatible with the BEM framework, such as axial inductions, but also due to the dependency of the axial induction on axial and radial coordinates, as discussed in chapter 5.

Additional insight into the turbulent wake models can be provided by utilising the available blade-resolved CFD simulations, summarised in chapter 4.2. The SAM flow-sampling method, described in section 5, allows the extraction of induction factors over the span of the blade in a consistent manner, while the thrust coefficients can be easily calculated by integrating pressure and shear stress on the blades.

The result of the analysis can be seen in fig. 8.2. This shows a comparison between CFD data, Lock's experimental data, the analytical momentum function and Buhl's empirical model. The CFD data in fig. 8.2 corresponds to the Sch15B and MEXICO datasets. The Sch15B cases are those simulated at a blockage ratio $B = 0.04$, at different tip-speed ratios ($\lambda \in \{4.00, 5.00, 6.00, 7.00\}$) and under the different available twist deformations. The cases for the MEXICO rotor correspond to those simulated by Wimshurst and Willden [37] at three tip-speed ratios ($\lambda \in \{4.17, 6.67, 10.00\}$) with no blade deformations. The CFD data is presented at two different radial locations: at the middle of the span ($r/R = 0.50$),

and in close proximity to the tip ($r/R = 0.90$). The momentum models are presented without tip-loss corrections to show the impact of tip proximity on the CFD results.

Note that the cases where the Sch15B rotor had flapwise deformation were omitted from fig. 8.2 given the augmented near-tip losses discussed in chapter 6.

The plot around the inboard section in fig. 8.2 shows that divergence between the analytical momentum function and the empirical data occurs much earlier than the transition $a_c = 0.40$ used by Buhl. This value of a_c, however, is unlikely to affect the accuracy of BEM modelling at the low induction factors at which wind rotors typically operate, which may explain why the performance prediction for such devices might not be adversely affected during model validation. However, the difference between the empirical data and the analytical model increases with the induction factor and, at the operational regime where the Sch15B rotor was analysed, the difference is significant.

The results at $r/R = 0.9$ shows how the sectional thrust coefficients decrease as the tip of the rotor is approached. This effect occurs due to the tip-loss effects and would normally be captured, within most BEM implementations, by a tip-loss factor T_L. The T_L factor acts in Ning's BEM by scaling the momentum model function, as shown in eq. 8.9. Note that no tip-loss correction has been used to plot the curves in fig. 8.2.

The CFD data shows lower scatter than Lock's experiments, possibly due to the more highly controlled flow sampling achievable on the simulated flow and the nature of the simulations (e.g. steady-state solution and the lack of discrete fluctuations due to the use of a turbulence model), with only one outlier observed on the Sch15B simulations. Interestingly, and although generalisation is limited by the available data, both the Sch15B and the MEXICO data points appear to align well with each other, with the exception of the highest induction case for the MEXICO rotor at $r/R = 0.9$, and the aforementioned outlier of the Sch15B rotor. The discrepancies at high inductions are likely to be related to larger tip-loss effects on the Sch15B rotor, and highlight the complexity of near-tip flows, especially under turbulent wake regimes.

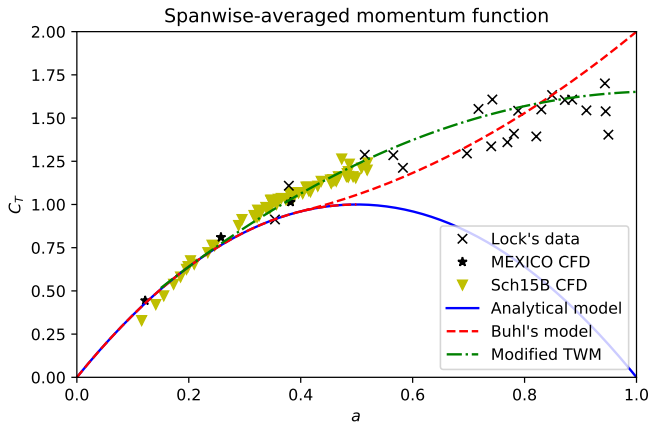

Figure 8.3: Comparison of the momentum models with CFD and empirical data. The Sch15B data includes the cases simulated with and without twist deformation. The Sch15B and MEXICO cases include the tip-speed ratios described in chapter 5. Lock's empirical data is reproduced from [7].

A simple modification to Buhl's empirical model is proposed based on the available data. This model was derived using the spanwise-averaged axial induction factors and thrust coefficients from the full Sch15B dataset (including the cases with flapwise-only and coupled deformations), the spanwise-averaged MEXICO data and Lock's empirical data. Given the uncertainties in other parts of the model (including the influence of rotor design; tip and root losses; spanwise variations of lift and drag coefficients [2, 37, 40]; stall delay effects [6], among others), the average across results is considered to provide the best approximation. Thus, taking $a_c = 0.20$ and fitting the free variable on the empirical equation in eq. 8.9 to the aforementioned data with the least-squares method, leads to $b_1 = -1.06$.

The modified empirical model for the turbulent wake regime is plotted in fig. 8.3 alongside with the data used for fitting the modified model. This new TWM provides a better agreement with the CFD data than Buhl's original model, addressing the discrepancy at axial induction factors between 0.30 and 0.60.

Modifying the TWM affects the BEM results for thrust and torque on the Sch15B rotor. Fig. 8.4 shows a comparison between the thrust and power coefficients calculated with Ning's BEM implementation using Buhl's momentum model (labelled as Standard BEM), using the modified TWM (labelled as Modified

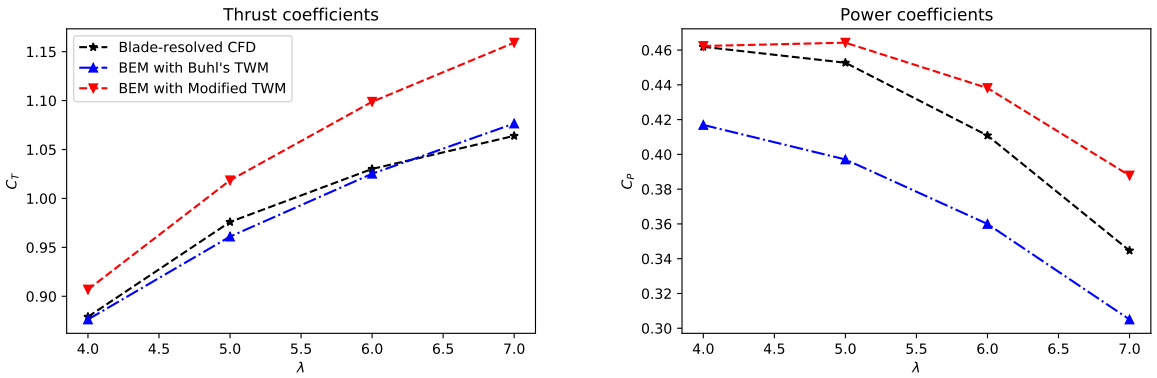

Figure 8.4: Thrust and power coefficients calculated for the Sch15B rotor with blade-resolved CFD, BEM with Buhl's turbulent wake empirical model [7, 25] and BEM with the modified TWM.

TWM BEM), and the blade-resolved CFD results for verification. Two-dimensional lift and drag coefficients, calculated with RANS CFD and extracted from Zilic de Arcos et al. [39], were used for the BEM computations.

A first inspection of the integrated power and thrust reveals an apparently good agreement between the standard BEM and the CFD results for C_T (relative error in the range of 0.3% to 1.2%) which is adversely affected by changing the TWM (relative error increases to 3.2% to 9.0%), while C_P shows a relatively poor agreement for both BEM results compared with CFD, with both cases showing a maximum relative error in the order of 12%. The integrated quantities, however, hide the poor predictions generated by the standard BEM, as can be observed in the spanwise force distributions plotted in fig. 8.5.

The small differences in C_T between the standard BEM and the CFD simulations are a consequence of a substantial overestimation of the loads near the tip (i.e. due to deficiencies of the tip-loss model) in conjunction with consistent underestimation of the loads through the inboard sections of the blade. The two opposing errors cancel each other, leading to a coincidental and misleading agreement in thrust coefficient for this particular rotor.

A substantial improvement in the predictions of the spanwise thrust and torque distributions is observed using the modified TWM. This improvement is seen at the inboard sections of the blade for both thrust and torque ($r/R \leq 0.70$),

while differences due to a deficient tip-loss modelling near the tip leads to an overestimation of both C_T and C_P. These deficiencies in tip-loss modelling will be discussed in more detail in sec. 8.4.

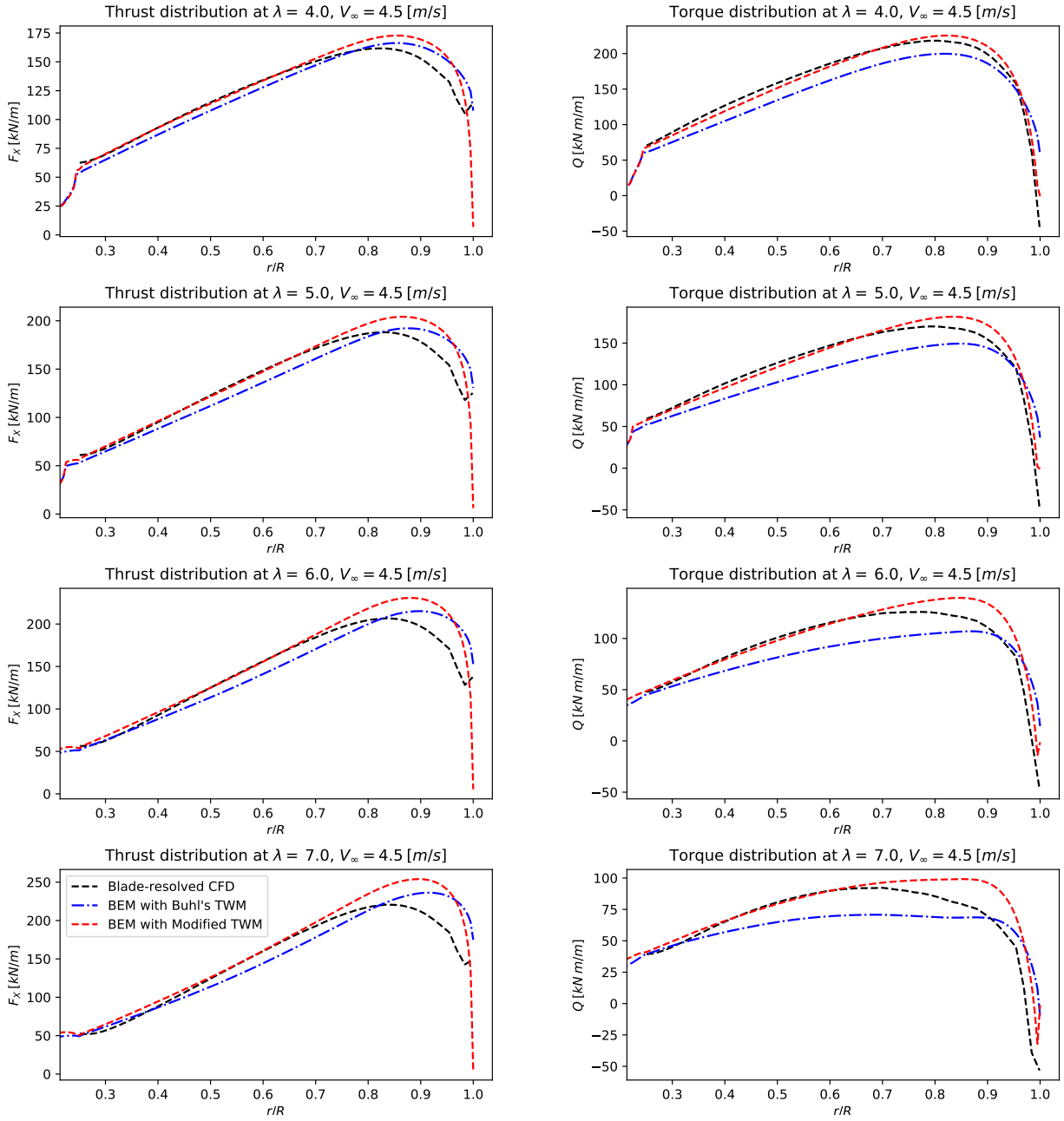

Figure 8.5: Comparison of the spanwise thrust (left column) and torque (right column) distributions for different tip-speed ratios λ calculated for the Sch15B rotor with blade-resolved CFD, BEM with Buhl's TWM [7, 25] (Standard BEM), and a modified TWM.

8.4 Tip-loss modelling

Thrust and torque distributions along the blade are generated by the pressure difference between the suction and pressure sides of the blade. Along much of the blade the flow remains largely two-dimensional. As the blade tip is approached, however, the fluid on the pressure side is driven towards the suction side, creating spanwise flows, vorticity shedding, pressure equalisation between both sides of the blade and consequently a reduction in thrust and torque as the tip is approached. The aggregated effect of these phenomena are often termed the tip losses.

Wimshurst and Willden [36] explains tip losses as a consequence of two main effects. Firstly, the vorticity shed from the tip causes a down-wash which reduces the effective angle of attack on the near-tip sections. Secondly, the pressure difference between the suction and pressure sides of the blade induce spanwise flows on both sides of the blade, transporting momentum and affecting the magnitude and shape of the pressure distributions along the aerofoil chords. The authors note that, although there is a reduction in angle of attack, the phenomenon is essentially three-dimensional, making the concept of two-dimensional lift and drag less valid near the tip of a rotor blade.

Traditional BEM models only consider axial and rotational flow components with two-dimensional blade elements. The radial-flow and the vorticity shed from the rotor and the tip of the blade are, thus, neglected in classical formulations. To account for this modelling deficiency, several tip-loss correction models have been proposed. The most widespread family of corrections stem from the work of Prandtl [4, 28], based on vortex theory, which seek to account for the flow differences between an actuator disc (i.e. a rotor with an infinite number of blades), and a real rotor with a discrete number of blades within a BEM model. Different implementations include the expressions derived by Glauert [14] , Lindenburg [22], and Burton et al. [8], among others. A discussion about these different derivations is addressed by Branlard [5].

Prandtl's correction model forces the axial induction factor to 1 as the tip is approached. This brings the inflow angle to zero, in turn reducing the lift and

drag coefficients and, consequently, the forces near the tip. The trend obtained with this model is similar to the effects seen in real rotors. However, Prandtl-like corrections correct just for the finite number of blades and are based on idealised rotor assumptions which do not necessarily hold for real situations. Differences might be encountered in, e.g., wake expansion (neglected in Prandtl formulation), airfoil departure from two-dimensional blade section characteristics as observed for rotor flows with spanwise components, viscosity-driven effects at high-load operational regimes, or rotors operating with non-constant circulations.

Fig. 8.5 highlights the limitations of Prandtl's correction for the Sch15B rotor. Specifically, Prandtl's correction of the BEM model with modified TWM performs best at low λ, where the rotor is closest to its optimum C_P (see fig. 8.4) and axial induction factors are lowest. The magnitude of the near-tip divergence between BEM and CFD then increases with tip-speed ratio for both thrust and torque.

As previously mentioned, tip-loss effects are not only a consequence of changes in angle of attack, since they affect pressure distributions along the chord of the aerofoil sections near the tip. The radial flow and consequent changes in pressure directly impact the lift and drag coefficients, similarly to the the observations and discussions presented in chapter 6. Corrections to the polar coefficients, also referred to as performance corrections [5], have been proposed. Shen et al. [31], for example, introduced an empirical correction factor based on Glauert's expression of a tip-loss factor [14] with the addition of extra parameters to be calibrated with empirical data. Their correction factor is then applied both to the normal and tangential force coefficients, to indirectly correct the lift and drag coefficients. Wimshurst [34], however, observed differences between the correction factors required for thrust and torque while comparing actuator-line with blade-resolved CFD simulations. He proposed a correction based on Shen's model, using different coefficients for the thrust and torque directions. However, none of these two corrections recognise that part of the problem, from a practical perspective, lies on the radial position where the correction starts taking effect.

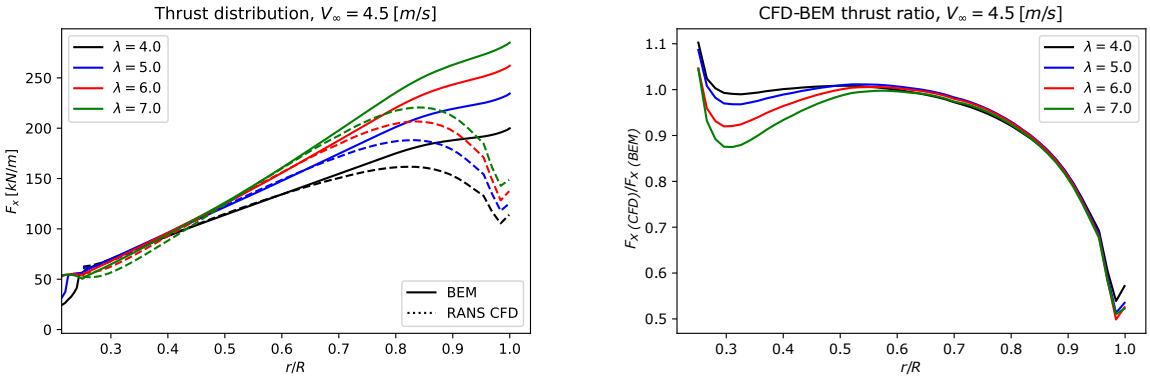

Figure 8.6: Left: Comparison between the spanwise thrust distributions calculated with blade-resolved CFD and BEM with no tip-loss correction. Right: Ratio between the thrust predicted by the blade-resolved CFD simulations and the BEM with no tip-loss correction. Both plots correspond to the Sch15B rotor at different tip-speed ratios.

Figure 8.6 shows a comparison between blade-resolved CFD and BEM thrust distributions, with the BEM results calculated without any tip-loss corrections and using the modified TWM. The plot on the left shows the thrust distributions calculated with both methods, showing that the models tend to start diverging from each other at approximately 65% of the span. The plot on the right presents the ratio between the CFD and BEM thrust distributions, showing the collapse of the curves at different tip-speed ratios in the tip region.

The Prandtl tip-loss factor, shown in fig. 8.7, not only is restricted to acting too close to the tip, but the radial onset of the correction moves outboard as λ, and therefore thrust, increases. However, this tip-loss model only corrects for having a finite number of blades on an actuator-disc representation, while tip losses include many other effects related to spanwise flows, vorticity and pressure equalisation.

The ratios between the CFD and BEM force distributions (fig. 8.6, right), which include the aforementioned flow effects, suggests that the spanwise onset of the corrections should not be affected by tip-speed ratio. Improving tip-loss modelling requires, then, the complete representation of three-dimensional tip-loss effects within a BEM framework, introducing further elements (and/or correction shapes) than just Prandtl's model, to correct for the implicit two-dimensional streamtube and foil assumptions of BEM.

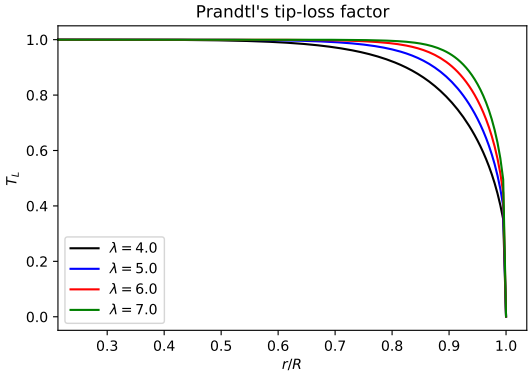

Figure 8.7: Prandtl's tip-loss factor calculated with BEM for the Sch15B rotor at different tip-speed ratios.

Despite the overestimation in tip loads predicted with Prandtl's tip loss models, the calculations presented in the following chapters make use of this correction model alongside with the modified turbulent wake. This decision is not due to the accuracy of Prandtl's model for tidal rotors, but to ensure the consistency and reproducibility of the results and methods presented. An engineering correction to improve the accuracy of the calculations could be attained by calibrating a correction model with the available CFD data. The simplest approach is to perform an *a posteriori* correction of thrust and torque based on the ratios in figure 8.6. An *in-the-loop* correction is also possible, as shown by Wimshurst and Willden [35], although a correction shape different than that of Prandtl's function, supported by a fluid-dynamics derivation, is still to be developed.

8.5 Blockage

Blockage can be defined as the aero- or hydrodynamic interaction between a body (e.g. an aerofoil, a ship or an axial-flow rotor) and its surrounding boundaries. The most basic form of blockage is normally described as the interaction between a body and the outer boundaries of a constrained flow. Other kinds of interference effects, such as the interaction between rotors in a wind or tidal farm [26], or the anisotropic interference between a tidal rotor and the free surface on an open-channel flow [21], can also be considered as forms of blockage.

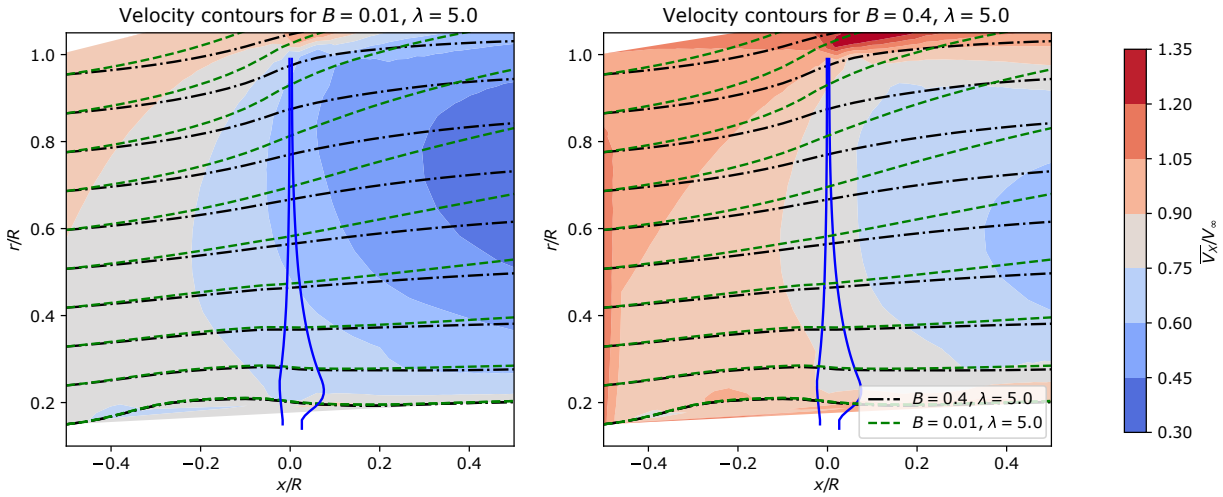

Figure 8.8: Azimuthally-averaged velocity contours and streamtubes extracted from the Sch15 rotor simulations, operating at a tip-speed ratio of $\lambda = 5.0$ at different isotropic blockage ratios and under equivalent upstream conditions.

The concept of blockage encompasses multiple flow effects, including an increased flow speed around the body due to confinement or interference, pressure changes on the wake, differences in flow development along lifting surfaces such as aerofoils, or even streamwise pressure gradients due to the boundary layer development on the external boundaries of a channel, among others [13, 27].

For the case of axial-flow rotors, blockage normally increases thrust and power for a given undisturbed velocity V_∞ and rotational speed, a change in loads which occurs due to an increased mass flow through the rotor. The change in mass flow is illustrated in fig. 8.8, which shows a comparison of the Sch15B rotor CFD simulations under two different blockage ratios. This figure highlights through-rotor streamtubes and azimuthally-averaged axial flow speeds at a tip-speed ratio of $\lambda = 5.0$. The plots also show the reduced expansion of the streamtubes in the high blockage case due to the constraining effects of the channel boundaries, as well as faster flow speeds through the rotor and bypass flows.

Blockage is a relevant factor for the design and operation of tidal rotors. However, most BEM models (e.g. Ning [25] or Burton et al. [8]) have been developed for wind energy applications and do not consider blockage effects. Vogel et al. [33] proposed a BEM implementation that incorporates blockage in its formulation through modifications to the momentum equations. This confined BEM incorporates

Prandtl's tip-loss correction model and the Buhl [7] turbulent wake model. The authors of this study showed an improvement in the predictive capabilities of their model compared with a standard BEM implementation when modelling a tidal rotor with blockage, although they recognise uncertainty regarding the turbulent wake model and the need for further studies in that area.

For the special case of axi-symmetric flows, where blockage can be characterised by the ratio between the swept area of the rotor and the cross-sectional area of the channel, methods have been developed to calculate correction factors. These corrections allow to convert the power and thrust coefficients of a rotor operating at a known condition (e.g. results calculated with BEM or experiments at a known blockage) into the corresponding coefficients at a different blockage ratio. Such methods are typically based on actuator disc and momentum theories, and rely on correcting the effective inflow velocity to modify C_P, C_T and λ.

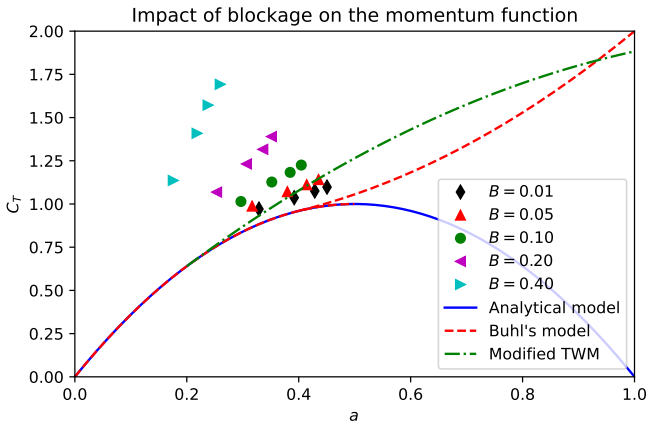

Figure 8.9: Impact of blockage on the relationship between thrust coefficient and axial induction factor for the Sch15B rotor.

Zilic de Arcos et al. [38] presented an evaluation of seven different blockage correction methods for axial-flow rotors. The benchmarking of these methods, six of them extracted from literature and one proposed by the authors, is based on blade-resolved CFD simulations of the Sch15B rotor. The rotor was simulated at different tip-speed ratios ($\lambda \in [4.0, 5.0, 6.0, 7.0]$) and at 5 different blockage ratios between 0.01 and 0.40. The conclusion of this work is that, for isotropic blockage

corrections, the methods proposed by [1] and [24], as well as the method proposed by the authors, are capable of accurately predicting the changes in λ, C_T and C_P due to blockage effects for the range of analysed cases. The work concludes that such methods can be used, for example, to correct performance predictions from different experimental facilities so they can be directly compared, or to determine the power and thrust of a rotor calculated with a standard BEM method under a specific blockage, but recognises limitations for non-isotropic blockage effects.

The CFD results available through the present study provide evidence regarding the impact of blockage on tidal rotor hydrodynamics. Fig. 8.9 shows the impact of blockage on the momentum function. This plot presents the $C_T(a, B)$ data points calculated from the Sch15B rotor CFD simulations of Zilic de Arcos et al. [38] at different blockage ratios, where the axial induction factors are spanwise-averaged. The CFD data is compared with Buhl's TWM and the modified TWM presented herein.

The $C_T(a, B)$ points in fig. 8.9 show that blockage has a significant impact on the relationship between thrust and the axial induction factor. The data shows an increase in thrust with increasing blockage, as well as a reduction in axial induction factors due to the increase in mass flow through the rotor. The data points, although limited, also suggest that the onset of the divergence between the empirical data and the analytical thrust function occurs at smaller a values as blockage increases.

Another interesting insight derived from the numerical simulations is the impact of blockage on the blade element sections. Fig. 8.10 shows the polar coefficients extracted with the SAM technique at three different span locations for the 5 different blockage ratios. Each simulated tip-speed ratio provides, at each spanwise location, a lift and drag value at an angle of attack that is calculated as part of the analysis of that flow simulation. The CFD results show a negligible effect of blockage on the lift and drag curves for all the analysed cases and throughout the entire range of available angles of attack for a given radial location. The spanwise location, however, shows a clear impact on lift and drag, a phenomenon which has been previously described in literature (see e.g. Wimshurst and Willden [37]).

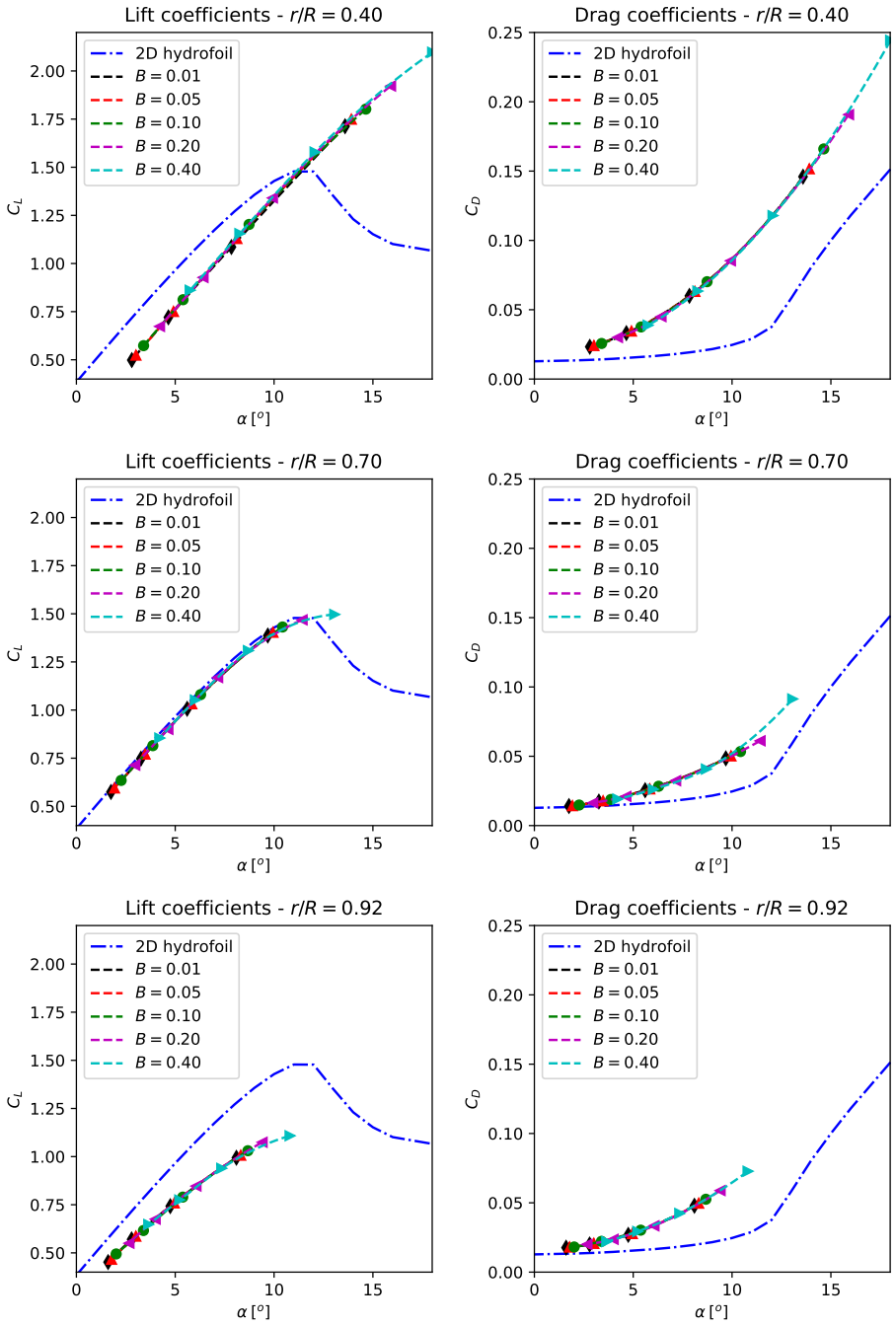

Figure 8.10: Impact of blockage on the lift and drag coefficients at different spanwise locations of the Sch15B rotor. 2D CFD simulated coefficients of a Risø-A1-24 aerofoil from [39] are plotted for reference.

Note that flapwise deformation, as dicussed throughout the part III of this thesis, showed a significant impact on the lift and drag coefficients. The changes in loads seen in bending blades were explained by changes in pressure concentrated on the suction surface and related to spanwise flows and wake expansion.

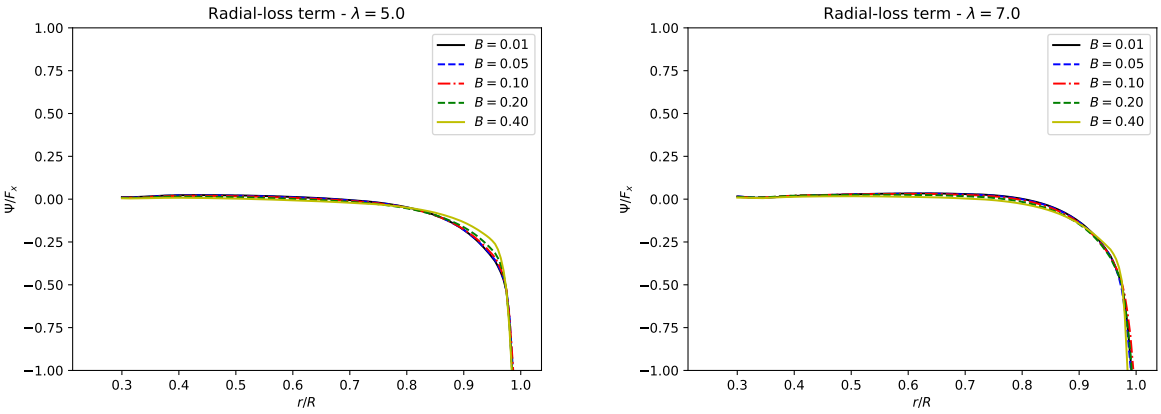

Figure 8.11: Radial loss on the Sch15B rotor at different blockages and tip-speed ratios.

On the contrary, for the case of blockage, the convergence between the C_L and C_D curves for different blockage ratios show that the changes in thrust and torque can be explained primarily through changes in angles of attack. This further explains the good performance of blockage corrections that correct the inflow speed to modify thrust, power and tip-speed ratio, as described by Zilic de Arcos et al. [38]. Furthermore, these results suggest that no further blockage-related corrections should be required on the blade-element part of a constrained BEM model such as presented by Vogel et al. [33].

As a final observation on blockage effects, fig. 8.11 shows the spanwise distribution of radial losses (see discussion in sec. 6.6.2.2) comparing the simulated blockage cases at two different tip-speed ratios. The results highlight a small effect of B on the shape of the spanwise radial-loss distribution for cases with low blockage. Despite the flow confinement, reduced streamtube expansion and, thus, overall reduction on spanwise three-dimensional flows across the rotor, the effects of blockage on the radial-loss do not appear to be large enough to justify modifications to tip-loss correction models for low and modest levels of blockage, $B \leq 0.2$.

References

[1] A. S. Bahaj et al. “Power and thrust measurements of marine current turbines under various hydrodynamic flow conditions in a cavitation tunnel and a towing tank”. In: *Renewable Energy* 32.3 (2007), pp. 407–426.

[2] G. Bangga et al. “CFD studies on rotational augmentation at the inboard sections of a 10 MW wind turbine rotor”. In: *Journal of Renewable and Sustainable Energy* 9.2 (2017), p. 023304.

[3] A. Betz. “Das Maximum der theoretisch möglichen Ausnützung des Windes durch Windmotoren”. In: *Zeitschrift für das gesamte Turbinenwesen* 26 (1920).

[4] A. Betz. “Schraubenpropeller mit geringstem Energieverlust”. In: *Gottinger Nachrichten* (1919), pp. 193–213.

[5] E. Branlard. “Tip-Losses with Focus on Prandlt’s Tip Loss Factor”. In: *Wind Turbine Aerodynamics and Vorticity-Based Methods*. Springer, 2017, pp. 227–245.

[6] S.-P. Breton, F. N. Coton, and G. Moe. “A study on rotational effects and different stall delay models using a prescribed wake vortex scheme and NREL phase VI experiment data”. In: *Wind Energy: An International Journal for Progress and Applications in Wind Power Conversion Technology* 11.5 (2008), pp. 459–482.

[7] M. L. Buhl. “A New Empirical Relationship between Thrust Coefficient and Induction Factor for the Turbulent Windmill State A New Empirical Relationship between Thrust Coefficient and Induction Factor for the Turbulent Windmill State”. In: *Technical Report NREL/TP-500-36834* August (2005).

[8] T. Burton et al. *Wind energy handbook*. John Wiley & Sons, 2011.

[9] C. Crawford. “Re-examining the precepts of the blade element momentum theory for coning rotors”. In: *Wind Energy: An International Journal for Progress and Applications in Wind Power Conversion Technology* 9.5 (2006), pp. 457–478.

[10] R. R. Damiani and G. Hayman. *The Unsteady Aerodynamics Module For FAST8*. Tech. rep. National Renewable Energy Lab.(NREL), Golden, CO (United States), 2019.

[11] F. Driscoll et al. “Validation of a FAST model of the statoil-hywind demo floating wind turbine”. In: *Energy Procedia* 94 (2016), pp. 3–19.

[12] W. Froude. “On the elementary relation between pitch, slip, and propulsive efficiency”. In: *Transactions of the Royal Institution of Naval Architects.* (1878).

[13] H. Glauert. “Wind Tunnel Interference on Wings, Bodies and Airscrews”. In: *Aeronautical Research Committee* 1566 (1933), pp. 1–52.

[14] H. Glauert. *Airplane propellers*. Springer, 1935.

[15] H. Glauert. *The analysis of experimental results in the windmill brake and vortex ring states of an airscrew*. Tech. rep. Aeronautical Research Committe Reports and Memoranda, Rept. 1026, 1926.

[16] H. Glauert. *The elements of aerofoil and airscrew theory*. Cambridge University Press, 1947.

[17] S. Guntur et al. “FAST v8 verification and validation for a MW-scale wind turbine with aeroelastically tailored blades”. In: *34th Wind Energy Symposium*. 2016, p. 1008.

[18] M. Hansen. *Aerodynamics of wind turbines*. 2nd ed. International Institute for Environment and Development, 2008.

[19] J. Jonkman. "The new modularization framework for the FAST wind turbine CAE tool". In: *51st AIAA Aerospace Sciences Meeting including the New Horizons Forum and Aerospace Exposition*. 2013, p. 202.

[20] J. M. Jonkman et al. "AeroDyn v15 users guide and theory manual". In: *NREL Draft Report* (2015).

[21] N. Kolekar, A. Vinod, and A. Banerjee. "On blockage effects for a tidal turbine in free surface proximity". In: *Energies* 12.17 (2019), p. 3325.

[22] C. Lindenburg. "Investigation into rotor blade aerodynamics". In: *Energy research Centre of the Netherlands (ECN) Wind Energy publication, ECN-C–03-025* (2003).

[23] C. N. H. Lock, H. Bateman, and H. C. H. Townend. *An extension of the vortex theory of airscrews with applications to airscrews of small pitch, including experimental results*. HM Stationery Office, 1926.

[24] R. Mikkelsen and J. N. Sørensen. "Modelling of Wind Turbine Blockage". In: *EWEC*. Paris, 2002.

[25] S. A. Ning. "A simple solution method for the blade element momentum equations with guaranteed convergence". In: *Wind Energy* 17.9 (2014), pp. 1327–1345.

[26] T. Nishino and R. H. J. Willden. "The efficiency of an array of tidal turbines partially blocking a wide channel". In: *Journal of Fluid Mechanics* 708 (2012), pp. 596–606.

[27] A. Pope and J. Harper. *Low-speed wind tunnel testing*. New York: John Wiley and Sons, 1966, p. 457.

[28] L. Prandtl. "Applications of modern hydrodynamics to aeronautics". In: *US Government Printing Office* (1921).

[29] H. Rahimi et al. "Evaluation of different methods for determining the angle of attack on wind turbine blades with CFD results under axial inflow conditions". In: *Renewable Energy* 125 (2018), pp. 866–876. arXiv: 1709.04298.

[30] W. J. M. Rankine. "On the mechanical principles of the action of propellers". In: *Transactions of the Institution of Naval Architects* 6 (1865).

[31] W. Z. Shen et al. "Tip loss corrections for wind turbine computations". In: *Wind Energy: An International Journal for Progress and Applications in Wind Power Conversion Technology* 8.4 (2005), pp. 457–475.

[32] D. A. Spera. *Wind Turbine Technology*. ASME Press, 1994.

[33] C. R. Vogel, R. H. J. Willden, and G. T. Houlsby. "Blade element momentum theory for a tidal turbine". In: *Ocean Engineering* 169 (2018), pp. 215–226.

[34] A. Wimshurst. "Tip flow corrections for horizontal axis wind and tidal turbine rotors". PhD thesis. University of Oxford, 2018.

[35] A. Wimshurst and R. H. J. Willden. "Analysis of a tip correction factor for horizontal axis turbines". In: *Wind Energy* 20.9 (2017), pp. 1515–1528.

[36] A. Wimshurst and R. H. J. Willden. "Computational observations of the tip loss mechanism experienced by horizontal axis rotors". In: *Wind Energy* 21.7 (2018), pp. 544–557.

[37] A. Wimshurst and R. H. J. Willden. "Extracting lift and drag polars from blade-resolved computational fluid dynamics for use in actuator line modelling of horizontal axis turbines". In: *Wind Energy* 20.5 (May 2017), pp. 815–833. arXiv: arXiv:1006.4405v1.

[38] F. Zilic de Arcos, G. Tampier, and C. R. Vogel. "Numerical analysis of blockage correction methods for tidal turbines". In: *Journal of Ocean Engineering and Marine Energy* 6.2 (2020), pp. 183–197.

[39] F. Zilic de Arcos, C. Vogel, and R. Willden. "Hydroelastic modelling of composite tidal turbine blades". In: *Advances in Renewable Energies Offshore: Proceedings of the 3rd International Conference on Renewable Energies Offshore (RENEW 2018), October 8-10, 2018, Lisbon, Portugal*. 2018, p. 877.

[40] F. Zilic de Arcos, C. Vogel, and R. Willden. "Extracting angles of attack from blade-resolved rotor CFD simulations". In: *Wind Energy* 23.9 (2020), pp. 1868–1885.

But where, after all, would be the poetry of the sea
were there no wild waves?

Joshua Slocum

9 Engineering modelling of transient flow effects

9.1 Introduction

Time-varying tidal currents, turbulence, shear, waves and floating rotor motions are likely to induce significant loads on rotor blades. Each phenomenon acts in different spatial and temporal scales and are strongly site-dependent, making their assessment difficult for practical engineering applications.

A utility-scale tidal rotor deployed at sea, operating for decades, will encounter a large number of combined wave and current conditions. These will range from typical operational conditions to events of extreme nature, involving irregular sea states with waves of different height and direction, and either opposing, following, or at an angle with a current which is continuously changing in speed, direction and turbulence levels. Modelling this type of problem is challenging, since the determination of statistically significant values of engineering importance (e.g. maximum stresses, significant accelerations, etc) during a storm event, for example, requires modelling time series in the order of tens of minutes to hours [2], and a large number of different events need to be analysed.

Modelling extended time series limits the potential use of high-fidelity methods for many practical engineering applications due to their computational cost. Thus,

engineering models are still likely to play an important role in the design and implementation of future tidal rotors, especially if industry aims towards rotors deployed in close proximity to the free surface.

Different BEM-based models have been proposed to account for dynamic phenomena. Specifically looking at the case of tidal rotors, models have been implemented to account for waves, shear, and turbulence. Faudot and Dahlhaug [3], for example, used a quasi-steady BEM model, a simplified added mass model and linear wave theory to account for wave effects on blade loading. They compared their model with tank experiments showing an adequate reproduction of the low-frequency wave loads in terms of integrated thrust and power, but determined that a steady BEM model is not sufficient for cases where the wave induced velocities are significant compared with the average current. Guo et al. [5] presented the validation of a BEM-based dynamic model. This model is a modified version of the dynamic BEM model of Hansen [6], and includes dynamic stall [7], dynamic wake [10], and added mass based on Morison's equation [8], as well as a PID (Proportional, Integral and Derivative) controller for blade rotation. They validated their model with tank experiments on a 1/25 scale rotor (0.80 m in diameter). Their model showed good agreement with the tank experiments for a relatively broad range of wave frequencies, heights and nacelle depths. Scarlett and Viola [11] and Scarlett et al. [12] proposed a different dynamic BEM-based model using a different dynamic stall model [13] and included waves, turbulence, shear and yaw. They validated the dynamic stall model with published results for the NREL S809 profile, and the steady state computations were compared with AeroDyn, showing good agreement for both cases. Their results highlight that waves are potentially the dominant source of transient loads.

Floating devices are likely to introduce an extra level of complexity to the transient loads problem. Prescribed rigid body motions of tidal turbines have been shown to induce transient loads of the same order of magnitude of those induced by, e.g., waves [9]. However, on a floating rotor, the motions are directly correlated

with wave characteristics and platform design. It is not yet clear what the combined effect of waves and the dynamic response of the floating platform and rotor will be.

The following sections show an evaluation of a slightly modified version of the model proposed by Guo et al. [5], referred to, in the following sections, as dynamic BEM. This engineering model was selected for analysing a floating tidal stream device in the last part of this thesis, given its extensive validation against wave experiments. The modifications were introduced by implementing the modified turbulent wake model, and by consideration of rigid body motion on the model formulation. The following sections present an analysis and verification of the model against published results, both experimental and from blade-resolved CFD computations.

9.2 Model description

The dynamic BEM model is based on the basic blade element momentum formulation discussed in the previous chapter. However, this dynamic BEM model has similarities with actuator-line models since flow speeds are determined at the time-dependent position of each blade section, rather than at averaged annuli. The momentum equations are, then, resolved on a fraction of the annular section (one-third for a three-bladed rotor) based on the undisturbed inflow velocity which considers current, waves, and relative motion. The time variable is introduced by the means of a dynamic inflow and a dynamic stall model.

Different reference frames are defined for this model: the foil section, where the axial and tangential velocities are resolved with respect to the rotor plane; the nacelle, around which the blades spin; the centre of mass of a floating platform or centre of rotation, around which rigid body rotations occur; and an inertial reference frame as the origin of coordinates. A diagram of the reference frames for a floating rotor is presented in fig. 9.1. Note that the six degrees of freedom representation of the rigid-body motions was presented in fig. 2.2.

The reference frame on the r_i foil section of blade B_j is related to the nacelle frame of reference by the rotation matrix R_Ω:

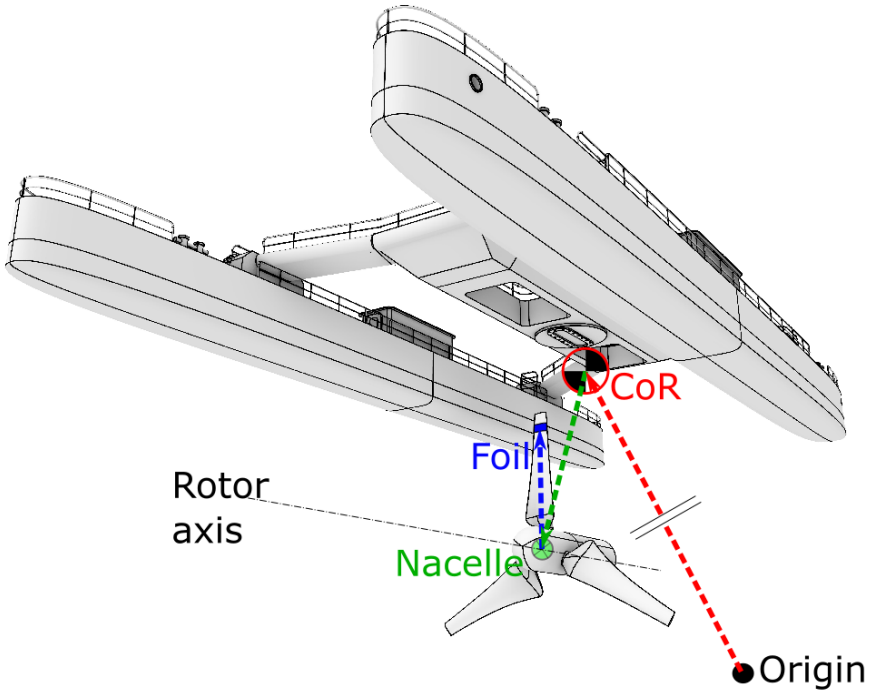

Figure 9.1: Diagram of the different frames of reference used in the dynamic BEM model.

$$\mathbf{R}_{\mathbf{\Omega_i}} = \begin{bmatrix} 1 & 0 & 0 \\ 0 & \cos\Omega_i & -\sin\Omega_i \\ 0 & \sin\Omega_i & \cos\Omega_i \end{bmatrix} \tag{9.1}$$

with Ω_i the azimuth angle of blade B_i.

Vectors on the nacelle reference frame are related to the global frame of reference by the rotational matrices of the Euler-angle representation of the body-fixed reference frame:

$$\mathbf{R}_{\mathbf{\Phi}} = \begin{bmatrix} 1 & 0 & 0 \\ 0 & \cos\Phi & -\sin\Phi \\ 0 & \sin\Phi & \cos\Phi \end{bmatrix} \tag{9.2}$$

$$\mathbf{R}_{\mathbf{\Theta}} = \begin{bmatrix} \cos\Theta & 0 & \sin\Theta \\ 0 & 1 & 0 \\ -\sin\Theta & 0 & \cos\Theta \end{bmatrix} \tag{9.3}$$

$$\mathbf{R}_{\mathbf{\Psi}} = \begin{bmatrix} \cos\Psi & -\sin\Psi & 0 \\ \sin\Psi & \cos\Psi & 0 \\ 0 & 0 & 1 \end{bmatrix} \tag{9.4}$$

where Φ, Θ and Ψ are the roll, pitch and yaw angles.

9.2.0.1 Inflow velocity

The relative or apparent inflow velocity on the r_i blade section of blade B_j is defined as:

$$\vec{V}_{rel} = \vec{V_\infty} + \vec{V}_{rot} + \vec{V}_W - \vec{V}_{motion} + \vec{W} \tag{9.5}$$

where $\vec{V_\infty}$ is the undisturbed current speed, $\vec{V}_{rot}$ the rotational speed, $\vec{V}_W$ the wave induced velocity, $\vec{V}_{motion}$ the rigid body motions at the r_i blade section of blade B_i and $\vec{W}$ the rotor-induced velocities.

Wave velocities are modelled using linear wave theory. This theory assumes a potential flow with homogeneous depth d, and describes wave elevation and velocities as:

$$\eta = \zeta_a \sin(\omega_e t - k_W x) \tag{9.6}$$

$$V_{W,X} = \omega_W \zeta_a \frac{\cosh k_W(d+z)}{\sinh k_W d} \sin(\omega_e t - k_W x) \tag{9.7}$$

$$V_{W,Z} = \omega_W \zeta_a \frac{\sinh k_W(d+z)}{\sinh k_W d} \cos(\omega_e t - k_W x) \tag{9.8}$$

with $V_{W,X}$ and $V_{W,Z}$ the axial and vertical components of the wave velocity vector $\vec{V}_W$ for a wave aligned with the current, ζ_a the wave amplitude, ω_W the wave frequency, L_W the wave length, ω_e the encounter frequency, k_W the wave number, t the time, and x and z the horizontal and vertical coordinates, respectively. The encounter frequency is a simplification introduced to account for changes in wave period due to the presence of a homogeneous current [1] and is defined as:

$$\omega_e = \omega_W + k_W V_\infty \tag{9.9}$$

with V_∞ the undisturbed current speed aligned with the wave propagation direction. Finally, the wave length is related to the wave period $T_W = 2\pi/\omega_W$ by:

$$L_W = \frac{g}{2\pi} T_W^2 \tanh k_W d \tag{9.10}$$

9.2.0.2 Dynamic inflow model

The induced velocities are resolved in time using a dynamic inflow model proposed by Øye [10]. This is an engineering model which introduces a time delay between inflow changes and the setting of the system on a new hydrodynamic equilibrium by filtering the induced velocities using two first-order differential equations:

$$W_{int} + \tau_1 \frac{dW_{int}}{dt} = W_{qs} + g\tau_1 \frac{dW_{qs}}{dt} \tag{9.11}$$

$$W + \tau_2 \frac{dW}{dt} = W_{int} \tag{9.12}$$

where W_{int} is an intermediate induced velocity, W_{qs} the quasi-steady induced velocity calculated using the steady-state BEM equations (following from chapter 8, the modified TWM and Prandtl's tip-loss correction are used to calculate the quasi-steady induced velocity), $g = 0.6$ is a relaxation parameter, and τ_1 and τ_2 two empirical time constants defined by Hansen [6] as:

$$\tau_1 = \frac{1.1}{1 - 1.3a} \frac{R}{V_\infty} \tag{9.13}$$

$$\tau_2 = \left(0.39 - 0.26 \left(\frac{r}{R}\right)^2\right) \tau_1 \tag{9.14}$$

with a the axial induction factor.

9.2.0.3 Dynamic stall model

The transient inflow conditions affect the development of the forces on the foil sections beyond the steady-state polars. This is especially important when the angle of attack on a foil oscillates between the attached- and separated-flow regimes. As the angle of attack dynamically increases beyond the stall point, an increase in lift and drag to values greater than the corresponding steady-state coefficients for a specific angle of attack is typically observed for a short period time. As the oscillation of α continues, a hysteresis around the steady-state polar coefficients occurs. To account for these transient effects, the dynamic BEM model implements

a dynamic stall model [6] to correct the lift coefficients. This model corrects only for trailing edge separation, considered by Hansen et al. [7] as the dominant phenomenon for axial rotor applications.

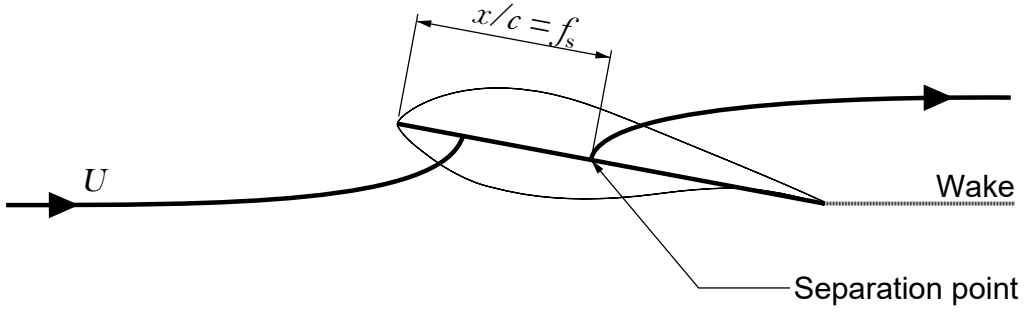

Figure 9.2: Diagram of the trailing edge separation point f_s used by the dynamic stall model. Figure reproduced from the work presented by Hansen et al. [7]

The model assumes that a lift coefficient can be represented by the interpolation between the lift coefficients for fully-attached flow C_L^{inv}, and fully-separated flow C_L^{fs}. These are related by a separation function, f_s, that represents the portion of the aerofoil chord where the flow has separated, as shown in fig. 9.2. When the flow is fully-attached to the foil, $f_s = 1$, and when the flow is completely separated, $f_s = 0$. The lift coefficient is, thus, defined as:

$$C_L = f_s C_L^{inv}(\alpha) + (1 - f_s) C_L^{fs}(\alpha) \tag{9.15}$$

where C_L^{inv} is represented by a linear fit to the steady-state lift coefficients at low angles of attack, and C_L^{fs}, the fully-separated lift coefficient computed from the steady lift coefficients C_L^{st}:

$$C_L^{fs} = \frac{C_L^{st} - f_{st} C_L^{inv}}{1 - f_{st}} \tag{9.16}$$

where f_{st} is the value of f_s that converts C_L, in eq. 9.15, to the steady lift coefficient and is defined by Hansen et al. [7] as:

$$f_{st} = \left(2\sqrt{\frac{C_L^{st}}{C_L^{inv}}} - 1 \right)^2 \tag{9.17}$$

Note that C_L^{st} also corresponds to the tabulated lift coefficients normally determined using numerical methods or from experiments. Finally, the time-dependent lift coefficient, and the time lag between flow separation and reattachment, are modelled through a time filter applied to the separation function by the following differential equation:

$$\frac{df_s}{dt} = \frac{(f_{st} - f_s)}{4.0 \cdot c/V_{rel}} \tag{9.18}$$

with V_{rel} the magnitude of the apparent velocity seen by the foil [6]. The solution of the differential equation provides the value of f_s over time, required to calculate the dynamic lift coefficients.

The dynamic stall model accounts for, e.g., when the angle of attack suddenly increases above stall. Under such circumstances, and over a relatively short period of time, the C_L^{inv} coefficient will dominate, and an overshot in lift above the steady-state lift coefficient, past the separation point, will be observed.

9.2.0.4 Wave forces

The effects of wave kinematics are directly captured in this dynamic BEM model by introducing the wave velocities in the relative velocity computation (eq. 9.5). The inertial forces on the rotor, however, are calculated independently using the inertial term in Morison's equation for each blade section. The inertial force, in the foil frame of reference, is defined as:

$$\vec{F}_{inertial} = \vec{F}_{FK} + \vec{F}_a \tag{9.19}$$

where $\vec{F}_{FK}$ is the Froude-Krylov force, caused by the unsteady changes in the pressure field associated with wave kinematics:

$$\vec{F}_{FK} = \rho A_i \frac{d\vec{V_W}}{dt} \tag{9.20}$$

with A_i the cross-sectional area of the foil section.

$\vec{F}_a$ is the added mass force. Guo et al. [5] assume the blade element to behave as a flat plate, considering only the added mass in the direction normal to the foil

chord and an added mass coefficient of 1. Their assumption leads to an added mass force defined on the foil reference frame as:

$$\vec{F}_a = \vec{m}_a \odot \frac{d\vec{V_{rel}}}{dt} \tag{9.21}$$

where $\odot$ is the operator for the Hadamard product, a per-vector-element multiplication. The added mass is defined in the axial and tangential directions as:

$$\vec{m}_a = \left[\frac{1}{4}\rho\pi c^2 \cos\beta, \frac{1}{4}\rho\pi c^2 \sin\beta\right] \tag{9.22}$$

where β is the local twist angle, and c the local chord.

9.2.0.5 Total forces on a blade section

The axial and tangential force on a foil section are finally defined as:

$$F_x = L\cos\phi + D\sin\phi + F_{inertial,x} \tag{9.23}$$

$$F_\theta = L\sin\phi + D\cos\phi + F_{inertial,\theta} \tag{9.24}$$

where x and θ are the axial and tangential directions, L is the lift force calculated with the dynamic lift coefficient (eq. 9.15), local chord, and the relative inflow velocity (eq. 9.5) considering the dynamic inflow corrections; D is the drag force derived from the steady-state drag coefficients at the instantaneous angle of attack α; and ϕ the instantaneous inflow angle.

The forces and moments on each blade section are finally integrated over the span of each blade, and the integrated forces and moments are calculated in the corresponding six degrees of freedom representation.

9.3 Model verification

9.3.1 Dynamic stall model

The dynamic stall model used in the dynamic BEM implementation [7] was validated against experimental results. The model predictions were compared to the wind

tunnel experiments of a Risø-A1-24 aerofoil, the same foil section used in the design of the Sch15B rotor. The experimental results, published by Fuglsang et al. [4], include the steady-state lift coefficients and dynamic lift hysteresis loops for different foil pitch oscillations.

The Risø-A1-24 aerofoil was tested in a wind tunnel with a smooth surface, a 0.6 m chord and 1.9 m span. The wind tunnel had a cross-section of 7.5 m × 7.5 m, and end-plates were fitted to the foil to reduce three-dimensional flow effects. The dynamic lift coefficients were obtained by pitching the aerofoil about the point $x/c = 0.40$, following a sinusoidal function with a frequency of 12.9 rad/s, with a reduced frequency of 0.092, and oscillation amplitudes between ±1.4° and ±2.0°. The inflow speed was 42.0 m/s with turbulence intensity of 1%. Reynolds number was approximately 1.6×10^6. Further details about the tests and experimental setup are given in the original reference [4].

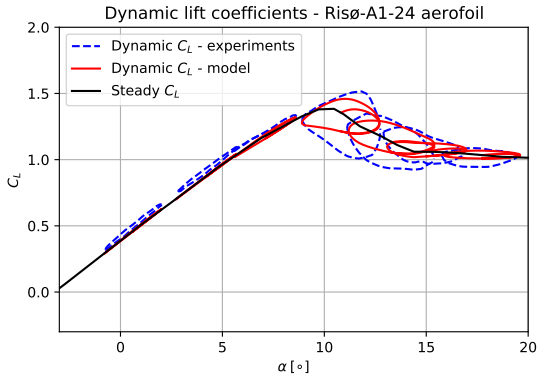

Figure 9.3: Steady and dynamic lift coefficients of the Risø-A1-24 aerofoil. The plot compares the dynamic stall model of Hansen et al. [7] with the experimental results published by Fuglsang et al. [4]. The dynamic lift coefficients correspond to a pitching motion with a frequency of 12.9 rad/s.

The experiments performed by Fuglsang et al. [4] were reproduced using the dynamic stall model implemented with the dynamic BEM model. The steady C_L curve from the experimental results was used to ensure consistency in the comparison because variables such as Reynolds number and environmental turbulence can influence the steady lift function and the angle of attack at which separation

occurs. The results are shown in fig. 9.3 for the steady C_L along with dynamic lift coefficients from experiments and model predictions.

The comparison highlights a small effect of the pitching motion on the dynamic lift coefficient, compared with the steady-state curve, at angles of attack below the separation point. This is correctly described by the dynamic stall model compared with the experimental hysteresis loops. Interestingly, however, the experimental loops below separation are not centred around the steady lift curve, although no further details about this are given by the authors of the experiments.

At angles of attack above stall, the model broadly captures the hysteresis loops observed in the experimental dynamic lift coefficients. The accuracy of the results, however, is variable. The larger C_L values on most loops are represented with a slight underestimation compared with the experiments, whereas the lower end of the loops appear to overestimate C_L in all cases above stall. The relative error shows an underestimation of 13% of the maximum C_L, and an overestimation of minimum C_L of 20% for the loop centred at $\alpha = 11.8°$.

9.3.2 Prescribed pendular motions

Osman and Willden [9] performed a numerical study on the Sch15B rotor under prescribed harmonic motions in a homogeneous flow. Their work is focused on pendular motion, described as a pitching rotation centred around an axis located far from the rotor (see fig. 9.4). This motion mimicks the transient effects on a rotor attached to a floating platform.

Their work simulated the rotor using blade-resolved RANS CFD computations with a $k-\omega$ SST turbulence model. The motions were captured using sliding meshes with three different subdomains: a fixed external domain, a pitching domain for the pendular motion, and an inner rotary domain for the turbine. The angle of pendular motion in time was determined by a sinusoidal function and characterised by: a normalised pendular frequency, $\omega^* = \omega_{osc}/\omega_{rot}$, where ω_{osc} is the pendular frequency and ω_{rot} is the rotor spinning frequency; by a pendular amplitude A_0; and by the rotor tip-speed ratio.

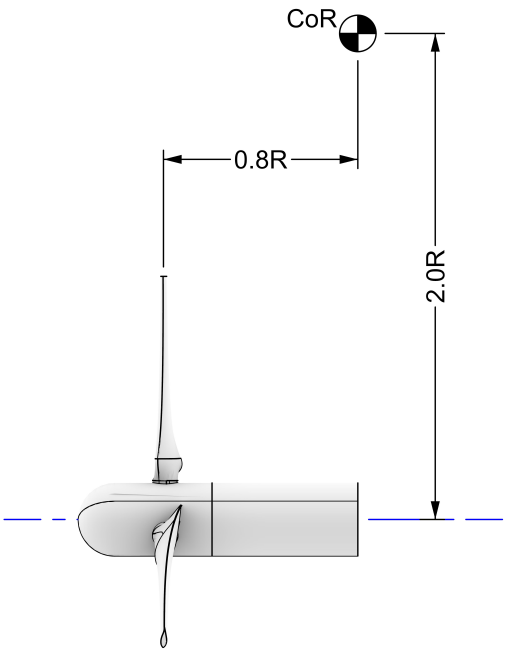

Figure 9.4: Relative position of the rotor with respect to the Centre of Rotation (CoR) used for the pendular motion simulations described by Osman and Willden [9].

Given the similarities between the pendular motion and the motions expected from a floating tidal rotor, the results published by Osman and Willden [9] were used to verify the dynamic BEM model and, specifically, the modifications introduced to account for rigid body motions.

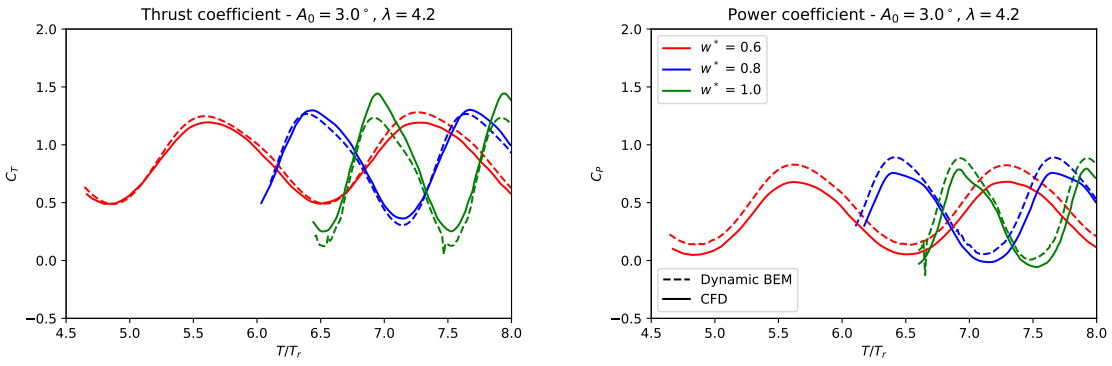

Figure 9.5: Thrust (left) and power (right) coefficient comparison between Osman and Willden [9] blade-resolved CFD and the dynamic BEM computations of the Sch15B rotor under a prescribed pendular motion at varying ω^*.

Fig. 9.5 shows a comparison between the dynamic BEM model and the CFD results of Osman and Willden [9] for varying ω^* values, with $A_0 = 3.0°$ and a

tip-speed ratio $\lambda = 4.2$. This comparison shows the dynamic BEM to reproduce well the CFD results both in terms of frequency and oscillation amplitude.

The power coefficients predicted by the dynamic BEM model, however, show a relatively constant overestimation compared with CFD through the entire time series. This is attributed to a combination of the deficiencies in tip-loss modelling, described in sec. 8.4, as well as to a lack of dynamic stall corrections for the drag coefficients within the model.

Thrust shows better agreement between the CFD and the engineering model throughout the time series. Nevertheless, the dynamic BEM model underestimates the peak loads at $\omega^* = 1.0$ by approximately 13%, an error of the same order of magnitude as was observed for the dynamic stall model. The deficiencies in tip-loss modelling also affect thrust, suggesting that the agreement between CFD and the engineering model is due to a combination of a tip-loss related overestimation and the peak-load underestimations observed on the dynamic stall model. Unlike power, however, the lack of dynamic stall corrections for the drag coefficients is not likely to have a significant impact on thrust due to the lower relative contribution of drag to the thrust forces (see discussion in sec. 6.6.1 for more details).

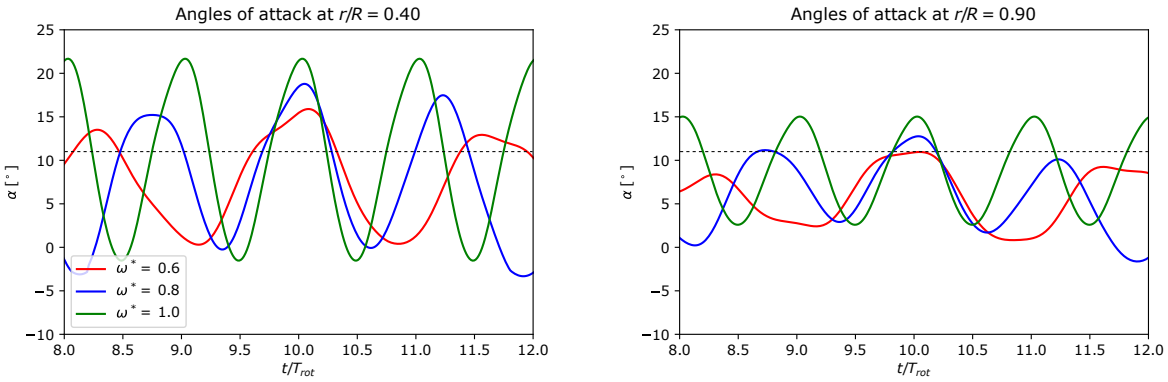

Figure 9.6: Time series of the angle of attack on one blade, at two radial locations, $r/R = 0.40$ (left) and $r/R = 0.90$ (right), for different oscillation frequencies, and calculated with the dynamic BEM model. The dashed line marks the stalling point for the Risø-A1-24 aerofoil

As the oscillation frequency increases, so too does the variation in sectional angles of attack. Fig. 9.6 shows the variation in α over four blade rotations, at two different

spanwise locations of one of the rotor blades. The plots show that larger frequencies tend to induce larger oscillations in angle of attack, with larger fluctuations around the inboard blade sections. The three pendular frequencies shown in the figure show blade sections periodically entering and leaving the stall region, which occurs at an angle of attack of approximately 11° for the Risø-A1-24 aerofoil.

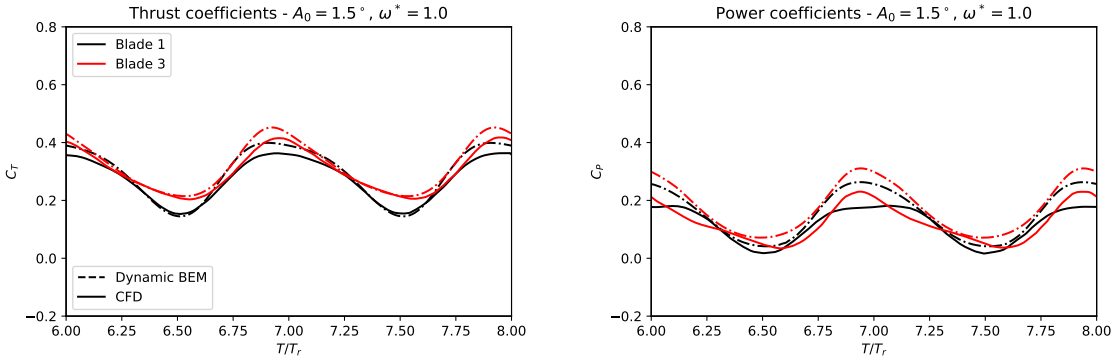

Figure 9.7: Thrust (left) and power (right) coefficients on two blades for a rotor operating at $\lambda = 4.2$ under a prescribed pendular motion with $A_0 = 1.5°$ and $\omega^* = 1.0$. The continuous and dashed lines present the CFD results of Osman and Willden [9] and the dynamic BEM results, respectively.

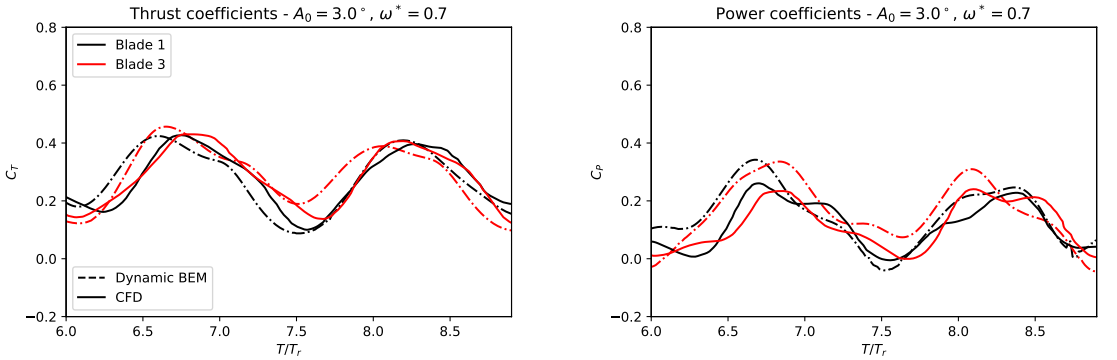

Figure 9.8: Thrust (left) and power (right) coefficients on two blades for a rotor operating at $\lambda = 4.2$ under a prescribed pendular motion with $A_0 = 3.0°$ and $\omega^* = 0.7$. The continuous and dashed lines present the CFD results of Osman and Willden [9] and the dynamic BEM results, respectively.

The sectional angles of attack also highlight that, under the prescribed pendular motions, different blades will be affected by different inflow variations depending on the pendular and rotational frequencies. The pendular motion induces larger fluctuations on the relative inflow speed on blade sections located far from the

centre of rotation. As the blades spin around the rotor axis, the distance from the centre of rotation changes, and on a given rotation, different blades will encounter different inflow conditions depending on the relative frequency ω^*. This results in different blades displaying different load fluctuations over a set period of time.

Figs. 9.7 and 9.8 show a comparison of the thrust and power predicted by the CFD and dynamic BEM models on individual blades, with the rotor operating at $\lambda = 4.2$ and with a different pendular motion for each figure: fig. 9.7 shows a relatively small oscillation amplitude $A_0 = 1.5°$ at an $\omega^* = 1.0$, while fig. 9.8 shows a larger amplitude $A_0 = 3.0°$ with $\omega^* = 0.7$.

Figs. 9.7 and 9.8 show that, as with the integrated loads and for both cases, the dynamic BEM model captures the general trends and amplitudes calculated with CFD. However, a substantial difference in accuracy is observed between the two cases. For the case where $A_0 = 1.5°$, fig. 9.7, the dynamic BEM model shows good agreement in thrust coefficient for the two blades in terms of frequency and amplitude, with an overestimation of the peak loads of approximately 10%. The power coefficients show larger differences between the two models, with the dynamic BEM presenting an overestimation of the blade's C_P that was also observed for the full rotor C_P. However, the CFD simulations show a *plateau* for blade 1 at peak C_P which is not reproduced by the dynamic BEM model. This leads to a relative overestimation of C_P of approximately 50% for that blade at that point in time.

Fig. 9.8, with $A_0 = 3.0°$, shows larger differences between the dynamic BEM and the CFD models. As before, the trends, main frequencies and amplitudes in thrust and power are adequately reproduced by the dynamic BEM model, with thrust showing better agreement than power. However, this case shows a more significant contribution of secondary harmonics, especially for C_P, at frequencies higher than ω_{osc}. In this case, and since $\omega^* = 0.7$, the rotational and pendular frequencies are not locked to each other. The secondary harmonics are, thus, caused by the interactions between the pendular motion and rotational frequencies. In addition to the large oscillations in angle of attack, these extra harmonics result in short-term changes in the apparent flow and angle of attack on the blades, inducing

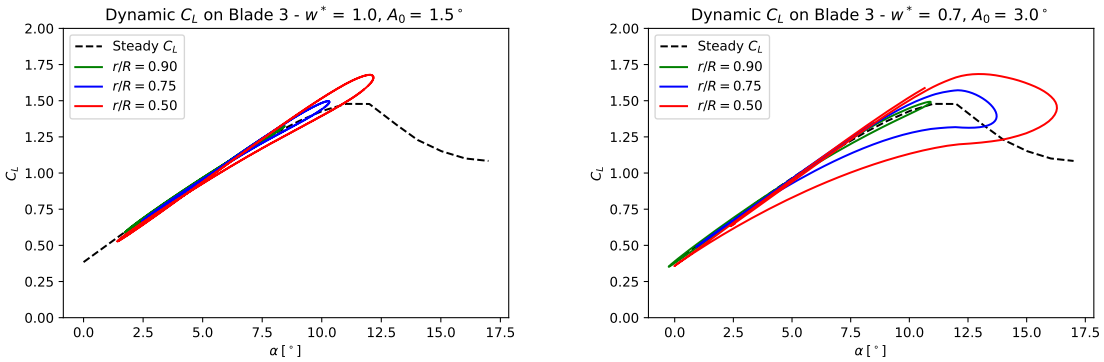

Figure 9.9: Dynamic lift coefficient of the Sch15B rotor under prescribed motions at three radial locations predicted with the dynamic BEM model. The plots are presented for two oscillation cases: $\{\omega^* = 1.0, A_0 = 1.5°\}$ (left) and $\{\omega^* = 0.7, A_0 = 3.0°\}$ (right). The coefficients plotted correspond to a time range $5.0 \leq T/T_r \leq 10.0$.

dynamic effects that result in greater use and thus reliance on the accuracy of the dynamic stall and dynamic inflow models.

The dynamic lift coefficients, predicted by the dynamic BEM model, are shown in fig. 9.9. The coefficients correspond to the previous cases where $\{A_0 = 1.5, \omega^* = 1.0\}$ and $\{A_0 = 3.0, \omega^* = 0.7\}$, and are presented at three different radial locations over the same period shown for figs. 9.7 and 9.8. The dynamic C_L plots demonstrate the large amplitude of the α fluctuations for both cases, and especially for the larger A_0. The $A_0 = 1.5°$ case shows that the lift coefficients remain mostly within the pre-stall region on the outboard sections of the blade, where most of the thrust and torque are generated. However, for this relatively moderate case α still reaches the stalling point near the inboard sections. The case where $A_0 = 3.0°$ shows significantly larger α oscillations, with most of the blade periodically entering into stall, and with a significant contribution of the stall delay effects to the maximum C_L. The larger fluctuations on α imply a stronger reliance on the dynamic stall and dynamic inflow models to predict blade loads, potentially inducing larger modelling errors.

9.4 Discussion

The dynamic BEM model, initially validated by Guo et al. [5] for a rotor in waves, and modified to account for rigid body motions, has been shown to broadly

reproduce oscillatory loads caused by pendular motion for moderate oscillation amplitudes and frequencies, with higher accuracy for cases where no significant flow separation occurs.

Some of the cases modelled by Osman and Willden [9], however, lead to large oscillations in angles of attack which are likely to induce flow separation over large portions of the rotor blades. These cases show more significant errors in the dynamic BEM predictions compared with the CFD results due to the engineering model predictions relying heavily on the dynamic stall and dynamic inflow models.

The dynamic stall model, specifically, showed deficiencies at computing the peaks and troughs of the C_L hysteresis loops above stall. These modelling deficiencies are likely to be aggravated in the more extreme pendular motion cases, given that the experimental results of Fuglsang et al. [4], and used for validation, were produced for relatively small α oscillation amplitudes (between $\pm 1.4°$ and $\pm 2.0°$), while the more extreme cases modelled by Osman and Willden [9] lead to oscillations in excess of $\pm 12°$. Under such extreme conditions, however, it is expected that most models, including those based on BEM and RANS CFD alike, would yield large errors.

Nevertheless, most axial-flow rotors, including the Sch15B rotor, are expected to operate below stall and, thus, the results showed by the dynamic BEM model under attached-flow regimes could be considered sufficient for typical engineering applications. Further work, however, is still required to improve the predictive capabilities of the dynamic BEM model across the entire range of transient dynamics a turbine might encounter.

References

[1] N. Barltrop et al. “Investigation into wave-current interactions in marine current turbines”. In: *Proceedings of the Institution of Mechanical Engineers, Part A: Journal of Power and Energy* 221.2 (2007), pp. 233–242.

[2] Det Norske Veritas (DNV). *Tidal turbines rules and standards*. Tech. rep. DNVGL-ST-0164. Standard. 2015.

[3] C. Faudot and O. G. Dahlhaug. “Prediction of wave loads on tidal turbine blades”. In: *Energy Procedia* 20 (2012), pp. 116–133.

[4] P. Fuglsang, K. S. Dahl, and I. Antoniou. *Wind tunnel tests of the Risø-A1-18, Risø-A1-21 and Risø-A1-24 airfoils*. Risø National Laboratory, 1999.

[5] X. Guo et al. “The surface wave effects on the performance and the loading of a tidal turbine”. In: *Ocean Engineering* 156 (2018), pp. 120–134.

[6] M. Hansen. *Aerodynamics of wind turbines*. 2nd ed. International Institute for Environment and Development, 2008.

[7] M. H. Hansen, M. Gaunaa, and H. A. Madsen. *Beddoes-Leishman type dynamic stall model in state-space and indicial formulations*. Tech. rep. Risoe-R No. 1354(EN). Forskningscenter Risoe, 2004.

[8] J. R. Morison, J. W. Johnson, and S. A. Schaaf. “The force exerted by surface waves on piles”. In: *Journal of Petroleum Technology* 2.05 (1950), pp. 149–154.

[9] M. H. B. Osman and R. H. J. Willden. “Unsteady loading of a floating tidal turbine oscillating in a pendulum motion”. In: *Developments in Renewable Energies Offshore*. CRC Press, 2020, pp. 563–570.

[10] S. Øye. “Dynamic stall simulated as time lag of separation”. In: *Proceedings of the 4th IEA Symposium on the Aerodynamics of Wind Turbines*. Vol. 27. Rome, Italy. 1991, p. 28.

[11] G. T. Scarlett and I. M. Viola. “Unsteady hydrodynamics of tidal turbine blades”. In: *Renewable Energy* 146 (2020), pp. 843–855.

[12] G. T. Scarlett et al. “Unsteady hydrodynamics of a full-scale tidal turbine operating in large wave conditions”. In: *Renewable Energy* 143 (2019), pp. 199–213.

[13] W. Sheng, R. A. Galbraith, and F. N. Coton. “A new stall onset criterion for low speed dynamic stall”. In: *Journal of Solar Energy Engineering* 128.4 (2006), pp. 461–471.

Part V

Hydrodynamics of a floating tidal turbine device

You must then know the sea, and know that you know it, and not forget that it was made to be sailed over.

Joshua Slocum

10 Floating tidal rotors

10.1 Introduction

Many of the latest developments in pre-commercial tidal stream energy are based on axial-flow rotors supported by floating platforms. These systems have the advantage of easier deployment, maintenance access and decommissioning, alongside with higher current speeds when compared with bottom-fixed devices. Floating platforms also enable deployment in deep-water locations where bottom-fixed rotors are not viable, increasing feasible resource availability. Nonetheless, there are non-trivial challenges to resolve when operating rotors in close proximity to the free surface.

Surface waves have been demonstrated experimentally to induce significant load variations on fixed axial-flow rotors[1] (see sec. 2.4.0.3), loads which could produce premature failure on blades or another part of the energy conversion system. Waves are also likely to be the dominant source of load unsteadiness even for bottom-fixed tidal stream devices [13].

Prescribed rigid-body motions on a rotor were shown to be a significant source of unsteady loading. The work of Osman and Willden [12] shows, for the Sch15B rotor, that rigid-body motions could induce load variations on the same order

[1]The term "fixed rotors" is used in this section for devices that are not under the influence of rigid-body motions e.g. bottom-fixed tidal rotors.

of magnitude as those caused by waves even for moderate oscillatory amplitudes and frequencies (see sec. 9.3.2).

Brown et al. [3] presented the results of one of the few studies on floating tidal devices. They performed an experimental campaign in the COAST laboratory at the University of Plymouth using a scaled model of a generic catamaran-style floating platform. The platform was allowed to move in six degrees of freedom, with a porous disc representing the rotor, and restrained by catenary moorings. Their research showed that, similar to cases with waves and currents for fixed rotors presented in other studies, mean loads are largely unaffected by the coupled effects of waves and platform motions compared with current-only cases. However, they observed an amplification of unsteady loading due to platform motions and especially with wave frequencies that correspond to harmonics of the pitch natural frequency, raising concerns about fatigue and the quality of power delivery.

The current understanding, however, is insufficient. Floating platforms in waves oscillate with multiple degrees of freedom. The amplitudes of these oscillations change depending on platform design, mass, moorings, etc. The frequency of these oscillations is the same as the excitation force (i.e., the wave frequency) but the response occurs with a phase which is a function of the excitation frequency, platform design and, potentially, of the rotor response.

In this work, a numerical approach to study the effects of coupled current and waves on a floating platform [2] is presented. The following sections describe, first, a concept for a catamaran-style floating platform designed for the 20 m diameter Sch15B rotor. The design is followed by a methodological description where a time-domain numerical model to capture the floating platform response and non-linear rotor loads is presented. Finally, the floating platform is modelled under different combinations of regular waves and currents.

[2]The term "floating platform" is used to reference the system that consists of a rotor and a supporting float. The term "float" is used to reference the flotation device that supports the rotor.

10.2 Preliminary design of a floating platform for tidal stream energy

A twin-hulled floating platform for tidal stream energy conversion was designed as a utility-scale concept. The platform supports a single Sch15B rotor (radius $R = 10\,\text{m}$) and was designed considering potential for scalability as part of multi-rotor arrays. The nacelle is located at $1.5R$ depth (i.e. $0.5R$ of tip clearance with respect to the free surface) with the blades located longitudinally at the same position of the platform's centre of mass. The length of the demi-hulls is $7.0R$, the beam of the demi-hulls is $0.4R$ and the total beam of the catamaran is $3.0R$.

Table 10.1: Main design characteristics of a tidal floating platform.

Description	Value	Unit	Description	Value	Unit
Total displaced volume	492.0	[m^3]	Waterplane area	519.5	[m^2]
Total displacement	504036.0	[kg]	Vertical centre of mass	-3.2	[m]
Total length	70.0	[m]	Vertical centre of buoyancy	-3.0	[m]
Beam overall	30.0	[m]	Metacentric height (roll)	179.9	[m]
Beam demi-hull	4.0	[m]	Metacentric height (pitch)	386.13	[m]
Maximum draft	25.0	[m]			
Roll inertia	8.4E+07	[kg · m^2]			
Pitch inertia	1.4E+08	[kg · m^2]			
Yaw inertia	1.1E+08	[kg · m^2]			

The conceptual platform was designed to allow a maximum static trim angle of 1.5° with the rotor operating at cut-out speed ($V_\infty = 4.5\,\text{m/s}$). The total displaced volume[3], including float and rotor, was estimated to be 492 m^3. The float mass was estimated by assuming a steel hull with a plating thickness of 7 mm on the float, following Det Norske Veritas (DNV) [5], with a factor of 1.7 to account for other structures and equipment. The vertical centre of mass and centre of buoyancy were estimated to be located at 3.2 m and 3.0 m from the free surface, respectively, both located below the waterline. The turbine mass was estimated in 150000 kg, following published data from commercial manufacturers, and with a displaced volume of 90 m^3 calculated from the CAD model. The roll and pitch radii of gyration for the platform were assumed to be 40% of the catamaran beam and 25%

[3]Note that Orbital's O2 2 MW floating tidal platform, with two rotors, has a displacement of approximately 600 m^3 [11]

of its length, respectively (ITTC [7]). The rotor mass inertia was added to the platform by modelling it as a homogeneously distributed mass across the nacelle. The effect of the mass distribution on blades was deemed to be small compared with the rest of the system and, thus, neglected.

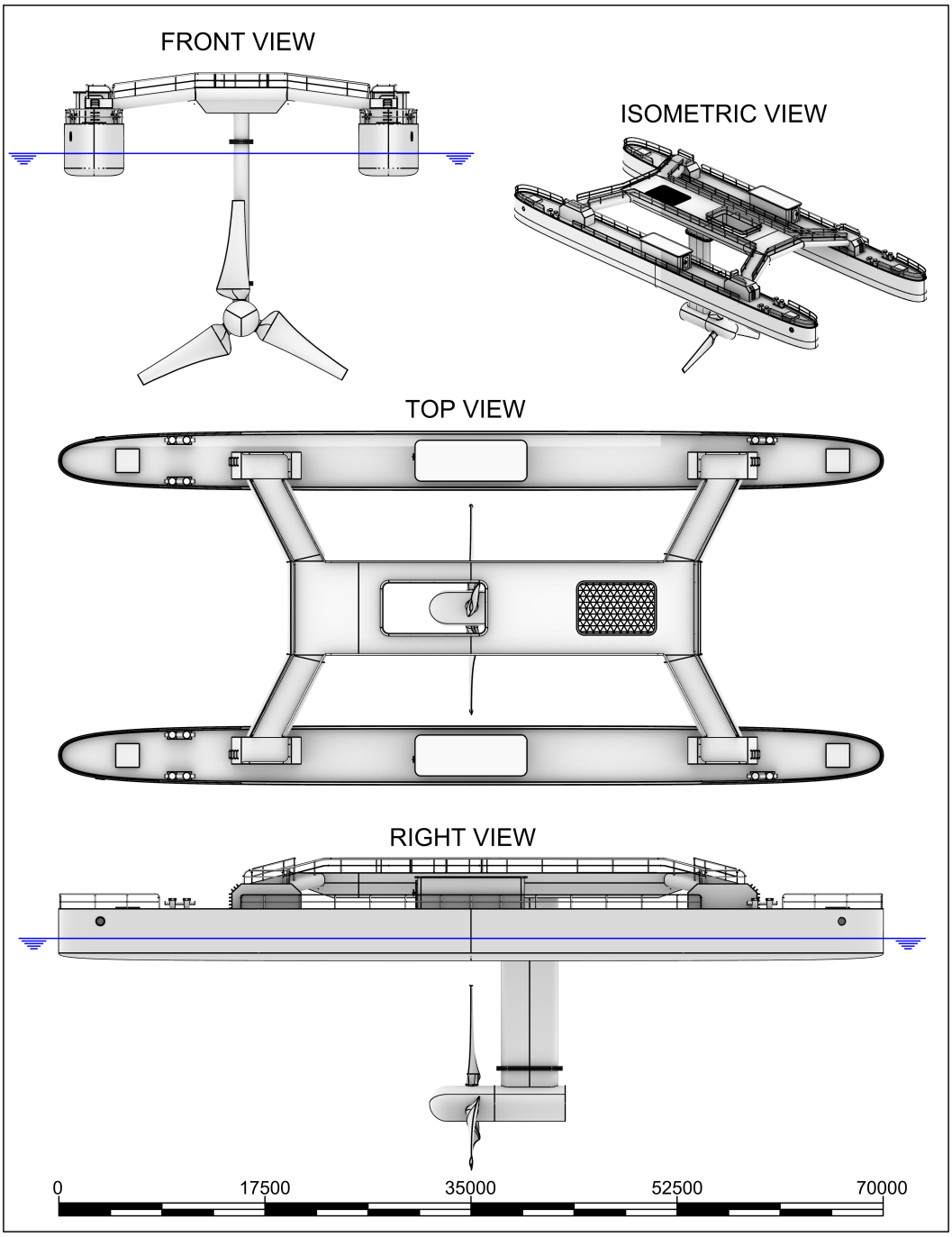

Figure 10.1: Conceptual design of a floating platform for a 20m diameter tidal rotor.

A summary of the platform characteristics can be found in table 10.1 and a

render of the conceptual design in fig. 10.1.

10.3 Numerical model description

The floating platform concept was modelled with a time-domain seakeeping model coupled with the dynamic BEM model presented in chapter 9. The seakeeping model is based on the hydrodynamic coefficients calculated from the radiation and diffraction solutions of a boundary-element model in frequency-domain, and solved with ANSYS AQWA 2020.

The time-domain model is set by Cummins [4] equation of motion:

$$\{M_{RB} + \bar{A}(t)\}\ddot{X}(t) + \int_{-\infty}^{t} \bar{K}(t-\tau)\dot{X}(\tau)d\tau + \bar{C}X(t) = F_{ext}(t) \tag{10.1}$$

with M_{RB} the floating platform rigid-body mass matrix, $\bar{A}(t)$ the time-domain added mass matrix, X the platform position vector, $\bar{C}$ the stiffness matrix and F_{ext} the excitation forces which considers the environmental and rotor forces.

The coefficients in eq. 10.1 are related to the hydrodynamic coefficients in frequency-domain. Ogilvie [10] demonstrated that, for the case of harmonic motions, Cummins' model is equivalent to a frequency-domain model. Ogilvie's result enables the calculation of the hydrodynamic coefficients for the time-domain model using frequency-domain hydrodynamic coefficients, with the relationship between frequency and time-domain coefficients determined by:

$$\bar{A}(t) = A(\infty) \tag{10.2}$$

and

$$\bar{K}(t) = \frac{2}{\pi}\int_{0}^{\infty} B_{tot}(\omega)\cos(\omega t)d\omega \tag{10.3}$$

where $A(\infty)$ is the frequency-domain added mass evaluated at the limit where $\omega \to \infty$, and B_{tot} is the frequency-domain total damping matrix.

The frequency-domain coefficients can be determined using potential-flow models for seakeeping such as WAMIT [9], AQWA [1], or the open source code NEMOH [2]. AQWA, the code used in this work, calculates the hydrodynamic coefficients and first order wave forces by describing the flow around a floating body with a velocity potential. This potential is represented by the incident waves, diffraction and radiation terms. To obtain the incident forces and hydrodynamic coefficients, the surface of the floating body is discretised into panels on which the potentials are calculated. The potentials are then used to compute the active forces, from the incident wave and diffraction potentials, and the reactive forces, obtained from the radiation potentials solved for each degree of freedom. The reactive forces are finally used by the model to calculate the frequency-domain added mass and damping coefficients [1].

The dynamic BEM model resolves the inflow velocities on each blade section considering the current, wave and relative motion velocities. First-order wave theory is used to calculate the wave-induced velocities, and wave diffraction caused by the rotor is neglected. The dynamic BEM model was coupled with the seakeeping model through an external server connection to AQWA. The dynamic BEM model receives, at each time step, the simulated time, used to synchronise the wave velocity fields, the position, and velocity of the platform centre of gravity. Using this data, the relative inflow speed on each blade section is determined and the forces are calculated as described in chapter 9. The blade forces are integrated at the nacelle and returned to AQWA in a six degrees of freedom representation to be added to the F_{ext} term in eq. 10.1. Finally, the equation of motion is integrated in time using a predictor-corrector approach to create a time history of the solution, as described in [1]. The coupling between the two models is in terms of forces and motions, and no further fluid dynamic interactions are considered.

Given the research objective of studying float and rotor interactions, the rigid-body motions were restricted to only account for heave and pitch. These motion components are self-restoring, thus eliminating the need for moorings or other station-keeping devices. Roll was restricted since the current and sea conditions

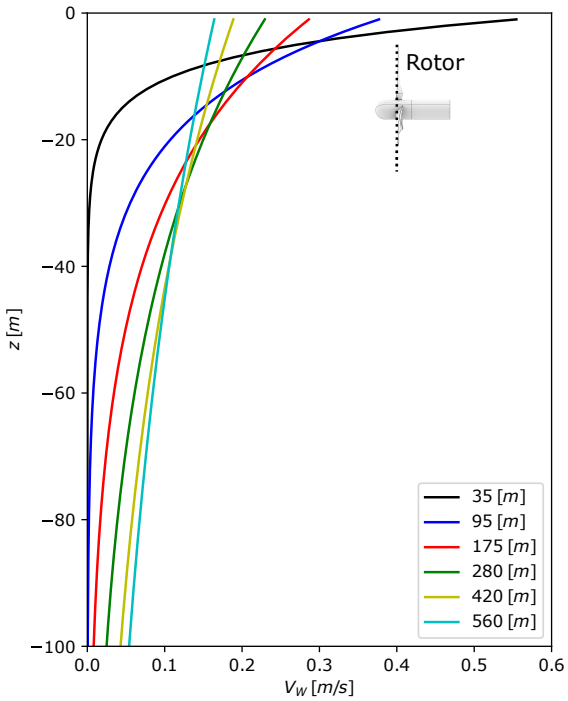

Figure 10.2: Depth-dependent profile of maximum wave-induced velocities for different wave lengths at a constant wave height of 1 m. The origin is placed at the mean free-surface level.

analysed were aligned with the platform centre line, and thus the excitation of this degree of freedom was considered negligible.

10.4 Floating rotor analysis

10.4.1 Modelling conditions

The floating platform was modelled with and without rigid-body motions at four currents ($V_\infty \in \{1.0, 2.0, 3.0, 4.0\}$ [m/s]) aligned with the platform centreline, and under the effects of 12 different following waves. The waves were modelled with a constant wave height of 1 m, and with wavelengths $\lambda_W \in \{35, 70, 105, 140, 175, 210, 280, 350, 420, 490, 560, 630\}$ [m], which corresponds to wavelengths of 0.5 to 9 platform lengths. For each current, wave periods were adjusted to account for the Doppler shift using eq. 9.9 for the encounter frequency. The depth profile

of the maximum wave-induced velocities, for some of the waves modelled, are plotted in fig. 10.2.

The 48 time series were modelled for at least 30 wave periods and with a 10 seconds ramping period. The simulations were initiated from a static equilibrium condition. The rotor was modelled operating at a constant tip-speed ratio $\lambda = 5.0$, and the initial transients of the time series were discarded at post-processing.

10.4.2 Effects of the rotor on platform motions

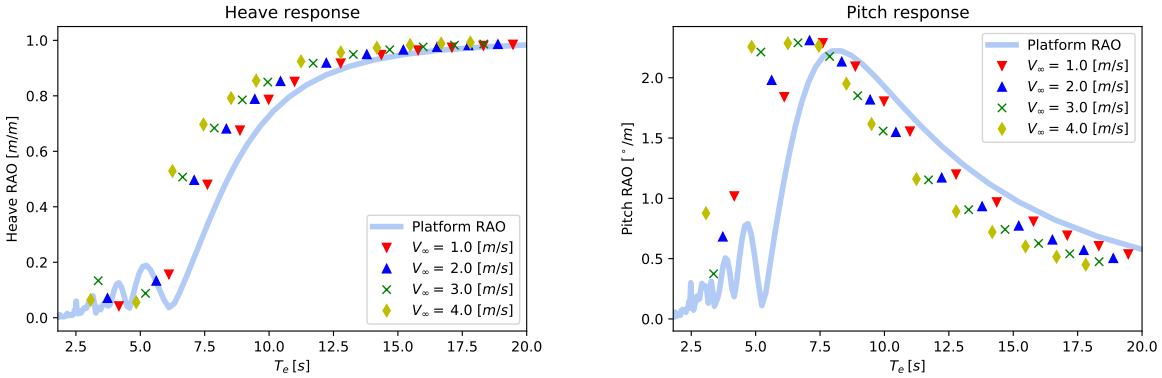

Figure 10.3: Frequency-domain RAOs of the floating platform without the rotor (blue line) compared with the time domain response of the platform operating with the rotor (bullets) at a constant tip-speed ratio $\lambda = 5.0$ and at different inflow velocities.

Fig. 10.3 shows a comparison of the float potential-flow frequency-domain solution for the pitch and heave Response Amplitude Operators (RAOs) with the platform and rotor time-domain results. The Response Amplitude Operators are the ratio of the amplitude of a vessel's motion to the amplitude of incoming regular waves, presented for different encounter periods. The bullet points on the figure show the response of the floating platform in time domain, with the rotor, at different encounter periods and flow speeds. On this figure, a small yet non-negligible influence of the rotor on platform response is observed, in agreement with the results presented by Brown et al. [3].

Larger heave oscillations throughout the studied encounter periods are observed for the time-domain solution. The pitch response with rotor, however, varies depending on the encounter period. The pitch oscillations at encounter periods

below resonance show much larger amplitudes than the potential-flow RAOs, whereas above the maximum pitch RAO the amplitudes of the simulated time series are smaller than the frequency-domain response.

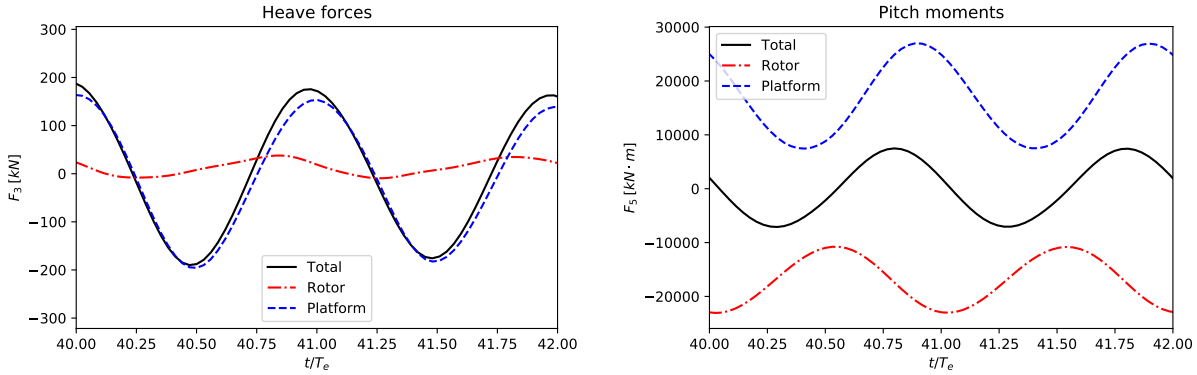

Figure 10.4: Extract from the time series: heave forces (left) and pitch moments (right) acting on the platform at a current speed $V_\infty = 3.0\,[m/s]$ and with a wave encounter period $T_e = 3.4\,[s]$.

The changes in pitch and heave responses are caused by a combination of factors, but mainly due to the rotor inducing large non-linear hydrodynamic loads on the system. Figure 10.4 shows an example comparing the sum of heave forces and pitch moments on the float, rotor and the total forces on the system, for waves with an encounter period $T_e = 3.4\,\mathrm{s}$ and a current speed $V_\infty = 3.0\,\mathrm{m/s}$. The figure highlights the importance and non-linear nature of the rotor loads for both degrees of freedom. The resulting interactions, however, between rotor and platform, depend not only on oscillation amplitudes but also on their phases, as discussed in the following section.

10.4.3 Rotor loads and performance

Fig. 10.5 shows thrust as a function of the encounter period for different inflow speeds. The points show the average loads and the shaded area represents the load fluctuations measured by two standard deviations. The plots compare a fixed rotor, with no degrees of freedom, with the floating rotor, free to move in pitch and heave.

The results show that the time averaged loads, both for the floating and fixed rotors, are not significantly affected by wave conditions nor by platform motions. Nevertheless, significant differences in oscillatory loads are observed between the

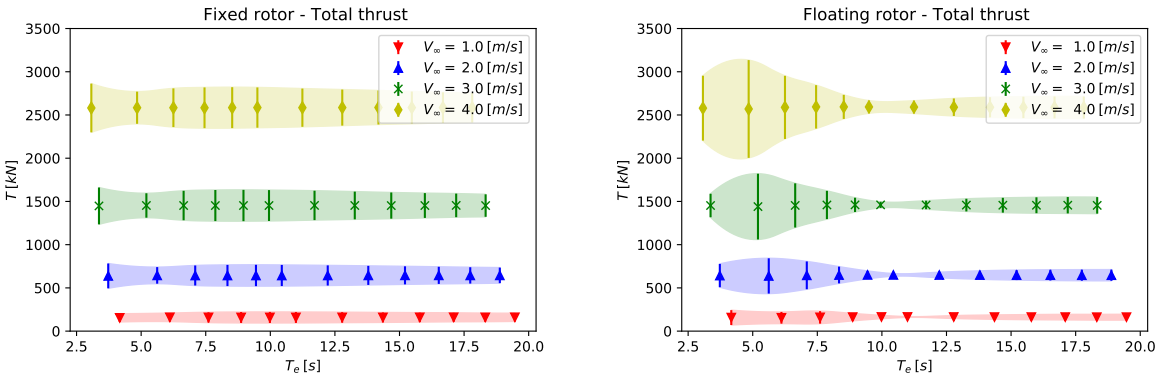

Figure 10.5: Mean thrust (bullet points) and thrust fluctuations for the fixed (left) and floating (right) rotors at different current and wave conditions. The thrust fluctuations are represented by two standard deviations (vertical bars and shaded areas).

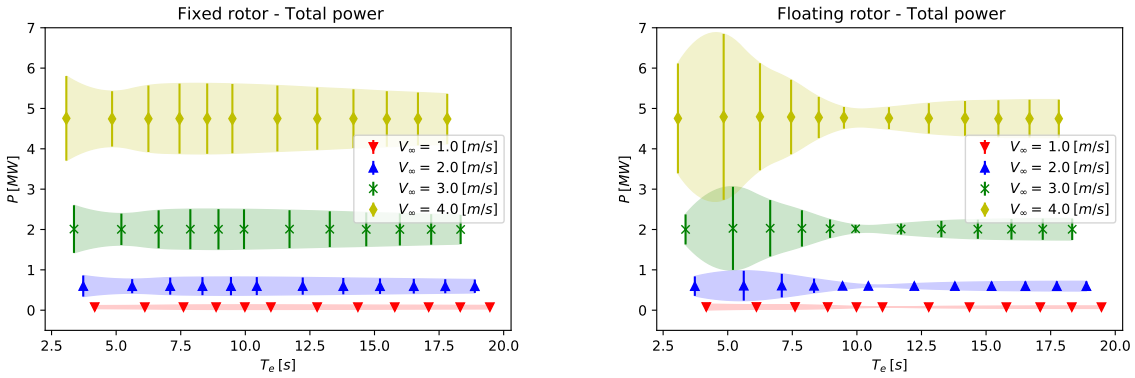

Figure 10.6: Mean power (bullet points) and power fluctuations for the fixed (left) and floating (right) rotors at different current and wave conditions. Power fluctuations represented by two standard deviations (vertical bars and shaded areas).

floating and the fixed rotors. At low encounter periods and for all flow speeds, the floating rotor shows larger oscillations in thrust. At encounter periods around 11 seconds, however, an abrupt reduction in load oscillations is observed for the floating rotor for all the inflow speeds. As the wave period increases beyond the cancellation zone, load oscillations increase on the floating platform but remain lower than for the fixed rotor. The same trends are observed for power, as shown in fig. 10.6.

The substantial change in the transient load amplitudes throughout the analysed period range on a floating rotor highlights the complexity of the rotor-platform interactions. The changes in oscillation amplitude, and especially the cancellation of transient loads at around 11 seconds encounter period, cannot be explained

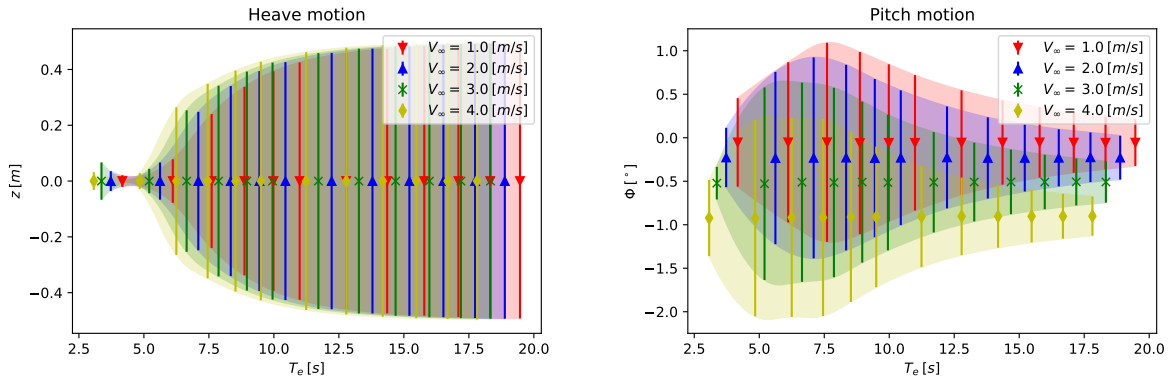

Figure 10.7: Mean and oscillatory fluctuations of heave (left) and pitch (right) motions for the floating platform with rotor as a function of encounter period for different inflow speeds. The motion fluctuations are represented by two standard deviations (error bars and shaded areas).

by abrupt changes in platform motion response, as evidenced by fig. 10.7. This figure shows that the heave and pitch responses present no abrupt changes in mean nor oscillatory components across the simulated wave periods, despite the influence of the wave frequency on rotor loads.

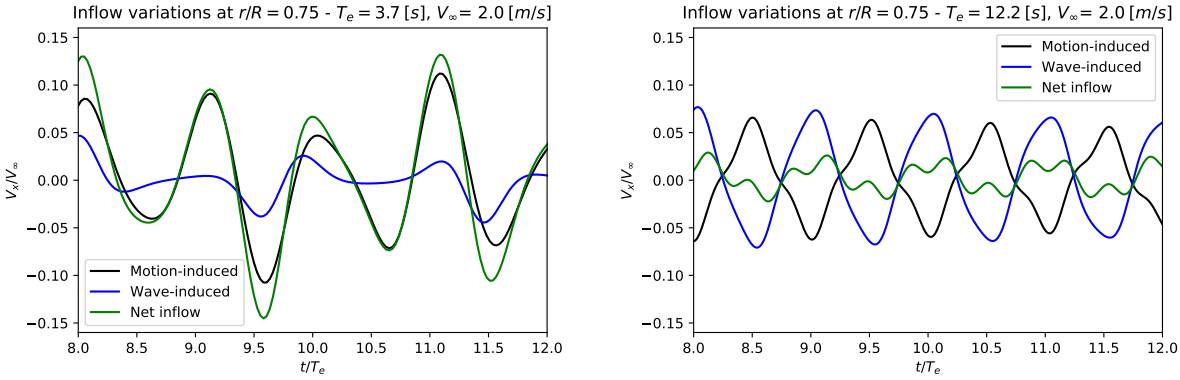

Figure 10.8: Axial inflow speed variations at $r/R = 0.75$ for a floating rotor operating at $V_\infty = 2.0\ [m/s]$ at two different wave encounter periods. The plots show the net inflow fluctuations alongside the wave- and motion-induced velocities. Note that only the velocity fluctuations, and not the undisturbed current, are shown.

Instead, the load cancellations are explained by the interactions between the inflow velocity fluctuations on the rotor blades that are induced by waves and platform motions. These two components affect the rotor blades in terms of frequency, phase and amplitude. The frequency of both components corresponds,

mainly, to the encounter frequency; their magnitude on wave height, excitation frequency, and platform response; and the phase, finally, depends on platform design, and excitation frequency.

Fig. 10.8 shows the axial velocity fluctuations induced by waves and motions for a blade section located at $r/R = 0.75$. The rotor is operating at the same inflow speed in both cases but the two plots show different encounter periods. The plot corresponding to $T_e = 3.7$ s shows a case where the inflow fluctuations are dominated by platform motions and where, given the phase between wave and motion oscillations, both components contribute to larger net inflow oscillations.

The second case in fig. 10.8, where $T_e = 12.2$ s, corresponds to the load cancellation previously discussed. This case shows similar oscillatory amplitudes for both the wave and motion induced velocities, but with a phase difference close to 180°. The result is a cancellation between the two components, resulting in a substantially smaller net inflow fluctuation which explains the significant reduction in thrust and power oscillations for this wave condition.

Note that, however, the time series in fig. 10.8 are the result of the wave and platform motion frequencies as sampled by the blade section at rotational frequency. The frequency components in the time series include, in addition to wave and rotational frequencies, harmonics of the combinations between those two components.

The amplitude of the velocity fluctuations also depends on the submergence depth, which for a blade section is a function of the azimuthal position of the blade. The different nature of waves and platform motions drive different azimuthal variations in blade loading. Waves, as shown in fig. 10.2, induce larger velocities near the free surface. Pitch motions, on the contrary, are likely to induce larger velocity fluctuations on blades at the bottom dead centre, the furthest possible location from the platform's centre of gravity.

Fig. 10.9 compares the mean and oscillatory components of thrust for a fixed rotor blade subject to a short and a long wave over the azimuth. The results show that the impact of waves on load fluctuations varies as a function of azimuthal

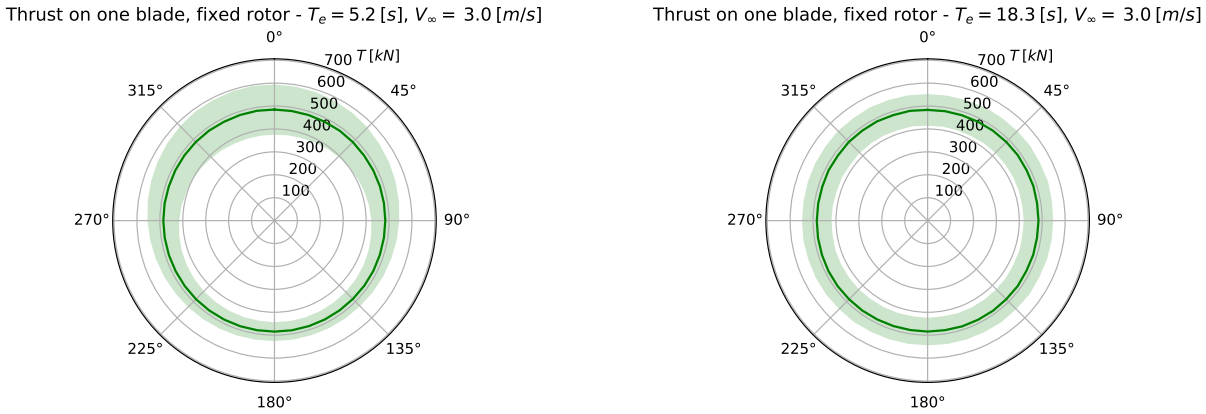

Figure 10.9: Azimuthal distribution of thrust on a single blade of a fixed rotor. The plot shows the mean thrust (solid line) and its oscillatory component, represented by two standard deviations (shaded area). The two plots present the rotor operating at different encounter periods and at a current speed $V_\infty = 3.0$ m/s. 0° corresponds to the top dead centre.

position, unlike the mean thrust. The transient loads show an asymmetry which is a consequence of the decay of wave-induced velocities with depth, with short wave effects more localised near the free surface. This is reflected in the results: for the short wave, the plot shows load fluctuations that are considerably larger near the top dead centre, whereas for the longer wave the load fluctuations are more symmetrical throughout the azimuth.

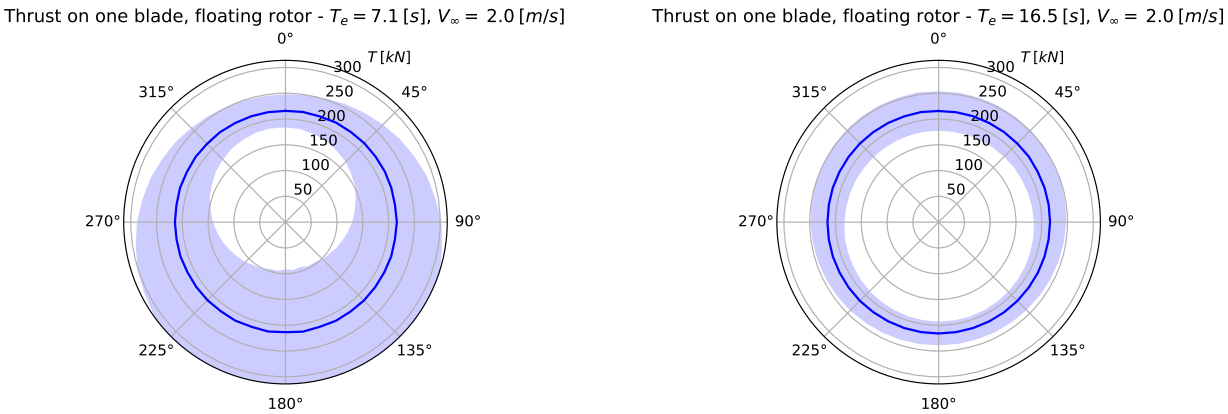

Figure 10.10: Azimuthal distribution of thrust on a single blade of a floating rotor. The plot shows the mean thrust (solid line) and its oscillatory component, represented by two standard deviations (shaded area). The two plots present the rotor operating at different encounter periods and at a current speed $V_\infty = 2.0$ m/s. 0° corresponds to the top dead centre.

The azimuthal fluctuations of thrust on a floating rotor depend on the dominant unsteady inflow component, waves or motions, and their interactions. Fig. 10.10 shows the azimuthal thrust distributions for one blade at $V_\infty = 2.0\,\mathrm{m/s}$ and under two wave periods. The periods were selected to be above and below the load cancellation region observed at encounter periods of approximately 11 s.

For the shorter wave, the azimuthal plot shows substantially larger thrust fluctuations at the bottom dead centre. These fluctuations are a consequence of the pitch motion, and explain the magnification of load fluctuations for the floating rotor below the load cancellation region. Shorter waves induce fast-frequency pitch motions, resulting in more significant changes in inflow speed, especially at the bottom dead centre. For the longer wave period, the load fluctuations are more symmetric through the azimuth compared with the shorter wave. Nevertheless, the plot highlights larger fluctuations at the top dead centre, implying a larger contribution of wave induced velocities to the inflow and load fluctuations. Finally, these results also highlight that the cancellations of the transient loads occurs in the transition between wave and pitch dominated load fluctuations.

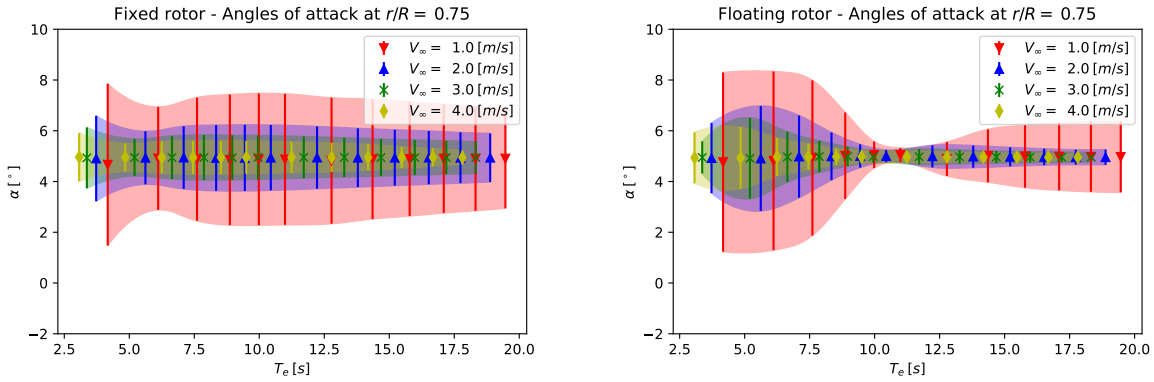

Figure 10.11: Mean angle of attack (bullet points) and angle of attack fluctuations (vertical bars and shaded areas) for the fixed (left) and floating (right) rotors at different currents and wave conditions. The variations in angle of attack are represented by two standard deviations.

The large thrust and power fluctuations predicted by the model are the consequence of significant variations in angles of attack. Fig. 10.11 shows the mean values and the fluctuations in angle of attack, measured by two standard deviations,

at a blade section $r/R = 0.75$. The plots present the different wave and current conditions on a fixed and a floating rotor.

The angles of attack show the same trends observed for the power and thrust: the mean angle of attack is not affected by waves nor current speed. The fluctuations of α, however, vary between the fixed and floating cases for different wave periods, as well as a function of the inflow speed.

Both the fixed and floating cases show decreasing fluctuations on angle of attack for increasing flow speeds. The cases where $V_\infty = 1.0\,\mathrm{m/s}$, both for the fixed and the floating rotors, show maximum fluctuations in the order $\pm 4°$. These are reduced to approximately $\pm 1°$ for the highest current due to a smaller relative magnitude of the wave- and motion-induced velocities with respect to the current speed.

The fixed rotor shows more stable fluctuations on α, compared to the floating rotor, through the range of encounter periods. Similar to the thrust case, the floating rotor shows an area at low encounter periods where the α oscillations are magnified due to the pitch-dominated induced velocities. The low encounter period zone is followed by the cancellation zone at approximately 11 s of encounter period previously discussed and, finally, the floating rotor shows smaller fluctuations on α than the fixed rotor for longer waves.

10.5 Discussion

This work presented an analysis of fixed and floating tidal rotors operating at current speeds between 1.0 and 4.0 m/s, under the influence of following waves aligned with the current. The wave lengths analysed had lengths between 35 m and 630 m, with a constant wave height of 1 m. The analysis was performed by coupling a time-domain seakeeping model with the dynamic BEM model described in chapter 9.

The results of the engineering model show three interesting aspects for floating tidal rotors. First, that the mean thrust and power show no variations due to the combined effects of currents and waves for fixed and floating rotors within the analysed range of conditions. This is in agreement with Brown et al. [3], Osman and Willden [12], and most of the literature presented in sec. 2.4.0.3. Second,

both the fixed and the floating rotors display significant oscillations in thrust and power under the combined effects of waves and currents. However, the results show that the oscillations are not necessarily larger for the floating rotor. The third interesting aspect is that a floating device might show increased or reduced fluctuations in thrust and power, compared with a fixed rotor, depending on the relative phase between motions and waves.

The floating rotor showed a cancellation of transient thrust and power fluctuations at an encounter period of approximately 11 s. This occurs at a specific frequency range where the amplitude of wave and motion induced velocities on the blades are of similar magnitude, and due to their relative phase, tend to cancel each other. This is a noteworthy result, since it implies that platform motions, often considered to be an undesirable effect, could instead be used to reduce the large fluctuations in power and thrust seen for a fixed rotor in waves aligned with the current direction. The specific frequency range where this occurs, however, depends on platform design and rotor response, and further studies are required to determine whether this could be effectively exploited as part of system design.

At encounter periods longer than the cancellation region, the floating rotor also displays lower thrust and power fluctuations than the fixed counterpart. At such low frequencies, wave-induced velocities change slowly, and the floating platform reacts, almost in a quasi-static manner, by moving and thus damping the fluctuations on the apparent inflow. It is not possible to generalise from this specific platform design, but the results suggest that even if complete load cancellation could not be attained on a practical basis, a floating platform could still operate with lower load fluctuations than a fixed rotor.

These results are to be regarded as preliminary. Several questions arise from the simplified conditions analysed, including the assumption of regular and following waves, which is just a set of special cases amongst a range of possible current and wave combinations. Irregular waves, affecting the platform from different directions, and exciting different degrees of freedom, are likely to induce effects that are relevant for study. The mooring system, not considered in this study, is

another key aspect for floating tidal energy. A specific mooring configuration will dominate the platform surge, sway and yaw responses, and it could, potentially, influence the response of the remaining degrees of freedom.

Similarly, questions arise regarding the limitations of the numerical model. In this study, the limitations associated with the physics that are being modelled have been minimised by the verification of the dynamic BEM model in section 9.3.2, and by selecting the analysis cases for the model to operate within the boundaries where its validity is sufficient, i.e. where no significant flow separation occurs.

Specifically, the analysis on the angles of attack show that the dynamic BEM model predictions were, for the analysed cases and at least for the areas of the blade where power and thrust are concentrated, within the boundaries considered valid for the dynamic BEM model in chapter 9. Note, however, that the case where $V_\infty = 1.0\,\mathrm{m/s}$ showed fluctuations at $r/R = 0.75$ close to the static stalling point for the Risø-A1-24 foil ($\alpha \approx 11°$). Nevertheless, no significantly different behaviours were observed for this flow speed in particular.

Fluid dynamic effects not captured by the model could be a significant source of uncertainty. The dynamic BEM model does not consider wave diffraction, and effects such as the added mass model are based on simplifications which ought to be tested in more detail. Even though the added mass has been shown not to significantly affect blade loads [6], its impact on platform motions is likely to be significant, as suggested by the changes in heave and pitch response in time-domain for the floating platform with rotor, compared with the frequency-domain RAOs. The interactions between the rotor, the platform, and the free surface are also neglected in this model, despite shown to affect performance and loads [3, 8]. In the presence of such interactions, the azimuthal symmetry of the mean thrust, shown in this study, is likely to be affected.

Nonetheless, and the availability of high-fidelity CFD models notwithstanding, engineering models are still likely to play a significant role in the analysis and design of offshore devices, where large number of cases and time-series make CFD computations prohibitive. The implementation, improvement and verification of

the engineering numerical model used in this study, based on the observations made on higher fidelity simulations, has enabled the analysis of a broad range of current and wave conditions for fixed and floating tidal rotors, showing interesting aspects and establishing potential areas for future research which could contribute to the development of cost-competitive renewable energies.

References

[1] ANSYS. "ANSYS AQWA theory manual 19.0". In: *ANSYS, Canonsburg, PA* (2018).

[2] A. Babarit and G. Delhommeau. "Theoretical and numerical aspects of the open source BEM solver NEMOH". In: *11th European wave and tidal energy conference (EWTEC2015)*. 2015.

[3] S. A. Brown et al. "On the impact of motion-thrust coupling in floating tidal energy applications". In: *Applied Energy* 282 (2021), p. 116246.

[4] W. E. Cummins. "The Impulse Response Function and Ship Motion". In: *Report 1661, Department of the Navy, David W. Taylor Model Basin, Hydromechanics Laboratory, Research and Development Report, October 1962* (1962).

[5] Det Norske Veritas (DNV). *Design of offshore steel structures, general - LRFD method*. Tech. rep. DNVGL-OS-C101. Standard. 2015.

[6] X. Guo et al. "The surface wave effects on the performance and the loading of a tidal turbine". In: *Ocean Engineering* 156 (2018), pp. 120–134.

[7] ITTC. *Seakeeping experiments*. Recommended Procedures and Guidelines. 2017.

[8] N. Kolekar, A. Vinod, and A. Banerjee. "On blockage effects for a tidal turbine in free surface proximity". In: *Energies* 12.17 (2019), p. 3325.

[9] C.-H. Lee. *WAMIT theory manual*. Massachusetts Institute of Technology, Department of Ocean Engineering, 1995.

[10] T. F. Ogilvie. "Recent Progress Toward the Understanding and Prediction of Ships Motion". In: *Proceedings of the 5th Symposium on Naval Hydrodynamics*. 1964, pp. 3–128.

[11] Orbital Marine Power. *Orbital O2 2MW*. `https://orbitalmarine.com/O2`. Accessed:2021-06-23. 2021.

[12] M. H. B. Osman and R. H. J. Willden. "Unsteady loading of a floating tidal turbine oscillating in a pendulum motion". In: *Developments in Renewable Energies Offshore*. CRC Press, 2020, pp. 563–570.

[13] G. T. Scarlett and I. M. Viola. "Unsteady hydrodynamics of tidal turbine blades". In: *Renewable Energy* 146 (2020), pp. 843–855.

Part VI

Conclusions

11
Conclusions

11.1 Blade deformation hydrodynamics

The study of flow-sampling methodologies enabled a consistent analysis of the hydrodynamics of a tidal rotor under different conditions, including tip-speed ratios, blockage, and blade deformations.

The flapwise and twist deformations of a tidal rotor blade were studied using blade-resolved CFD RANS simulations and shown to produce significant changes in the spanwise distribution of thrust and torque. The study was based on a parametrically-deformed rotor blade, with flapwise deformations in the range of 7.5% to 17.5% of rotor radius, and a range of $-5.0°$ to $+15.0°$ of twist deformation at the tip (positive angles deforming towards feather).

The two deformation components affect blade hydrodynamics through different mechanisms. The force changes due to modest twist deformations can be largely explained through blade element theory, as the force changes can be explained as a consequence of changes in local inflow speed and angle of attack. Flapwise deformations, to the contrary, induce spanwise flows that ultimately affect the sectional lift and drag coefficients, changes that cannot be explained through two-dimensional blade element theory.

Two different mechanisms affect thrust and torque on a blade bent in the streamwise direction. First, the deformed blade imposes a radial force on the flow. The radial force increments the radial flow speed through the rotor and forces streamtube expansion, which causes a reduction in static pressure on the suction side of the blade. The increase in suction drives an inboard load augmentation. Secondly, the radial flow affects the near-tip region. The onset of tip-loss effects moves inboard, and blades shed more thrust and torque than an undeformed blade would. For the case of thrust, these two opposite effects tend to cancel each other, showing a low net effect in integrated thrust. For the case of torque, however, the near-tip shedding is more significant and rotor performance is significantly affected.

The hydrodynamic effects of the flapwise and twist deformation were shown to be approximately independent from each other for moderate blade deflections. This has significant implications for the development and correction of models based on, e.g., blade element theory.

The hydrodynamic independence of modest flapwise and twist deformations was exploited to explore the potential of passive blade deformations for turbine control. A parameter space of tip-speed ratio, flapwise and twist deformations was constructed based on the hydrodynamic independence between the twist and flapwise deformations. Two control paths were designed within this parameter space, showing that moderate blade deflections, within what literature shows to be structurally feasible, can produce significant thrust and torque shedding at high flow speeds. The designed strategies outperformed a speed-controlled rotor with rigid blades, showing lower maximum thrust and a significant power capping above rated flow. The passive strategies showed a potential to achieve a similar maximum thrust and power capping compared to an idealised rotor with active pitch control.

11.2 Engineering modelling

The development of blade-resolved CFD simulations alongside a robust methodology for flow analysis allowed studying the constituents of a BEM model.

BEM models are based on solving blade element and momentum equations. The momentum equation is presented by a relationship between blade forces and axial and tangential induction factors. For the case of thrust, this combines an analytical model at low axial induction factors, and an empirical turbulent wake model used at high load regimes.

The CFD simulations highlighted substantial differences in the relationship between thrust coefficient and the axial induction factor when compared with a widespread turbulent wake model. The correction of this turbulent wake model produced an improvement in the BEM predictions of thrust and torque at the inboard sections of the blade.

With the corrected turbulent wake model, the biggest deficiency still remaining in BEM models is, potentially, tip-loss modelling. Prandtl's tip-loss model was shown to be insufficient to capture the hydrodynamic effects in the proximity of the blade tip, affecting the accuracy of BEM calculations and driving significant overestimations of thrust and torque, especially at high tip-speed ratios.

An analysis of a set of CFD simulations of a tidal rotor operating under different blockage ratios revealed an influence of blockage in the relationship between thrust and axial induction factors. Blockage was also shown to have no significant effects in the lift and drag coefficients, alongside a negligible influence in tip-loss effects for moderate blockage ratios.

Future work in this area is required for the improvement of BEM models for tidal rotors. A larger set of simulations and/or experiments will be studied in the future to understand whether the proposed turbulent wake model can be generalised for all rotor designs. This study will also enable to determine the effects of rotor design variables in the empirical momentum model, as well as generating a model for different blockage conditions. A further exploration of tip-loss effects is also considered, including the integration of the radial-loss observations within BEM-based models (where radial flow is neglected), and the exploration of correction models beyond function shape proposed by Prandtl.

11.3 Dynamic flow effects

The thrust and torque predicted with a dynamic BEM model was shown to produce a good agreement with blade-resolved CFD simulations for a tidal rotor under a prescribed pendular motion, for cases where no significant flow separation occurs.

This dynamic BEM model was coupled with a seakeeping time-domain model to analyse a floating tidal rotor under the combined influence of current and current-aligned following waves. This analysis showed that mean thrust and power were not significantly affected by waves nor by platform motions. However, significant load oscillations were observed for both fixed and floating rotors under combined waves and currents.

The floating rotor showed magnifications and reductions in thrust and power oscillations, compared with a fixed rotor, for following waves aligned with the current. The oscillation range depends on wave conditions, platform motion, and the relative phase between them. The floating rotor magnified the load oscillations at short waves, where the inflow fluctuations were dominated by pitch and increased by the wave-induced velocities. For longer waves, however, smaller load oscillations were observed for the floating platform. A load cancellation zone was identified at wave periods where wave- and motion-induced velocity fluctuations had a similar magnitude and a phase of approximately 180°

The analysis of a floating tidal platform highlights that load fluctuations are not necessarily larger for a floating rotor compared with a fixed device. Platform motions, initially considered as undesirable, could be exploited to reduce load fluctuations and, potentially, to improve the quality of power delivery.

Tidal rotors operating in proximity to the free surface, however, are still likely to be affected by significant thrust and torque fluctuations. The passive deformation strategies, shown as potential alternative to active pitch systems under steady-state assumptions, could also be exploited to reduce transient loads on rotor blades. Further studies, however, will be required to assess the feasibility of using passively deforming blades under transient flow effects.

Future work will include a further analysis and improvement of the dynamic BEM model to increase the predictive capabilities under separated-flow regimes that are necessary for extreme events analysis, as well as the extension of the analysis conditions to include misaligned waves and currents, other transient flow effects (shear, turbulence), and the inclusion of more elements in the model. More elements considered interesting to study are, e.g., mooring systems, blade deformations and multi-rotor interactions.

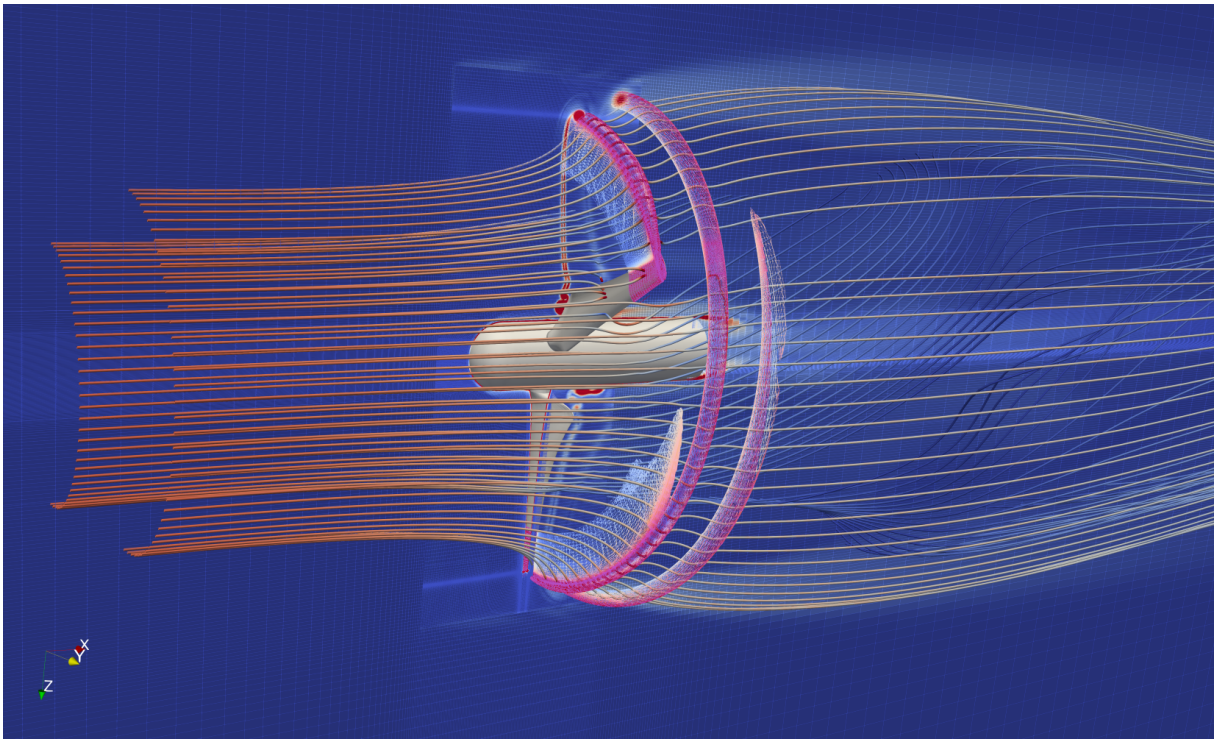
Y
Z